UNIVERSITÉ DE STRASBOURG

EDSC
École Doctorale des
Sciences Chimiques

ÉCOLE DOCTORALE SCIENCES CHIMIQUES

Institut de Chimie et Procédés pour l'Energie, l'Environnement et la Santé (ICPEES)

THÈSE présentée par :

Dingkai Chen

soutenue le : 15 décembre **2021**

pour obtenir le grade de : **Docteur de l'Université de Strasbourg**

Discipline/ Spécialité: Chimie / Chimie Physique

Etude de la chimie de surface d'électrodes en cermet pendant l'électrolyse du CO₂ à haute température

Investigation of the surface chemistry of cermet electrodes during high-temperature CO₂ Electrolysis

---

THÈSE dirigée par :

   M. ZAFEIRATOS Spyridon   Directeur de recherche CNRS, ICPEES

RAPPORTEURS :

   Mme. Le Gal La Salle Annie   Chargée de recherches CNRS, Université de Nantes
   M. Marnellos George   Professeur**,** University of Western Macedonia

---

AUTRES MEMBRES DU JURY :

   Mme. ROGER Anne-Cécile   Professeure, Université de Strasbourg
   M. Knop-Gericke Axel   Chef de Département, Fritz Haber Institute
                         of the Max Planck Society

This page intentionally left blank

To my family

This page intentionally left blank

Dingkai Chen

Etude de la chimie de surface d'électrodes en cermet pendant l'électrolyse du CO₂ à haute température

Abstract

Ni-yttria-stabilized zirconia (YSZ) and Ni-gadolinia-doped ceria (GDC) are the SoA cathode electrodes for SOEC operating under H_2O, CO_2 and CO_2/H_2O fuels. However, they are still facing degradation issues and low activation/conversion efficiency issues. Degradation can be categorized into irreversible and reversible effects. The former is related to the mechanical stability of the SOEC device such as loss of the TPB, delamination, and microstructural changes etc., which can be easily demonstrated by post-mortem analysis of the SOEC devices. Reversible phenomena, such as electrode oxidation, and reversible pollution (especially carbon) etc., are dynamic and depend very much on the operational conditions. Therefore, operando characterization technologies are required to understand the exact degradation mechanism to eradicate the degradation issues. In terms of low conversion efficiency issues, despite the fact that Ni/YSZ is promising as SOEC cathode electrocatalyst due to its low cost and good mechanical strength, it exhibits high overpotential losses and poor durability both in single cell and stacks studies. In response to these problems, modification/decoration of present Ni/YSZ material is continuously being proposed as a main direction for CO_2 electrolysis in SOECs. The principal objective of this work is to understand the electrode oxidation, which is believed to be one of the main caused for reversible degradation. This will be done through investigating the surface chemistry of two nickel-based cathode electrodes, Ni/GDC and Ni/YSZ, under SOEC feed gases and the effect of the electrode surface state in the electrocatalytic performance using near ambient-pressure X-ray photoelectron spectroscopy (NAP-XPS). Finally, based on the above research, our goal is to develop a more robust and active solid oxide electrode for SOC applications via modification/decoration of SoA Ni/YSZ.

Résumé

Les matériaux à base de Ni et zircone stabilisée à l'oxyde d'yttrium (YSZ) ou d'oxyde de cérium dopé au gadolinium (GDC) sont les électrodes cathodiques de référence pour les SOEC fonctionnant avec des combustibles comme H_2O, CO_2 et CO_2/H_2O. Cependant, elles sont toujours confrontées à des problèmes de dégradation et de faible efficacité d'activation/conversion. Les dégradations peuvent être classées en effets irréversibles et réversibles. Les premiers sont liés à la stabilité mécanique du dispositif SOEC, comme la perte du TPB, la délamination, les changements microstructuraux, etc. qui peuvent être facilement démontrés par l'analyse post-mortem des dispositifs SOEC. Les phénomènes réversibles, tels que l'oxydation des électrodes et la pollution réversible (en particulier le carbone), sont quant à eux dynamiques et dépendent fortement des conditions opérationnelles. Par conséquent, les technologies de caractérisation en conditions opératoires sont nécessaires pour comprendre les mécanismes de dégradation exacts et envisager leur éradication. En ce qui concerne les problèmes de faible activité, malgré le fait que le Ni/YSZ soit prometteur comme électrocatalyseur de cathode SOEC en raison de son faible coût et de sa bonne résistance mécanique, il présente néanmoins des pertes de surtension élevées ainsi qu'une faible durabilité dans les études de cellules individuelles et de piles. En réponse à ces problèmes, la modification/décoration du matériau Ni/YSZ actuel

est continuellement proposée comme solution principale pour l'électrolyse du CO_2 dans les SOECs. L'objectif principal de ce travail est de comprendre l'oxydation de l'électrode, qui est considérée comme l'une des principales causes de dégradation réversible du matériau. Pour ce faire, nous étudierons la chimie de surface de deux électrodes cathodiques à base de nickel, Ni/GDC et Ni/YSZ, sous gaz d'alimentation SOEC et l'effet de l'état de surface de l'électrode sur leurs performances électrocatalytiques en utilisant la spectroscopie photoélectronique à rayons X à pression quasi ambiante (NAP-XPS). Enfin, sur la base des recherches ci-dessus, notre objectif est de développer une électrode à oxyde solide plus robuste et plus active pour les applications en SOC via la modification/décoration du matériau Ni/YSZ de référence.

Acknowledgements

I would like to express my gratitude to all the people who supported me during my study for the PhD degree of Université de Strasbourg in ICPEES (Institut de chimie et procédés pour l'énergie, l'environnement et la santé). The **China Scholarship Council (CSC)** is greatly acknowledged for the financial supporting of my PhD study.

I will be always grateful to my PhD supervisor **Dr. Spiros Zafeiratos**, for his scientific guidance, fruitful discussion and constant support during my PhD. He is always readily available to help me to solve the problems and to provide me the instructions on my research. He is so kind and patient which provides a great atmosphere in the lab for conducting research. I really enjoy the time of staying in the lab.

I would like to thank my colleagues in our group, **Dr. Liping Zhong, Dr. Mathias Barreau and Dr. Vasiliki Papaefthimiou**. They are so generous to share their experience and knowledge with me and offer enormous help to me on both technical and scientific issues. I would like to thank **Liping** for recommending me to come here for my PhD. I am thankful for **Mathias** in helping me on the French summary and abstract. I am truly thankful also for **Vasiliki** in helping me on the revision of the thesis.

I would like to thank **Dr. Fabrice Bournel** and **Dr. Jean-Jacques Gallet** at TEMPO beamline of SOLEIL; thank **Dr. Knop-Gericke**, **Dr. Detre Teschner** and **Dr. Michael Hävecker** at ISISS beamline of HZB/BESSY II; The synchrotron experiments presented in this thesis would not be possible without their assistance.

I would like to thank **Dr. Dimitrios K. Niakolas** and **Dr. Stylianos G. Neophytides** from FORTH/ICE-HT for their collaboration in electro-catalytic measurements and calculations discussed in this thesis and their generous discussions and support.

I would like to thank **Dr. Sylwia Turczyniak-Surdacka, Kamil Sobczak** and **Marcin Strawski** in University of Warsaw for their collaboration in FIB-SEM-EDX, TEM-EDX and TOF-SIMS measurements in this thesis.

I would like to thank the members of my jury, **Dr. Le Gal La Salle Annie**, **Dr. Marnellos George**, **Dr. ROGER Anne-Cécile**, and **Dr. Knop-Gericke Axel** for their valuable comments and suggestions.

I would also like to thank the staff of the technical and administrative department in ICPEES, **Alain Rach**, **Sécou Sall**, **Michèle Thomas, Agnès Orb, and Julien Bertrand.** Thanks to **Dr. Thierry Dintzer** for helping me with SEM experiments.

Thanks of all my Chinese friends in Strasbourg (**Xiong Zhang**, **Qianwen Zheng**, **Jinming Zhang, Han Peng** …) for their company and help in my daily life and PhD study. Special thanks to **Yu Zhang** for her understanding, supporting and companionship.

Above all, I would like to thank **my parents and my brothers** for their enormous support during my PhD.

Table of Content

Résumé

a) Introduction

Ces dernières années, l'industrialisation mondiale a entraîné une forte demande en combustibles fossiles tels que le gaz naturel, le pétrole et le charbon, ce qui a considérablement augmenté les niveaux de gaz à effet de serre dans notre atmosphère, responsables du changement climatique indésirable et de la destruction de l'environnement [1]. Il est donc urgent de développer des alternatives écologiques aux combustibles fossiles et des technologies énergétiques neutres en carbone pour résoudre les problèmes environnementaux et énergétiques. Pour convertir le CO_2 en produits à plus haute valeur ajoutée, il faut d'abord le transformer en une molécule plus active chimiquement, par exemple le monoxyde de carbone. L'électrolyse du CO_2 en CO à température élevée à l'aide de Cellules d'Electrolyse à Oxyde Solide (SOEC) apparaît comme une solution très prometteuse pour un stockage d'énergie à grande échelle hautement efficace [2], car elle offre un rendement énergétique élevé par rapport aux méthodes à basse température. En outre, l'électrolyse à oxyde solide du CO_2 est également étudiée comme technique de régénération de l'oxygène pour les missions spatiales vers Mars. Cette année, une démonstration technologique "Mars Oxygen In-Situ Resource Utilization Experiment (MOXIE)" a permis de convertir le dioxyde de carbone en oxygène sur Mars, ce qui constitue une étape importante dans l'exploration humaine future de la planète rouge. Cette technologie pourrait être mise à l'échelle pour être utilisée dans le cadre d'une mission sur la planète afin de fournir de l'oxygène respirable, un oxydant et un propergol [3].

Malgré les efforts considérables consacrés à la conception et la préparation de nouveaux électrocatalyseurs présentant une activité et une stabilité élevées, les composites de céramique et de métal (cermets), qui ont été précédemment optimisés pour les piles à combustible à oxyde solide (SOFC), restent les électrodes cathodiques de référence pour les SOEC [4]. Actuellement, les deux principales électrodes cathodiques de référence en cermet sont le nickel combiné à la zircone stabilisée à l'oxyde d'yttrium (Ni/YSZ) ou à l'oxyde de cérium dopé au gadolinium (Ni/GDC). Cependant, les SOEC basées sur des cathodes en cermet à base de nickel sont encore confrontées à de nombreux défis, principalement associés à des problèmes de dégradation et à une faible efficacité d'activation/conversion du CO_2. Les problèmes de dégradation peuvent être classés en effets réversibles et irréversibles. Les effets irréversibles sont liés à la stabilité mécanique du dispositif SOEC, comme la perte de la frontière triphasée (TPB pour « Three-Phase Boundary »),

la délamination, les changements microstructuraux, etc. Tous ces problèmes peuvent être facilement démontrés par l'analyse post-mortem des dispositifs SOEC et sont donc bien décrits dans la littérature [5]. Les phénomènes réversibles, tels que l'oxydation des électrodes, la pollution réversible par les contaminants, etc. sont dynamiques et dépendent beaucoup des conditions opérationnelles. Par conséquent, de nouvelles technologies de caractérisation *operando* sont nécessaires pour comprendre le mécanisme exact de dégradation et éradiquer les problèmes de dégradation.

Ce travail se concentre sur la compréhension de l'oxydation de la surface de l'électrode, qui est considérée comme l'une des principales raisons de la dégradation réversible. Il s'agit d'abord d'étudier la chimie de surface de deux électrodes cathodiques de référence à base de nickel, Ni/GDC et Ni/YSZ, sous atmosphère d'alimentation SOEC, puis d'étudier l'effet de l'état de surface de l'électrode sur la performance électrocatalytique en utilisant principalement la spectroscopie photoélectronique à rayons X à pression quasi ambiante (NAP-XPS). Enfin, sur la base des recherches ci-dessus, une électrode à oxyde solide robuste et active a été développée pour les applications SOC *via* la modification/décoration de la surface de Ni/YSZ avec des nanoparticules d'oxyde de cérium.

b) Résultats et discussions

I. Oxydation superficielle d'électrodes cermet à base de Ni par CO_2 et H_2O et fabrication d'électrodes Ni/YSZ à surface modifiée tolérant l'oxydation par CO_2

Au début de mes recherches, j'ai utilisé la technique de NAP-XPS en conditions *in situ* pour comparer l'oxydation du Ni/GDC et du Ni/YSZ sous atmosphère de H_2O et de CO_2 à 700 °C. Pour assurer la reproductibilité des conditions de traitement, deux échantillons ou plus ont été montés ensemble à proximité immédiate de la céramique chauffante et traités ensemble dans des atmosphères de CO_2 ou de H_2O (pression maximale jusqu'à 10 mbar). Initialement, les échantillons ont été traités à la température (700 °C) et à la pression de gaz souhaitées, pendant une durée déterminée, puis ont été refroidis à 350 °C (la température minimale possible pour garantir l'absence de charge électrostatique importante pendant l'analyse XPS). Une atmosphère gazeuse a été maintenue pendant les mesures de NAP-XPS mais la pression a été abaissée à 0,1 mbar. Les spectres NAP-XPS ont été obtenus en sélectionnant les énergies des photons d'excitation de manière à produire des photoélectrons ayant la même énergie cinétique (environ 200 eV et 480eV)

pour les éléments examinés, ce qui permet d'effectuer des mesures à deux profondeurs différentes (1,5 nm ou 3 nm).

L'état chimique à la surface des électrodes en cermet à base de Ni pré-réduites a d'abord été examiné après exposition à des atmosphères de H_2O ou de CO_2 dans des conditions isothermes. La Figure 1 présente une comparaison des pics de photoémission Ni 2p3/2 des électrodes Ni/YSZ et Ni/GDC après des traitements sous H_2O et sous CO_2 à 700 °C. Il est évident que le dosage, ou l'exposition (c'est-à-dire la pression du gaz × le temps) des deux gaz est très différente dans les deux cas (0,12 MPa-s pour H_2O contre 4,35 MPa-s pour CO_2). Ceci est lié au fait que des expériences préliminaires NAP-XPS ont été utilisées pour estimer l'efficacité des deux gaz à oxyder les électrodes dans les conditions employées. Ces expériences ont révélé que dans le cas de H_2O, l'oxydation du nickel a lieu à des pressions et des temps d'exposition nettement inférieurs à ceux du CO_2. Par conséquent, les conditions de traitement ici n'étaient pas identiques pour les deux atmosphères gazeuses, comme on pourrait le prévoir, mais elles ont été correctement sélectionnées de manière à produire des états d'oxydation du nickel similaires. Dans les deux atmosphères gazeuses, les spectres Ni 2p3/2 (figure 1a) sont une convolution des contributions métalliques (Ni^0) et oxydées (Ni^{2+}) du nickel à 852,7 et 855,6 eV [6,7]. L'état d'oxydation moyen du nickel x (NiO_x) montré dans la figure 1b, a ainsi été estimé par déconvolution du pic Ni 2p3/2 en composantes Ni^0 et Ni^{2+}.

La figure 1b montre l'état d'oxydation du nickel pour les deux électrodes sous le même gaz, calculé par déconvolution des spectres Ni 2p3/2. Il a été trouvé que dans le cas du CO_2 le nickel est plus oxydé dans le matériau Ni/YSZ comparé au matériau Ni/GDC, tandis que la tendance est inversée dans H_2O où plus de nickel oxydé est trouvé pour le Ni/GDC. Ces résultats montrent que le degré d'oxydation du nickel par le CO_2 et le H_2O n'est pas similaire, comme il est généralement anticipé, mais qu'il est régulé par la présence ou non d'oxyde de cérium dans le cermet. En particulier, la cérine favorise l'oxydation du nickel par H_2O mais la modère dans le CO_2.
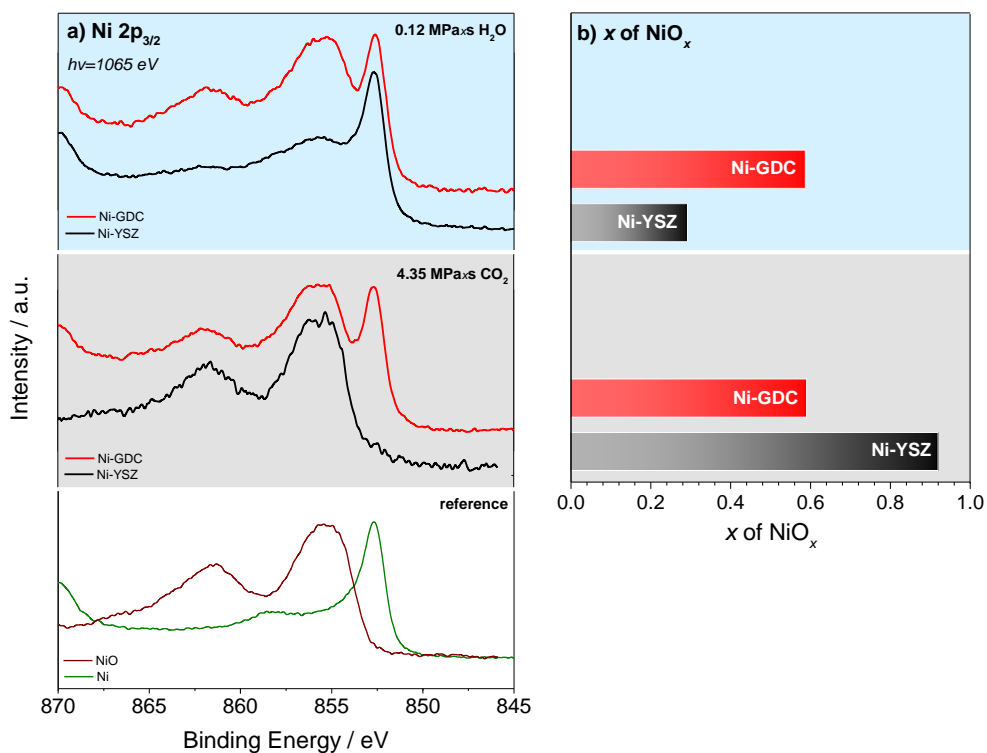
Figure 1. (a) Spectres NAP-XPS de Ni 2p (hν = 1065 eV) des cermets Ni/YSZ et Ni/GDC après traitement sous H_2O (en haut) et CO_2 (au milieu). Les spectres Ni 2p3/2 enregistrés sous O_2 et H_2 sont utilisés comme référence des états d'oxydation NiO et Ni^0 respectivement. (b) Diagramme à barres montrant l'état d'oxydation moyen x du nickel à 1,8 nm de la surface calculé après déconvolution des spectres Ni 2p3/2 NAP-XPS montrés dans la figure 1a en utilisant les pics de référence NiO et Ni^0. Avant l'exposition à H_2O ou à CO_2, les deux cermets ont été réduits sous H_2. Conditions de traitement pour H_2O : 0.5 mbar pendant 40 min à 700 °C (dosage global 0.12 MPa-s). Conditions de traitement pour CO_2 : 3,5 mbar pendant 90 min, 7 mbar pendant 30 min, 10 mbar pendant 20 min (consécutives) à 700 °C (dosage global 4,35 MPa-s). L'échantillon a été maintenu à 350 °C sous 0,1 mbar dans la même atmosphère gazeuse que le traitement pour éviter les changements d'état d'oxydation pendant les mesures NAP-XPS.

Afin de montrer que la cérine, lorsqu'elle est située en surface, peut augmenter la tolérance du Ni à l'oxydation par le CO_2, des électrodes Ni/YSZ ont été modifiées en introduisant des nanoparticules d'oxyde de cérium (NiCe) directement à leur surface. Les figures 2a et b présentent les spectres de Ni 2p3/2 des échantillons pré-réduits après des traitements identiques dans 1 et 10 mbar de CO_2 à 700 °C. L'état d'oxydation du nickel des deux échantillons obtenu à partir de la

déconvolution du pic Ni 2p est comparé dans la figure 2c. Dans le cas de l'électrode Ni/YSZ, l'oxydation du nickel commence déjà à de très faibles dosages de CO_2 (même à 1 mbar de pression) et continue presque linéairement avec le dosage. Au contraire, dans le cas du Ni/YSZ modifié avec NiCe, le nickel résiste à l'oxydation même après des expositions au CO_2 relativement élevées (jusqu'à 80 min d'exposition à 10 mbar de CO_2). Des tests comparatifs ont montré que l'oxydation de surface du Ni/YSZ par le CO_2 peut être empêchée jusqu'à 100 % dans certaines conditions après modification avec de l'oxyde de cérium, ce qui suggère une stratégie prometteuse pour produire des cellules à oxyde solide plus robustes et plus stables en termes d'oxydoréduction pour l'électrolyse du CO_2.
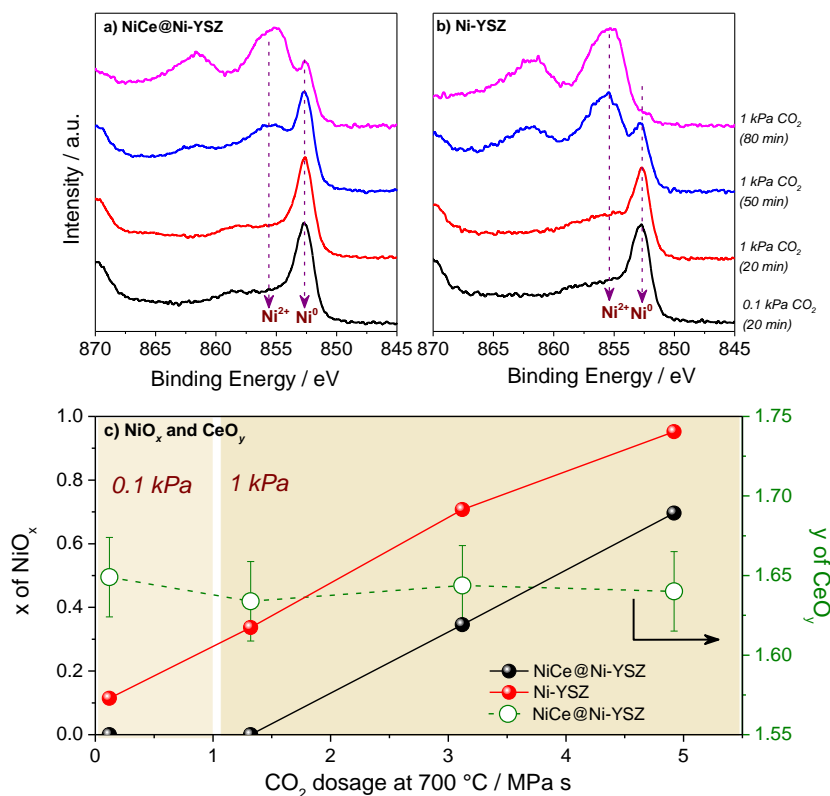
Figure 2. Spectres Ni 2p3/2 (hv=1065 eV) après différents dosages consécutifs de CO_2 à 700 °C pour a) les électrodes NiCe@Ni/YSZ et b) Ni/YSZ, c) Les états d'oxydation de surface de Ni (x de NiO_x) et Ce (y de CeO_y) des deux électrodes, selon l'analyse des spectres NAP-XPS de Ni 2p (hv=1065 eV) et Ce 3d (hv=1350 eV) en fonction de la dose de CO_2 à 700 °C.

II. Comment l'état de surface des cathodes au nickel/oxyde de cérium dopé au gadolinium influence les performances électrochimiques dans l'électrolyse directe du CO_2

Après l'étude du processus d'oxydation du Ni/GDC et du Ni/YSZ en équilibre avec le CO_2 et le H_2O, la thèse continue en étudiant l'effet de l'état de surface de l'électrode sur la performance électrochimique du CO_2. Pour ce faire, des SOEC avec des cathodes poreuses réalistes en Ni/GDC ont été étudiées dans des conditions d'électrolyse directe du CO_2 (c'est-à-dire sans gaz réducteur dans l'alimentation) en partant de différents états d'oxydation de surface. Ceci a été réalisé en combinant la technique NAP-XPS avec des mesures électriques et de spectrométrie de masse en ligne, comme le montre la figure 3a. Les conditions de fonctionnement choisies, à savoir du CO_2 pur et des tensions inférieures au seuil de dépôt de carbone, permettent de se concentrer sur l'effet de l'état d'oxydation de la surface et de lever les complications liées aux modifications dues au dépôt irréversible de carbone. Plus précisément, les SOEC avec des cathodes Ni/GDC ont été prétraitées dans la cellule du spectromètre sous H_2, O_2 ou H_2O à 700°C avant l'introduction du CO_2 pour son électrolyse. Dans tous les cas, la pression a été maintenue à 0,1 mbar. Les spectres XPS de Ni 2p et de Ce 3d ont été analysés à l'aide du logiciel CasaXPS pour révéler l'état d'oxydation du Ni et du GDC respectivement.

L'analyse en ligne de la phase gazeuse combinée aux spectres NAP-XPS (Fig. 3b, c, d) de la cellule Ni/GDC prétraitée dans H_2O (ci-après dénommée NiGDC pré-ox) montre que du CO est détecté dans la phase gazeuse uniquement après réduction partielle du NiO. Sur la base de cette observation, on peut affirmer que l'électrolyse du CO_2 ne peut pas avoir lieu sur des cathodes dont le NiO est complètement oxydé, ce qui révèle que le Ni métallique est une condition préalable à l'électrolyse du CO_2, du moins à des potentiels faibles. La réduction du NiO lors de la polarisation dans le CO_2 montrée dans la Figure 3c implique que l'addition de gaz réducteurs au CO_2 n'est pas indispensable pour maintenir l'électrode en cermet à l'état réduit. Afin de démontrer le rôle de l'oxyde de cérium pendant le processus électrochimique du CO_2, la valence moyenne de l'oxyde de cérium (CeO_y) en fonction de la densité de courant de la cellule est présentée dans la Figure 3e. Il ressort clairement de la figure 3e que, bien que l'état d'oxydation de l'oxyde de cérium s'adapte rapidement à l'atmosphère de CO_2, juste avant la polarisation, l'électrode NiGDC pré-ox reste plus oxydée que la.NiGDC pré-réd. Cependant, pendant la polarisation ascendante, l'état d'oxydation de l'oxyde de cérium est réajusté à un état d'équilibre de $CeO_{1.72}$ et reste pratiquement inchangé dans la courbe descendante, même après un prétraitement réducteur (NiGDC pré-réd). Cette

découverte indique que les zones GDC sont une source d'ions oxygène mobiles, soit en stockant et en libérant de l'O₂ dans les sites vacants, soit en adaptant leur état d'oxydation.
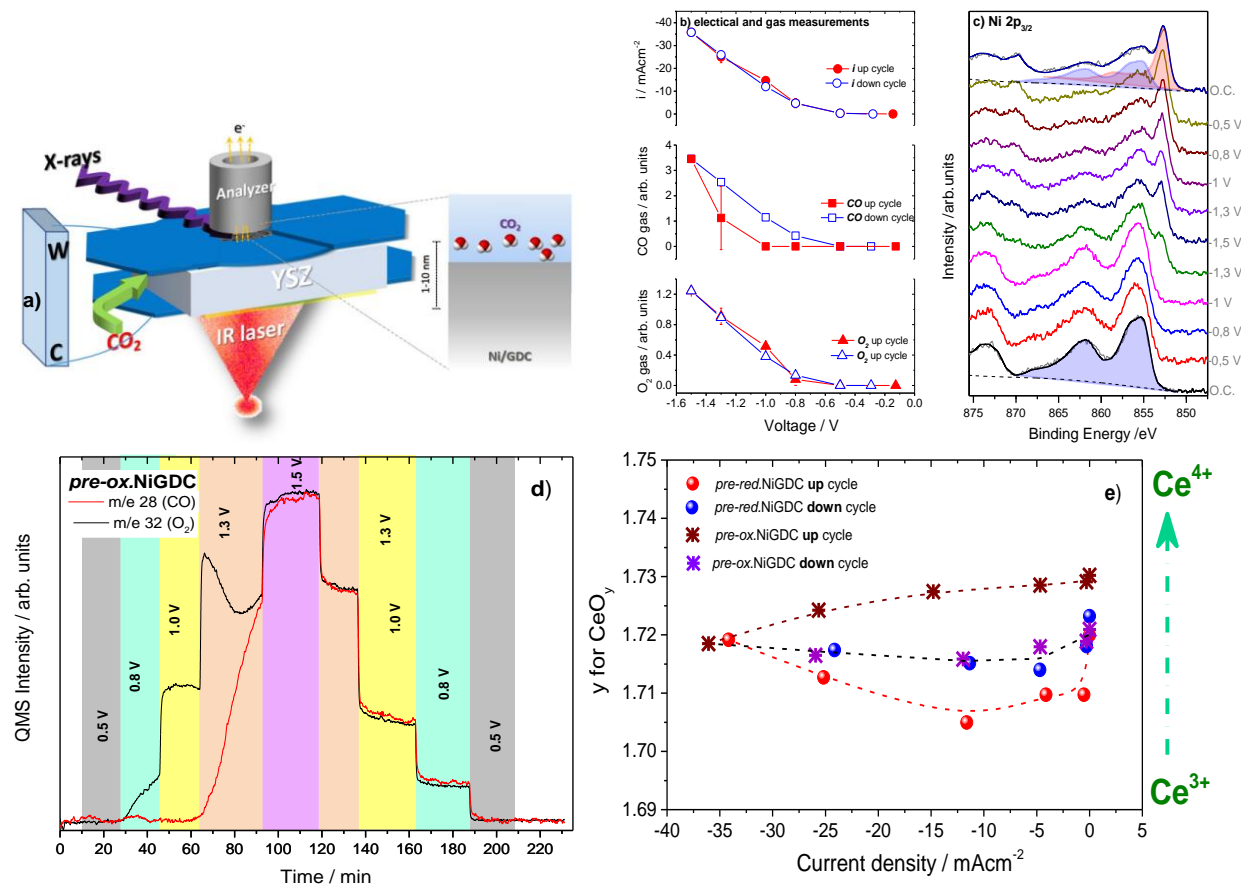
Figure 3. (a) Schéma décrivant le montage expérimental. La cellule est basée sur un électrolyte à oxyde solide dense en zircone stabilisée à l'yttrium (YSZ), avec de l'oxyde de cérium poreux dopé au Gd (Ni/GDC) comme électrode de travail et du Pt poreux comme contre-électrode. Cathode NiGDC pré-oxydée (b) Evolution de la densité de courant de la cellule (en haut), du signal QMS du gaz CO (au milieu) et du signal QMS du gaz O₂ (en bas) en fonction de la tension appliquée pour les courbes de potentiel haut (rouge) et bas (bleu). (c) Spectres NAP-XPS de la raie Ni 2p3/2 (hν =1065 eV) enregistrés sous différents potentiels appliqués dans 0,1 mbar de CO₂ à 700 °C. (d) Evolution des signaux CO (m/e 28) et O₂ (m/e 32) de la phase gaz en fonction du temps enregistrés dans la chambre NAP-XPS par spectrométrie de masse en ligne. Les mesures ont été effectuées à 700 °C dans 0.1 mbar de CO₂ sous différents potentiels appliqués (mis en évidence par des couleurs différentes dans la figure) sur une cellule pré-oxydée dans le spectromètre. Avant les tests électrochimiques, la cellule a été prétraitée dans le spectromètre sous 0,1 mbar de O₂ à 500 °C puis

dans 0,1 mbar de H_2O à 700 °C pendant une durée totale de 1 h.(e) La valence moyenne de l'oxyde de cérium, calculée par le pic photoélectronique Ce 3d en fonction de la densité de courant de la cellule. Les données ont été enregistrées lors de la polarisation cathodique dans 0,1 mbar de CO_2 à 700 °C. Le prétraitement et la séquence d'enregistrement sont indiqués dans la figure. Les lignes servent de guide à l'œil.

III. Une méthode simple et efficace pour infiltrer des nanoparticules d'oxyde de cérium dans des électrodes cermet Ni/YSZ préfabriquées

Pour une application pratique en électrolyse du CO_2, dans les mêmes conditions de réaction, le Ni/GDC possède généralement une meilleure performance électrochimique et est potentiellement plus stable que le Ni/YSZ [8], car il peut tolérer de meilleures conditions oxydantes en cas de fuite ou pendant les périodes d'arrêt [9]. Cependant, les cermets Ni/GDC présentent certains inconvénients par rapport au Ni/YSZ, liés à leur moindre stabilité mécanique et à leur coût plus élevé [10]. Intrigués par cette observation, nous tentons de combiner les propriétés mécaniques robustes du Ni/YSZ avec la résistance accrue à l'oxydation du CO_2 du matériau à base de cérium. La cérine fonctionnera comme une source d'ions oxygène mobiles pendant la polarisation, comme démontré dans les deux parties précédentes. En théorie, l'introduction de cérine à la surface du Ni/YSZ peut fournir des sites d'interface d'oxyde de cérium abondants dans l'électrode Ni/YSZ et améliorer les pertes de surtension élevées et les problèmes de faible durabilité, tout en conservant les avantages du Ni/YSZ, à savoir une excellente stabilité thermique et mécanique. Cependant, passer d'un concept à un dispositif électrochimique pratique n'est pas simple et nécessite d'affronter et de résoudre de nombreux problèmes techniques. En examinant la littérature sur les méthodes d'infiltration sur les électrodes en cermet, nous avons rencontré plusieurs difficultés majeures, telles que des méthodes de préparation laborieuses avec de multiples cycles d'imprégnation/calcinations/réduction, des problèmes de colmatage des pores, etc. qui sont en fait un frein à la mise à l'échelle et à l'utilisation pratique.

Par conséquent, dans cette thèse, une stratégie d'infiltration nouvelle et simple a été développée pour introduire de la cérine à la surface d'électrodes de cermet Ni/YSZ préfabriquées *via* l'imprégnation de nanoparticules (NPs) de cérine diluées dans une solution d'hexane. De cette façon, les défis de l'infiltration avec des solutions aqueuses (faible mouillabilité, précipitation des précurseurs, etc.) et les complexités de l'utilisation de surfactants, ont pu être surmontés. Afin de mieux comprendre et contrôler la méthode d'infiltration, deux types de nanoparticules d'oxyde de

cérium ont été préparés en solution organique: i) des NPs de CeO_x et ii) des NPs de $Ni_{0.1}Ce_{0.9}O_{2-y}$ (ci-après dénommées $NiCeO_y$), selon la méthode proposée [11,12]. Dans un premier temps, les propriétés physico-chimiques des nanoparticules de cérium en solution ont été étudiées par plusieurs méthodes de caractérisation. Ensuite, les deux types NPs ont été infiltrées dans le Ni/YSZ et leur morphologie et microstructure ont été étudiées après infiltration sur le squelette poreux de la cathode.

Tout d'abord, des analyses par FTIR indiquent que la composition de la couche organique autour des deux types de NPs est identique, et correspond à l'oléylamine (OLA). Les résultats d'ATG montrent que les solutions organiques des NPs de CeO_x et $NiCeO_y$ ont une concentration massique similaire (4.4 ± 0.3 mg/ml). Les résultats de XRD montrent que la taille des cristallites des NPs de CeO_x et $NiCeO_y$ est d'environ 4.8 ± 0.2 nm et 3.8 ± 0.2 nm respectivement, ce qui démontre que les deux nanoparticules à base de cérium diluées dans une solution d'hexane sont relativement petites (3~5 nm), confirmant que la méthode de synthèse appliquée est capable de produire des particules de cérium de taille nanométrique. La technique de diffusion dynamique de la lumière (DLS) est utilisée pour déterminer le profil de distribution de taille des particules de CeO_x et $NiCeO_y$ dans leur solution [13]. Il est à noter que les mesures de DLS fournissent ce que l'on appelle le rayon hydrodynamique, qui est la taille globale des particules incluant également la couche protectrice organique. Les résultats de la DLS (Fig. 4a) montrent que la majorité (73%) des NPs de CeO_x dans la solution d'hexane forme des agrégats avec une taille d'environ 2.29 µm, ce qui est presque 3 fois plus grand que les NPs de $NiCeO_y$ (0.82 µm, 87% des particules). Bien que l'on s'attende à des NPs de CeO_x plus grandes d'après les résultats de la XRD (4.8 vs. 3.8 nm), la taille des particules mesurée par DLS est à de l'ordre du micron, ce qui bien sûr ne peut pas être simplement dû au revêtement environnant (en général la molécule d'OLA a une longueur de chaîne d'environ 2.0 nm). Par conséquent, les résultats de la DLS reflètent que les nanoparticules de CeO_x forment des agglomérats plus grands dans la solution d'hexane par rapport au $NiCeO_y$, comme le montre la figure 4b.
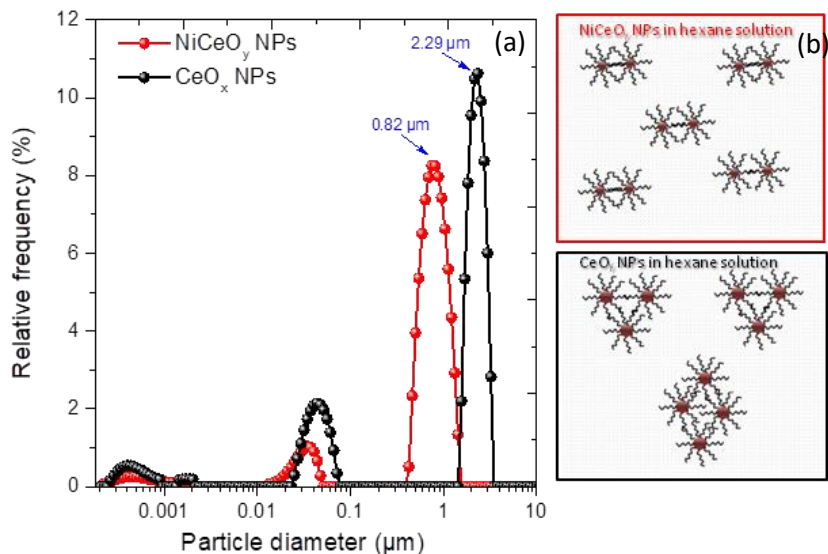
Figure 4. (a) Distribution de la taille des particules de NiCeO$_y$ et CeO$_x$ dans leurs solutions organiques par mesure DLS. (b) Représentation schématique de l'arrangement des NPs de NiCeO$_y$ et CeO$_x$ dans leurs solutions organiques.

Ainsi, les solutions de NPs de CeO$_x$ et de NiCeO$_y$ ont été infiltrées directement à la surface des électrodes Ni/YSZ sur une surface d'environ 64 mm^2 à l'aide d'une micropipette de 10 µL, comme le montre schématiquement la figure 5a. La distribution verticale de l'oxyde de cérium dans l'électrode Ni/YSZ a été examinée par microscopie électronique à balayage à faisceau d'ions focalisé (FIB-MEB) en coupe transversale, combinée à une cartographie élémentaire par spectroscopie de rayons X à dispersion d'énergie (EDS). Les images présentées dans les figures 5b,c correspondent à deux demi-cellules Ni/YSZ//YSZ identiques infiltrées avec 100 µL de NPs de NiCeO$_y$ (figure 5b) ou de CeO$_x$ (figure 5c) (soit une charge de cérium de 170 mg/cm^3). Dans les deux cas, la solution a été déposée sur des électrodes Ni/YSZ pré-réduites, en deux étapes d'infiltration/co-cuisson (50 µL à chaque fois). La couche poreuse du cermet Ni/YSZ, la barrière dense de YSZ et l'électrolyte peuvent être distinguées dans les micrographies MEB. La cartographie élémentaire EDS met en évidence les zones de nickel (bleu) et d'YSZ (vert), ainsi que les vides (pores) dans le cermet. Ce qui est bien sûr plus intéressant ici est la distribution du signal de cérium (en rouge) dans le volume Ni/YSZ. Il est clair que dans le cas du 100NiCeOy@Ni/YSZ, les nanoparticules de cérium sont uniformément dispersées dans le volume de l'électrode Ni/YSZ. Il est remarquable qu'il n'y ait pas de différence claire dans les zones de cérium entre les parties internes et externes de l'électrode. Au contraire, pour le 100CeOx@Ni/YSZ, le dépôt préférentiel

d'oxyde de cérium sur le dessus de l'électrode est évident, bien qu'une minuscule fraction de particules d'oxyde de cérium puisse être détectée dans les couches plus profondes (évidemment, celles-ci sont liées aux agrégats de NPs plus petits).

Les résultats présentés ci-dessus suggèrent que la meilleure dispersion des NPs en solution (i.e. $NiCeO_y$) influence la perméabilité dans l'électrode pendant le processus d'infiltration et favorise la distribution à l'intérieur des pores de l'électrode Ni/YSZ. Au contraire, les solutions contenant des NPs agglomérées (i.e. CeO_x) mèneront éventuellement à la précipitation des NPs principalement sur la surface de l'électrode, ce qui devrait en principe être évité.
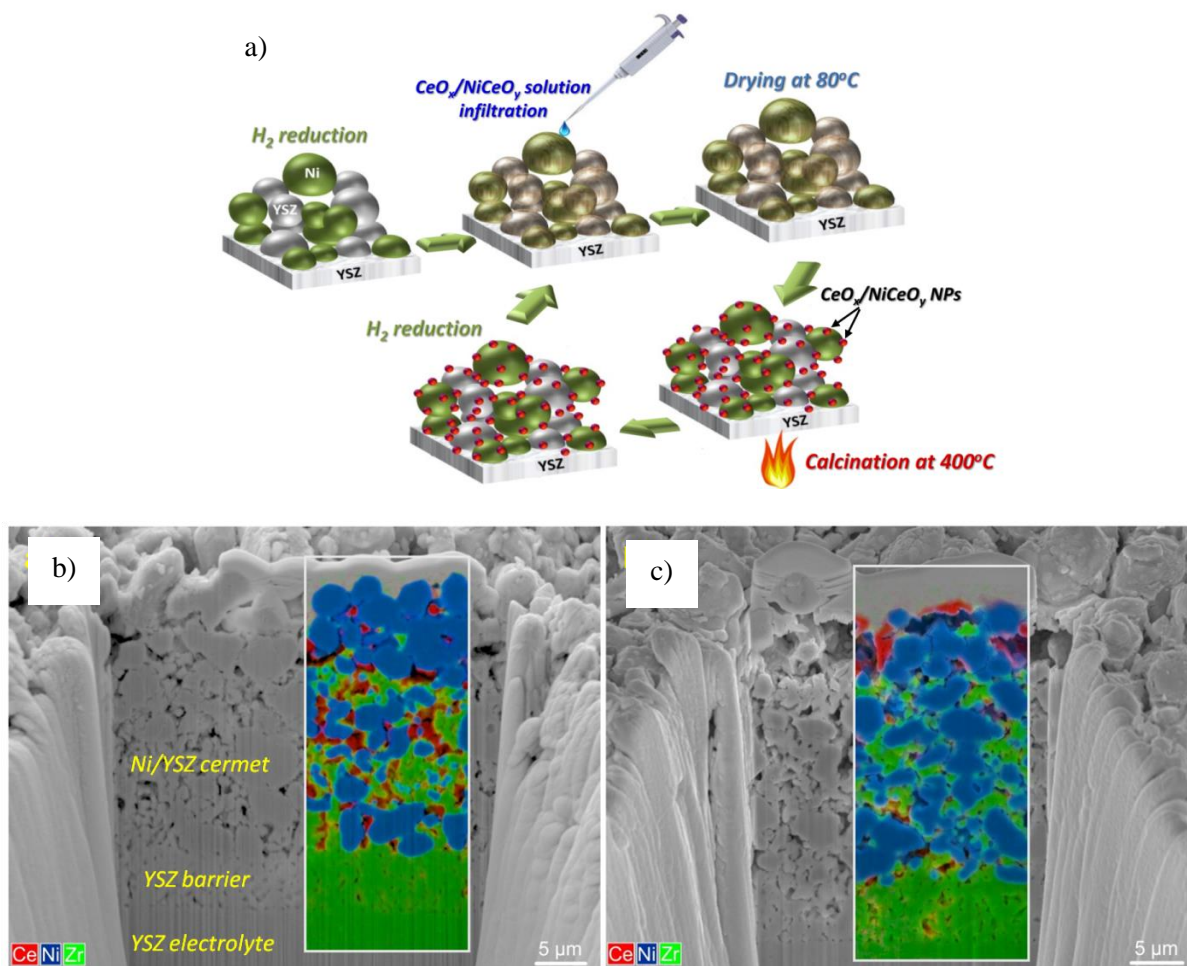
Figure 5. a) Représentation schématique du processus d'infiltration des NPs de CeO_x et de $NiCeO_y$ sur des électrodes Ni/YSZ pré-fabriquées. Images FIB-MEB en coupe et cartographie élémentaire EDS correspondante de b) 100 $NiCeO_y$@Ni/YSZ et c) 100CeO_x@Ni/YSZ après calcination.

IV. Étude de la réaction d'électrolyse du CO₂ sur des cathodes Ni/YSZ modifiées par des nanoparticules de cérium

Comme nous l'avons vu dans la section précédente, les NPs de NiCe peuvent se déposer efficacement dans les pores des électrodes de cermet Ni/YSZ préfabriquées en utilisant une méthode relativement simplifiée. Il est donc raisonnable de supposer qu'une meilleure distribution de l'oxyde de cérium dans les pores de l'électrode devrait améliorer les performances de la cellule. Pour valider cette hypothèse, nous comparons dans la dernière partie les performances des électrodes Ni/YSZ vierges et modifiées dans des conditions d'électrolyse directe du CO₂.

Afin d'étudier l'activité électrocatalytique du Ni/YSZ modifié, la solution organique de NiCe a été infiltrée directement dans l'électrode Ni/YSZ de cellules Ni/YSZ/YSZ/Pt préformées et soumises à des traitements d'oxydation et de réduction pour éliminer les résidus organiques. La cellule Ni/YSZ/YSZ/Pt a été imprégnée de 100 µL de NPs NiCe (par deux étapes d'infiltration/co-cuisson, chaque fois pour 50 µL), ci-après dénommée 100 NiCe NiYSZ. Les tests électrochimiques ont été réalisés dans une atmosphère de CO₂ à 100% (sans gaz diluant ou réducteur) sous 0,5 mbar à une température relativement basse (550±5°C) à l'aide d'une installation interne, possédant l'avantage de la caractérisation de la surface des électrodes avant et après les tests électrochimiques. La caractérisation peut aider à identifier l'état chimique de la surface, les éventuelles impuretés de surface ou le dépôt de carbone qui pourraient affecter les performances électrochimiques et masquer l'effet de la modification de surface. Veuillez noter que dans cette expérience particulière, l'électrolyse du CO₂ a été initialement testée sur une cellule Ni/YSZ//YSZ//Pt, puis la cellule a été retirée du réacteur et imprégnée d'une solution de NPs NiCe, avant d'être réintroduite dans le réacteur et testée à nouveau. De cette façon, la comparaison des cellules Ni/YSZ vierges et infiltrées est directe.

Les mesures de chronoampérométrie des cellules avec des électrodes Ni/YSZ et 100NiCe Ni/YSZ dans 0,5 mbar de CO₂ pur à 550 °C sont présentées dans la figure 6. La densité de courant à chaque potentiel appliqué, montrée dans la figure 6a, est améliorée de manière significative après l'infiltration. L'amélioration devient plus importante avec la tension appliquée. Afin de prendre en compte les différences dans l'évolution du courant en fonction du temps, la figure 6b présente les résultats de l'intégration du courant dans le temps, ou en d'autres termes la charge électrique totale qui traverse la cellule pendant l'expérience électrochimique. Ce graphique montre clairement que

les cellules modifiées sont jusqu'à 5 fois plus actives (charge totale ou CO_2 électro-réduit) par rapport à la cellule Ni/YSZ vierge.
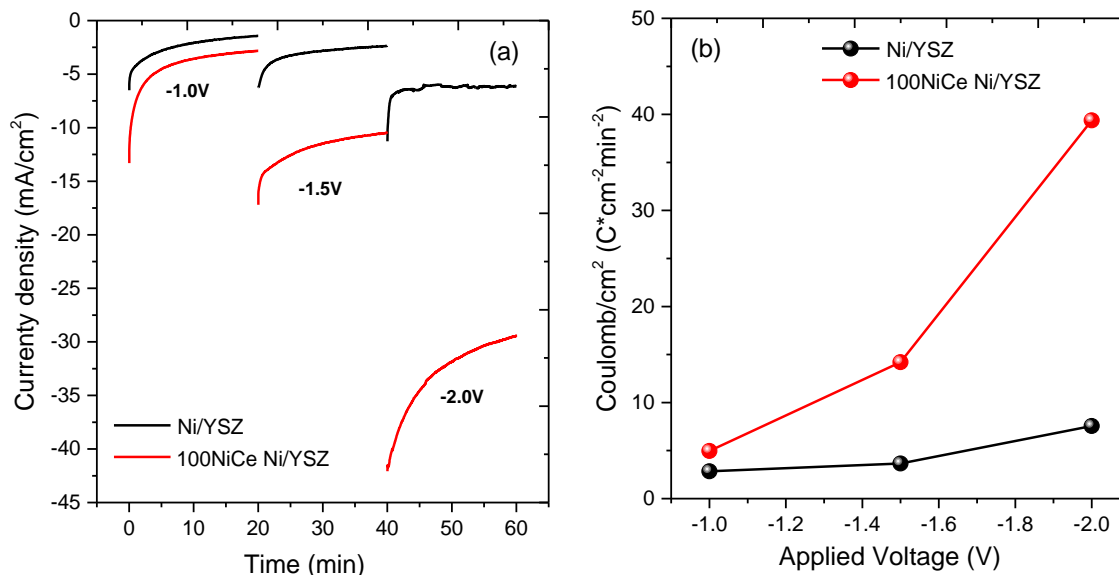
Figure 6. a) Mesures chronoampérométriques en trois étapes de potentiel ainsi que la charge totale correspondante en coulomb (b) sur Ni/YSZ (lignes noires) et 100NiCe Ni/YSZ (lignes rouges) Les conditions de réaction sont: 0,5 mbar de CO_2 à 550 °C.

Dans les tests électrochimiques, on a également examiné la possibilité de réactiver les électrodes Ni/YSZ dégradées, en les infiltrant post-mortem avec une solution de NPs de NiCe. Dans nos tests, et afin d'accélérer la dégradation, les électrodes Ni/YSZ ont été soumises à une série de cycles rédox sous H_2 et O_2 (1,0 mbar H_2 à 650 °C et 5,0 mbar O_2 à 400 °C pendant 30 min à chaque fois, au total pendant cinq fois). Chaque traitement rédox a été suivi d'essais en électrolyse directe du CO_2 dans 0,5 mbar de CO_2 à 550 °C pendant 60 min sous une tension appliquée constante de 2,0 V. L'évolution du courant de la cellule en fonction du temps ainsi que la charge totale correspondante en coulomb sont rassemblées dans les figures 7a et b. Dans le cas du Ni/YSZ vierge, il est clair que la performance de réduction électrocatalytique du CO_2 diminue constamment après chaque prétraitement, même si une légère amélioration après le deuxième cycle de réduction et d'oxydation a été observée. Globalement, à la fin du 5ème cycle d'oxydoréduction, la quantité de courant ou de coulomb à l'électrode Ni/YSZ diminue d'environ 70% (environ 66% pour le coulomb). En particulier, la densité de courant à 2 V chute de 10,22 mA/cm^2 (45.8 C/cm^2) à 3,05 mA/cm^2 (15.6 C/cm^2) entre le premier et le troisième traitement sous H_2 (Figure 7a,b).

Les performances de l'électrode Ni/YSZ après infiltration avec des NPs de NiCe montrent une amélioration spectaculaire. L'observation la plus frappante est que le courant mesuré ne revient pas simplement au courant initial de Ni/YSZ, mais devient presque 3 fois plus élevé que celui de l'électrode mère. En particulier, après le premier prétraitement sous H_2, la densité de courant de la cellule Ni/YSZ à 100NiCe augmente à environ 30 mA/cm^2, alors que dans des conditions équivalentes pour Ni/YSZ, elle n'était que de 10 mA/cm^2 (figure 7a,b). Après 3 cycles redox, la cellule avec l'électrode Ni/YSZ modifiée (100NiCe Ni/YSZ) conserve environ 63% de sa densité de courant initiale, ce qui correspond à 56% de coulomb (18,82mA/cm^2 (80.0 C/cm^2) après le troisième prétraitement sous H_2, ce qui indique que la durabilité de l'électrode modifiée a été nettement améliorée.
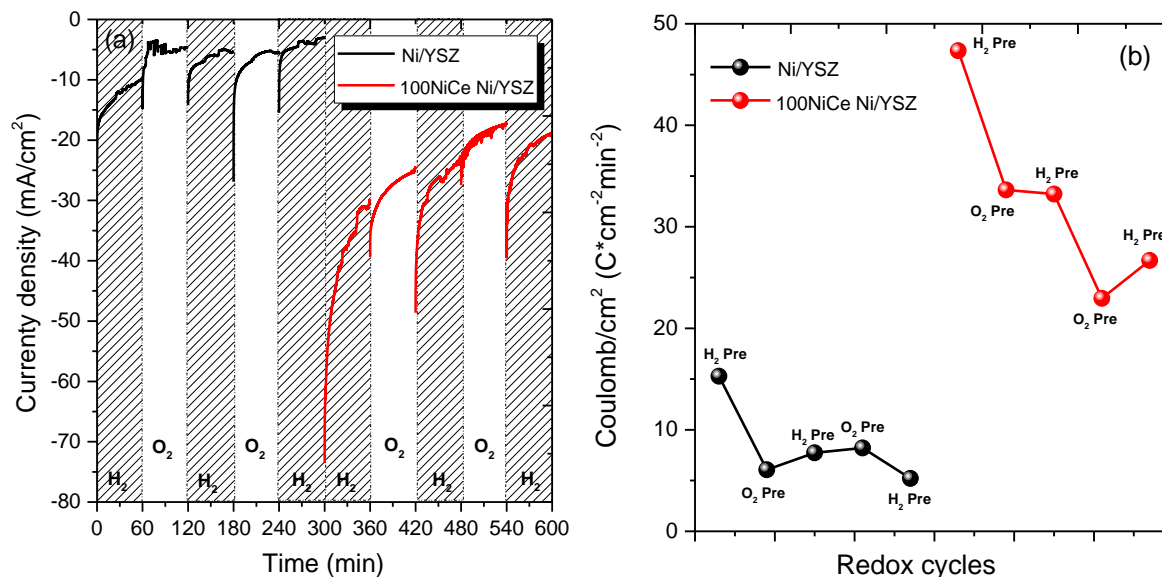
Figure.7. Mesures chronoampérométriques (a) ainsi que la charge totale correspondante en coulomb (b) sur Ni/YSZ (lignes noires) et 100NiCe Ni/YSZ (lignes rouges) dans 0,5mbar de CO_2 à différents cycles de prétraitement rédox et à une température de fonctionnement de 550 °C sous une tension appliquée constante de -2,0 V.

Dans l'ensemble, l'introduction de nanoparticules de cérium par le biais de cette nouvelle stratégie d'imprégnation présentée dans cette étude peut non seulement améliorer la performance électrocatalytique de la réaction de réduction du CO_2, mais aussi restaurer efficacement et même améliorer la performance des cellules avec des électrodes Ni/YSZ désactivées.

c) Conclusion générale

L'oxydation des électrodes en cermet Ni/YSZ et Ni/GDC par le CO_2 et H_2O dans des conditions pertinentes pour le fonctionnement des cellules d'électrolyse à oxyde solide a été étudiée par XPS *in situ* à pression ambiante. Les résultats montrent que le degré d'oxydation du nickel en présence de CO_2 et de H_2O n'est pas similaire, mais qu'il est régulé par la présence ou non d'oxyde de cérium dans le cermet. En particulier, la cérine favorise l'oxydation du nickel par H_2O mais la modère dans le CO_2. Sur la base de cette observation, les électrodes Ni/YSZ ont été modifiées en introduisant des nanoparticules de cérium directement sur leur surface. Des tests comparatifs ont suggéré que l'électrode Ni/YSZ modifiée possède une haute résistance à l'oxydation au CO_2.

Par la suite, nous avons combiné la NAP-XPS en conditions réactives (*operando*) avec des mesures électriques couplées à l'analyse de la phase gazeuse sur des cellules avec des cathodes Ni/GDC poreuses, pour étudier comment les états d'oxydation du nickel et de l'oxyde de cérium affectent les performances en électrolyse du CO_2. Les résultats ont révélé que la surface du Ni/GDC est constituée de nickel métallique et d'oxyde de cérium partiellement réduit. L'activation de la réaction d'électrolyse du CO_2 pur a été corrélée à l'électroréduction de NiO en Ni à des potentiels d'électrolyse du CO_2 relativement faibles. En outre, pendant l'électrolyse du CO_2 pur, le GDC agit comme une source ou un puits d'ions d'oxygène mobiles.

Sur la base de ces informations, nous avons tenté de combiner les propriétés mécaniques robustes du Ni/YSZ avec les propriétés de surface bénéfiques de l'oxyde de cérium pour résister à l'oxydation par le CO_2 et agir comme une source d'ions oxygène mobiles pendant la polarisation. Pour ce faire, une nouvelle stratégie de fabrication a été développée pour infiltrer des nanoparticules de cérium dans les pores des électrodes Ni/YSZ préfabriquées. La méthode proposée peut être facilement mise à l'échelle et intégrée dans les technologies actuelles de préparation des électrodes, puisqu'elle nécessite un nombre minimal d'étapes d'infiltration. La caractérisation morphologique et microstructurale a révélé que les nanoparticules de $NiCeO_y$, même après seulement deux étapes d'infiltration/co-cuisson, décorent uniformément les pores du squelette Ni/YSZ, profondément jusqu'à l'interface avec l'électrolyte. Au contraire, les nanoparticules de CeO_x restent principalement à la surface du Ni/YSZ avec une insertion limitée dans son volume. Cette différence est liée à la dispersion plus élevée de NiCe dans la solution mère formant des particules agglomérées relativement plus petites, qui peuvent facilement pénétrer les

pores du Ni/YSZ par des forces capillaires et produire une décoration homogène dans le volume entier de l'électrode.

Les résultats de l'évaluation électrochimique démontrent que l'introduction de nanoparticules de cérium dopées, par le biais de la nouvelle stratégie d'imprégnation, favorise non seulement les performances électrocatalytiques du Ni/YSZ pour l'électrolyse du CO_2, mais peut également être utilisée comme une méthode efficace et simple pour récupérer l'activité des électrodes Ni/YSZ partiellement désactivées. Par conséquent, la cérine dopée au Ni est un candidat prometteur pour la modification de la cathode Ni/YSZ par la méthode d'infiltration d'une solution organique dans les applications SOEC.

Chapter 1. Literature Review

I. Chapter 1. Literature Review

Introduction

In recent years, global industrialization has resulted in an urgent demand for fossil fuels such as natural gas, petroleum as well as coal, greatly increasing the levels of greenhouse gases in our atmosphere, finally leading to undesired climate changes and environmental destruction [1,2]. Therefore, developing environmentally friendly alternatives to fossil fuels and carbon-neutral energy technologies is urgently needed, to solve the environmental and energy issues. For this purpose, apart from employing renewable energy resources to substitute fossil fuels, two main treatment strategies have been developed, as shown in Table 1.1. Carbon capture and storage (CCS) processes are usually high costing and uncertain (due to the risk of CO_2 leakage) and need intensive energy requirements [14]. The second strategy, CO_2 conversion and utilization (CCU) processes, can convert the captured CO_2 to value-added carbon-containing chemicals, has attracted significant research interest among the catalysis community [15]. In that direction, several approaches for CO_2 conversion have been developed, including photosynthesis, photocatalysis, thermocatalysis, and electrochemical reduction (Figure 1.1).

Table 1.1. Two main strategies for reducing CO_2 emission [16].

Strategies	Features	Limitations
Carbon capture and storage (CCS)	(1) Large potential in CO_2 storage; (2) Storage in natural fields;	(1) Security and economic drawbacks (increasing cost, uncertainty, intensive energy requirements); (2) Has not been accepted by many countries;
CO_2 conversion and utilization (CCU)	(1) Recycles carbon; (2) Reduces the extraction of fossil-C; (3) Less CO_2emission;	
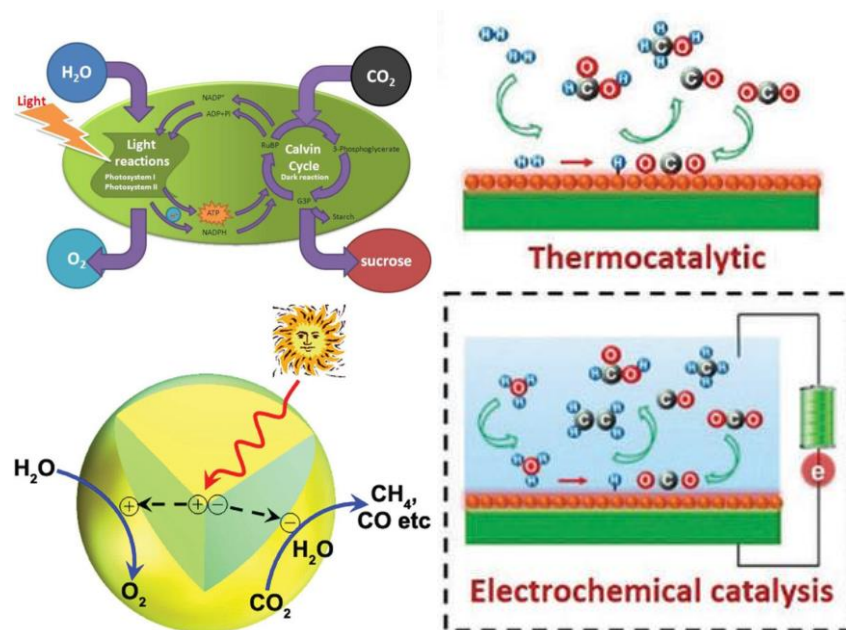
Figure 1.1. Typical processes of CO_2 conversion: photosynthesis, photocatalysis, thermocatalytic and electrochemical catalysis. Reproduced with permission [16]. Copyright 2017, the RSC.

Among the different approaches for CO_2 conversion, electrochemical reduction is more attractive, especially in terms of energy efficiency and cost requirements, due to the following reasons: 1) the electrochemical process is more precise and easier to control by adjusting the electrode potentials and reaction temperature; 2) the conversion systems can utilize renewable energy resources such as geothermal, tidal, wind, solar, as well as surplus electricity from nuclear and hydroelectric sources to electrochemically convert CO_2 to hydrocarbon fuels, forming a carbon-neutral energy cycle, and providing an efficient storage method for clean energy sources [17].

At present, there are several types of electrolysis cells for CO_2 electrochemical conversion, as listed in Table 1.2. In terms of the electrochemical reduction in aqueous solutions (H-type electrolysis cell) [18–20], the electrolytes are usually $NaHCO_3$, $KHCO_3$ etc., and the electrochemical reactors are simple and easily fabricated, while products are various, such as CO, HCOOH, HCOH, C_2H_5OH, and C_2H_4. However, the current densities are very low due to the limitation of the mass transport of CO_2 to the cathode surface and the competitive hydrogen evolution reaction in aqueous solution. The optimization in the design of the gas-diffusion-electrode and the fabrication of electrochemical reactors such as flow electrolysis cells [21,22] can allow CO_2 to be transported through the gas diffusion layer onto the catalyst surface and may solve

this problem. However, fabrication of new type of electrochemical reactors is relatively complex and the energy efficiency might be still insufficient.

Molten salt electrolysis cells [23–25] is another approach for the electrochemical reduction of CO_2, which has higher CO_2 solubility and wider potential windows, making the electrochemical reduction of CO_2 much easier and the hydrogen evolution more difficult compared to aqueous electrolytes. Nevertheless, its application is limited due to the frequent and time-consuming replacement of cathodes (carbon spheres, carbon nanotubes, and carbon flakes) that interrupts the electrolysis reaction.

The last, but not least, type of electrolysis technology is the solid oxide electrolysis [26], which utilize an ion-conducting solid oxide as electrolyte and usually operates at high temperatures. Since cell is a ceramic and there is no liquid electrolyte, the CO_2 produced in solid oxide electrolysis cell (SOECs) can directly diffus out of the electrode pores, making the electrode reaction more simple and stable. Besides, the high-operating temperature can also highly accelerate the electrode reaction, resulting in a higher current density than that in the liquid electrolyte electrolysis cell under the same electrolysis voltage. Therefore, compared with other electrolysis cells, CO_2 electrolysis in SOECs at high temperature shows a higher current density, energy efficiency, and stability, which has gained much attention for its important and promising applications in the solution of environmental and energy issues, as shown in Figure 1.2.

In addition, solid oxide electrolysis of CO_2 is a promising method under investigation for oxygen (re)generation in space missions to Mars [27]. In the last few years a technology demonstrator with acronym MOXIE "Mars Oxygen In-Situ Resource Utilization Experiment" is in progress. The first prototype has been carried by the NASA Mars 2020 Perseverance rover with an objective to demonstrate the feasibility of solid oxide electrolysis technology to dissociate the atmospheric CO_2 into O_2 (In Situ Resource Utilization (ISRU)) [28]. The success of this project is critical for possible future human exploration in Mars. This year, the MOXIE instrument achieved conversion of carbon dioxide into oxygen on Mars, which is a milestone pointing the way to future human exploration of the red planet. This technology should be scaled up for application in a human mission to the planet to provide oxidizer, breathable oxygen, and propellant [3].
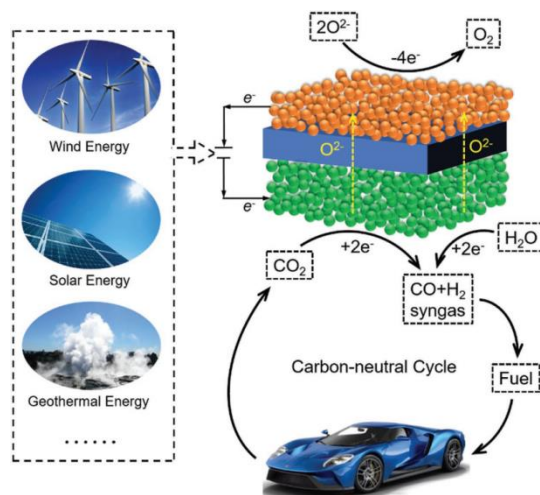
Figure 1.2. Carbon-neutral cycle based on CO_2 electrolysis in SOECs. Reproduced with permission [29]. Copyright 2019, Wiley-VCH.

Table 1.2. Comparison of different CO_2 electrolysis cells. Reproduced with permission [29]. Copyright 2019, Wiley-VCH.

	H-type electrolysis cell	Flow electrolysis cell	Molten salt electrolysis cell	Solid oxide electrolysis cell
Temperature	<100 ºC	<100 ºC	400-800 ºC	600-1000 ºC
Electrolyte	Liquid solution	Flowing liquid solution/polymer electrolyte membrane	Molten salt	Solid oxide
Cathode	Metal	Metal	Fe, alloy	Ni, perovskite
Anode	Pt	IrO_2	Ni, SnO_2	Perovskite
Charge carrier	K^+ or H^-	OH^-	CO_3^{2-}	O^{2-}
Advantages	Rich products High faradaic efficiency	Rich products High current density High faradaic efficiency	High current density High faradaic efficiency	High current density High faradaic efficiency Good stability
Disadvantages	Low current density Poor energy efficiency Insufficient stability	Poor energy efficiency Insufficient stability	Simple products Insufficient energy efficiency Poor stability	Simple products

1.1. Thermodynamics of High-Temperature CO₂ Electrolysis

The energy demands for high-temperature CO_2 electrolysis are shown in Figure 1.3. As indicated in this figure, ΔH, ΔG and $T\Delta S$ correspond to the total energy demand, electrical energy demand and heat demand, respectively. When the temperature increases, the total energy demand (ΔH) is almost invariant, while the heat demand increases and the electrical energy demand decreases due to the positive entropy change ($\Delta S > 0$). Compared to low or intermediate temperature electrolysis, high temperature electrolysis can use both electricity and heat effectively (the efficiency is up to 100%), and can achieve high reaction rates, which in turn lead to a significant decrease in the ohmic resistance and acceleration of the electrode reaction processes, guaranteeing the fast reaction kinetics. In other words, as for CO_2 electrolysis, from a thermodynamic viewpoint, high temperature operation is the better choice for both efficiency and cost. Furthermore, better economic competitiveness can be achieved if waste heat from other industrial processes is integrated to save energy during the startup of the stacks. Of course in order for the process to be sustainable the electricity should be generated from renewable energy sources, such as wind, solar, hydra or tidal energy [30].
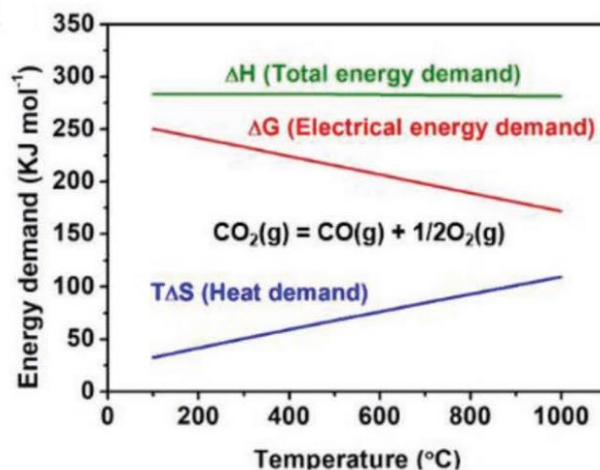
Figure 1.3. Energy demanded as a function of temperature for the CO_2 electrolysis process. Reproduced with permission [29]. Copyright 2019, Wiley-VCH.

1.2. SOEC for High-Temperature CO₂ Electrolysis

A typical SOEC single cell includes an electrolyte for ionic transport, an anode for the evolution of oxygen and a cathode for the electrochemical reduction of CO_2. The solid electrolytes can also be classified into two types, i.e. oxygen ionic conductors and protonic conductors. In oxygen ion-

conducting electrolytes, CO_2 molecules at the cathode receive electrons and decompose to produce CO and oxygen ions, and then the oxygen ions are transported through the electrolyte to arrive at the anode, losing electrons to form oxygen molecules. In solid oxide electrolysis cells using protonic electrolytes, the H_2O molecules at the anode lose electrons to generate oxygen molecules and protons. Then, the protons pass through the electrolyte to arrive at the cathode where they receive electrons and react with the adsorbed-CO_2 molecules, producing CO or other value-added chemicals. However, due to the requirement of high sintering temperature and poor CO_2 tolerance of the proton conducting SOECs [31,32], nowadays most studies are focused on the oxygen ion conducting SOECs.

1.3. Key materials of SOECs for CO_2 electrolysis

In SOECs, the electrode material is a key aspect for achieving high electrolytic efficiency by controlling polarization reactions. In general, for SOECs electrodes there are three essential functionalities: ionic conduction (IC), electronic conduction (EC) and catalytic activity [16]. These functionalities can be either achieved in a single phase material, for example by a mixed ionic and electronic conductor (MIEC) or in a composite. In case of electrodes with MIEC characteristics, the active place of reaction is the interface between the solid phase and the gas phase, called the two-phase boundaries (2PBs). A composite electrode consists of separated EC and IC phases. In this case the interface between the IC, the EC and the reactant gases is an active area usually called the triple-phase boundaries (TPBs). Therefore, investigating advanced electrode materials containing a large number of TPBs or 2PBs is crucial for improving CO_2 electrolysis performance at high temperature.

1.3.1. Fuel electrode materials

Since the SOEC cathode offers active sites for CO_2 electroreduction, it should have high electronic and ionic conductivity, excellent catalytic activity, great chemical and mechanical stability, as well as proper porosity and good compatibility with electrolyte materials. At present, the common cathode materials include metal-cermet electrodes and perovskite electrodes.

1.3.1.1 Metal-cermet electrodes and their performance in electrolysis

Despite the great efforts devoted to design and prepare new electrocatalysts with high activity and stability, composites of ceramic and metal (cermets) that have been previously optimized for solid oxide fuel cells (SOFCs), remain the state-of-the-art (SoA) cathode electrodes for SOECc as well

[4]. As an example, the cathode electrode in MOXIE is based on cermet composite [33]. At present, two principal SoA cermet cathode electrodes, nickel combined with yttria stabilized zirconia (Ni/YSZ) or gadolinium doped ceria (Ni/GDC), are the most widespread electrode materials in CO_2 electrolysis [34–40]. These two electrodes are also in the core of research described in this thesis. Ni-YSZ is widely used in both SOFC and SOEC applications as the fuel electrode material. This is because it offers good electrochemical performance, low cost, high stability, as well it has a thermal expansion coefficient which match well with this of YSZ electrolyte [41,42].

Ebbesen et al. studied the long-term stability of a Ni-YSZ electrode under high-temperature CO_2 electrolysis conditions (CO$_2$/CO ratio 70/30 or 98/2, 850°C), showing the feasibility of long term CO_2 electrolysis over nickel based electrodes in SOECs. They found that the passivation (deactivation) rate is not dependent on the current density and it is irreversible under oxidizing environment, which clearly indicates that the passivation is not due to the coke formation on the cathode material. Furthermore, the passivation is partly reversible when introducing hydrogen. Finally, researchers ascribe the passivation to impurities in the gas stream, especially sulphur, which can adsorb on some specific nickel sites and react with hydrogen to form the volatile compound H_2S in the cathode. However, long-time operation of CO_2 electrolysis in Ni/YSZ electrodes is feasible, since adsorption of sulphur is site specific therefore just passivates only part of the nickel sites. At present, Ni-YSZ has been studied as a working electrode for CO_2 electroreduction in solid electrolyte cells with different air electrode materials including LSCF-LSM ((La$_{0.8}$Sr$_{0.2}$)$_{0.95}$MnO$_{3-x}$) [43], LSM-YSZ [44], LSCF (La$_{0.6}$Sr$_{0.4}$Co$_{0.2}$Fe$_{0.8}$O$_3$)-GDC (Ce$_{0.9}$Gd$_{0.1}$O$_{1.95}$) [36], and LSM [45]. For high-temperature CO_2 electrolysis, the above studies showed that the cell operation temperature has a significant influence in the cell activity, and low temperatures are more favorable to coke formation on Ni-YSZ. Therefore, temperatures higher than 700°C and CO_2 inlet concentrations higher than 50% are recommended for higher activity and stability.

Another advantage of cells with Ni-YSZ electrodes is that they can work reversibly, since Ni-YSZ is an active working electrode for both reactions. It is noteworthy that pure CO_2 atmospheres may lead to oxidation of Ni to NiO, decreasing cell activity. As a consequence, reductive gases such as CO or H_2 are usually added to overcome the oxidation problem in CO_2 electrolysis. However, when H_2 is used as the protective gas, the reverse water gas shift reaction ($CO_2 + H_2 \rightleftharpoons CO + H_2O$) will first occur, accompanied by the formation of CO and H_2O, and the electrochemical reaction

is partially shifted from CO_2 electrolysis to H_2O electrolysis. When CO is used as the protective gas there are two main problems. First is that at the high electrolysis voltages CO might be electroreduced and deposit carbon. Second the CO addition in the CO_2 feed gas increases CO concentration, and high CO concentration can block the active sites during cathode reaction, resulting in the degradation of SOECs [46].

Apart of the type of protective gas, its concentration in the fuel mixture is also very important. The addition of a protective gas in the reactants declines the oxygen partial pressure at the cathode, further increasing the open-circuit voltage (OCV) value, which requires more power during electrolysis [47,48]. Addition of a high concentration of a protective gas in the reactant also dilutes the CO_2 concentration, decreasing the electrochemical performance of the SOEC at the same applied voltage. Actually, the protective gas is not considered indispensable by some researchers, since the cathodic potential appears to provide continuous electrons across the Ni-YSZ cathode to reduce Ni oxidation, as shown in Figure 1.4[26]. A Pd-GDC nanoparticles layer coated onto the surface of Ni-YSZ cathode was also found beneficial to prevent Ni oxidation [49].
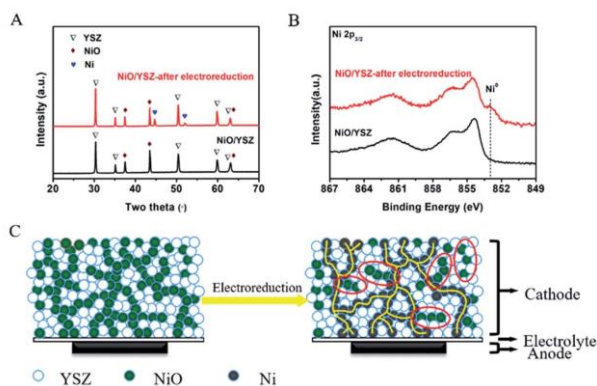
Figure 1.4. (A) XRD patterns and (B) Ni 2p3/2 XPS spectra of the NiO/YSZ cathode before and after electroreduction. (C) Schematic of the circuit model. Reproduced with permission [26]. Copyright 2018, the RSC.

Ni-GDC is also a promising cathode material for CO_2 electrolysis studies. Singh et al.[40] investigated high-temperature CO_2 electrolysis over two different cathodes: Ni-YSZ and Ni-GDC. According to the activity comparison of Ni-YSZ and Ni-GDC under the same reaction conditions (Figure 1.5), Ni-GDC was found to possess higher CO_2 electrochemical performance compared to Ni-YSZ, because of its excellent ionic and electronic conductivity, which can expand the TPB

region. However, Ni-GDC cermets have some disadvantages as compared to Ni-YSZ, related to their lower mechanical stability and their higher cost [10].
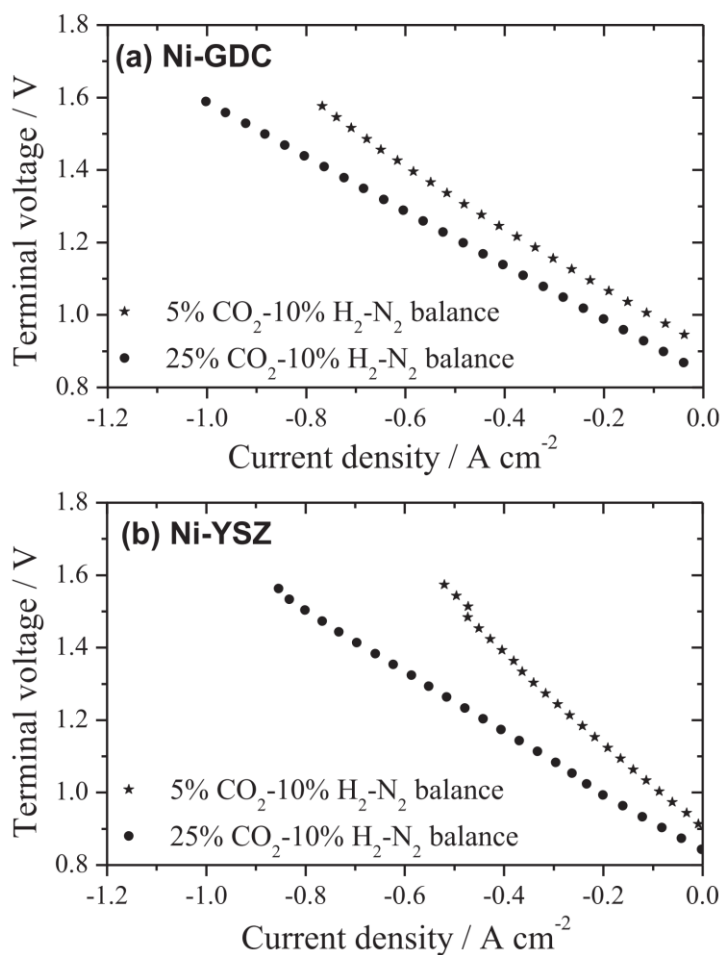
Figure 1.5. I-V curves for (a) Ni-GDC/YSZ/GDC/LSCF and (b) Ni-YSZ/YSZ/GDC/LSCF cells with a supply of 5 and 25% CO_2/10% H_2/N_2 balance to the cathode at 1000 °C. Anode gas: 100% O_2. Reproduced with permission [40]. Copyright 2015, Elsevier.

1.3.1.2. Perovskite electrodes

Conventional metal-ceramic materials (particularly, Ni/YSZ and Ni/GDC cermet) are widely used as the cathode in SOECs because of their outstanding electrocatalytic activity and excellent conductivities, but they still suffer from issues such as the requirement of a reducing agent in the feed stream, carbon deposition at low temperatures and further reduction of CO to carbon at high cathodic potentials, grain coarsening, as well as impurities contamination [16,50,51]. Therefore, some researchers have shifted from the improvement of metal-cermet electrodes to the development of alternative materials. Oxide-based mixed ionic and electrical conductors (MIECs),

specifically perovskite-type MIEC oxides, as shown in Figure 1.6, have attracted more and more attention as the new candidates for cathode materials in SOECs, due to their adequate ionic and electrical conductivity, high stability at high temperatures, improved impurity tolerance, and excellent coking resistance. However, the comparatively poor catalytic activity is the main challenge for most perovskite-related oxides.
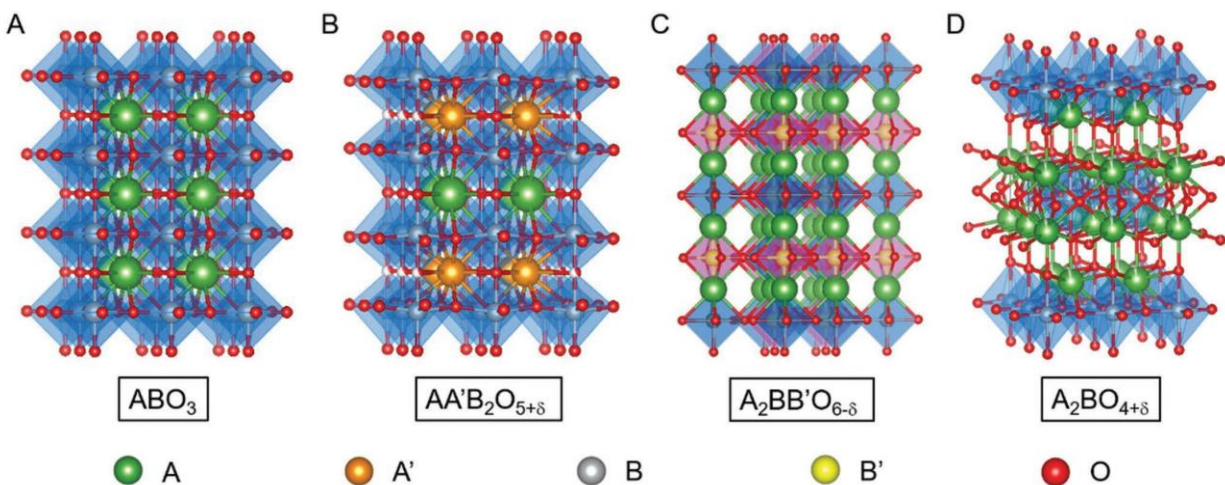
Figure 1.6. crystal structure of A) perovskite oxide (ABO_3), B) double perovskite oxides ($AA'B_2O_{5+\delta}$), C) double perovskite oxides ($A_2BB'O_{6-\delta}$), and D) Ruddlesden–Popper phase ($A_{n+1}B_nO_{3n+1}$, $n = 1$). Reproduced with permission [29]. Copyright 2019, Wiley-VCH.

Different perovskite materials with various A-site and/or B-site doping, synthesized and screen-printed on electrolyte materials via different techniques, have been studied. The most common type of perovskites for CO_2 electrolysis are B-site-doped $La_xSr_{1-x}FeO_3$-type materials. Ti-doped lanthanum strontium ferrite ($La_{0.3}Sr_{0.7}Fe_{0.7}Ti_{0.3}O_3$)-type perovskites (LSFT) were examined as cathode and anode materials for CO_2 electrolysis [51]. It was shown that LSFT possesses high activity and stability while no significant coke deposition occurs on the LSFT cathodes under pure CO_2 atmosphere, even at high voltages.

The effect of A-site and B-site doping on the activity and stability of lanthanum strontium ferrite-type perovskites when using Ce-doped $La_{0.7}Sr_{0.3}Cr_{0.5}Fe_{0.5}O_{3-\delta}$ (Ce-LSCrF) and Ni-doped $La_{0.6}Sr_{0.4}Fe_{0.8}Ni_{0.2}O_{3-\delta}$ (LSNF) as working electrodes in CO_2 electrolysis reaction was studied by Luo's research group, respectively [52,53]. The results of these studies showed that both Ce-LSCrF and LSNF cathodes displayed superior electrocatalytic activity and stability as compared to undoped lanthanum strontium ferrite. This improvement is assigned to the increase of the

oxygen vacancies number with the addition of Ce into the perovskite lattice and the extension of the TPB (active sites) due to the improved ionic and electronic conductivity with Ni doping. Precious metal Pd-doped $La_{0.6}Sr_{0.4}Co_{0.2}Fe_{0.8}O_{3-\delta}$ (LSCF-Pd) perovskite cathode has also been studied in high-temperature CO_2 electrolysis [54]. This study showed that its performance was significantly better than that of LSCF, while the long-term stability test revealed no degradation.

In addition, some new types of perovskite materials also show great conductivity and activity for high-temperature CO_2 electrolysis. These novel materials are obtained under reducing environment via exsolution of the B-site transition metals (active components) to the surface, becoming more accessible to the reactant molecules. Examples of this type of perovskite electrodes are i) the SrO-exsolved from $La_{0.2}Sr_{0.8}TiO_{3+\delta}$ [55], ii) the Co-Fe alloy-exsolved from $(P_{r0.4}Sr_{0.6})_3(Fe_{0.85}Mo_{0.15})_2O_7$ [56], iii) the Ni-exsolved from $(La_{0.3}Sr_{0.7})_{0.9}Ti_{0.95}Ni_{0.05}O_{3-\delta}$ [57], iv) the Ni-Fe alloy-exsolved from $Sr_{1.9}Fe_{1.5}Mo_{0.4}Ni0.1O_{6-\delta}$ [58], and finally v) the Fe-Ni alloy-exsolved from A-site-deficient LSNF [59,60]. Studies on these materials showed that bimetal alloys- or transition metal-exsolved perovskites exhibit predominant conductivity and catalytic activity as compared to their corresponding parent perovskites.

1.3.2. Oxygen/air electrodes

In high temperature SOECs, the oxygen evolution reaction (OER) for CO_2 electrolysis occurs at the anode. Just like the cathode materials, the anode should have both high ionic and electronic conductivities, excellent catalytic activity for OER, high stability in oxidizing atmosphere, and good compatibility with other cell components. At present, there are two main types of materials for SOEC anodes: i) noble metals such as Au and Pt; and ii) electron conducting oxides, such as perovskite oxides, double perovskite oxides and Ruddlesden-Popper (RP) phases. Less expensive electron-conducting oxides, especially $La_{1-x}Sr_xMnO_{3\pm\delta}$ (LSM) [61], and $La_{1-x}Sr_xCo_{1-y}Fe_yO_{3-\delta}$ (LSCF) [62], are the most frequently investigated candidates for the anodes of SOECs nowadays. LSM usually mixes with an ion-conducting component to form composite anodes such as LSM-SSZ, LSM-GDC, and LSM-YSZ. LSM-based composite anodes not only possessing larger TPBs and higher anodic performance than the pure LSM, but also has better mechanical compatibility with the electrolyte materials.

1.3.3. Electrolytes

In SOECs, the conduction of oxygen ions in the electrolyte contributes to the main ohmic resistance for CO_2 electrolysis. Thus, the electrolyte should have high ionic conductivity but negligible electronic conductivity [63], stability under variable redox conditions and CO_2 atmosphere, as well as to form a dense, strong, thin film impermeable to gases, in order to be able to prevent the recombination of the produced CO and O_2 at leaking from the cathode and anode sides [64]. Nowadays, there are several types of materials available as SOECs electrolytes, such as stabilized zirconia based oxides, doped ceria oxides, doped $LaGaO_3$ [65], bismuth oxides [66] etc., as shown in Figure 1.7. Among them, zirconia-based oxides, especially yttria-stabilized-zirconia (YSZ, where Y_2O_3 is usually at 8 mol%), is the most common electrolyte material due to its low electronic conductivity, excellent redox stability, high mechanical strength, low cost, as well as high oxygen ionic conductivity [67]. Alternatively, the Sc_2O_3 stabilized ZrO_2 (ScSZ) shows substantially higher ionic conductivity than YSZ at intermediate temperatures because of the similar size of Sc and Zr ions [68,69], but it is not widely used as electrolyte in SOECs, mainly due to the high cost of scandium and the poor sintering activity of ScSZ at high temperatures.
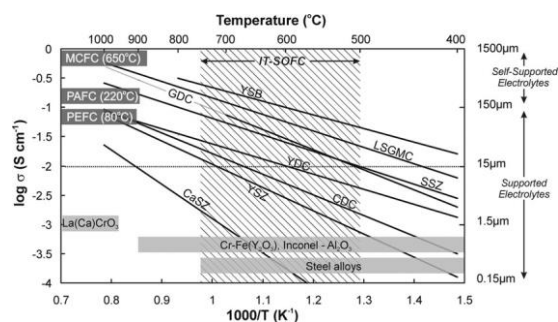
Figure 1.7. Conductivity as a function of reciprocal temperature for different electrolyte materials. Reproduced with permission [70]. Copyright 2008, the RSC.

1.4. Challenges and research directions of SOECs for CO_2 electrolysis

At present, conversion and durability of solid oxide CO_2 electrolysis technologies is not sufficient to meet the demands of practical implementation or commercialization, mainly due to two major challenges: degradation issues and low activation/conversion efficiency of CO_2.

1.4.1. Degradation in SOECs

It is well known that cell degradation is one of the most noteworthy issues affecting CO_2 electrolysis for the practical application of SOECs. Under practical operation, the lifetime of SOEC

for most applications should be at least 5 years to be economically competitive [71]. Thus, it is critical to have a deeper understanding and investigation of the degradation mechanism in SOECs, in order to reduce degradation and improve the SOEC lifetime for future commercialization. In general, degradation issues can be categorized into irreversible and reversible effects.

1.4.1.1 Irreversible degradation

Irreversible effects, such as the loss of the three-phase boundary (TPB), delamination, microstructural changes etc., are related to the mechanical stability of the SOEC devices. All these issues can be analyzed by post-mortem analysis of the SOEC devices. For CO_2 electrolysis in SOECs, the main electrode degradation issue, especially for the Ni-cermet electrodes, is agglomeration. Ni particles agglomeration is thermally induced at high temperatures and is independent of the applied voltage or gas composition. In long-term stability measurements is practically always observed in cells with Ni-YSZ cathodes. The main effect of agglomeration is to decline the specific surface areas of Ni and thus the length of TPBs gas. In addition, agglomeration can also reduce the effective contact areas of the electrode with the current collector mainly induced by nickel particles. This will increase the ohmic resistance of the cell and finally cause deactivation of the SOEC [5,72,73].

Another known cause of deactivation is nickel oxidation. The effect of oxidation is twofold. First oxidation of nickel reduces the electronic conductivity. Second it causes volume expansion of nickel particles [16], leading to mechanical stresses accompanied by microstructural changes such as crack formation and finally results to irreversible cell failure (Figure 1.8) [74,75].

Maybe the most well studied degradation cause for CO_2 electrolysis is carbon deposition. Carbon, in the form of carbon nanofibers or graphitic layers, usually forms at SOEC cathodes especially at the interface between cathode and electrolyte (such as Ni-YSZ cathode and YSZ electrolyte). The problem is more severe during long-term electrolysis reaction at high current densities and high fuel conversions [76,77]. According to equilibrium thermodynamics, the formation of carbon species can be ascribed to the compositional changes of the reactant gases because of the limited diffusion within the cathode. An increasing cathodic overpotential gradient between the outer (close to the current collector) and the inner (close to the YSZ electrolyte) parts of Ni-YSZ electrode, leads to the concentration of electrolysis products at the interface with YSZ, forming carbon species.
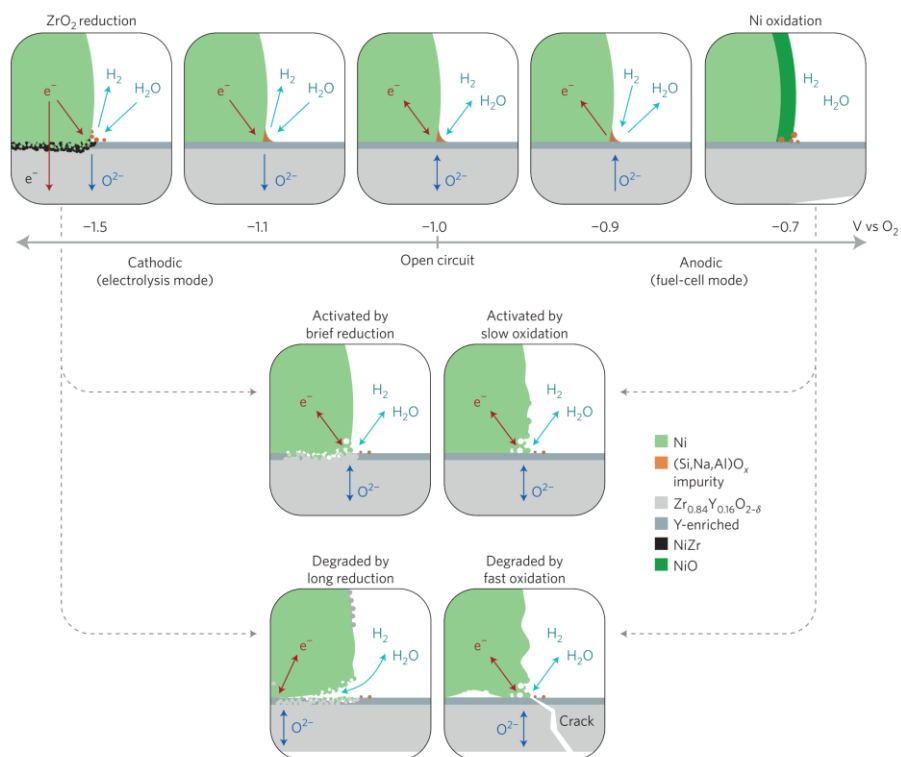
Figure 1.8. Electrode-potential-driven activation and passivation phenomena over Ni/YSZ/H_2, H_2O 3PB. Reproduced with permission [75]. Copyright 2016, Nature Publishing Group.

Another common irreversible degradation issue is poisoning of electrodes by impurities (such as S, Cr, Si). In general impurities originate from the raw materials used to fabricate the electrodes and the electrolyte, sealants or sometimes can be carried also by the reactant gases. For example, sulfur poisoning of lanthanum strontium cobalt oxide (LSC) anode in a SO_2 accelerated test, is due to the assembly of S impurities mainly at the interface between LSC anode and GDC barrier, probably caused by the high oxygen partial pressure at the interface [78].

Although the electrolyte is usually very stable in long-term SOECs operation, under severe operation conditions (i.e. high current densities and temperatures) irreversible degradation might occur in electrolyte. Most common of these are structural faults such as cracks, intergranular fracture and voids, especially along its grain boundaries [79–81]. For instance, voids can be generated at the boundaries of an YSZ electrolyte due to the nucleation and growth of oxygen gas under high electrolysis voltage, irreversibly increasing the ohmic resistance and decreasing the current efficiency of the SOEC [81]. As electrode-electrolyte interfaces are active areas of electrode reactions, they can also have some common irreversible degradation issues, such as the

delamination of the electrode and the formation of a secondary phase. According to literature [82–84], the delamination of the electrode layer from the electrolyte is attributed to two factors: i) at high current densities the oxygen partial pressure gradually increases at the electrode-electrolyte interface due to diffusion limitations of the generated oxygen gas by the anode layer, finally leading to the delamination of the electrode and ii) the migration of cations towards the electrode/electrolyte interface leads to the formation of a secondary phases, decreasing the interaction between electrode and electrolyte, further resulting in the separation of the anode layer.

1.4.1.2 Reversible degradation

Aside from irreversible degradation in SOECs, reversible phenomena, mainly including electrode reversible pollution from contaminants (especially carbon) and electrode oxidation, are dynamic and depend very much on the operational conditions. Therefore, new operando characterization technologies are required to understand the exact degradation mechanisms in order to eradicate these degradation issues.

Carbon deposition research in reversible degradation

Ni is the most commonly used electrocatalyst in fuel electrodes, typically as a porous composite with yttria-stabilized zirconia (YSZ), while it also contributes to destructive carbon formation as an excellent catalyst during electrolysis, finally fracturing the porous electrode [76,85,86]. Ceria catalysts are also known as carbon inhibitors for fuel cell oxidation reactions [75,87,88]. However, carbon inhibition mechanism on ceria under severe electrolysis conditions remains unclear. Theis et al.[89] revealed the crucial role of oxidized carbon intermediates in preventing carbon build-up over Ni/YSZ, Ni/SDC, and SDC via *operando* X-ray photoelectron spectroscopy during high-temperature CO_2 electrolysis, combined with DFT modeling calculations. Their results showed that during CO_2 electrolysis, surface oxygen vacancies on ceria can control the relative stability of carboxylate, carbonate, and adsorbed carbon monoxide reaction intermediates, and thus the onset overpotential for carbon deposition. Especially for oxygen-vacancy-rich ceria samples, operando experiments as well as theoretical simulations show that carbon atoms are energetically trapped moderately in the form of oxidized carbon species, relative to solid carbon and CO gas, thus postponing carbon formation. Besides, plentiful carbonate species on ceria, which are absent from Ni-YSZ, could also react and clear deposited carbon producing carboxylate via a surface reverse Boudouard reaction in two possibilities: 1) In order to kinetically inhibit carbon deposition during CO_2 electrolysis, carbon atoms need to be energetically trapped as oxidized carbon intermediates

so that CO_2(g) and CO(g) are not easily reduced to carbon; 2) high carbonate coverage improves the reverse Boudouard reaction, as shown in Figure 1.9.

In another study, Wang et al.[90] demonstrated for the first time the direct observation of carbon deposition on CeO_2 electrodes during CO_2 electrolysis at low operating temperatures (450°C) via operando ambient pressure X-ray photoelectron spectroscopy (APXPS). This is in contrast to the general opinion that CeO_2 is a carbon-tolerant material. In the same study the authors further revealed that carbon deposition on CeO_2 with relatively low or zero dopant concentration shows an intriguing threshold formation onset against surface Ce^{3+} concentration. Moreover, by combining APXPS results with Monte Carlo simulations, they proposed that the neighboring Ce^{3+}-Ce^{3+} pair on CeO_2 is a vital structure for accelerating carbon deposition from CO. Finally, the researchers proposed that doping CeO_2 with non-redox-active cations can effectively remove the carbon deposition, and subsequently verified this proposal using $Gd_{0.5}Ce_{0.5}O_{1.75}$ and $Zr_{0.5}Ce_{0.5}O_2$ as example systems, where the formation of carbon has proven to be effectually suppressed.
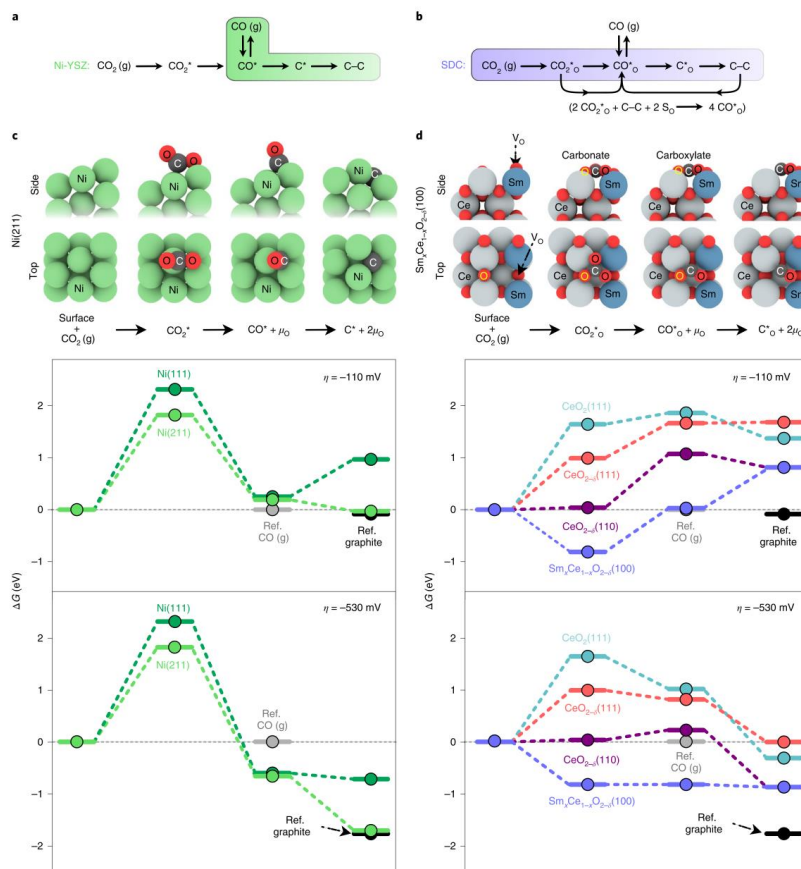
Figure 1.9. Proposed reaction mechanism and calculated energetics for carbon formation on nickel and ceria surfaces. Reproduced with permission [89]. Copyright 2019, Nature Publishing Group.

Electrode oxidation research in reversible degradation

In terms of the promising nickel/doped-ceria and nickel/yttria-stabilized zirconia cermet electrocatalysts for solid-oxide fuel and electrolysis cells, which is the main research focus in this thesis, a reversible degradation mechanism often anticipated involves the surface oxidation of nickel particles due to the interaction with the fuel. Since nickel oxide has lower electronic conductivity and chemical reactivity than the metal, it is expected that surface oxidized electrodes will have inferior electrical conductivity and catalytic activity. Therefore, it is necessary to examine in detail the oxidation process of nickel by the two typically used SEOC feed gases (CO_2 and H_2O). At present, the surface states of both Ni-based electrodes under steam have been explored by using in situ synchrotron-based near-ambient pressure X-ray photoelectron and absorption spectroscopy experiments [91,92]. Papaefthimiou et al. [91] explored the steam interaction with the surface of nickel/gadolinium-doped ceria (Ni/GDC) pre-treated under oxidizing and reducing environments via near-ambient-pressure X-ray photoelectron and absorption spectroscopies. Their results revealed that steam always acts as an oxidant for nickel but has a dual oxidant/reductant function for doped ceria, at least in the level of mbar pressure and at intermediate temperature conditions (500-700ºC). To be specific, when pre-reduced Ni/GDC was exposed to H_2O vapors, ceria species were rapidly oxidized, but after a certain oxidation, they remain stable in a mixed Ce^{3+}/Ce^{4+} state with prolonged exposure time. About 30% of nickel was quickly transformed to NiO after pristine exposure, and was then further oxidized slowly at a linear rate. For pre-oxidized Ni/GDC, CeO_2 was reduced following an exponential decay function, while NiO was not impacted. Overall, under water vapor exposure conditions, the surface was gradually transformed to $NiO/CeO_{1.7}$, independent of the prior NiGDC oxidation state (Figure 1.10). The kinetics in the cell oxidation or reduction in H_2O are much slower as compared to the O_2 or H_2 environments. Using the same research method, Paloukis et al.[92] investigated the surface reactivity of Ni/YSZ electrodes in O_2, H_2, and steam environments, and showed that the Ni/YSZ electrode undergoes significant morphological and oxidation state (Ni species) changes in response to reactive gas atmospheres, as is schematically summarized in Figure 1.11.

Overall, the reactivity of steam with nickel/gadolinium-doped ceria and nickel/yttria-stabilized zirconia surfaces was investigated in the above studies. It is generally acknowledged that these SEOC feed gases can oxidize Ni to NiO. However, since the two Ni-based electrodes were inquired separately, little is known about the qualitative differences in their oxidation behavior, and it is

just assumed that nickel oxidation under SEOC feed gases (CO_2 or H_2O) is processing similarly in the cermet electrodes independent of the type of the ceramic (YSZ or GDC). ***Thus, comparison of the oxidation of Ni-GDC and Ni-YSZ under H_2O and CO_2 atmospheres at high temperature via in situ near ambient pressure XPS (NAP-XPS) will be the first part of the research content in this thesis.***
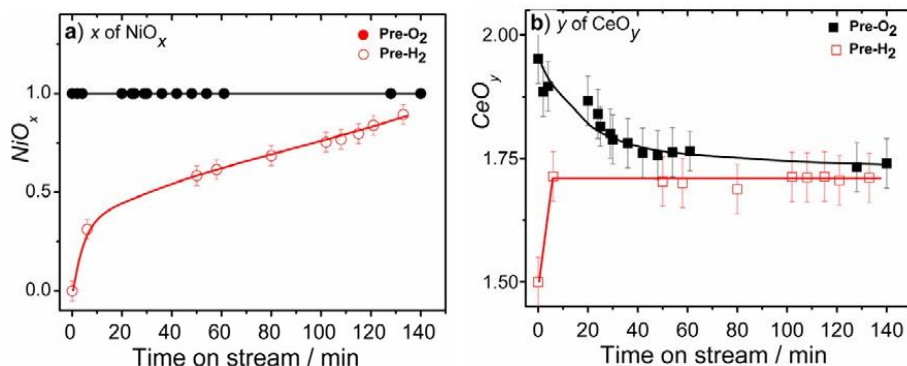
Figure 1.10. Isothermal time evolution of a) NiO_x and b) CeO_y surface stoichiometry. Reproduced with permission [91]. Copyright 2016, Wiley-VCH.
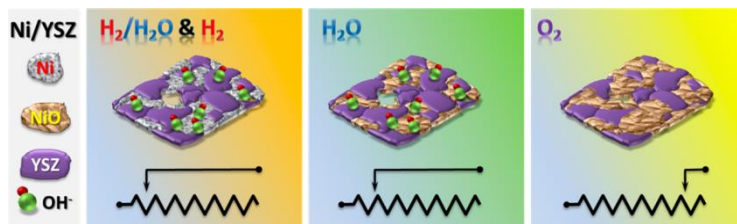
Figure 1.11. Schematic illustration of the surface configuration of the Ni/YSZ cermet electrode under various gas atmospheres. Reproduced with permission [92]. Copyright 2017, American Chemical Society.

Papaefthimiou et al.[93] also examined the effect of the surface oxidation state and composition of nickel/doped-ceria cermets cathode on the steam electrolysis performance using ambient pressure X-ray photoelectron and near edge X-ray absorption fine structure spectroscopies, combined with quantitative spectra simulation. In general, oxidation of nickel is supposed to reduce the electronic conductivity [94], thus decreasing electrolysis performance. However, in this study, nickel in a partially oxidized state was found to be beneficial to the cell performance under specific operational conditions, which is counterintuitive to the common behavior, as is shown in Figure 1.12. Based on depth profile measurements and simulations of the XPS Ni/Ce (peak area ratio), combined with electrochemical performance measurements, the results showed that the

oxidation state and composition of the Ni/GDC electrode are dynamic and depend on the fuel and the applied voltage. Surface segregation of oxidized nickel over ceria particles can be observed under oxidative atmosphere, and under specific operational conditions nickel species are maintained in a partially oxidized state in the form of a core-shell comprising a surface $Ni-CeO_{1.5}$ skin and a $NiO-CeO_2$ backbone. The surface shell can be beneficial to maintain high electronic conductivity and appropriate TPB length for the electrolysis reaction, and the interior oxidized core can help to keep particles volume, thus sustaining the microstructure of the electrode.
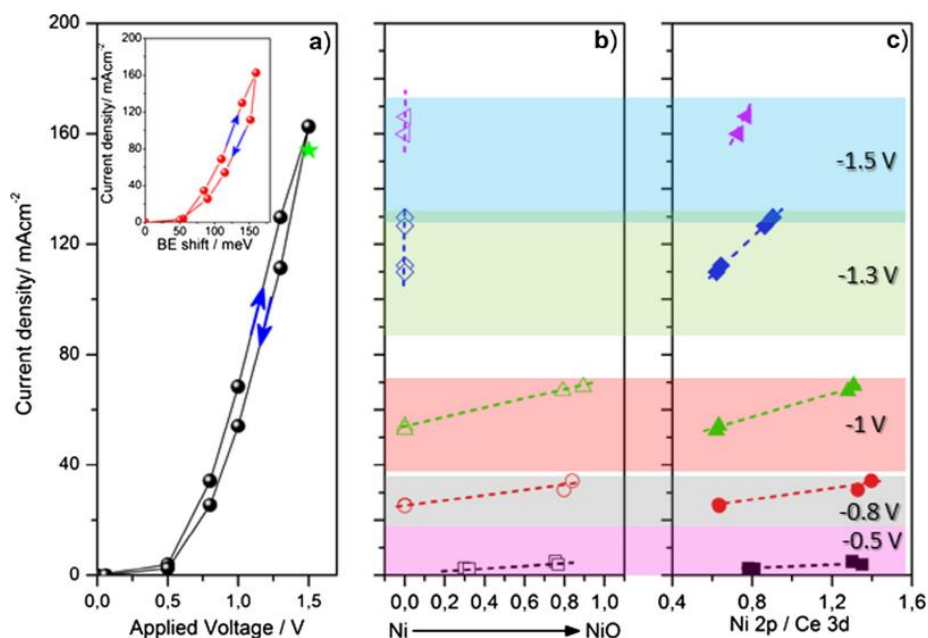
Figure 1.12. (a) I-V polarization curves for Ni/GDC electrode under H_2O feed recorded in potential step-up and down cycles. The current density for various applied potentials as a function of: (b) NiO_x valence and c) Ni/Ce AR measured by APXPS. Reproduced with permission [93]. Copyright 2017, Elsevier.

In a more recent study of our group, Mewafy et al.[95] provided a direct relationship between Ni-YSZ and Ni-GDC electrode surface oxidation states and their performance during steam electrolysis by using the same operando approach. It was shown that nickel surface oxidation can have a great negative influence in the electrolysis performance over a Ni-YSZ cathode, inducing significant performance degradation, while having minor effects over Ni-GDC, as shown in Figure 1.13. In this study, there were strong evidences about the effect of the GDC surface oxidation state on the cathode overpotential during steam electrolysis, especially for the improvement of the performance with the surface reduction degree of GDC. Both above mentioned studies, reveal that

small and reversible changes on the few nanometers thick surface of the cathode electrodes may have a great impact on the electrochemical performance of the cell during steam electrolysis.
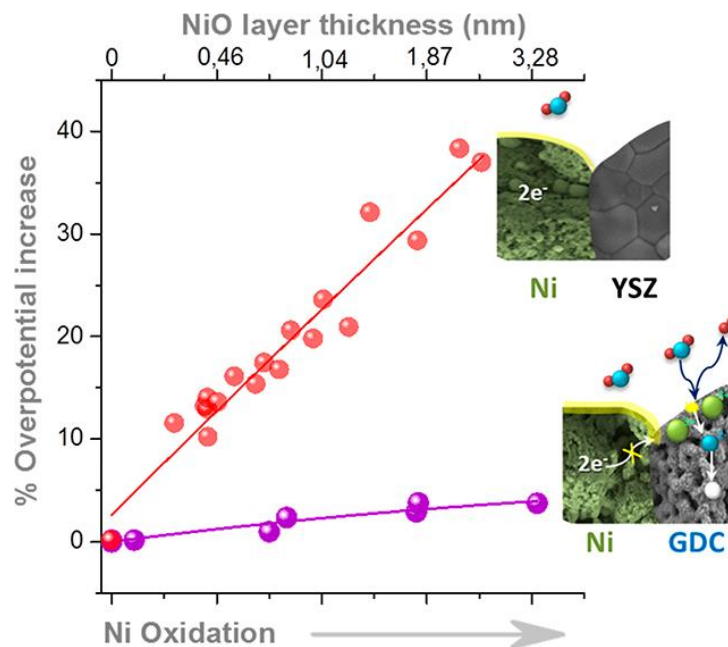
Figure 1.13. Comparison of the percent overpotential increase of cells with Ni-YSZ and Ni-GDC cathode electrodes as a function of the relative amount of NiO and the average NiO film thickness [95].

However, in terms of the CO_2 electroreduction process, similar research based on the operando X-ray photoelectron spectroscopy (NAP-XPS) just focused on cells composed of porous doped-ceria fuel electrodes, mainly Gd and Sm doped ceria electrodes, i.e. without nickel [96,97]. In these studies, carbonate is identified as the vital intermediate for the electro-chemical reaction via operando APXPS technique. Yu et al.[96] proposed that CO_2 first reacts with the lattice oxide on the ceria surface to form the carbonate (CO_3^{2-}) intermediate species, and then the CO_3^{2-} receives two electrons in one step to decompose into CO and two oxygen ions together with the simultaneous oxidation of Ce^{3+} to Ce^{4+} (rate-determining step). In the final step, electroreduction of Ce^{4+} occurs on the surface, which is accompanied by the formation of a surface oxide vacancy. All above reactions are listed in Eqs. (1)-(3).

$$CO_{2(g)} + O^{2-}_{(surface)} \leftrightarrow CO_3^{2-}_{(surface)} \tag{1}$$

$$CO_3^{2-}_{(surface)} + V_{o(s)} + 2Ce^{3+} \leftrightarrow CO_{(g)} + 2O^{2-}_{(surface)} + 2Ce^{4+} \tag{2}$$

$$2Ce^{4+} + 2e^- \leftrightarrow 2Ce^{3+} + V_{o(s)} \tag{3}$$
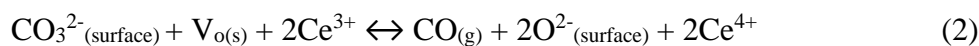
On the other hand, Feng et al. [97] proposed another CO_2 electro-reduction process on the cathode/electrolyte interface, which is schemed in Figure 1.14. Compared with the above process, the reaction starts with the electron transfer from the current collector to the SDC cathode bulk, and simultaneously the oxygen vacancy transfers from the electrolyte to the bulk of ceria electrode as step 1. Subsequently, these species migrate to the surface (step 2). Then the CO_2 molecule adsorbed on a surface $O^{\times}_{O,s}$ accepts a single electron on localized electron ($Ce'_{Ce,s}$) (Ce^{3+}) from the ceria electrode, forming a carbonate adsorbate $(CO_3)'_{O,s}$ (Step 3). At the end the carbonate adsorbate accepts a second electron to decompose into CO and two oxygen ions (Step 4), which can be regarded as the rate-determining step. The detailed reaction steps (1)-(4) are listed in Eqs. (4)-(7).

Step 1 $2(Ce^{\times}_{Ce,b} + e^{-}_{M} \Leftrightarrow Ce'_{Ce,b})$

$$V^{\cdot\cdot}_{O,YSZ} \Leftrightarrow V^{\cdot\cdot}_{O,b} \tag{4}$$

Step 2 $2(Ce'_{Ce,b} + e^{-}_{M} \Leftrightarrow Ce'_{Ce,s})$

$$V^{\cdot\cdot}_{O,b} \Leftrightarrow V^{\cdot\cdot}_{O,s} \tag{5}$$

Step 3 $CO_{2(g)} + O^{\times}_{O,s} + Ce'_{Ce,s} \Leftrightarrow (CO_3)'_{O,s} + Ce^{\times}_{Ce,s} \tag{6}$

Step 4 $(CO_3)'_{O,s} + Ce'_{Ce,s} + V^{\cdot\cdot}_{O,s} \Leftrightarrow CO_{(g)} + 2O^{\times}_{O,s} + Ce^{\times}_{Ce,s} \tag{7}$
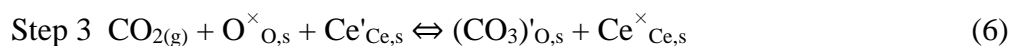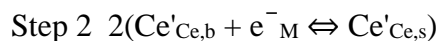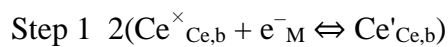
where the subscripts "b", "s", "M" and "YSZ" denote the bulk and surface species of the ceria electrode, the metal current collector, and the YSZ electrolyte, respectively.
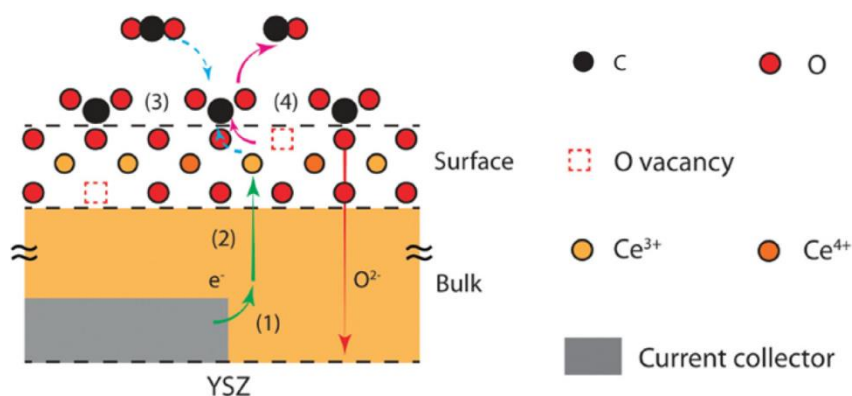
Figure 1.14. Schematic of the proposed reaction mechanism of CO_2 electrochemical reduction. Reproduced with permission [97]. Copyright 2015, the RSC.

Although significant effort has been devoted to understand the CO_2 electrolysis process over these ceria-based cathodes, the effect of the electrode surface state in the electrocatalytic performance

are much less studied for the state-of-the-art (SoA) cathode electrodes in SOECs, i.e. Ni-based cathodes. Typically, literature considers that the active electrode area of Ni/YSZ is the convergence of Ni, YSZ and gaseous phase, the so-called three-phase boundaries (TPBs), while for Ni/GDC, due to the mixed ionic electronic conduction of GDC, the reaction may occur at the two-phase boundaries (2PBs) of GDC and the gas phase. However, *Ni/GDC cathode contains more than 65% nickel, the role of which has not been systematically studied yet. Therefore, the aim of the second part of this thesis is to examine how nickel and ceria oxidation states affect the CO$_2$ electrolysis performance and, in particular, to find evidence about the role of nickel in the reaction via operando near ambient-pressure X-ray photoelectron spectroscopy (NAP-XPS).*

1.4.2. Improve conversion efficiency and durability of SOECs

In order to overcome the challenge of conversion efficiency and durability of SOECs, one major research direction is to focus on the development of SOECs materials. At present, modification/decoration of present state of the art (SoA) materials and development of new advanced materials are the two main directions to improve electrolysis performance of the electrode material. Up to date, the most commonly used cathode material for SOECs is nickel yttrium-stabilized zirconia cermet (Ni/YSZ) due to its low cost, high electron conductivity, and thermal compatibility with the other cell components. However, it also exhibits some drawbacks, such as the high overpotential losses and poor durability both in single cell and stacks [98]. Infiltration of SoA electrodes with active nanoparticles is a promising way to improve both the electrochemical activity and stability of SOEC [99]. First, the properties of SoA electrodes, such as Ni/YSZ, can be further enhanced via correct selection of nanoscale catalysts. Second, infiltration method does not only improve the original electrodes, but can also make the low temperature deposition of advanced but incompatible nano-sized catalysts within a stable electrode backbone possible after sintering at high temperatures, eliminating the limitations dictated by the mechanical incompatibility of the materials (i.e. different thermal expansion coefficients). Besides, the high surface areas of the as-synthesized nanoscale catalysts can be preserved due to low temperature requirements in their synthesis. Moreover, since there are no additional processing steps at elevated temperatures after cell production, synthesis/calcination at low temperature can also reduce the manufacture cost.

Actually, there are two main motivations to modify the electrodes by depositing nanoparticles: i) introduction of catalytic function; ii) enhancement of conduction pathways. To be specific,

infiltrated particles can be dispersed as catalysts, or form connected networks or layers as extra conduction pathways on the preformed electrodes, as shown in Figure 1.15. ***Since in this study we mainly focus on further improvement of the ionic and electronic conductivity of the state-of-the-art Ni/YSZ electrode, introduction of dispersed nanoscale catalysts and their (electro)catalytic function is one of the topics of this thesis.***
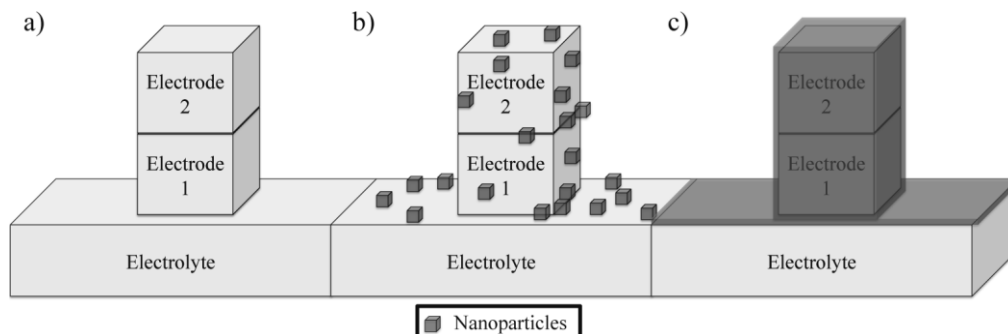
Figure 1.15. Schematic electrode (a) as sintered, (b) after impregnation of dispersed particles and (c) after impregnation of connected particles. Reproduced with permission [100]. Copyright 2008, Wiley-VCH.

At present, there are three prominent impregnation methods to infiltrate dispersed nanoscale catalysts into SOEC electrodes: nanoparticle dispersion, metal salt precipitation, and metal salt plus additive precipitation.

Nanoparticle dispersion

In terms of infiltration methods, the most easy and straightforward way is to directly disperse catalyst nanoparticles into a solvent, then infiltrate the suspension into the electrode, and finally calcine to obtain the modified electrode [101]. This method can allow for a high level of control in the catalysts, because the synthesis of the nanoparticles solution can be done in advance under controlled environments. However, the biggest limitation is the difficult control of nanoparticle agglomeration inside the pores of the electrode. Actually the electrode itself can act as a filter and prevent significant deposition on the areas deep inside the electrode close to the interface with the electrolyte. The electrode pore clogging limits the diffusion of the gas inside the electrode's volume and causes gas starvation during operation [102]. For example, P.K. Lohsoontorn et al. infiltrated a GDC catalyst into a Ni-YSZ electrode [103]. According to their results, GDC solid loading was 20 wt % within butanol-mixed xylene solvent. Figure 1.16.a shows the SEM image of the GDC starting powder from the impregnating solution, where it can be seen that the particles

are submicron-sized but highly agglomerated. Moreover, it was noted that the infiltrated GDC particles are not homogenous on the Ni/YSZ substrate (Figure 1.16.b).
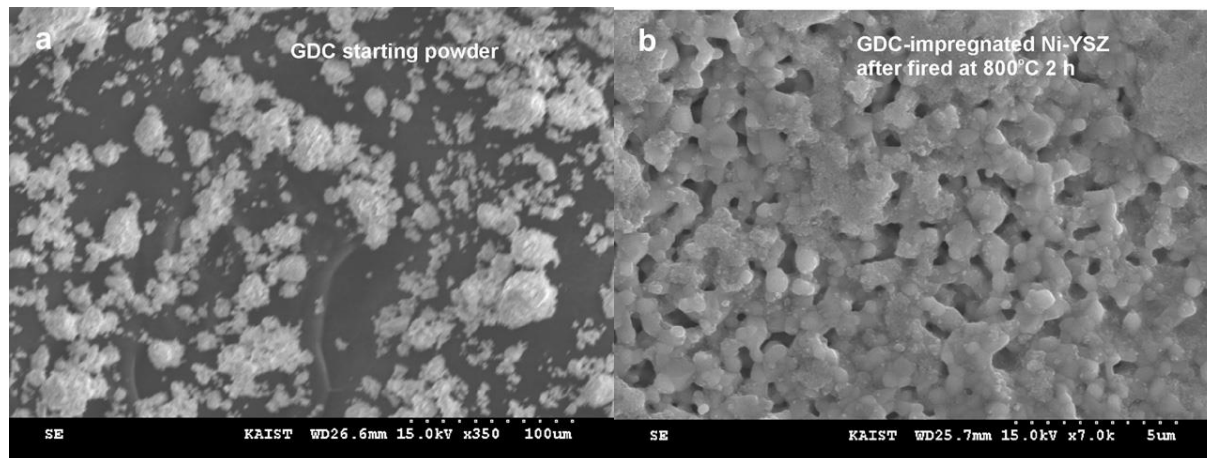
Figure 1.16. The SEM images of (a) GDC starting powder; and, (b) GDC-impregnated Ni/YSZ electrode after fired at 800°C for 2 h. Reproduced with permission [103]. Copyright 2011, Elsevier.

Metal salt precipitation

At present, metal precursor solution infiltration is the most popular strategy reported in the literature. To be specific, the precursor solution comprises metal salts (chlorides, sulfides, and mostly nitrides) dissolved into water/alcohol. After the above precursor solution is impregnated into the electrode, the solution dries and precipitates out the dissolved metal salt. Finally the infiltrated electrode is fired to 400-1000 °C to form nano-sized infiltrated particles. However, in general the infiltration process should be carried by repetitive steps due to the solubility limit of metal salts, as shown in Figure 1.17. Although repetitive steps increase the catalyst loading, which can improve electronic conductivity, tedious infiltration/drying/calcination steps are very labor-intensive. More importantly, each preferential drying at the surface of the porous structure results in precipitate segregation and agglomeration, eliminating the ability to further incorporate more salt solution deeper into the microstructure. In addition, the promoting grain growth during each firing step further reduces the efficacy of the infiltration, increasing potential clogging risks.
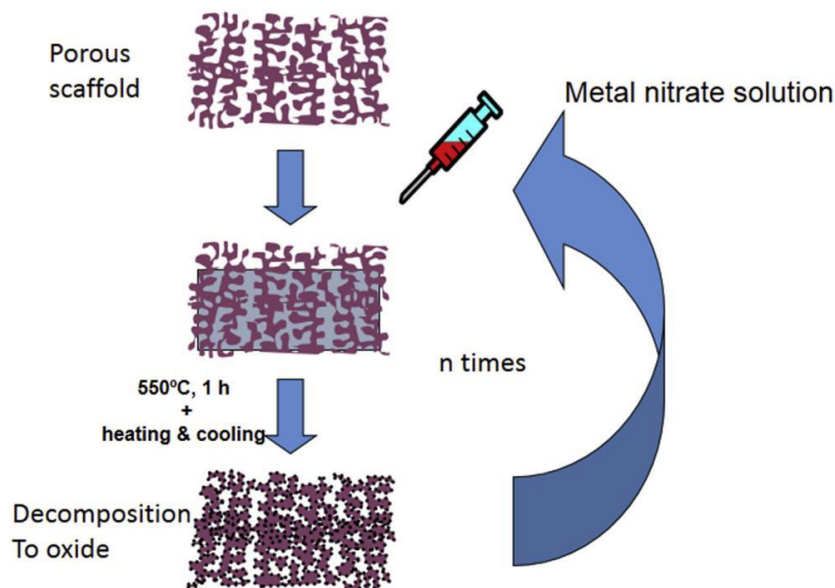
Figure 1.17. Typical process for the infiltration of metal salt nitrate solution or nanoparticle suspension into the porous scaffold. Reproduced with permission [104]. Copyright 2015, Elsevier.

Metal-salt plus additive precipitation

In order to decrease the number of infiltration steps and control the dispersion of porous structures with metal salt solutions, various dispersant and surfactant additives, such as glycol, citric acid, urea, and Triton X-1 [105,106] are added into the metal salt solutions to induce precipitation before evaporation of the solvent, since the surfactant not only can complex with metal cations to assist the formation of the crystal phase, but can also control the particle size via formation of a proper micelle [107]. If Triton X surfactant is added for example, as is exhibited in Figure 1.18, direct decomposing of LSM occurs, not yielding a phase-pure LSM perovskite. In contrast, metal nitrate precursors can produce a pure LSM perovskite phase in the presence of the Triton X surfactant [100]. However, the additives utilized in these studies are specifically associated with the composition of the substrates and/or nano-catalysts. One example is the study of Nicholas et al. [106], reporting that citric acid complex additive reduces the impurity content of the $Sm_{0.5}Sr_{0.5}CoO_{3-x}$ (SSC) phase, compared with Triton-X additive, as shown in Figure 1.19. Therefore, the surfactant system always needs to be re-engineered to respond to the change of SOEC electrodes or nano-catalyst compositions.
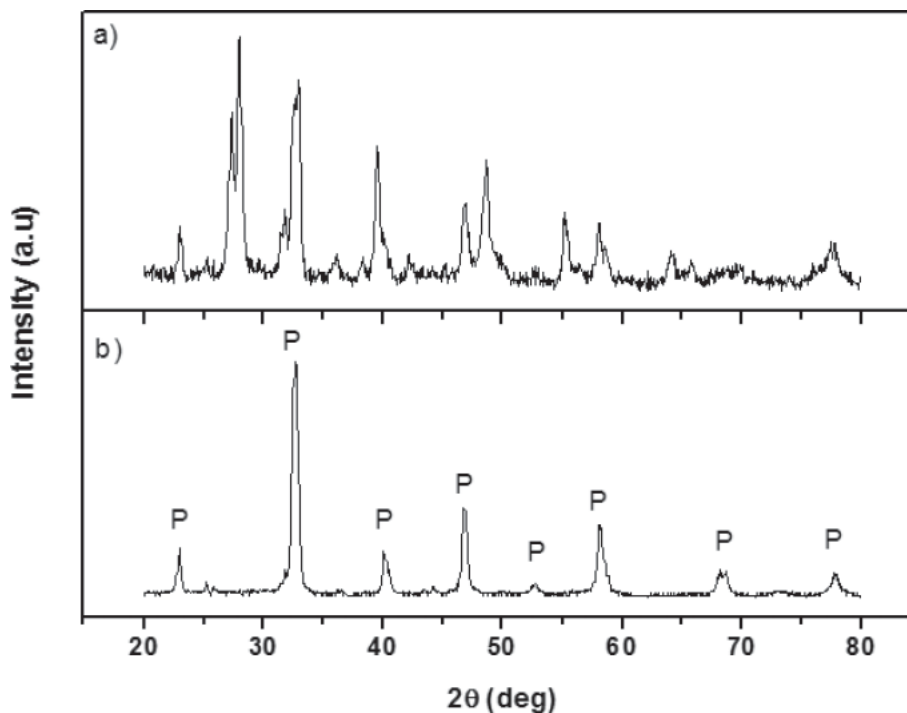
Figure 1.18. XRD patterns of the decomposition products from LSM precursor (a) without and (b) with Triton-X 100, sintered at 800°C for 1h. Reproduced with permission [100]. Copyright 2008, Wiley-VCH.
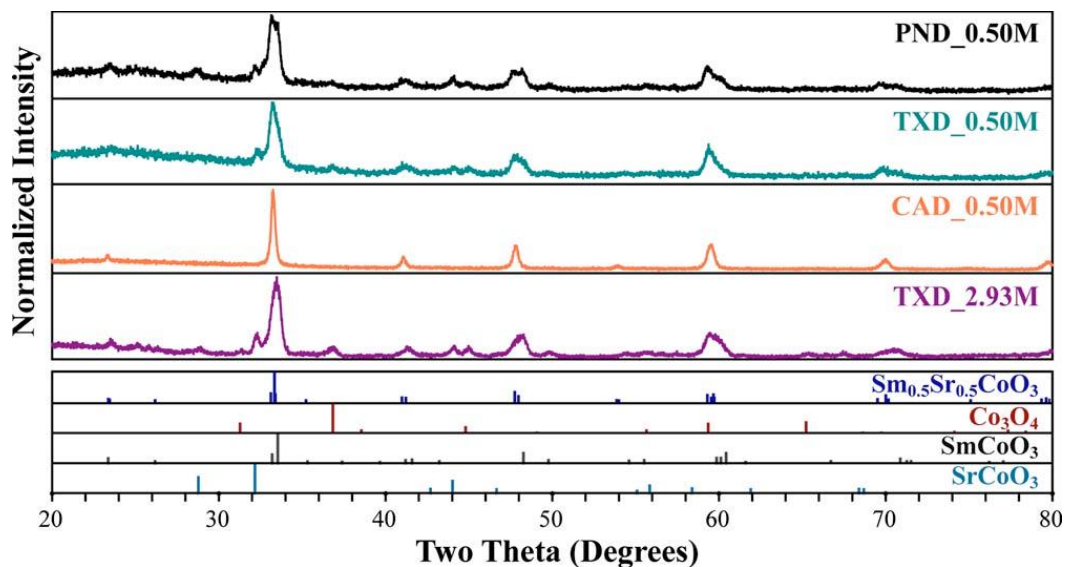
Figure 1.19. XRD scans for powders produced by firing various $Sm(NO_3)$-$Sr(NO_3)_2$-$Co(NO_3)_2$. PND= Pure nitride derived, TXD=Triton X-100 derived, CAD=Citric acid derived. Reproduced with permission [106]. Copyright 2010, The Electrochemical Society.

Wet Chemistry

It is common knowledge that the modification of wet chemistry for the precursor solution plays an important role in improving the penetration ability and hence increases the yield of material deposition per step. In addition to some external engineering solutions such as pressure or vacuum assistance, the surface tension of the precursor system is vital to the wettability of the electrode backbone. Alcohol-based solvents have lower surface tension than water, hence in order to achive a better wettability of the electrode's pores, ethanol is sometimes added into the aqueous solution as a solvent additive to modify the liquid surface tension of the solution carrying the promoter [108–111]. For example, Lou et al. controlled the wetting property of SSC ($Sm_{0.6}Sr_{0.4}CoO_{3-\delta}$) precursor by tuning the solvent mixture [107]. In Figure 1.20 shows the wetting angles of 3 precursor solutions (with or without mixing) over 4 substrates commonly used for electrode fabrication (LSCF, LSM, YSZ; GDC). This experiment showed that higher ethanol content in the precursor solution produce lower contact angles regardless of the substrate material. However, using 100% ethanol as a solvent can limit the solubility hence it can adversely affect the solution/suspension stability and drying kinetics after infiltration. Therefore, no matter the infiltration way (dispersed pre-synthesized nanoparticles suspension or infiltration of metal precursor solutions), the ratios of water-alcohol mixed solvents must be adjusted to reduce the number of infiltration steps as much as possible, which further increases the complexity of the infiltrating experiments.
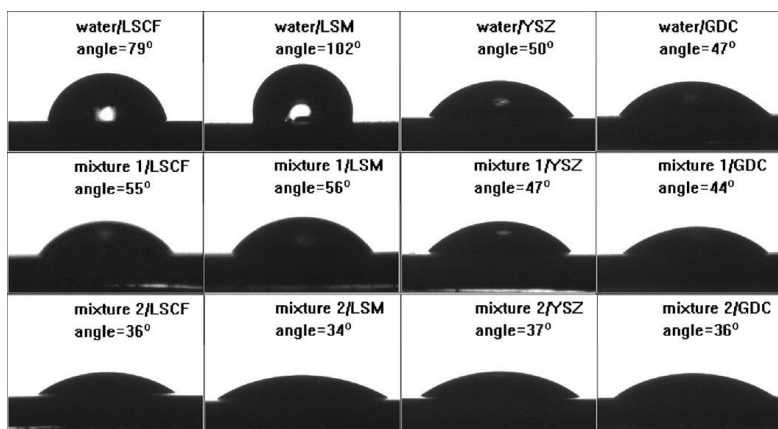
Figure 1.20. Wetting angles of different SSC precursor solutions on LSCF, LSM, YSZ and GDC substrates (note: mixture 1 had a water-to-ethanol volume ratio of 1:0.3 and mixture 2 has a water-to-ethanol volume ratio of 1:0.6). Reproduced with permission [107]. Copyright 2010, Elsevier.

End-goal of the infiltration strategy

In the infiltration process, in order to improve the triple- and/or double-phase boundary length in SOEC electrode, the infiltrated nanoparticles should be located close to the electrochemical active area. Many studies propose that this area is primarily deep within the porous electrode layer near to the interface with the electrolyte [112]. If these precipitated salt solutions are far from the active area (such as near the outer surface or in the middle of the electrode volume), the electrode performance may not present obvious enhancement after infiltration, or even have negative effects due to the limitation of gas diffusion (porosity blockage caused by nanoparticle accumulation). Actually, the real electrode layer is usually engineered to have a relatively higher density and thickness (>500um) in order to provide mechanical strength to the SOEC cell, which makes the infiltration process much challenging and inefficient. On the other hand, since SOECs are relatively high-temperature systems, infiltrated nanoparticles easily tend to coarsening/sintering during operation, adversely affecting the long-term stability of the fuel cell [113,114]. In order to overcome above issues, the infiltrated nanoparticles should be uniformly decorated and have small effect to the micro and macro characteristics of the electrode.

Overall, the end-goal of infiltration of SOECs is to minimize the infiltration/co-firing step(s) with the optimum concentration of the proper nano-particles within the active electrode area, finally enhancing and stabilizing the performance. However, the present infiltrating ways, either disperse pre-synthesized nanoparticles suspension infiltration or metal precursor solutions infiltration using surfactant additives, are far from achieving this goal. ***Therefore, one of the aims of this thesis is to further develop the infiltration strategy for more active and stable infiltrated fuel cells.***

1.5. Structure and Objectives of this PhD Thesis

As described above at present Ni-yttria-stabilized zirconia (YSZ) and Ni-gadolinia-doped ceria (GDC) are the SoA cathode electrodes for SOEC operating under H_2O, CO_2 and CO_2/H_2O fuels. However, they are still facing degradation issues and low activation/conversion efficiency issues. Degradation can be categorized into irreversible and reversible effects. The former is related to the mechanical stability of the SOEC device such as loss of the TPB, delamination, and microstructural changes *etc.*, which can be easily demonstrated by post-mortem analysis of the SOEC devices. Reversible phenomena, such as electrode oxidation, and reversible pollution (especially carbon) *etc.*, are dynamic and depend very much on the operational conditions.

Therefore, *operando* characterization technologies are required to understand the exact degradation mechanism to eradicate the degradation issues. In terms of low conversion efficiency issues, despite the fact that Ni/YSZ is promising as SOEC cathode electrocatalyst due to its low cost and good mechanical strength, it exhibits high overpotential losses and poor durability both in single cell and stacks studies. In response to these problems, modification/decoration of present Ni/YSZ material is continuously being proposed as a main direction for CO_2 electrolysis in SOECs.

The principal objective of this work is to understand the electrode oxidation, which is believed to be one of the main caused for reversible degradation. This will be done through investigating the surface chemistry of two nickel-based cathode electrodes, Ni/GDC and Ni/YSZ, under SEOC feed gases and the effect of the electrode surface state in the electrocatalytic performance using near ambient-pressure X-ray photoelectron spectroscopy (NAP-XPS). Finally, based on the above research, our goal is to develop a more robust and active solid oxide electrode for SOC applications via modification/decoration of SoA Ni/YSZ.

In chapter 3, we used *in situ* near ambient pressure XPS to investigate the oxidation of Ni-YSZ and Ni-GDC cermet electrodes by CO_2 and H_2O at conditions relevant to solid oxide electrolysis cells operation. We show that the degree of nickel oxidation by CO_2 and H_2O is not similar, but it is regulated by the presence or not of ceria in the cermet. In particular, ceria promotes nickel oxidation by H_2O but moderates it in CO_2. Based on this observation we modified the Ni-YSZ electrodes by introducing ceria nanoparticles directly on their surface. Comparative tests suggested that the modified Ni-YSZ electrode possesses high oxidation resistance to CO_2.

In the next chapter, we combined operando near ambient-pressure X-ray photoelectron spectroscopy (NAP-XPS) with online gas phase and electrical measurements over cells with porous Ni/GDC cathodes, to research how nickel and ceria oxidation states affect the CO_2 electrolysis performance. Here we employed pure CO_2 (i.e. not mixed with a reductant gas) as well as operational conditions bellow the carbon deposition threshold, to focus on the surface oxidation state and lift complications related to modifications due to carbon deposition. Results show that the functional Ni/GDC surface consists of metallic nickel and partially reduced ceria. Activation of the pure CO_2 electrolysis reaction is correlated to electro-reduction of NiO to Ni at relatively low CO_2 electrolysis potentials. Partially reduced nickel particles are organized in a core-shell structure, with metallic nickel in the shell and NiO underneath, and the formation of a nanometer-thick surface Ni layer is adequate to activate and maintain CO_2 electrolysis. During pure CO_2

electrolysis, GDC acts as a source or sink of mobile oxygen ions. Besides, our research results also confirm that pure CO_2 electrolysis over Ni/GDC cathodes is feasible at an optimal electrode surface state, providing insights that can be useful for the design of efficient electrochemical devices, particularly for direct CO_2 conversion without reductive gas in the feed.

For practical CO_2 electrolysis applications, under the same reaction conditions, Ni/GDC usually possesses higher CO_2 electrochemical performance, and is potentially more stable than Ni-YSZ [40], since it can tolerate better oxidizing conditions occurred in the event of leakage or during shutdown periods [9]. However, Ni-GDC cermets have some disadvantages as compared to Ni-YSZ, related to their lower mechanical stability and the higher cost [10]. Intrigued by this observation, we attempt to combine the robust mechanical properties of Ni-YSZ with the enhanced CO_2 oxidation resistance of cerium-based material. Ceria will be functioning as a source of mobile oxygen ions during the polarization as proposed by the two chapters above.

To do so, in chapter 5, we impregnated cerium nanoparticles into Ni/YSZ in order to improve CO_2 electroreduction of SOEC devices. In principle this method can provide abundant cerium oxide interface sites in the Ni/YSZ cathode to eradicate its high overpotential losses and poor durability issues, retaining at the same time its own advantages of excellent thermal and mechanical stability. In this study, we described the procedure of cerium nanoparticles synthesis and mainly focused on the preparation of the Ce modified Ni/YSZ electrodes. Results showed that NiCe nanoparticles can uniformly decorate the pores of a 40 µm thick Ni/YSZ electrode just after two infiltration/co-firing steps with the employed infiltration strategy. On the contrary, under the same infiltration conditions, the distribution of CeO_2 NPs inside the electrode is less homogenous with particles preferentially located at the outermost surface of the electrode. This difference is connected to the higher dispersion of NiCe in the parent solution forming relatively small agglomerated particles, which can easily penetrate the pores of the Ni/YSZ scaffold by capillary forces and produce a homogenous decoration in the entire volume of the electrode. Good dispersion of the Ni-doped ceria particles in the pores of the electrode support favors the maintenance of the grain size of nanoparticles after both infiltration/co-firing steps and the enhancement of cerium surface reducibility. In the last chapter, E/C experiments of Ni/YSZ cermets before and after modification were performed, indicating that introduction of doped cerium nanoparticles through the novel impregnation strategy not only can obviously promote the electrocatalytic performance for CO_2 electrolysis, but also effectively recover the property of irreversible activated electrode, which

confirmed that nanosized doped CeO_2 oxide is a promising candidate for modification of Ni/YSZ cathode through infiltration method of organic solution. The research in this thesis may serve as a paradigm of how to develop more robust and active solid oxide electrodes for SOC applications, using rational improvement strategies.

Chapter 2. Materials and Experimental Techniques

II.   Chapter 2. Materials and Experimental Techniques

2.1. Cell fabrication

The electrolyte-supported electrochemical Ni-based (Ni/YSZ and Ni/GDC) cermet half-cells (only cathode and electrolyte) used in this study were commercial and purchased from **Kerafol GmbH.** The commercial Ni/YSZ electrodes were used as scaffold and impregnated with ceria NanoParticles (NiCeO$_X$ NPs) as electrocatalytic promoters. The synthesis and characterization of NiCeO$_X$ NPs, as well as the preparation of ceria nanoparticles modified cells will be described in chapter 5. The half SOEC Ni-based cermets cells consisted of a 40 µm NiO/YSZ (66/34 wt.% ratio, 8-mol % Y$_2$O$_3$-doped ZrO$_2$) or NiO/GDC (65/35 wt.% ratio, 10-mol % GdO$_2$-doped CeO$_2$) cermet functional layer acting as the working electrode (cathode electrode) and a 150 or 300 µm thick yttria-stabilized zirconia (YSZ) dense pellet (Kerafol, 8YSZ) by means of screen printing (STV, mesh 40 µm) as the electrolyte [7,115]. Pt was used as the counter electrode (anode) due to its known performance stability in oxidizing and reducing environments [103]. For the preparation of the counter electrode, platinum paste (Pt ink 5542-DG, ESL) was painted symmetrically opposite of the working electrode (abbreviated as NiO/YSZ//YSZ//Pt or NiO/GDC//YSZ//Pt) and then the cells were dried for about 30 min at 100 °C and subsequently fired in air at 980 °C for 10 min, as shown in Figure 2.1. The mean thickness of Pt counter electrode was around 5 µm.
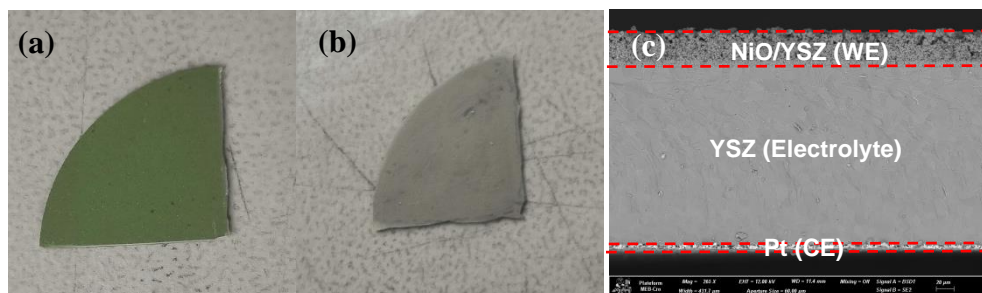
Figure 2.1. Top view of NiO/YSZ cathode (WE) (a) and Pt anode (CE) (b) for the NiO/YSZ//YSZ//Pt cell, (c) cross-sectional SEM image of NiO/YSZ//YSZ//Pt**.**

2.2. ICPEES-based laboratory[1] setups used for preliminary studies

CO_2 electrochemical performance of Ni-based cermets and modified Ni/YSZ electrodes has been studied in the laboratory set-up to simulate the conditions of the NAP chamber at synchrotron facilities. All electrochemical measurements during the laboratory tests and synchrotron measurements were performed using a computer controlled VersaSTAT3 potensiostat/galvanostat (AMETEK Scientific Instruments).

2.2.1. Batch laboratory setup (Just for CO_2 electrochemical tests)

The set-up was constructed for primary CO_2 electrolysis tests under low CO_2 pressure conditions and in batch mode. It consists of a stainless steel cylindrical chamber equipped with an infra-red lamp (Figure 2.2c) for heating and a sample holder (Figure 2.2d), three micro gas cylinders (containing pure O_2, H_2 and CO_2, respectively), a capacitance gauge CMR 362 and a control unit TPG 362 (Pfeiffer Vacuum), vacuum pipeline valves and a dry scroll vacuum pump IDP-15 (Agilent). The electrochemical cell was fixed on the quartz sample holder via two stainless steel clamps and heated from behind using the infra-red lamp. Two gold grids are used as the current collector at both cathode and anode side. The current collectors were connected to 6–way UHV connectors to the manipulator through Au wires protected by ceramic rings, as shown in Figure 2.2d. The temperature was controlled using a PID controller using the reading of a thermocouple mounted on the ceramic sample holder close to the sample.
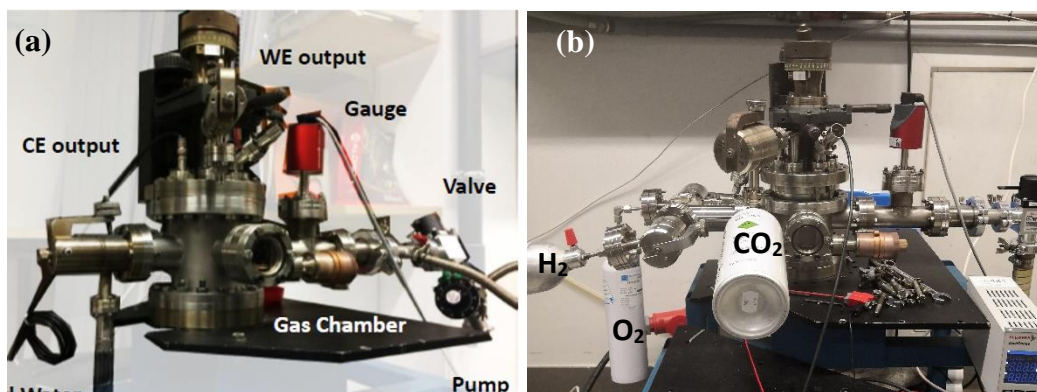
(c)

(d)
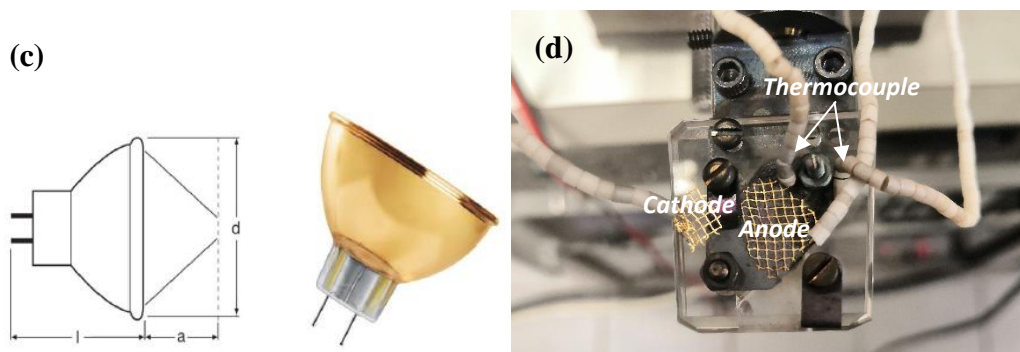
Figure 2.2. (a) Detailed photograph of the laboratory device for the electrochemical tests of the cells under the gas-phase conditions [116]. (b) Photograph of the laboratory set-up. (c) Infra-red lamp 64635 HLX, Halogen lamps with reflector MR16; temperature at the focal point, approximately 1300°C. (d) The two electrode configuration connection sample holder containing Au grid current collectors and a thermocouple in the primary setup.

2.2.2. Flow through variable pressure reactor for *quasi in situ* XPS measurements and CO_2 electrochemical experiments

Most of the laboratory-based characterization was performed in an in-house under ultra-high vacuum (UHV) setup coupling several surface analysis techniques with a flow-though catalytic reactor. Samples were treated in the reactor and then transferred under vacuum to the analysis chamber of the spectrometer for surface characterization mainly by X-ray photoelectron spectroscopy (XPS) measurements. This type of XPS experiments are referred thereafter as "*quasi in situ XPS experiments*". Unless otherwise stated, the aforementioned reactor was used also for the electrochemical and/or gas treatment experiments, described in the thesis.

As shown in Figure 2.4, the *quasi in situ* XPS device consists of four chambers: i) the main chamber, namely, UHV analysis chamber (base pressure 1×10^{-9} mbar) equipped with a VSW Class WA hemispherical electron analyzer (150 mm radius), a monochromatic Al Ka X-ray source (hv=1486.6 eV) and a dual anode X-ray gun; ii) the preparation chamber with a base pressure of 10^{-8} mbar, iii) a load-lock chamber for fast insert the sample into the setup; iv) the variable pressure reaction chamber for electrochemical and/or gas treatment experiments, which can operate in five orders of magnitude pressure range, between 0.01 mbar and 1.0 bar.
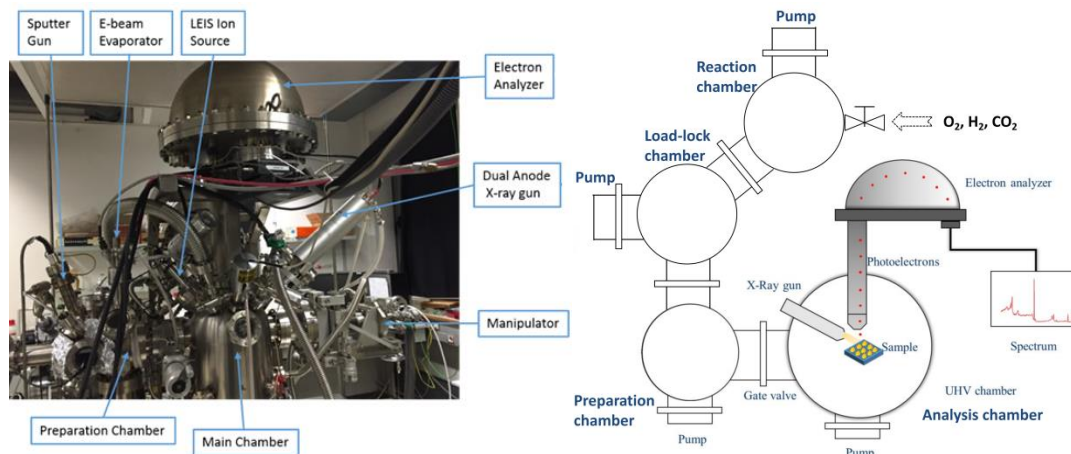
Figure 2.4. Quasi in situ XPS laboratory setup [117] and its schematic drawing for the operation process at (ICPEES, France).
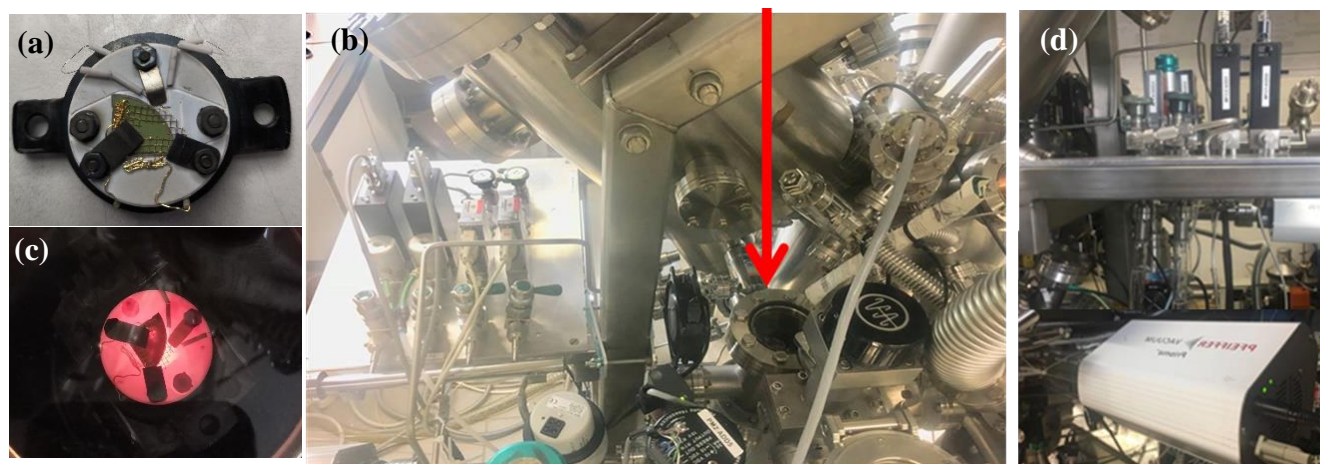
Figure 2.5. (a) The two electrode configuration connection setup sample holder containing the electrochemical cell. (b) Variable pressure reaction chamber of the laboratory equipment for the pretreatment and electrochemical tests of the cells under the gas-phase conditions. (c) The sample holder heated inside the variable pressure reaction chamber. (d) Mass flow controllers which control the gas flow into the reaction cell and quadrupole mass spectrometer (QMS) to monitor the gas phase.

The electrochemical tests were performed in the reaction chamber (Figure 2.5 b) of the quasi in situ X-ray photoelectron spectroscopy (XPS) set-up. The electrochemical cells were fixed directly on a BN-heater (Omnivac) heater via two stainless steel clamps. Two gold grids were used at both cathode and anode side as contacts for current collectors. The temperature was controlled by a K-type thermocouple mounted on the side of the heater, as shown in Figure 2.5 a,c. The gas flow into

the reaction cell was controlled by calibrated mass flow controllers and the products were monitored by an online quadrupole mass spectrometer (*Pfeiffer PRISMA*, QMS) (Figure 2.5d).

2.3. In-situ Near-Ambient Pressure spectroscopy (NAP-XPS) Setup

Although XPS is a powerful spectroscopic tool to obtain chemical information of solid surfaces, conventional XPS instruments need to operate under ultra-high vacuum conditions ($<10^{-8}$ mbar) to avoid the scattering of electrons by gas molecules above the sample. However, operating in UHV conditions does not allow the characterization of catalysts under conditions that resemble their operation, i.e. high pressure and temperature reaction conditions. In order to deal with the above problem, a new type of XPS apparatus has emerged the last 15 years, which allows *in situ* and *operando* measurements of catalysts in gaseous environments in the mbar pressure range. These "environmental XPS" systems, commonly referred to as near ambient pressure XPS (NAP-XPS), have opened up new opportunities to study dynamic modifications at surfaces and correlate them with the catalytic performance.

In the NAP-XPS technique, the attenuation of the electrons, because of their scattering by gas molecules, can be reduced by minimizing the path length of the electrons in the high-pressure region (between the sample and the entrance of the analyzer lenses).This is achieved by moving the sample closer to a differentially-pumped aperture (see the examples in Figure 2.6), allowing to increase the operating pressure limit up to 130 mbar [118]. As shown in Panel A, the most basic set-up contains two or more pumping stages placed between the sample and the entrance to the electron analyzer input lens, which is a quite simple configuration as no modification of the lens system is required and the differential pumping stages can be easily added to the system. However, in this configuration a large number of electrons de-focus inside the lenses and don't reach the detector. Therefore the efficiency of the electron detection is limited. In order to overcome the above drawback, differential pumping directly into the electrostatic lens system was integrated [119] (Panel B is an example of this system currently in use at the ISISS beamline of BESSY II synchrotron). Compared to panel A design, this scheme provides a pumping difference of 10^{-8} between the in-situ cell and the hemispherical analyzer and allows increasing of the detection efficiency of the photoelectrons by up to a few orders of magnitude. Actually all the modern NAP-XPS instruments operate using the principles shown in panel B.
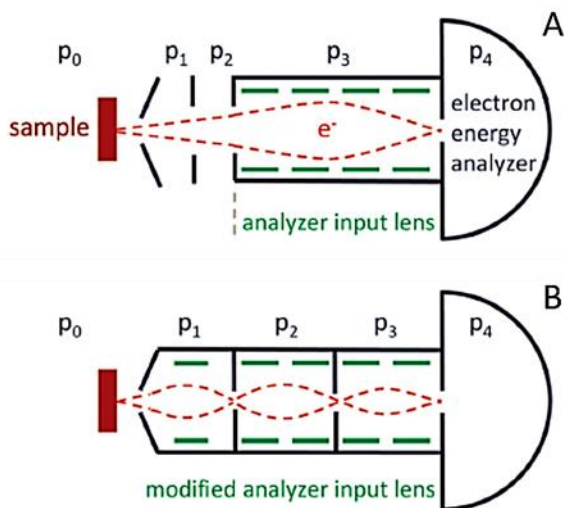
Figure 2.6. Schemes of differential pumping systems used in NAP-XPS. Panel A represents a standard analyzer lens with a set of pumping apertures in front of it, while Panel B shows the principle used at ISISS beamline of BESSY II synchrotron with a differentially-pumped lens system. Reproduced with permission [118]. Copyright 2013, the RSC.

In this thesis, the NAP-XPS technique plays a crucial role in the establishment of the relationship between the surface oxidation state of Ni-based electrodes and their CO_2 electrocatalytic performance. The NAP-XPS measurements were performed at the third generation synchrotron facilities HZB/BESSY II (Berlin, Germany) and SOLEIL (Gif-sur-Yvette, France). The unique properties of synchrotron radiation are wide-energy tunability, high brilliance and high photon flux [120,121]. The set-ups and instrumentations of the beamlines as well as the measurement conditions are described below.

2.3.1. HZB/BESSY II-ISISS Beamline

In-situ or operando near ambient pressure XPS of Ni/GDC during electrolysis reaction was performed at the ISISS (Innovative station for *in-situ* spectroscopy) beam line build and operated by the Inorganic Chemistry department of the Fritz Haber Institute (FHI) in Berlin. The beamline is a bending magnet beamline. The 3 stages differential pumping electrostatic lens system configuration of the set-up allows recording photoemission spectra at the gas-phase pressure up to few mbars (Figure 2.7). The Phoibos 150 electron analyzer (SPECS) is equipped with a 2D Delay Line detector from Surface Concept. The beam was separated by the analysis chamber by a nm-thick silicon nitrate window. The electrochemical cells were mounted between two stainless steel

clamps, and gold wires were acting as the current collectors, similar to the configuration shown in Figure 2.2d. Heating was performed from the rear using an IR-laser, while the temperature was monitored at the center of the working electrode using a calibrated pyrometer (Figure 2.7).

The gases were introduced into the NAP-XPS chamber using calibrated mass flow controllers. The composition of the ambient in the analysis chamber was constantly monitored by an on-line quadrupole mass spectrometer (QMS, Prisma, Pfeiffer Vacuum, Inc., Germany). The working electrode was grounded, in order to avoid sample charging, and the bias voltage was applied on the counter electrode. For the XPS measurements performed at ISISS beamline, pass energies of 50 eV were used for both survey and core-level spectra. The depth-dependent measurements were carried out using photon energies of 1065 eV and 1320 eV for the Ce3d Ni2p spectra (corresponding around 1.5 and 3 nm of the analysis depth respectivelly).
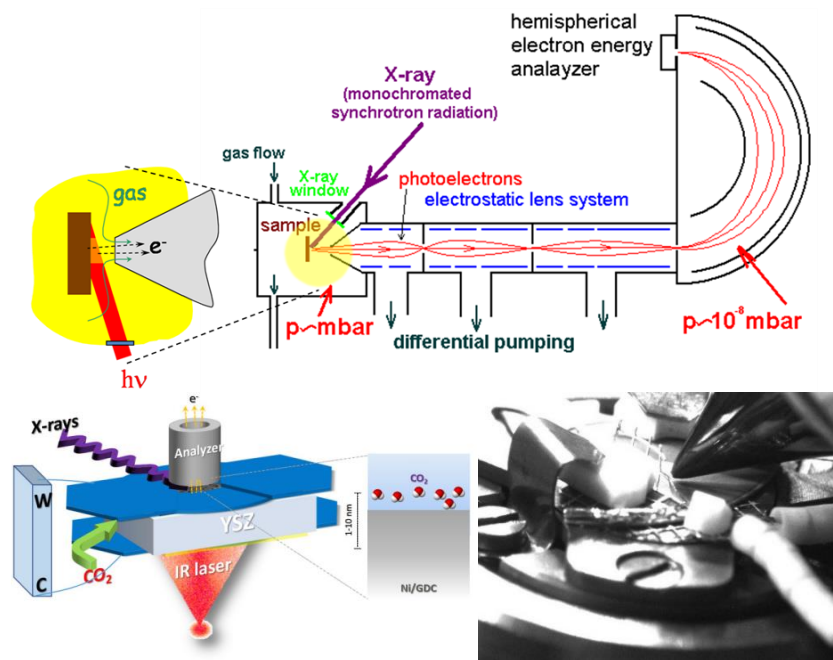
Figure 2.7. (Top) Schematic diagram of the in-situ NAP-XPS set-up under the electrochemical gas-phase conditions. Reproduced with permission [122]. Copyright 2019, the RSC. (**Bottom**) A schematic depicting the experimental setup. The cell is based on dense yttria-stabilized zirconia (YSZ) solid-oxide electrolyte, with porous Ni/Gd-doped ceria (Ni/GDC) as the working electrode and porous Pt as the counter electrode. The sample holder was mounted inside the NAP-XPS chamber.

2.3.2. SOLEIL-TEMPO Beamline

The TEMPO beamline of the SOLEIL synchrotron was utilized to accomplish the NAP-XPS measurements of Ni based electrodes under CO_2 and steam atmosphere. The analysis chamber of the NAP-XPS set-up is equipped with a SPECS Phoibos 150-NAP hemispherical electron analyzer including an electrostatic lens with four differential pumping stages, similar to ISISS station setup. The aperture size is 300 μm and the beam diameter around 100 μm. A windowless beamline entrance with 3 differential pumping stages secures the pressure of the beamline below a limit of 5×10^{-8} mbar. In addition, in contrast to ISISS station which was attached to a bending magnet beamline, TEMPO use radiation coming from an undulator which has significant higher photon flux. This provides a major advance at TEMO as compared to ISISS, because it allows to acquire measurements at higher gas pressures, theoretically up to 20 mbar.

The photograph of the heated holder with loaded samples used in the NAP-XPS experiments of the TEMPO beamline of SOLEIL synchrotron is shown in Figure 2.8. Different electrochemical cells could be mounted together on a ceramic button heater with a K-type thermocouple and fixed in position with stainless steel clamps. This offers an advantage that the tow or more samples can be treated and measured assuring exactly the sample conditions, which is beneficial when samples are characterized in a comparative basis. As in the case of ISISS, the NAP-XPS chamber of TEMPO is also equipped with a QMS, allowing constant controlling of the gas-phase composition of the chamber. The gas was introduced into the chamber through a leak valve in a flow mode. The pass energies of 50 eV were utilized at TEMPO as well. The depth-dependent measurements for Ce3d Ni2p spectra were also carried out using photon energies of 1065 eV and 1320 eV.

Figure 2.8. Photograph of the sample holder used to fix the cells for the TEMPO beamline.

2.3.3. XPS data Processing

This section demonstrates the methods of fitting of the Ni2p Ce3d spectra and the quantitative analysis of XPS results. For XPS data, the deconvolution was done using the CasaXPS software. The relative amount of NiO, Ni, CeO_2 and $CeO_{1.5}$ was estimated by deconvolution of the overall Ni 2p and Ce3d spectra to individual components, using reference peaks of the pure phases.

Ni 2p and Ce 3d peak fitting method

There are two main approaches to fit complex photoemission spectra like Ni 2p and Ce 3d. The first involves the use of a synthetic line-shape defined by a combination of individual Voigt–type peaks, each one of them corresponds to a photoemission or a satellite peak. Very few of these peaks can be resolved in the Ni 2p and Ce 3d spectra [123–126], and therefore, in order to avoid over-interpretation, several constrains should be applied on the intensity ratio and the relative position of each component. For example, 10 individual peaks are typically used for Ce 3d spectra containing Ce^{3+} and Ce^{4+} oxidation states [125], while for Ni^0 and Ni^{2+} another 20 components are required [127], which levels the overall number of individual peaks needed for the fitting of our Ni 2p and Ce 3d spectra at up to 30 ! A universal determination of the constrains that should be applied for the fitting is difficult, therefore the reproducibility of the fitting results is often questionable [128]. Alternatively, when spectra of reference materials are available, it is easier to fit the overall spectrum by using a linear combination of predefined peak line-shapes (measured under identical recording conditions) on the reference components [6]. In this latter case the fitting procedure is simplified, since considerably lower amount of peaks is used. For example, in the case of Ni 2p and Ce 3d spectra, maximum 4 peaks are required [95], instead of 30 needed with the previous method (individual peaks).

In the present work the Ni 2p and Ce 3d spectra were fitted using line shapes (i.e. spectra) recorded on reference materials in-situ under oxidative or reductive treatments. The reference Ni 2p peak of metallic Ni (Ni^0) was measured on a nickel powder fully reduced in H_2, while this of NiO under O_2 at 400 °C. In case of the Ce 3d peak, ceria powder samples were used. For the Ce^{3+} ($CeO_{1.5}$) spectrum the ceria powder was reduced in CH_4 at 650 °C, while for the Ce^{4+} (CeO_2) spectrum the powder was oxidized in O_2 at 400 °C. For the fitting procedure the full width at half maximum and the energy difference between the various reference peaks were fixed. The absolute binding energy and intensity (area) of each peak were allowed to vary until the difference between their sum and the experimental spectrum (residual standard deviation, STD) was minimized (typical STD values

between 0.8 and 1.6). The background subtraction was performed using a flexible background shape based on Cubic Spline Polynomials (spline linear profile) which was allowed to adapt for the eventual differences in the background profiles between reference peaks and spectra of the catalysts. For example, Fig. 2.09 illustrates fitting results in both Ni/GDC and Ni/YSZ electrodes under CO_2 atmosphere. The Ni 2p peak can be deconvoluted into two components; one sharp Ni $2p_{3/2}$ peak around 853 eV, corresponding to Ni metal, and a broader Ni $2p_{3/2}$ feature at 856 eV, associated to Ni oxide [91,129,130]. In the case of the Ni/GDC electrode, the analysis of the Ce 3d spectrum in 10 mbar CO_2 shows that GDC contains both Ce^{3+} and Ce^{4+} cations. Thereinto, the cerium component at ca. 886 and 904 eV is attributed to the Ce^{3+} state, and the peak at 917 eV is ascribed to the Ce^{4+} state[91,93,131,132].
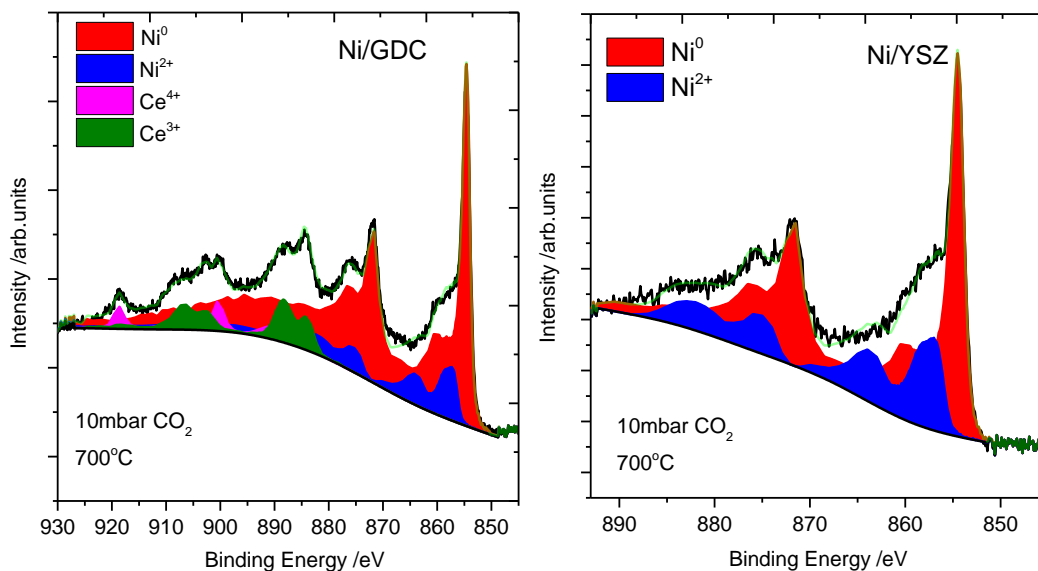
Figure 2.9. Example of the peak fitting results for the estimation of ceria and nickel stoichiometry of Ni/GDC and Ni/YSZ cathodes via NAP-XPS measurements at 400°C under 0.1mbar CO_2 atmosphere after pretreatment in the 10mbar CO_2 gas atmosphere at 700°C for 30 min.

Calculation of Ni and Ce oxidation states using XPS spectra

Initially the relative amount of NiO, Ni, CeO_2 and $CeO_{1.5}$ were estimated by deconvolution of the overall Ni 2p and Ce 3d spectra to individual components, using reference spectra of the pure phases. The mean valence y and x for cerium and nickel respectively are calculated according to the formulas:

$$y = 2 \times \left(\frac{CeO_2}{CeO_2+Ce_2O_3}\right) + 1{,}5 \times \left(\frac{Ce_2O_3}{CeO_2+Ce_2O_3}\right) \qquad (8)$$

$$x = \frac{NiO}{NiO + Ni} \qquad (9)$$

Where: CeO_2, $CeO_{1.5}$, NiO and Ni are the areas of each component in the photoelectron spectrum calculated after the deconvolution procedure.

Estimation of the error in the oxidation state

The error in the calculation of Ni and Ce oxidation states is the sum of the *systematic* and *random* (statistical) errors. The systematic error is primarily related to the reference peak profiles, while the random one is caused by the difference in the signal to noise ratio among the spectra and the choice of the background. In our case the systematic errors are canceled out, since the fitting results are evaluated in comparison basis. The signal to noise ratio of the various Ni2p&Ce3d spectra (typically around 40) does not change significantly, therefore the error in the fitting results is mainly due to the choice of the background of the start and end points as well as the shape. The standard deviation was estimated from the variation of the NiO, Ni, CeO_2 and $CeO_{1.5}$ areas resulted from 4 different fitting attempts of the same Ni2p&Ce3d spectrum. In each fitting attempt the background was selected to be a bit different (however the choice was always rational) and the 4 reference spectra are left to vary so as to minimize the STD value. Following this approach the STD in the area of each spectra component was around 0.5% in the 4 fitting attempts. From this number, an error in the *x* and *y* valence calculations of about 0.01 was estimated.

Quantitative calculations

The surface atomic ratios for nickel based electrodes were calculated based on the intensities of the XPS spectra using the following equation[120]:

$$\frac{A.r(a)}{A.r\,(b)} = \frac{I(a)/(Cs(a).f(a))}{I(b)/(Cs(b).f(b))} \qquad (10)$$

where $\frac{A.r(a)}{A.r\,(b)}$ is the atomic ratio of elements (a) and (b),

I– the intensities obtained from the XPS spectra for the corresponding element,

f– the energy dependent incident photon flux,

Cs– the photoelectric cross-section for the interested atomic orbital taken from [133],

The incident photon fluxes as a function of their photon energy recorded at BESSY II and SOLEIL synchrotrons are shown in Figure 2.10.
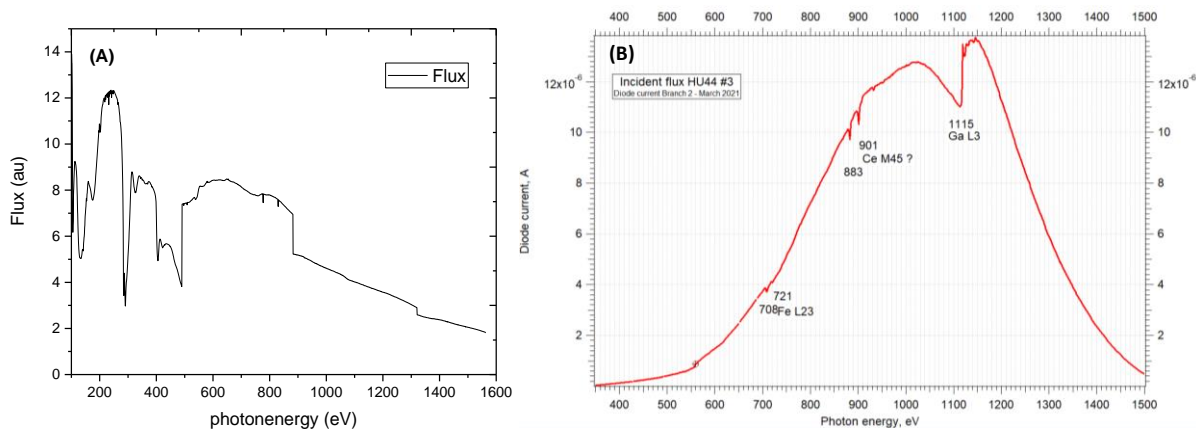
Figure 2.10. Incident photon flux vs photon energy recorded at ISISS (A) and TEMPO (B) beamlines of BESSY II and SOLEIL synchrotron correspondingly. Please note that this graphs are given as an indication of the flux in each energy but the absolute flux between the two beamlines cannot be compared by this graph.

2.4. Electrochemical testing techniques (EIS and Chronoamperometry)

2.4.1. Electrochemical Impedance Spectroscopy (EIS)

Electrochemical impedance spectroscopy (EIS), in which a sinusoidal test voltage or current is applied to the sample under test to measure its impedance over a suitable frequency range, is a useful technique to investigate the electrical performance of electrode materials. The measured impedance spectra, which are usually fitted with an equivalent electrical model, represent an electrical fingerprint of the sample, providing an insight into its properties and behavior. EIS is essentially carried out as follows: In one of its two versions, "potentiostat EIS", a sine-wave voltage (eq.11) is applied to the sample under measurement and the induced current is measured as shown in (eq.12). Then, the complex impedance is calculated as shown in (eq.13) [134].

$$V(t) = \bar{V} + \hat{V} \cdot \sin(\omega t) \ (11)$$

$$I(t) = \bar{I} + \hat{I} \cdot \sin(\omega t + \varphi) \ (12)$$

$$Z(j\omega) = \frac{V(j\omega)}{I(j\omega)} = \frac{\hat{V}}{\hat{I}} \cdot e^{-j\theta} = |Z| \cdot e^{j.Arg(z)} \ (13)$$

$$= Re(z) + j \cdot Im(Z)$$

There into, $\hat{V}$ and $\hat{I}$ are the voltage and the current amplitude, respectively; $\bar{V}$ and $\bar{I}$ are the voltage and the direct current (DC) values; f is the signal frequency; $\omega = 2\pi f$ is the angular frequency; φ is the phase difference between V(t) and I(t); $V(j\omega)$ and $I(j\omega)$ are the Steinmetz transforms of V(t) and I(t), respectively. For the other version of EIS, "galvanostat EIS", the sample is stimulated with a sine-wave current and the voltage drop is measured (of course, the impedance still being given by (eq.13). In most cases, the investigation by potentiostat EIS or galvanostat EIS is equivalent and provides the same results. The optimal choice usually depends on application-specific conditions. The impedance $z(j\omega)$ is defined in the case of linear time invariant systems, exhibiting three conditions: (a) linearity, (b) stability and (c) causality. However, since electrochemical systems typically exhibit a non-linear behavior, and in order to avoid excessive perturbations to the SUT (Sample under the test), small values of $\hat{V}$ (usually in the range 10 to 100 mV) are used to operate in a pseudo-linear region where $z(j\omega)$ does not depend on $\hat{V}$.

2.4.2. Chronoamperometry

The chronoamperometry technique is a very useful indication for the changing of the oxidation state of the electrode materials, and it can also clearly exhibit the degradation phenomena which illustrate in the increasing current. NAP-XPS measurements in synchrotron facilities and most of the performance tests of CO_2 electrolysis were conducted under constant applied voltages between the working and counter electrodes. These measurements will be discussed in more detail in Chapters 4 and 6.

2.4.3. EIS and Chronoamperometry normalization

This section demonstrates the normalization procedure of the electrochemical measurements (both EIS and Chronoamperometry) used in most of the experiments in this thesis. The following procedure was applied the same for Ni/GDC//YSZ//Pt or Ni/YSZ//YSZ//Pt as well as modified Ni/YSZ//YSZ//Pt electrochemical cells. The normalization process for Nyquist plot by galvanostatic EIS measurements and chronoamperometry were done by taking into account the surface area of the electrodes (WE). The simple formulas (14), (15) and (16) were used to normalize the plots and current density I (mA/cm^2). A characteristic example is shown in Figure 2.11.

$$\text{Zre (Ohm.cm}^2\text{)=Zre*WE surface area} \qquad (14)$$

$$\text{Zim (Ohm.cm}^2\text{)=|Zim|*WE surface area} \qquad (15)$$

$$I = \frac{\text{Current}}{\text{WE surface area}} \qquad (16)$$
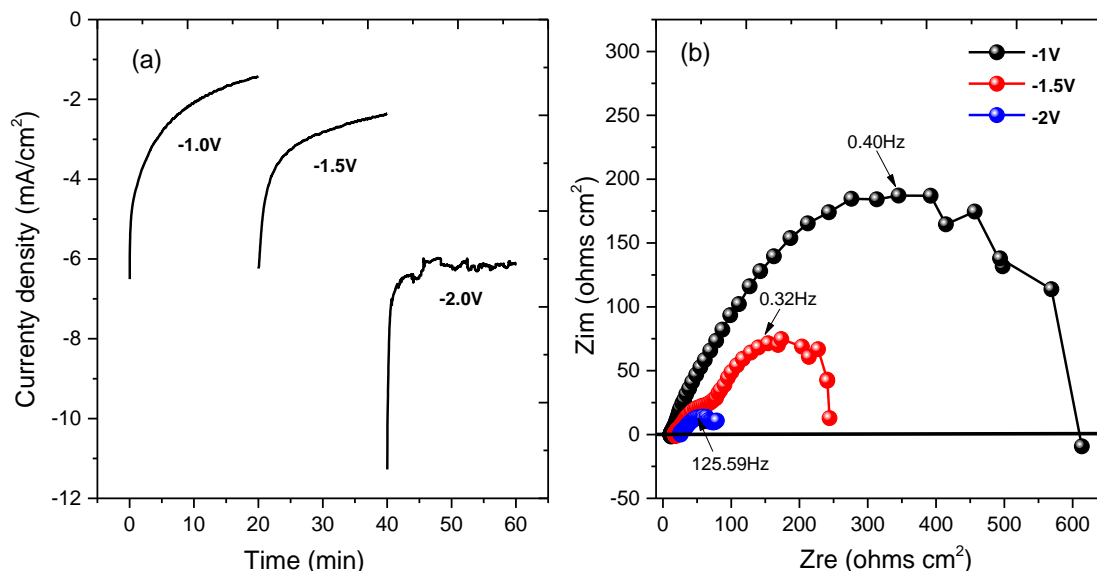
Figure 2.11. Current density (a) and Nyquist plot (b) after normalization over Ni/YSZ//YSZ//Pt cell under 0.5mbar CO_2 electrolysis at 550 °C at the advanced laboratory setup (ICPEES, France).

2.5. Estimation of potential curves between NiCeO$_y$ NPs and CeO$_x$ NPs in hexane

According to DLVO theory [135–137] the total interaction forces between two particles coated by an organic protective layer V_{Total} is the sum of van der Waals attraction V_{vdW}, and total steric repulsive forces (osmotic V_{osm} and elastic V_{elas}) [135–137].

$$V_{Total} = V_{vdW} + V_{osm} + V_{elas} \text{ (eq. 17)}$$

The osmotic repulsion results from the energetic balance between solvent-ligand tail and tail-tail interactions, and the elastic repulsion originates from the entropy loss that occurs upon compression of the stabilizing ligands. The dispersion stability is essentially controlled by the osmotic term since it becomes effective as soon as the ligands start to overlap, while the elastic term does not contribute significantly to V$_{Total}$ until the ligands are forced to compress.

The V_{vdW} can be calculated based on eq. 18:

$$V_{vdW} = -\frac{A}{6}\left[\frac{2r^2}{d^2-4r^2} + \frac{2r^2}{d^2} + ln\left(\frac{d^2-4r^2}{d^2}\right)\right] \text{ (eq. 18)}$$

A is Hamaker constant of cerium nanoparticle in the hexane (3.5×10^{-20}J)[138], r is nanoparticles radius, d is center-to-center separation distance between two nanoparticle cores.

According to Vincent et al.,[135,136,139] V_{osm} results from the energetic balance between solvent-ligand tail and tail-tail interactions, which was estimated as following:

$$V_{osm} = \frac{4\pi r k_B T}{v_{hexane}} \emptyset^2 \left(\frac{1}{2} - \chi\right)\left(l - \frac{d-2r}{2}\right)^2 \quad (l < d - 2r < 2l) \text{ (eq.19)}$$

$$V_{osm} = \frac{4\pi r k_B T}{v_{hexane}} \emptyset^2 \left(\frac{1}{2} - \chi\right)\left[l^2\left(\frac{d-2r}{2l} - \frac{1}{4} - ln\left(\frac{d-2r}{2}\right)\right)\right] \quad (d - 2r < l) \text{ (eq.20)}$$

k_B is Boltzmann's constant, v_{hexane} is the molecular volume of the solvent hexane, $\emptyset$ is the volume fraction profile of the organic species surrounded nanoparticle (oleylamine) ($\emptyset = 1 - \frac{r^3}{(r+l)^3}$), l is oleylamine length ~2 nm, and χ is the Flory-Huggins interaction parameter, which is written as the follows [137]:

$$\chi = \frac{v_{hexane}}{RT}(\delta_{hexane} - \delta_{oleylamine})^2 + 0.34 \text{ (eq.21)}$$

Here, R is gas constant, T is the temperature (298 K), δ_{hexane} (14.9MPa$^{1/2}$) and $\delta_{oleylamine}$ (16.6MPa$^{1/2}$) are the solubility parameters of hexane and oleylamine, respectively. v_{hexane} is calculated to be 2.17x10^{-28} m^3. By using eq.21 χ parameter is calculated to be 0.49.

The elastic repulsion V_{elas} originates from the entropy loss that occurs upon compression of the organic species oleylamine, namely, in the range of $d - 2r < l$.

$$V_{elas} = \frac{2\pi r k_B T l^2 \emptyset \rho_{oleylamine}}{M_{oleylamine}}\left\{xln\left[x\left(\frac{3-x}{2}\right)^2\right] - 6ln\left(\frac{3-x}{2}\right) + 3(1-x)\right\} \quad (d - 2r < l) \text{ (eq.22)}$$

$$x = \frac{d-2r}{l} \text{ (eq.23)}$$

where, $\rho_{oleylamine}$ and $M_{oleylamine}$ represent the oleylamine density and molecular weight, respectively.

Table 1.1. The parameters for the calculation of the potential curves of NiCeO$_y$ and CeO$_x$ NPs in organic solution.

	NiCeO$_y$ NPs	CeO$_x$ NPs
r (nm)[a]	1.91	2.41
l (nm)	2	2
$\emptyset$	0.88	0.84

[a]Nanoparticle radius values r are taken from XRD results of pristine cerium-based nanoparticles in chapter 5.

2.6. Ex-situ Material Characterization

Pristine and post-mortem electrochemical cells have been characterized ex-situ using methods described in the following subsections.

2.6.1. X-ray Diffraction

The phase composition of the catalyst powders and electrodes were studied with X-ray powder diffraction (XRD) using a Bruker D8 Advance diffractometer with a Cu source. For the analysis of pristine ceria NPs, the hexane solution was drop casted on an amorphous glass substrate and let the solvent dry in air. The reference data were taken from the database of the International Centre for Diffraction Data (ICDD). The XRD patterns were recorded in the 20–80° (2θ) range with a scan step of 0.02°.

2.6.2. Scanning Electron Microscopy and Energy-Dispersive X-ray Spectroscopy

The SEM instrument used in chapter 3 is Zeiss Gemini SEM 500 with a lattice resolution of 1 nm. The measurements were done by Thierry Dintzer (ICPEES, France). Energy dispersive X-ray spectroscopy (EDXS) was combined with the SEM images to resolve the different elements at the surface of the electrodes.

FIB-SEM-EDX characterization in chapter 3 and 5 was carried out with the use of a ZEISS Crossbeam 540X scanning electron microscope with X-FEG cathode. The measurements were done by Sylwia Turczyniak-Surdacka (University of Warsaw, Poland). Electrode samples were mounted on aluminum pin stubs with the use of silver cement (Agar Scientific) and placed in the analysis chamber. A focused ion beam (FIB) was applied for cross-sectional sample preparation were done with an accelerating FIB voltage of 30 keV and a beam current of 100 nA, whereas polishing was performed with 30 keV and 1.5 nA. In order to protect the surface, platinum layer was deposited by ion beam deposition (30 keV, 300 pA). The EDX maps were collected with the X-MAXN spectrometer (Oxford Instrument) at 15 keV after tilt correction.

2.6.3. Scanning Transmission Electron Microscopy

The TEM investigations of nanoparticles were carried out using a FEI Talos F200X microscope operated at 200 kV. The measurements were done by Kamil Sobczak (University of Warsaw, Poland). Observations were performed in scanning transmission electron microscopy (STEM) mode using a high-angle annular dark-field (HAADF) imaging. Energy dispersive X-ray

spectroscopy (EDX) using a Super-X system with four silicon drift detectors (SDDs) was applied to the detection of differences in local chemical composition.

2.6.4. Time-of-flight secondary ion mass spectrometry (TOF-SIMS)

The vertical distribution of ceria inside the electrode's volume in chapter 5 was examined by time-of-flight secondary ion mass spectrometry (TOF-SIMS). The measurements were performed using a TOF-SIMS.5 spectrometer (ION-TOF GmbH, Germany) by Marcin Strawski (University of Warsaw, Poland). The ceria-modified Ni/YSZ electrode was transferred without special pre-treatment to the analytical chamber (base pressure $< 2 \times 10^{-9}$ mbar). The TOF-SIMS instrument was operated in spectroscopy mode with 30 keV energy and 0.5 pA Bi_3^+ ion current conditions. The sample was sputtered by oxygen ions (2 keV, 667 nA), rastered over a total sputter area 130 μm × 130 μm. The analyzed area was 40 μm × 40 μm within the total sputter area of 130 μm × 130 μm. The internal mass calibration was performed using mass a series of ions: Na^+, Ni^+, $^{60}Ni^+$, Ni_2^+, Ni_3^+.

2.6.5. FTIR spectroscopy

FTIR spectra of nanoparticle organic solution were obtained by using a PerkinElmer infrared spectrometer model Spectrum 1000. Spectra were taken using 4 cm^{-1} resolution and 32 scans for statistical averaging.

2.6.6. Thermogravimetric analysis (TGA)

The TGA tests of nanoparticle organic solutions were conducted on a thermal analyzer at 10^oC/min with the flow rate of air (99.99%) at 20 ml/min via using Q 5000IR from TA Instruments.

2.6.7. Dynamic Light Scattering (DLS)

The hydrodynamic particle size analysis was performed using Litesizer™ 500 Particle Analyzer (Anton Paar) by DLS (Dynamic Light Scattering) method (ECPM, France). Nanoparticle solution was diluted and then sonicated in a bath sonicator for 10min. Particle size measurement was carried out at room temperature (25°C) and laser wavelength of 660 nm.

Chapter 3. Surface oxidation of Ni-cermet electrodes by CO_2 and H_2O and fabrication of surface-modified Ni/YSZ electrodes tolerant to oxidation by CO_2

III. Chapter 3. Surface oxidation of Ni-cermet electrodes by CO_2 and H_2O and fabrication of surface-modified Ni/YSZ electrodes tolerant to oxidation by CO_2

3.1. Introduction

Solid oxide electrolysis cell (SOEC) technology is a promising way to convert surplus electricity to chemical energy and, if required, reconvert it back to produce electricity [140]. Typically water, carbon dioxide, or a mixture of the two is used as a fuel to produce hydrogen, carbon monoxide or synthesis gas ($CO+H_2$), respectively. Porous ceramic-metal (cermet) composites, in particular Ni-yttria-stabilized zirconia (YSZ) and Ni-gadolinia-doped ceria (GDC), are the most widely tested cathode electrodes for SOEC operating under H_2O, CO_2 and CO_2/H_2O [10,141]. A main challenge remains their poor redox stability in CO_2 or/and H_2O atmosphere, which induces fast degradation of the performance [142]. A reversible degradation mechanism often anticipated in case of Ni-cermet electrodes, is the surface oxidation of nickel particles due to the interaction with the CO_2 or H_2O. Since nickel oxide has lower electronic conductivity and chemical reactivity than metallic nickel, it is expected that the surface oxidized electrodes will have inferior electrical conductivity and catalytic activity. In order to overcome this problem, a reducing gas, typically H_2 or CO, is co-fed with H_2O or CO_2 to maintain nickel in the metallic state [4,141,143]. However, the addition of a reducing agent complicates the cell design and increase the operation cost of the systems. Therefore, it is surprising that although nickel oxidation by H_2O or CO_2 is a major concern of this technology, to the author's knowledge there are no reports detailing the oxidation process of nickel by the two typically used SOEC feed gases.

It is generally acknowledged that both, CO_2 and H_2O can oxidize Ni to NiO, but little is known about the qualitative differences in the oxidation behavior of the two gases. In addition, it is assumed that nickel oxidation is processing similarly in cermet electrodes independent of the type of the ceramic (YSZ or GDC). In this chapter we use in situ near ambient pressure XPS (NAP-XPS) to compare the oxidation of Ni-GDC and Ni-YSZ under H_2O and CO_2 atmosphere at 700 °C. We show that the oxidation of nickel by the two gases is not similar, as is commonly believed, but it depends on the ceramic type. Nickel in Ni-GDC is vulnerable to oxidation in H_2O, but it resists in CO_2, as compared to Ni-YSZ electrode. Inspired by this observation we conceptualize and fabricate Ni-YSZ electrodes modified by ceria nanoparticles, showing significantly higher resistance to CO_2 oxidation as compared to conventional Ni-YSZ. The preparation of tailor-made cermet electrodes with identical bulk/mechanical characteristics but very different surface

properties, offers a promising fabrication strategy for high-performance and durability solid oxide electrolysis cells for CO_2 conversion.

This chapter is based on the published article: Dingkai Chen, Mathias Barreau, Thierry Dintzer, Sylwia Turczyniak-Surdacka, Fabrice Bournel, Jean-Jacques Gallet and Spyridon Zafeiratos. Surface oxidation of Ni-cermet electrodes by CO_2 and H_2O and how to moderate it. Journal of Energy chemistry, 2022, 67, 300-308.

3.2. Experimental Methods

3.2.1. Sample Preparation

The experiments were performed using commercial, electrolyte supported half-cells Ni-YSZ or Ni-GDC electrodes, which have been described in 2.1 section of chapter 2. The $Ni_{0.1}Ce_{0.9}O_{2-x}$ nanoparticles (abbreviated as NiCe NPs) were synthesized and kindly provided by Dr M. Barreau (post-doctoral researcher in our group). The synthesis method of NiCe NPs involves mixing and pyrolysis of Schiff base metal complexes in oleylamine media [11,144]. Surface-modified Ni-YSZ (NiCe@Ni-YSZ) samples were prepared by direct infiltration of the NiCe nanoparticles diluted in an hexane solution (around 4.3 mg ml^{-1}) at the surface of the Ni-YSZ electrodes. Prior to the infiltration the Ni-YSZ electrode was reduced in 1 mbar H_2 at 550°C for 30 min and consequently the NiCe/hexane solution was dropped casted [145] over the Ni/YSZ surface, in air and at ambient temperature, using a 10 µl micropipette. The infiltration step was followed by a firing step at 400 ^{o}C in 1 mbar O_2 for 30min. In total the loading was 150 µl of NiCe/hexane solution per cm^2 of Ni-YSZ, which corresponds to about 0.65 mg of NiCe per cm^2 of Ni-YSZ. The details of the method will be described in Chapter 5.

3.2.2. Synchrotron-Based Experiments

NAP-XPS experiments were carried out at the NAP-XPS end station of Sorbonne Université attached to the TEMPO beamline of the SOLEIL Synchrotron radiation facility in France. Details of the experimental apparatus can be found elsewhere [92,146]. The sample was heated using a button heater, and the temperature was measured with a K-type thermocouple attached on the top of the sample. The gas flows into the analysis chamber were regulated by leak valves and their purity was monitored by a quadrupole mass spectrometer. To assure the reproducibility of the treatment conditions in comparative experiments, two or more samples were mounted together and in close proximity on the ceramic heater. The excitation photon energies were selected so as to

produce photoelectrons with the same kinetic energy (ca. 200 eV and 480 eV) of the examined elements, assuring for the same information depth. The binding energy (BE) of the Ni 2p and Ce 3d spectra were calibrated by setting the Ni 2p3/2 peak of metallic nickel at 852.7 eV [92]. The peak areas were estimated after subtraction of a spline-Shirley type background, using the CasaXPS software. The Ni 2p and Ce 3d peaks were deconvoluted using peak shapes recorded on fully reduced and fully oxidized reference samples. Eventual differences in the background line profiles between deconvoluted and reference spectra justify the choice of a spline-Shirley instead of a Shirley background type. More details about the fitting procedure are provided in 2.3.3 section of chapter 2.

In the design of the NAP-XPS experiment we had to deal with two particularities. The first is related to the necessity to treat the samples at relatively high CO_2 pressure (up to 10 mbar), where the photoemission signal is dramatically attenuated, and the second was that the samples should be treated simultaneously but then measured consecutively, which has the risk that the chemical state of the second sample is modified while measuring the first one and vice versa. Therefore, the following routine was followed during the in situ NAP-XPS measurements: initially the samples were set to the desired temperature (700 °C) and gas pressure for a fix amount of time and subsequently they were cooled down at about 350 °C (the minimum possible temperature to assure no severe electrostatic charging during XPS). The gas was maintained during the NAP-XPS measurements but the pressure was dropped down to 0.1 mbar. Preliminary tests and repetition of spectra at different time periods verified that under these measurement conditions the modification of the sample state during measurements was negligible (Figure 3.1). Photon beam damage effects were tested by shifting the analysis spot to a new sample position, and the lack of differences in the spectra manifests the stability of the samples under the photon beam in the time frame of the experiment.
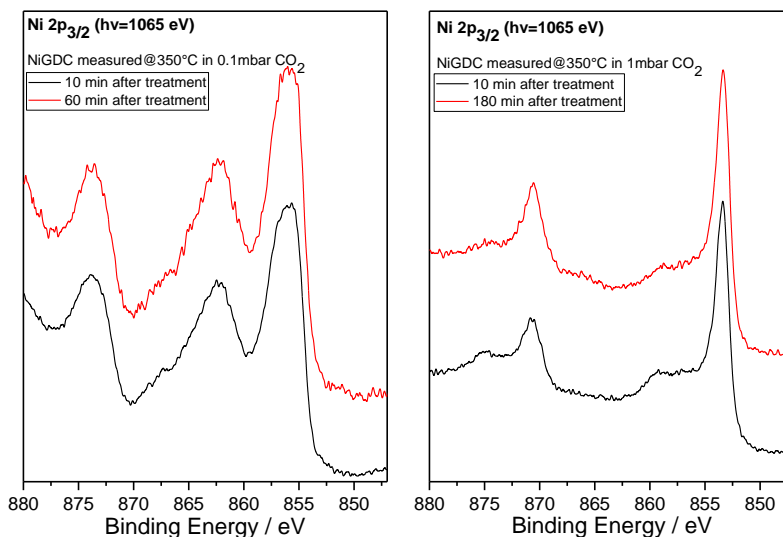
Figure 3.1. Ni $2p_{3/2}$ spectra recorded at the beginning (black) and at the end (red) of the measurement sequel for *(left)* oxidized and (*right*) reduced NiGDC samples. The time between the acquisition of the two spectra is indicated in the figure cation. All spectra were measured at 350 °C in 0.1 mbar CO_2.

3.2.3. Morphology, Structure and laboratory XPS characterization

Morphology and Structure characterization, such as SEM-EDXS, FIB-SEM-EDXS, and XRD, have been described in section 2.6 of chapter 2. Laboratory-based XPS measurements were carried out in an ultrahigh-vacuum (UHV) setup coupled with a variable-pressure reactor (VPR) described in details elsewhere [147,148]. The samples were exposed to gases in the VPR reactor at the desired temperature and pressure and subsequently were transferred under vacuum for XPS analysis. The NiCe-modified Ni/YSZ, pristine Ni/YSZ and Ni/GDC samples were mounted together on the sample holder and pretreated in 1 mbar H_2 at 400 °C for 60 min. Next H_2 was replaced by CO_2 and the samples treated at 6 different CO_2 pressures ranging from 0.5 mbar to 20 mbar for 60 min at 700 °C. After each pressure treatment, the samples was characterized by XPS. During XPS measurements the sample temperature was maintained at 240 °C to avoid electrostatic charging.

3.3. Results and Discussion

3.3.1. Interaction of H_2O and CO_2 with nickel on Ni-YSZ and Ni-GDC cermets

The chemical state at the surface of pre-reduced Ni-cermet electrodes upon exposure in H_2O or CO_2 atmospheres at isothermal conditions was examined first. Preliminary screening NAP-XPS experiments were used to estimate the efficiency of the two gasses to oxidize the electrodes under the employed conditions. These tests revealed that in H_2O, oxidation of nickel takes place at significantly lower pressure and exposure times than CO_2. Therefore, the treatment conditions were not identical for the two gas atmospheres, as might be anticipated, but they were properly selected so as to produce similar nickel oxidation states. Accordingly, figure 3.2 compares the Ni 2p3/2 photoemission peaks from Ni-YSZ and Ni-GDC electrodes after H_2O and CO_2 treatments at 700 °C. Evidently the dosage, or exposure (i.e. gas pressure × time), of the two gases is very different in the two cases (0.12 MPa·s H_2O vs. 4.35 MPa·s CO_2). In both gas atmospheres Ni 2p3/2 spectra (figure 3.2a) are a convolution of metallic (Ni^0) and oxidized (Ni^{2+}) nickel components at 852.7 and 855.6 eV respectively [6,92]. The average nickel oxidation state x (NiO_x) shown in figure 3.2b, was estimated by deconvolution of the Ni 2p3/2 peak into Ni^0 and Ni^{2+} components (figure 3.3). The results presented in figure 3.2 can be interpreted in two ways, either by discerning the oxidation effect of each gas on the same cermet, or alternatively by comparing the two cermets under the same gas atmosphere.

First we identify the differences in nickel oxidation between Ni-GDC and Ni-YSZ in each gas atmosphere. In case of Ni-GDC, $NiO_{0.59}$ is formed in both gas treatments, while for Ni-YSZ, nickel is significantly more oxidized in CO_2 as compared to H_2O ($NiO_{0.92}$ vs. $NiO_{0.30}$). The differences in the nickel chemical state observed on the Ni-YSZ electrode are justified by the 35 times higher CO_2 dosage as compared to H_2O, however the fact that similar nickel states were found on Ni-GDC manifests the fact that dosage is not the sole parameter governing oxidation.

We now compare the oxidation state of the two electrodes under the same gas. As shown in figure 3.2b, in CO_2 nickel is more oxidized in Ni-YSZ as compared to Ni-GDC, while the trend is reversed in H_2O, where more oxidized nickel is found in Ni-GDC. This is an evidence for the fact that the nickel oxidation mechanism is not identical on the two electrodes but follows different paths depending on the gas type.
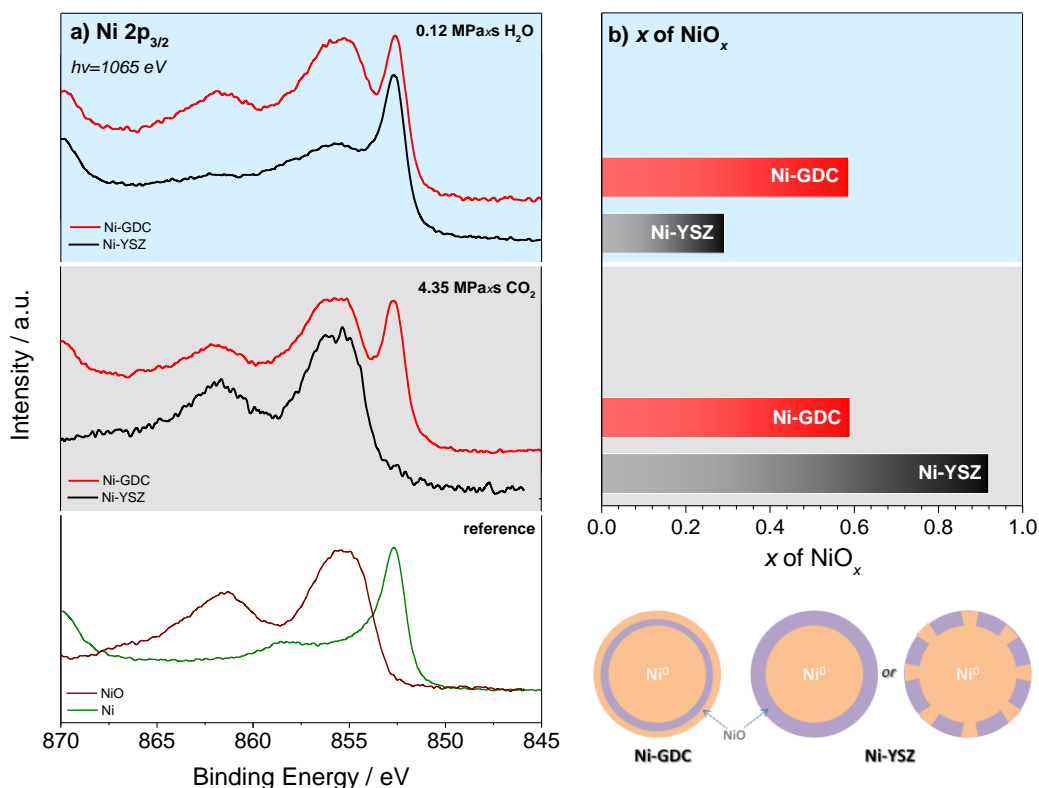
Figure 3.2. (a) Ni 2p (hν = 1065 eV) NAP-XPS spectra of the Ni-YSZ and Ni-GDC cermets after H_2O (top) and CO_2 (middle) gas treatments. Ni 2p3/2 spectra recorded in O_2 and H_2 atmospheres are used as reference of the NiO and Ni^0 oxidation states respectively. (b) Bar chart showing the average nickel oxidation state x at the outer 1.8 nm of the surface calculated after deconvolution of the Ni 2p3/2 NAP-XPS spectra shown in figure 3.2a using reference NiO and Ni^0 peaks. Prior to the H_2O or CO_2 exposure, both cermets were reduced in H_2. Treatment conditions for H_2O: 0.5mbar for 40 min at 700 °C (overall dosage 0.12 MPa·s) Treatment conditions for CO_2: 3.5 mbar for 90 min, 7 mbar for 30 min, 10 mbar for 20 min (consecutive) at 700 °C (overall dosage 4.35 MPa·s). The sample was maintained at 350 °C in 0.1 mbar at the same gas atmosphere with the treatment to avoid changes in the oxidation state during NAP-XPS measurements. The inset cartoon shows a schematic representation of the Ni and NiO arrangement in the two electrodes based on the depth-dependent NAP-XPS measurements.

Another argument about the divergent effect of the gas type on nickel oxidation comes from the in-depth distribution between Ni and NiO in the two electrodes. In particular, the Ni 2p3/2 spectra recorded using a higher incident photon energy, and thus higher analysis depth (2.9 nm, figure

3.3), show that nickel is systematically less oxidized at the surface in case of Ni-GDC, while for Ni-YSZ nickel oxidation state is either very similar in the two depths, or nickel is even more oxidized at the surface. This implies that in case of Ni-GDC, nickel and its oxide are arranged in
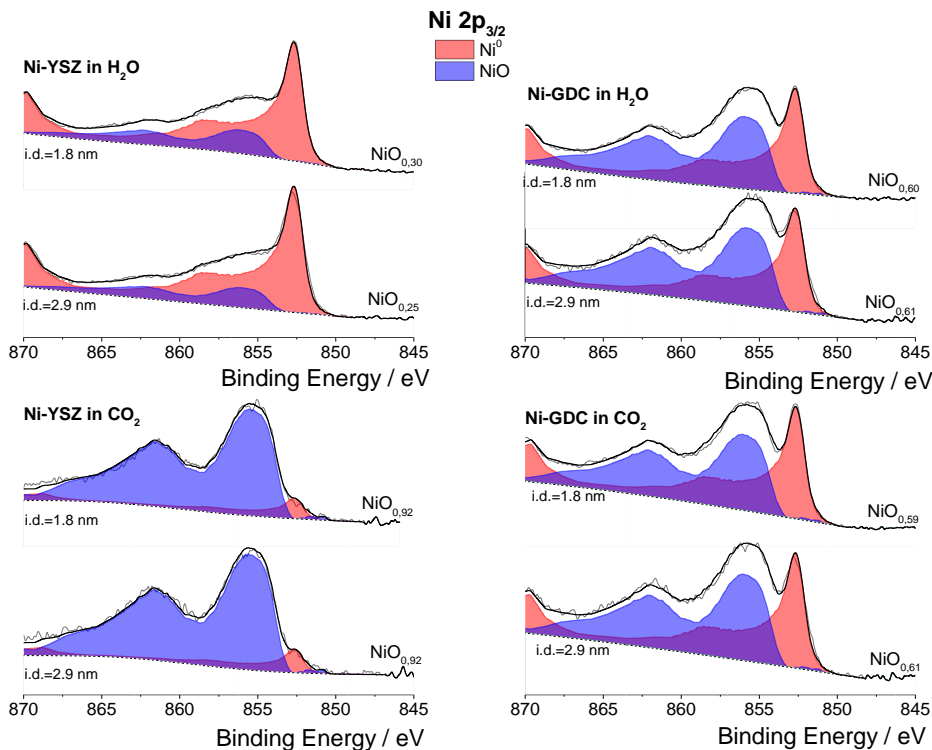
Figure 3.3. Ni 2p3/2 NAP-XPS of Ni-YSZ (left) and Ni-GDC (right) electrodes under H_2O (top) and CO_2 (bottom) atmospheres by using two different photon energies (hv=1065 eV and 1320 eV) which lead to measurements at two information depths (1.8 and 2.9 nm respectivelly). The oxidation state NiO_x calculated based on the deconvoluted spectra is given next to each spectrum. Samples were treated in situ in 0.5 mbar H_2O for 40 min (overall dosage 0.12 MPa·s) or 3.5 mbar CO_2 for 90 min, 7 mbar CO_2 for 30 min, 10 mbar CO_2 for 20 min (consecutive) at 700 °C (overall dosage 4.35 MPa·s). While measuring NAP-XPS the sample was maintained at 400 °C in 0.1 mbar of the same gas atmosphere with the treatment to avoid changes in the oxidation state during NAP-XPS measurements. The Ni2p3/2 peak is fitted by a linear combination of two peak profiles recorded on Ni^0 and NiO reference samples under similar acquisition conditions.

a core-shell type structure with Ni^0 located over NiO, while for Ni-YSZ the surface is either dominated by NiO or the two oxidation states are homogenously mixed. Since the XRD

diffractograms after the gas treatments indicate that both electrodes remain partially oxidized (figure 3.4), it is anticipated that Ni^0 is maintained in the bulk. A schematic representation of the proposed layout of nickel particles based on depth-dependent NAP-XPS and ex situ XRD measurements is inserted in figure 3.2. In case of Ni-GDC (indicated by (i) in the schematic), a core-shell NiO-Ni^0 layer (with Ni^0 on the top) of about 3 nm thickness dominates the surface, while deep in the bulk the nickel particles remain reduced. On the contrary, in Ni-YSZ, NiO is segregated on the outer surface layers. The results do not allow to distinguish whether NiO forms a thin shell over Ni^0 or a mixed phase with it (the two representations are indicated by (ii) in the schematic), however similarly to Ni-GDC, the bulk of the sample remains in the metallic state.
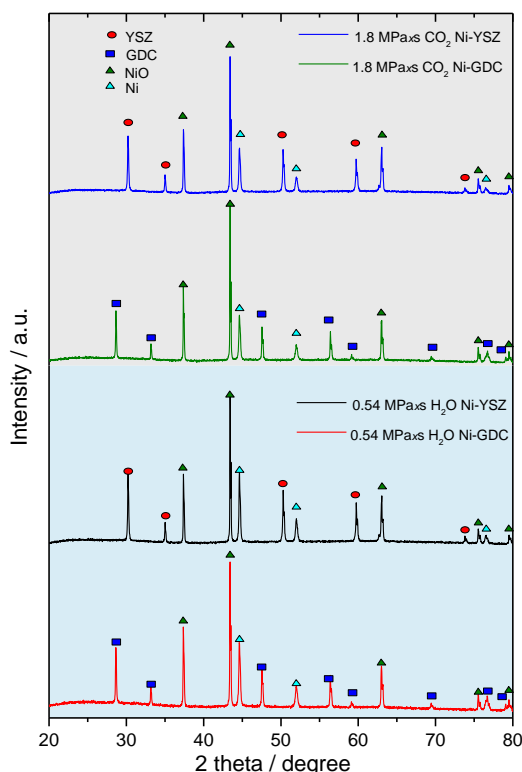
Figure 3.4. ex situ XRD patterns of the Ni-YSZ and Ni-GDC electrodes after calcination at 400 °C in 3 mbar O_2, reduction at 500 °C in 3 mbar H_2 and subsequent dosage of 1.8 MPa·s CO_2 (top) or 0.54 MPa·s H_2O (bottom) at 700 °C.

Eventual differences in the chemical state of nickel reacting with CO_2, H_2O and O_2 atmospheres can be identified based on distinct features of the Ni 2p3/2 line shape. As shown in figure 3.5, the Ni 2p3/2 spectra are practically the same in all cases. The Ni 2p3/2 binding energy position at 855.6 eV and the characteristic satellite peak at the high BE side, suggest the formation of NiO,

rather than Ni hydroxides (e.g. NiOOH or $Ni(OH)_2$) [127]. Although this might be expected for nickel reacting with CO_2 and O_2, formation of hydroxides is often reported in case of interaction with H_2O [149,150]. Apparently under the specific condition of H_2O exposure, fast decomposition of the adsorbed OH groups and consequent NiO formation occurs, similar to previous NAP-XPS observations [91,93].
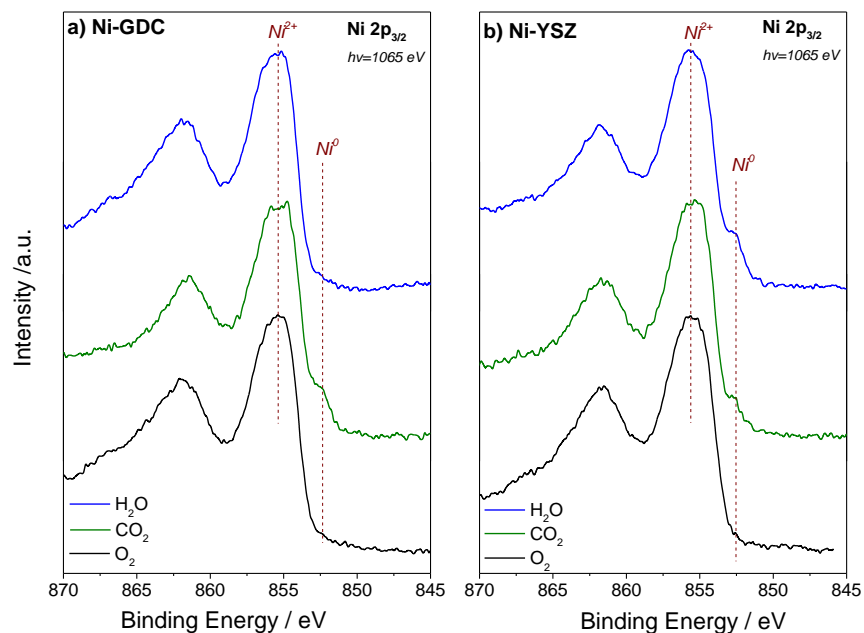
Figure 3.5. Ni 2p3/2 NAP-XPS (hv=1065 eV) NAP-XPS spectra recorded in O_2, CO_2 and H_2O atmospheres a) over Ni-GDC and b) Ni-YSZ electrodes. Prior to each gas exposure the electrodes were pre-reduced in situ under H_2 at 400 °C. The annealing temperatures were 400 °C for O_2 and 700 °C for CO_2 and H_2O. The pressure (between 1 and 10 mbar) and duration of gas treatment is different in each case and it was selected to induce a maximum nickel oxidation.

3.3.2. Interaction of H_2O and CO_2 with YSZ and GDC

The oxidation state of the ceramic part of the two electrodes (YSZ and GDC) is discussed next. The Zr 3d spectrum (figure 3.6) at 182.3 eV is identical in the two gases and characteristic of Zr^{4+} in YSZ [95,151], pointing to a stable YSZ valence state under the employed conditions, in agreement with previous studies [92]. On the contrary, in the case of Ni-GDC, the Ce 3d spectra in CO_2 and H_2O environments are quite different. The peak shape analysis using reference Ce^{3+} and Ce^{4+} peak profiles (figure 3.7) suggests that ceria is found in a mixed Ce^{3+}/Ce^{4+} oxidation state

in both gas atmospheres. The ceria stoichiometry, calculated from the deconvoluted Ce 3d spectra, signifies higher oxidation state in CO_2 ($CeO_{1.81}$) as compared to H_2O ($CeO_{1.64}$). This is another notable effect of the gas type, considering the fact that in these conditions nickel oxidation was found to be identical in the two gases (figure 3.2).
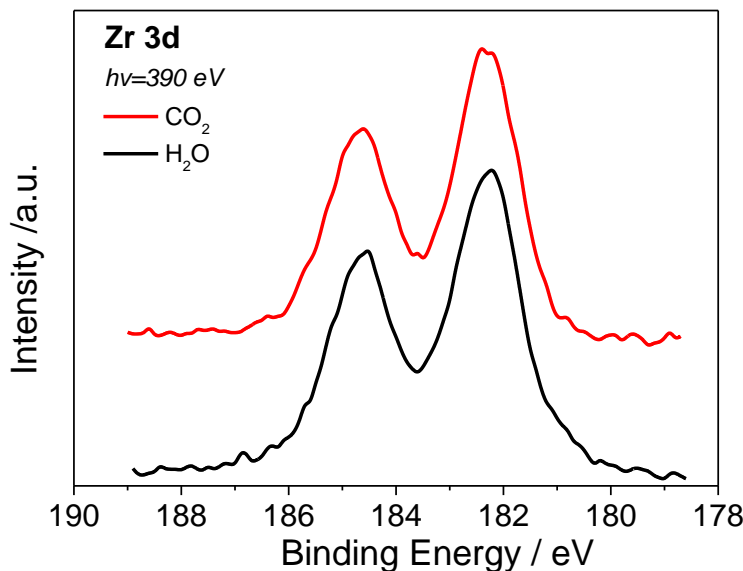
Figure 3.6. Zr 3d NAP-XPS (hv=390 eV) from Ni-YSZ electrodes under CO_2 and H_2O gas atmospheres.
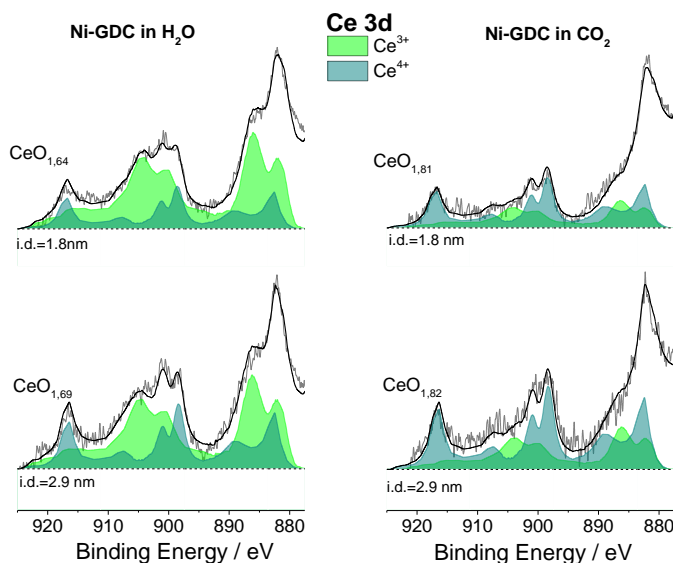
Figure 3.7. Ce 3d NAP-XPS of Ni-GDC electroded under H_2O (left) and CO_2 (right) atmospheres recorded by using two different photon energies (hv=1065 eV and 1320 eV) which lead to measurements at two information depths (1.8 and 2.9 nm respectivelly). The oxidation state CeO_y

as calculated based on the deconvoluted spectra is given next to each spectrum. Samples were treated in situ in 0.5 mbar H_2O for 40 min (overall dosage 0.12 MPa·s) or 3.5 mbar CO_2 for 90 min, 7 mbar CO_2 for 30 min, 10 mbar CO_2 for 20 min (consecutive) at 700 °C (overall dosage 4.35 MPa·s). While measuring NAP-XPS the sample was maintained at 400 °C in 0.1 mbar of the same gas atmosphere with the treatment to avoid changes in the oxidation state during NAP-XPS measurements. The Ce 3d peak is fitted by a linear combination of two peak profiles recorded on Ce_2O_3 and CeO_2 reference samples under similar acquisition conditions. The contribution of the Ni 2p1/2 satalite peak around 880 eV was taken into account in the peak fitting procedure, but for clarity this feature is not included in the figure.

3.3.3. Interaction of H_2O and CO_2 with $Ni_{0.1}Ce_{0.9}O_{2-x}$ nanoparticles

In order to detect possible synergy between nickel and ceria in the oxidation process, we examine the interaction of CO_2 and H_2O with Ni-doped ceria nanoparticles ($Ni_{0.1}Ce_{0.9}O_{2-x}$ or hereafter NiCe NPs). Unlike the Ni-GDC cermet, the NiCe NPs sample does not contain separated nickel particles, therefore it can be used as a reference sample to estimate the synergy between Ni and GDC (e.g. due to interdiffusion, migration or spillover of mobile oxygen ions). The choice of Ni-doped NPs instead of regular ceria powders, was based on their ability to undergo facile reduction under the employed conditions as compared to conventional bulk ceria powders [11], which is a prerequisite to study their oxidation. Prior to CO_2 or H_2O dosage, the NiCe NPs were calcined (2 mbar O_2 at 400 °C) and consequently reduced (2 mbar H_2 at 400 °C) in situ.

The Ce 3d spectra of the pre-reduced NiCe NPs after dosage of 0.42 MPa·s CO_2 or 0.05 MPa·s H_2O at 700 °C recorded with two different photon energies (i.e. information depths), are shown in figure 3.8. Deconvolution of the Ce 3d peak into Ce^{3+} and Ce^{4+} components indicates a mean ceria oxidation state of 1.76±0.1 and 1.78±0.1 for the two analysis depths, and almost identical in the two gas atmospheres. It is clear from this result that H_2O is more effective than CO_2 for ceria oxidation, since it can induce similar oxidation state with 8 times lower dosage. This is in line with theoretical studies comparing the H_2O and CO_2 dissociative adsorption on partially reduced ceria surfaces, which showed that H_2O adsorption [152] and dissociation [153] is more favorable on (reduced) ceria as compared to CO_2.

However, if one compares the ceria oxidation state on NiCe NPs with the findings on the Ni-GDC cermet (figure 3.7), there is an evident discrepancy in the two gas atmospheres oxidation behavior.
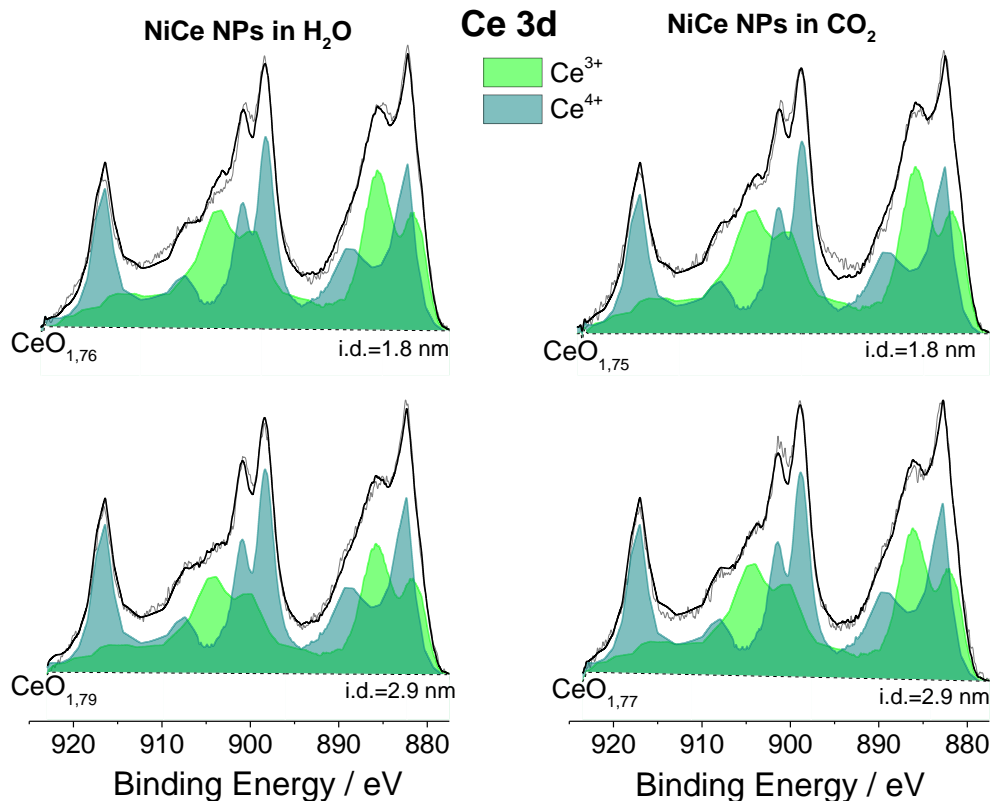
Figure 3.8. Ce 3d NAP-XPS of NiCe NPs under H_2O (left) and CO_2 (right) atmospheres recorded by using two different photon energies (hv=1065 eV and 1320 eV) which lead to measurements at two information depths (1.8 and 2.9 respectivelly). The oxidation state CeO_y, as calculated based on the deconvoluted spectra, is given next to each spectrum. Samples were treated in situ at 0.42 MPa·s CO_2 or 0.05 MPa·s H_2O at 700 °C. The sample was maintained at 400 °C in 0.1mbar of the same gas atmosphere with the treatment, in order to avoid changes in the oxidation state during NAP-XPS measurements. The Ce 3d peak is fitted by a linear combination of two peak profiles recorded on Ce_2O_3 and CeO_2 reference samples under similar acquisition conditions.

In particular, although in CO_2 the higher oxidation state of ceria ($CeO_{1.81}$ vs. $CeO_{1.75}$) on Ni-GDC cermet can be justified by the higher gas dosage (4.35 vs. 0.42 MPa·s), in case of H_2O ceria appears more reduced ($CeO_{1.64}$ vs. $CeO_{1.76}$) in the Ni-GDC despite the fact that it was treated with 2.5 times higher dosage than the NiCe NPs reference sample (0.12 vs. 0.05 MPa·s). A possible explanation is that the chemical state of ceria is influenced by nickel, or more specifically, that nickel particles facilitate the oxidation of ceria by CO_2, but hinder it in H_2O. The mechanism of this process is explained in the next section.

3.3.4. The role of ceria in nickel oxidation by H_2O and CO_2

Nickel and ceria oxidation involves adsorption and dissociation of the H_2O and CO_2 molecules according to the reactions: $CO_2(g) + * \rightarrow CO(g)+O*$ or $H_2O + * \rightarrow H_2(g) + O*$ (the intermediate adsorption step is omitted for brevity), where * is the adsorption site, O* is the adsorbed oxygen and (g) denotes the gas phase. The H_2O and CO_2 dissociation can take place on both nickel and ceramic part, as well as at their interfacial sites usually referred as the three phase boundaries (TPB). The consequent electrode oxidation may proceed via both direct and indirect pathways. In the direct pathway, oxidation takes place by adsorbed oxygen species (O*) generated locally in the vicinity of nickel or ceramic sites. There is however an indirect oxidation path, where mobile oxygen species spillover or diffuse between nickel and ceria parts in close proximity, contributing to the oxidation mechanism.

Based on the photoemission results one can estimate the contribution of each pathway and elucidate the differences observed in the reactivity of the two electrodes towards H_2O and CO_2. To facilitate the discussion, we assume that adsorption and dissociation of CO_2 and H_2O in large extended Ni areas and the consequent oxidation, proceeds in the same manner in the two cermet electrodes which, according to theoretical studies, is quite likely for big particles [154]. Accordingly, the observed differences in Ni oxidation state between Ni-YSZ and Ni-GDC electrodes should be related to the indirect oxidation pathway, i.e. to mobile oxygen formed by adsorption and dissociation of the gas on the ceramic part (GDC or YSZ) and the TPB. The direction in which mobile oxygen migrates, i.e. towards or away from nickel depends on the oxygen affinity of the two parts of the composite and is linked of course to the type of gas, the temperature and the pressure [91].

Ceria is known for its remarkable oxygen storage capacity which originates from the facile transformation between Ce^{3+} and Ce^{4+}, allowing to accept or donate oxygen ions while maintaining its fluorite-type structure [155,156]. These highly mobile oxygen species are known to enhance the oxidation activity of ceria in catalytic and electrocatalytic reactions [157–159]. Therefore, the capacity of the two gases to (re)oxidize ceria by producing mobile oxygen can be the key to understand the oxidation resistance of nickel in CO_2, and also this of ceria in H_2O, which were observed for the Ni-GDC electrode.
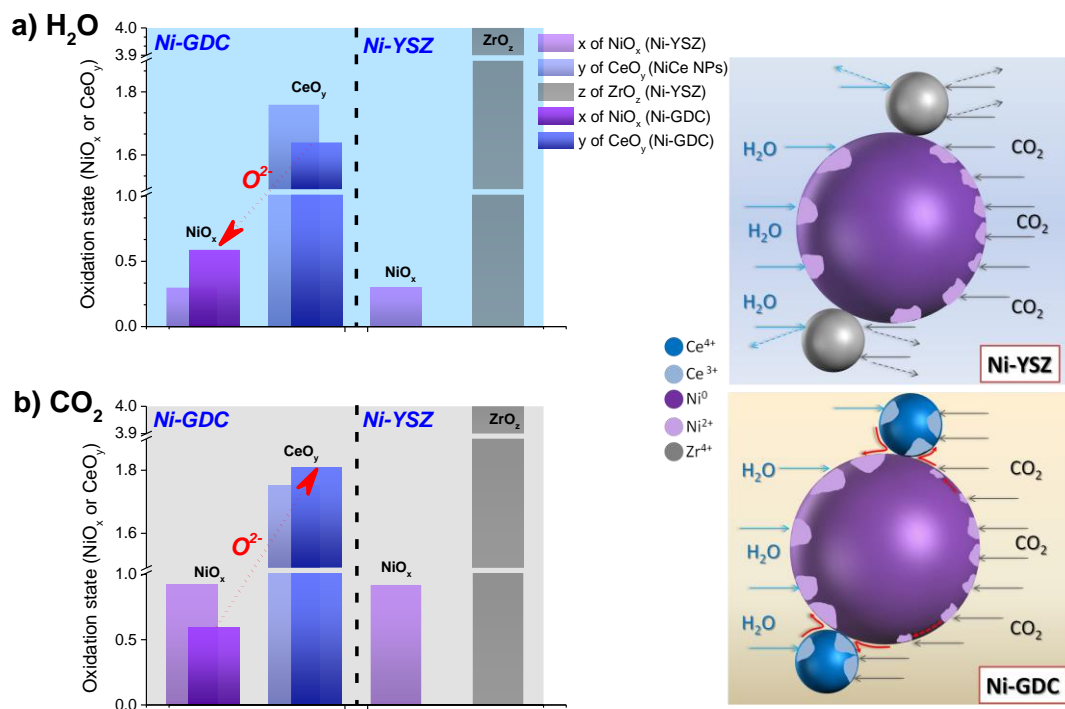
Figure 3.9. The oxidation states of Ni (x of NiO_x), Ce (y of CeO_y) and Zr (z of ZrO_z) of Ni-YSZ, NiCe NPs (light-coloured columns) and Ni-GDC (dark-coloured columns) based on the corresponding NAP-XPS spectra analysis, a) after 0.12 MPa·s H_2O and b) after 4.35 MPa·s CO_2. The red arrows show the direction of oxygen ion exchange. A schematic representation of the proposed oxidation scenario in case of the two cerments for each gas enviorement is given at the right part.

In order to demonstrate a possible scenario of how this is happening we use as an example the oxidation of the two electrodes shown in figure 3.2. Since YSZ is stable (figure 3.6), mobile oxygen does not form on YSZ and we assume that nickel oxidation on the Ni-YSZ electrode is primarily induced by gas directly adsorbed on nickel without extended oxygen spillover from YSZ [130]. This assumption is supported by DFT calculations showing that CO_2 adsorbs weakly on the ceramic part (YSZ) and is mainly activated at the interface with nickel [160], while H_2O can dissociatively adsorb only on the reduced vacant sites at the YSZ surface, which do not exist in our case [161]. Therefore, in the hypothetical case that this assumption also accounts for Ni-GDC, i.e. nickel oxidation it is not influenced by mobile oxygen, then the chemical state of nickel on Ni-YSZ and Ni-GDC should be comparable (light purple bars (Ni-YSZ) in the diagrams of figure 3.9). Likewise, in the absence of any nickel-ceria interaction, figure 3.8 suggests that GDC

oxidation should be very similar in H_2O and CO_2 (light blue bars (NiCe NPs) in figure 3.9). However, if the gas can oxidize one of the two components of the composite electrode more efficiently than the other, then it is expected that mobile oxygen will diffuse/spillover in the direction of the less oxidized component until the equilibrium is established between the two, at least at their interface region [162].

The experiments over Ni-YSZ described in figure 3.2, suggest that at the current employed conditions CO_2 is more efficient nickel oxidant than H_2O ($NiO_{0.92}$ in CO_2 vs. $NiO_{0.30}$ in H_2O), while according to figure 3.8 ceria valence should be similar in the two atmospheres (see also schematic representation in figure 3.9). This is supported by DFT studies of H_2O interaction with $Ni-CeO_2$ surfaces suggesting that H_2O dissociation is facilitated over ceria vacancies (i.e. Ce^{3+}) and Ni^{2+} sites but not over extended nickel areas [154]. Theory also suggests that the above trend is reversed for CO_2, with the most strongly adsorption site being the Ni-ceria interface, followed by those on nickel [163]. Thus in H_2O, mobile oxygen from GDC can migrate/spillover to Ni areas and oxidize them (see arrow in figure 3.9a and the corresponding schematic representation). This "auxiliary" oxidation path is excluded on Ni-YSZ which explains why nickel is less oxidized in this case. In CO_2 atmosphere direct ceria oxidation is limited [163], which drives oxygen from NiO to spillover/diffuse towards ceria and to oxidize it (see arrow in figure 3.9b and the corresponding schematic representation), keeping nickel in a more reduced state than Ni-YSZ.

It is interesting to compare the above proposed scenario with previous studies of cermet electrodes under electrolysis conditions. It has been shown that the surface is actively modified upon polarization in H_2O and in particular, mass transport and intermix of Ce^{3+} and Ni species on the surface may be involved [93,164]. This implies that the surface interaction between Ni and GDC can be more complex than a simple mobile oxygen transfer proposed in our scenario. Due to its high surface sensitivity and the ease in quantification, NAP-XPS is a powerful tool to examine possible surface intermixing in Ni/GDC by monitoring the Ni2p/Ce 3d peak area ratio [93]. Comparison of the Ni 2p&Ce 3d peaks between the two atmospheres (figure 3.10) suggests a considerable increase in the Ce 3d peak in H_2O as compared to CO_2, which is in agreement with morphology changes corresponding to ceria segregation over nickel particles. Therefore, surface intermixing is a general phenomenon occurring on Ni-GDC surfaces treated in H_2O and is not an effect exclusively related to polarization [93,164].
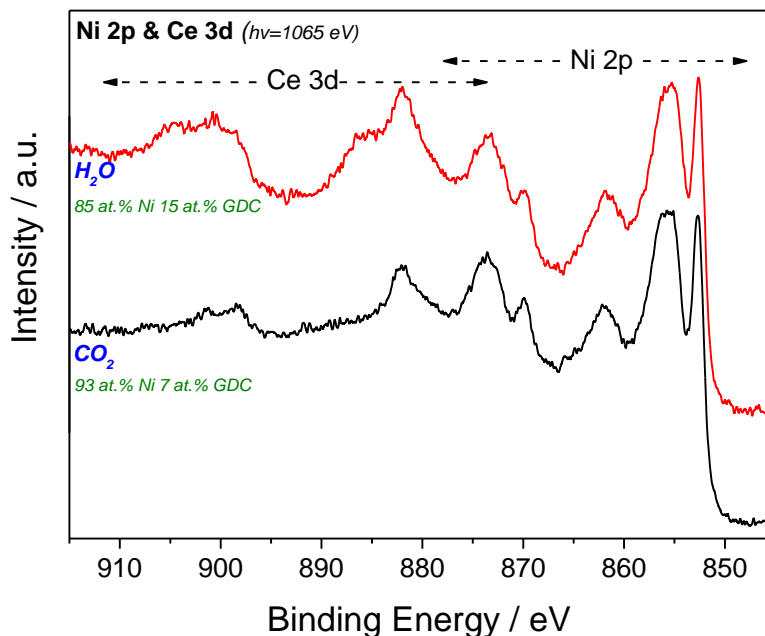
Figure 3.10. NAP-XPS of Ni 2p and Ce 3d binging energy region recorded over Ni-GDC electrodes in CO_2 and H_2O environment at 700 °C. The relative enchantment of the Ce 3d peak in H_2O atmosphere is evident by the comparison of the two spectra.

3.3.5. Surface modified Ni-YSZ electrodes with high oxidation resistance to CO_2

For practical CO_2 electrolysis applications, nickel oxidation is considered as one of the main reasons of cell degradation [165]. Therefore, according to the above presented results, Ni-GDC cathodes can be potentially more stable than Ni-YSZ for CO_2 electrolysis [40], since tolerates better oxidation by CO_2 and probably other oxidizing conditions occurring in the event of leakage or during shutdown periods [9]. However, Ni-GDC cermets have some disadvantages as compared to Ni-YSZ, related to their lower mechanical stability and their higher cost [10]. Intrigued by this observation, we attempt to combine the robust mechanical properties of Ni-YSZ with the enhanced CO_2 oxidation resistance of Ni-GDC found in our experiment, in a single electrode. A direct route to achieve this is to decorate the surface of Ni/YSZ by ceria. In fact, surface modification of cermets, by deposition of metals or oxides, is a common strategy to enhance both the performance and the stability of the electrodes [166,167] and in some cases even to re-activate them [168]. The aim of the surface modification discussed in this chapter is to deposited ceria homogenously on the outer surface of the electrode, so as to examine nickel tolerance towards oxidation by CO_2. In

chapter 5 the effectiveness of ceria nanoparticles impregnation into the pores of the Ni/YSZ will be discussed in detail.

For the surface modification of Ni/YSZ, NiCe NPs dissolved in hexane were infiltrated directly into the surface of the porous electrode. In this case the Ni/YSZ cermet acts as scaffold (hereafter NiCe@Ni-YSZ) [169]. Figure 3.11 shows representative SEM micrographs taken from the surface of the Ni-YSZ before and after impregnation with NiCe. The Ni and YSZ areas have a slightly different contrast in the SEM images, but YSZ areas are distinguishable from their smooth morphology, as was also confirmed by spot EDX analysis (not shown). The NiCe@Ni-YSZ images show fine nano-sized NiCe particles of about 20 nm, that are uniformly distributed over both Ni and YSZ areas. The presence of NiCe on the surface of NiCe@Ni-YSZ is confirmed by the NAP-XPS analysis presented below. The lower magnification images, shown in figure 3.12, suggest that the macroscopic morphology of the electrode (e.g. particle size, porous structure etc.) after NiCe NPs addition remains unaffected.

The morphology of NiCe aggregates inside the pores of Ni-YSZ was examined by cross-sectional focused ion beam-scanning electron microscopy (FIB-SEM) combined with energy dispersive X-ray spectroscopy (EDX) elemental mapping. The EDX signal of nickel (*in blue*), Zr from YSZ (*in green*) areas, Ce from NiCe NPs (in red), as well as empty voids (pores) inside the cermet can be clearly distinguished. The NiCe NPs aggregate to form an elongated particle with size of about 0.5 µm (please note that the resolution of EDX does not allow to distinguish smaller NiCe particles). Notable, NiCe is located in the empty space inside the pore, while is in contact with both Ni and YSZ areas.

The interaction of CO_2 with NiCe-modified and pristine Ni-YSZ is discussed next. Figures 3.13a and b present the Ni 2p3/2 spectra of pre-reduced samples after identical treatments in 1 and 10 mbar CO_2 at 700 °C. Please note here that the contribution of Ni derived from NiCe NPs in the Ni 2p signal is negligible as shown in previous work [11]. The nickel oxidation state of the two samples obtained from Ni 2p peak deconvolution is compared in figure 3.13c. In case of the Ni-YSZ electrode, nickel oxidation starts already at very low CO_2 dosages (even at 1 mbar pressure) and continues almost linearly with dosage. On the contrary, in case of the modified NiCe@Ni-YSZ nickel resists to oxidation even after relatively high CO_2 exposures (up to 80 min exposure at 10 mbar CO_2). The ceria oxidation state, given by the Ce 3d peak fitting (figure 3.13c), seems to remain stable independent of the CO_2 dosage.

Having shown the oxidation resistance of NiCe@Ni-YSZ electrodes as a function of CO_2 dosage, the effect of CO_2 pressure is examined in a separate experiment. Pre-reduced NiCe@Ni-YSZ, Ni/YSZ and Ni/GDC were exposed to various CO_2 pressures at isothermal conditions in the VPR reactor and consequently transferred under vacuum and characterized by a conventional AlKα monochromatic X-ray source (quasi in situ experiments). The evolution of nickel oxidation state, obtained from Ni2p spectra fitting, as a function of CO_2 pressure is shown in Figure 3.14.
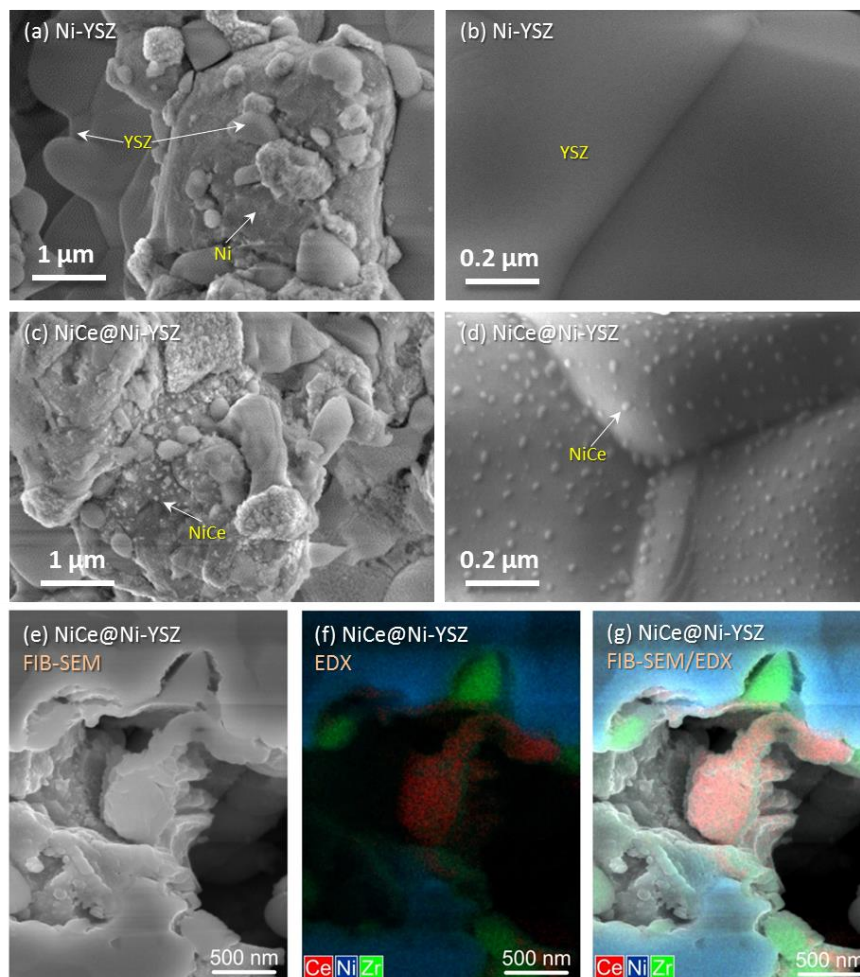
Figure 3.11. Characteristic SEM microgaphs of the Ni-YSZ surface (*a,* b) before and after (*c, d*) impregantion with the NiCe NPs solution. Both samples were subjected to calcination at 400 °C in 1 mbar O_2, reduction at 600 °C in 1 mbar H_2 and exposure in 20 mbar CO_2 for about 1h at 700 °C. The micrographs on the left column are electrode areas primarily occupied by nickel, while those on the left by YSZ. (e) Cross-sectional view of the inner parts of the NiCe@Ni-YSZ obtained by FIB-SEM. The corresponding EDX elemental mapping shown in (f) and (g) allows to identify the position of each element.
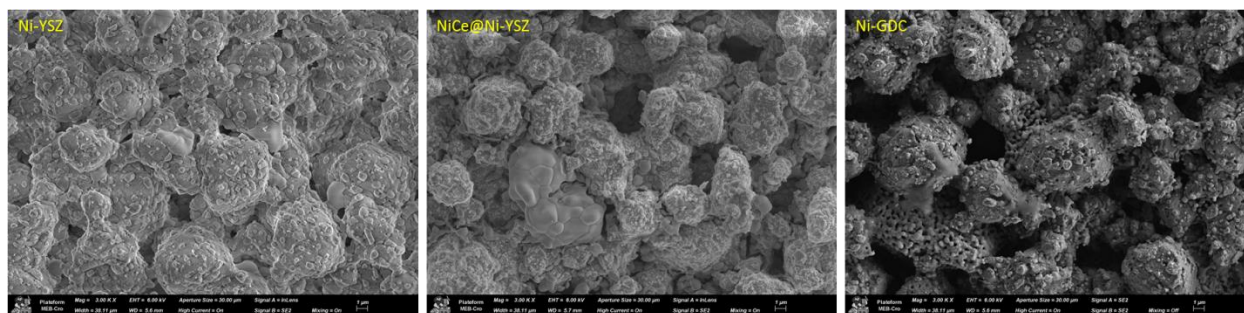
Figure 3.12. SEM images of the Ni-YSZ, NiCe@Ni-YSZ and Ni-GDC surface after calcination at 400 °C in 3 mbar O_2, reduction at 500 °C in 3 mbar H_2 and exposure in 10 mbar CO_2 for about 1 h at 700 °C.
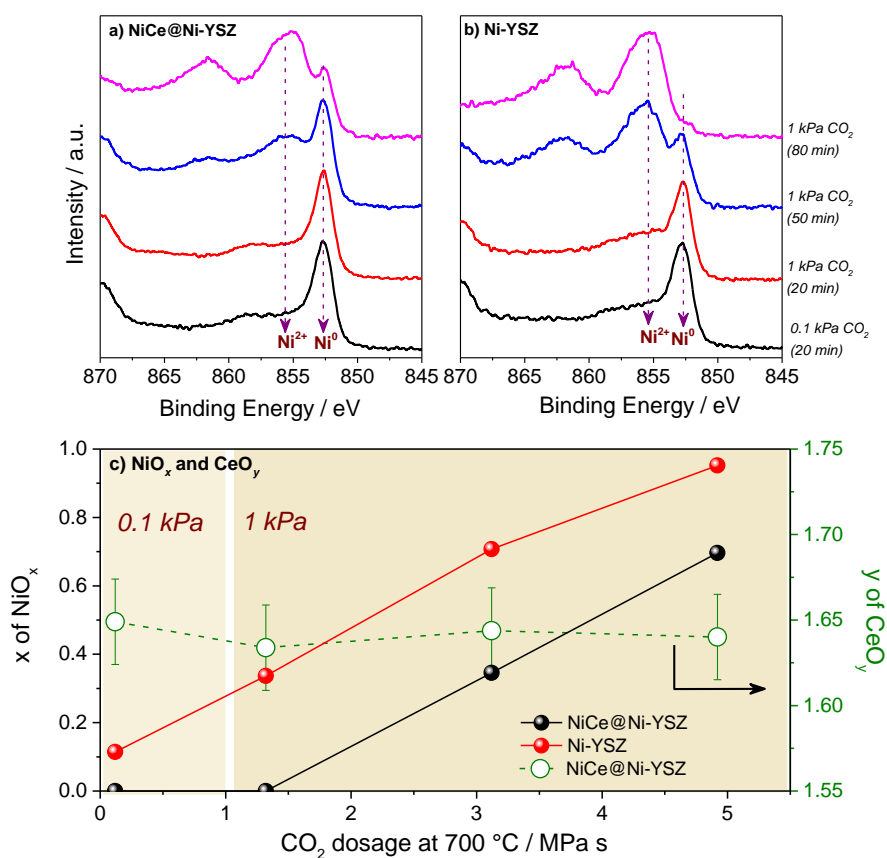
Figure 3.13. Ni 2p3/2 spectra (hv=1065 eV) after various consequitive CO_2 dosages at 700 °C for a) NiCe@Ni-YSZ and b) Ni-YSZ electrodes, c) The surface oxidation states of Ni (x of NiO_x) and Ce (y of CeO_y) of the two electrodes, according to the Ni 2p (hv=1065 eV) and Ce 3d (hv=1350 eV) NAP-XPS spectra analysis, as a function of the CO_2 dosage at 700 °C.
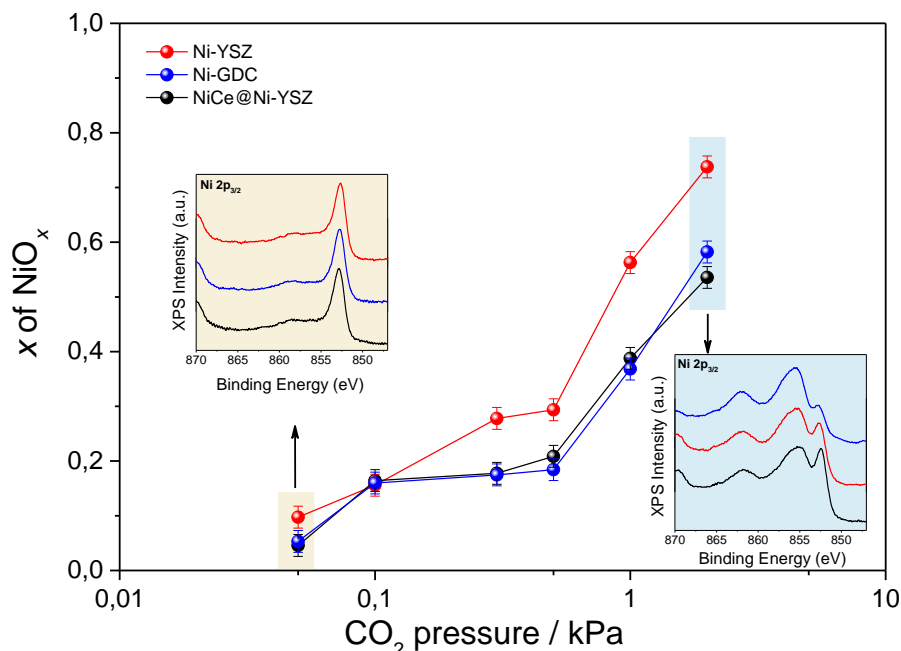
Figure 3.14. The evolution of the surface oxidation state of pre-reduced Ni-YSZ (●), Ni-GDC (●) and NiCe@Ni-YSZ (●) as a function of CO_2 pressure treatment at 700 °C for 1 h obtained by quasi-in situ XPS in vacuum using a conventional AlKα monochromatic X-ray source. Spectra were recorded at 235 °C to suppress electrostatic charging. The inset shows the Ni $2p_{3/2}$ peaks after CO_2 treatment at 0.5 mbar (left) and 20 mbar (right).

As expected, higher CO_2 pressures enhance nickel oxidation is all 3 samples. However, comparison of Ni oxidation state in case of Ni-YSZ with NiCe@Ni-YSZ and Ni-GDC samples, indicates that the former is systematically at higher oxidization state at almost all the examined CO_2 pressures. It is interesting to note that after modification with NiCe NPs the Ni-YSZ electrode mach Ni-GDC in terms of nickel oxidation state. The two experiments described above confirm that oxidation of Ni-YSZ is not affected by the bulk composition and validates the property of ceria to regulate oxidation acting as an oxygen source-and-sink, a fact well known in catalysis but poorly explored in solid state electrochemistry.

3.4. Conclusions

In conclusion, we investigated the oxidation of Ni-YSZ and Ni-GDC cermet electrodes by CO_2 and H_2O at conditions relevant to solid oxide electrolysis cells operation. We show that the degree of nickel oxidation by CO_2 and H_2O is not similar, as is usually anticipated, but it is regulated by the presence or not of ceria in the cermet. In particular, ceria promotes nickel oxidation by H_2O but moderates it in CO_2. Based on this observation we modified Ni-YSZ electrodes by introducing ceria nanoparticles directly on their surface. Comparative tests, showed that surface oxidation of Ni-YSZ by CO_2 can be prevented up to 100 % at certain conditions after modification with ceria, suggesting a promising strategy to produce more robust and redox stable solid oxide cells for CO_2 electrolysis.

Chapter 4. How the surface state of nickel/gadolinium-doped ceria cathodes influences the electrochemical performance in direct CO_2 electrolysis

IV. Chapter 4. How the surface state of nickel/gadolinium-doped ceria cathodes influences the electrochemical performance in direct CO₂ electrolysis

4.1. Introduction

After the investigation of the oxidation process of Ni/GDC and Ni/YSZ in equilibrium with CO_2 and H_2O, this chapter is to investigate the effect of the electrode surface state in the performance, under working electrochemical conditions. To this end it is primarily used *operando* near ambient-pressure X-ray photoelectron spectroscopy (NAP-XPS) technique. Ni oxidation and carbon formation of Ni-based cermet cathodes during CO_2 electrolysis are related to cells and stacks performance degradation [4,29,170]. To prevent Ni oxidation a reductive gas, such as H_2 or CO, is typically mixed with CO_2 [141,143]. However, recent studies demonstrated a stable operation in *direct* CO_2 electrolysis [26,171,172]. Please note that the term "direct" [58], or sometimes also called "pure" [26], or "without safe gas" [49,172] CO_2 electrolysis, refers to feed conditions where CO_2 is not mixed with a reductant gas. Carbon formation on Ni and ceria containing electrodes is attributed mainly to the Boudouard reaction ($2CO \rightarrow CO_2 + C$), while direct electrochemical carbon deposition reactions are also possible [86]. In this respect, C. Graves and coworkers demonstrated that cells with GDC cathodes can operate steadily in CO_2/CO mixtures, while in similar conditions their Ni/YSZ equivalents are rapidly deactivated due to carbon deposition [89]. Although significant effort has been devoted to understand the carbon deposition mechanism during CO_2 electrolysis over Ni-based cathodes [86,89,96,97,170,173–177], the effect of the electrode surface state in the electrocatalytic performance is much less studied. Typically, literature considers that the active electrode area of Ni/YSZ is the convergence of Ni, YSZ and gaseous phase, the so-called three-phase boundaries (TPBs), while for Ni/GDC, the mixed ionic electronic conduction of GDC allows the reaction to take place at the two-phase boundary (2PBs) between GDC and the gas phase [29,178]. Cells composed of porous doped-ceria fuel electrodes, i.e. without nickel, show considerable CO_2 electrolysis activity and stability [89], while the primary role of 2PBs on GDC, as compared to TPB, was also proposed as well for H_2O electrolysis [95] and H_2 electroxidation [179] reactions. The aforementioned observations put into question the essential role of nickel in electrochemical reactions over Ni/GDC, which is somehow surprising considering that SoA Ni/GDC electrodes are composed of 65 wt.% nickel.

The role of nickel surface state in the electrocatalytic performance of Ni/GDC electrodes during H_2O electrolysis [93,95], has been studied previously. It was shown that partially oxidized nickel

does not lead to deactivation, but on the contrary, can be even beneficial for the cell performance. The aim of the present chapter is to examine how nickel and ceria oxidation states affect to the CO_2 electrolysis performance and, in particular, to find evidences about the role of nickel in the reaction. To do so, we combine *operando* near ambient-pressure X-ray photoelectron spectroscopy (NAP-XPS) with *online* gas phase and electrical measurements over cells with porous Ni/GDC cathodes. It is important to underline that, contrary to the majority of CO_2 electrolysis NAP-XPS studies which concentrate to the carbon deposition mechanism [89,96,97,176,180–183], here are employed operational conditions bellow the carbon deposition threshold, in order to focus on the surface oxidation state and lift complications related to modifications due to irreversible carbon deposition. The results revealed the dynamic evolution of the Ni/GDC electrode surface and disclose the side reactions associated to electrode activation in CO_2 electrolysis. Comparison of reduced and oxidized electrodes shows that metallic Ni is a prerequisite for CO_2 electrolysis, at least at low potentials, suggesting that CO_2 electoreduction occurs primarily at the three phase boundaries between gas, metallic nickel and partially reduced ceria. We also provide evidences of *in situ* reduction of NiO upon polarization in CO_2, implying that addition of reductive gases to CO_2 is not indispensable to maintaining the cermet electrode in the reduced state.

This chapter is based on the published article: Dingkai Chen, Dimitrios K. Niakolas, Vasiliki Papaefthimiou, Evangelia Ioannidou, Stylianos G. Neophytides, and Spyridon Zafeiratos. How the surface state of nickel/gadolinium-doped ceria cathodes influences the electrochemical performance in direct CO_2 electrolysis. Journal of catalysis, 2021, 404, 518-528.

4.2. Experimental Materials and Methods

4.2.1. Fabrication of cells for NAP-XPS experiments

The cell was composed of a 40 µm thick $NiO/Gd_{0.1}Ce_{0.9}O_2$ (65/35 wt.% ratio) cathode (fuel electrode) with mass loading of approx. 25 mg/cm^2, deposited by screen printing method directly on a 300 µm thick 8YSZ electrolyte (Kerafol GmbH). A Pt layer on the reverse side, deposited by magnetron sputtering, was acting as the anode (O_2 electrode). The samples were sintered in air at 1250 °C for 5 h. Due to limitations related to the NAP-XPS sample holder dimensions, fragments of button cells with geometric surface area of about 0.35 cm^2 were used for the NAP-XPS measurements.

4.2.2. Quasi in situ and ex-situ electrode characterization

The *quasi in situ* laboratory-based XPS measurements were carried out in an ultrahigh-vacuum (UHV) setup coupled with a variable-pressure reactor (VPR) described in details elsewhere [147,184]. The cell was mounted on a sample holder equipped with a boron nitride heater and a K-type thermocouple. Pre-reduced Ni/GDC electrodes were exposed to pure CO_2 at pressures ranging from 0.5 mbar to 20 mbar and at 700 °C for 60 min. Consequently the VPR was evacuated and the sample was transferred under vacuum to the XPS chamber for analysis. During XPS measurements the sample temperature was maintained at 240 °C to avoid electrostatic charging problems. X-ray diffraction patterns were measured *ex situ* after electrode gas treatments in a Bruker D8 advance diffractometer using Cu Kα radiation.

4.2.3. Operando NAP-XPS measurements

Operando ambient pressure X-ray photoelectron spectroscopy measurements (NAP-XPS) were performed at ISISS beamline at BESSY synchrotron radiation facility at the Helmholtz-Zentrum-Berlin. The cell was fixed with two metal mounting clips on a stainless steel plate which were also used as the current collectors. Heating was performed from the rear using an IR-laser, while the temperature was measured with a K-type thermocouple. The gas flow into the reaction cell was controlled by calibrated mass flow controllers and the gas phase was monitored *online* by a quadrupole mass spectrometer (QMS-Prisma Pfeiffer). Electrical potentials were applied between the working and the counter electrodes and the current flow was measured using a computer controlled Autolab potensiostat/galvanostat. The working electrode was grounded, and voltage was applied to the counter electrode in order to avoid electrostatic energy shifts. Initial annealing of the sample in 0.2 mbar O_2 was used to eliminate residual carbon from the surface and after this procedure the C 1s signal was within the noise level during all experiments. Consequently the cell was subjected to reducing, humid and oxidizing pretreatment *in situ*. Prior to the CO_2 electrolysis measurements, the cell was stabilized in CO_2 atmosphere for about 30 min, and consequently a constant cathodic potential was applied stepwise between the anode and the cathode (negative electrode) and the cell current was recorded. The cell was maintained for about 20 min in each potential step to record a full set of NAP-XPS spectra (Ni 2p, Ce 3d, C 1s, O 1s and the Fermi edge). The stability of the surface in a given applied potential was verified by repeating Ce 3d and Ni 2p spectra at the beginning and at the end of the applied potential period. In this work, Ce 3d and Ni 2p spectra recorded at the end are shown to assure that the electrode had reached steady-

state. Eventual photon beam damage effects were tested by shifting the analysis spot to a new sample position during measurements, but no major differences were detected in the spectra indicating X-ray beam stability and homogeneity of the elecrtodes. The samples did not exhibit any electrostatic charging under open circuit conditions and the binding energies (BEs) are presented as measured without any correction.

For the electrolysis experiments in the NAP-XPS chamber the cell was heated at 700 °C in 0.1 mbar CO_2 and polarized stepwise from open circuit (O.C.) until 1.5 V (*upward curve*) and then decreased back again to O.C. (*downward curve*). Please note that since only cathodic polarization was applied, the negative sign of the voltage is omitted for clarity. The experimental routine was applied identical for cells pre-reduced in H_2 and pre-oxidized in H_2O. The current density (i) reported in the paper, is the average current density in a period of constant applied potential and it was calculated from integration of current i *vs time* curve *(in* C/cm^2*)* divided by the duration that the potential was applied (in s). A similar procedure was used to calculate the average QMS signal of CO and O_2 at each potential.

4.2.4. NAP-XPS data analysis

Shirley and liner-types background subtraction and peak fitting of the spectra were done with the software package Casa XPS vs. 2.3. The analysis of the Ni 2p and Ce 3d region is complicated by the overlapping of Ce^{4+}, Ce^{3+}, Ni^{2+} and Ni^0 photoemission peaks. In the present work the contribution of each species oxidation state in the overall spectrum was estimated by a linear combination of spectra measured at the same spectrometer over standard reference samples [6,91]. For the quantitative calculations the photon flux and the photo-ionization cross-sections were taken into account [185]. The stoichiometries of nickel (NiOx) and ceria (CeOy) oxides were calculated from the contribution of Ni^0, Ni^{2+} and Ce^{3+}, Ce^{4+} components in the Ni 2p-Ce 3d spectrum by using the formulas (9-10) given in chapter 2 [91,186]. More details about the fitting procedure, quantitative calculations, and stoichiometries of NiOx and CeOy oxides are given in 2.3.3. section in chapter 2.

4.3. Results and discussion

4.3.1. Interaction of CO_2 with Ni/GDC without polarization

Initially, we follow the capacity of CO_2 atmosphere to modify the surface oxidation state and composition of Ni/GDC under the specific conditions of the NAP-XPS experiment. To examine

this, the Ni/GDC was pre-treated in 0.1 mbar H_2, O_2 or H_2O and subsequently the gas atmosphere switched to 0.1 mbar CO_2 at 700 °C. The effect of H_2, O_2 or H_2O pre-treatment on the Ni/GDC surface state has been discussed in detail previously [91], here we focus on CO_2. Figure 4.1a shows Ni 2p and Ce 3d NAP-XPS spectra recorded initially in H_2 (hereafter referred as *pre-red.*NiGDC), and subsequently in CO_2, after about 30±5 min at 700° C. In 0.1 mbar CO_2 nickel remains in the metallic state (Ni^0), but ceria undergoes oxidation; from $CeO_{1.61}$ in H_2, to $CeO_{1.71}$ in CO_2 (see bar graphs in Figure 4.1). Since carbon deposition was not detected in the C 1s region (see Figure 4.2), ceria oxidation proceeds most probably according to the reaction: $Ce_2O_3 + CO_2 \rightarrow 2CeO_2 + CO$. In the case of O_2 pre-treated Ni/GDC (Figure 4.1b), NiO is preserved in CO_2 but ceria is partially reduced from $CeO_{1.89}$ to $CeO_{1.86}$. Finally, a comparable situation was also found for the H_2O pre-treated sample (hereafter referred as *pre-ox.*NiGDC), with NiO remaining stable while GDC undergoing reduction from $CeO_{1.82}$ in H_2O to $CeO_{1.72}$ in CO_2 (Figure 4.1b). Overall, nickel oxidation state is not affected under the employed CO_2 treatments, while ceria undergoes either reduction or oxidation depending on its prior oxidation state. Being an oxidant [156,187], CO_2 cannot be accountable for ceria reduction, leaving thermal decomposition of the oxide according to the reaction: $2CeO_2 \rightarrow Ce_2O_3 + ½ O_2$ as the most likely explanation of the results shown in Figure 4.1b and 4.1c.

In general CO_2 is considered capable to oxidize Ni in cermet electrodes [29,187], but contrary to the expected trend under the employed CO_2 conditions, nickel remains metallic. In order to clarify if the resistance of Ni to oxidation by CO_2 is related to the low pressure used in NAP-XPS cell, the dependence of the electrode oxidation state to the CO_2 pressure was examined in a separate experiment. The *pre-red.*NiGDC electrodes were exposed to various CO_2 pressures at isothermal conditions in the VPR reactor [147,148] and consequently transferred under vacuum and characterized by a conventional AlKα monochromatic X-ray source *(quasi in situ experiments)*.

The evolution of nickel and ceria oxidation states as a function of CO_2 pressure is shown in Figure 4.1d. From this graph it becomes evident that nickel oxidation begins above 1 mbar CO_2 and increases with the CO_2 pressure. On the contrary, ceria's oxidation state is less affected by CO_2 pressure and remains around $CeO_{1.8}$. The details behind the CO_2 pressure effect on Ni and ceria oxidation is out of the scope of this work and has been discussed in last chapter. However the results in figure 4.1d provide the link between NAP-XPS results and SOEC tests under atmospheric pressure conditions. In particular, in low pressure *operando* NAP-XPS experiments

(0.1 mbar) the oxidation effect of CO_2 was reproduced by applying Ni/GDC to an oxidative treatment prior to CO_2 electrolysis (section 4.3.4).
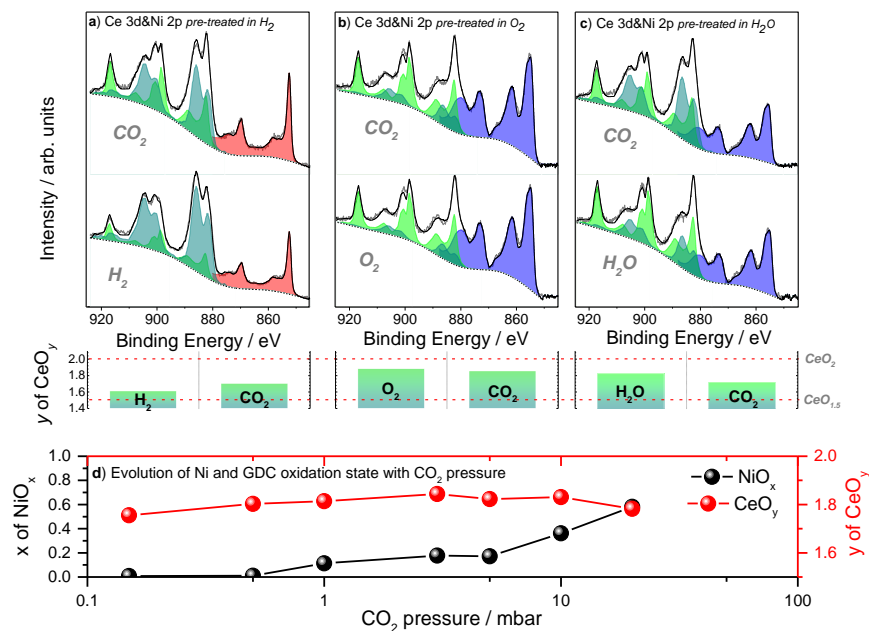
Figure 4.1. Synchrotron-radiation NAP-XPS measurements for Ce 3d and Ni 2p core-level spectra (hν =1065 eV) recorded in 0.1 mbar of a) H_2 and subsequently CO_2 b) O_2 and subsequently CO_2 c) H_2O and subsequently CO_2 atmospheres. The duration of each treatment was around 30 min while the temperature was kept at 700 °C. The gas and vapor feeds did not include any carrier/inert gas. The deconvolution of the overall peak to metallic Ni^0 (pink), Ni^{2+} (purple), Ce^{3+} (dark green) and Ce^{4+} (light green) is indicated. The mean surface oxidation state of GDC in each condition, calculated from the deconvoluted spectra, is shown in the bar-graph underneath. d) The evolution of the surface oxidation state of pre-reduced Ni/GDC electrodes as a function of CO_2 pressure treatment at 700 °C for 1h obtained by *quasi-in situ* XPS in vacuum using a conventional AlKα monochromatic X-ray source. Spectra were recorded at 235 °C to suppress electrostatic charging.

In order to verify the electrode state measured in the *quasi in situ* experiment is representative of the one in equilibrium with CO_2, the stability of Ni/GDC electrodes after CO_2 treatment in the VPR reactor and during the XPS measurements in UHV conditions was examined in two separate experiments. The first experiment examines the influence of the measuring temperature (235-240 °C) on the oxidation state of Ni and Ce. Based to literature results the decomposition of nickel oxides in vacuum takes place at around 400 °C [188,189]. Accordingly, at the temperature used in

our UHV measurements NiO should be stable. To verify this, the Ni 2p and Ce 3d spectra used for the data shown in Figure 4.1d were recorded systematically at the beginning and at the end of each measurement sequel. In fact, the points in figure 4.1d derive from spectra recorded at the end of the sequel. Figure 4.3a compares the Ni 2p and Ce 3d spectra at the beginning (black) and at the end (red) of the measurement sequel, for two of the CO_2 treatments. The time passed between the acquisition of two spectra was about 40 min, and as mentioned, during this time the sample was maintained at 235-240 °C. The close resemblance of the black and red spectra reveals that the chemical state of Ni/GDC is not affected by annealing in UHV, validating the results shown in figure 4.1d.
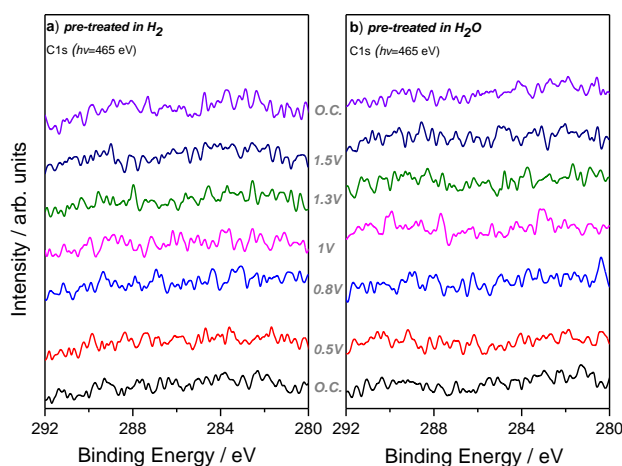
Figure 4.2. NAP-XPS C 1s (hν = 465 eV) core-level spectra recorded over Ni/GDC electrode under 0.1 mbar CO_2 atmosphere at open circuit (O.C.) and applied bias conditions for **a)** reduced electrodes pretreated in H_2 and **b)** oxidized electrodes pretreated in O_2 and consequently in H_2O. Details of the pretreatment conditions are given in the experimental part.

In addition to the temperature effect, we were also interested about the eventual changes of nickel oxidation state after CO_2 evacuation. Therefore, a NAP-XPS experiment was performed where a Ni-YSZ electrode (unfortunately similar data on NiGDC are not available) was oxidized at 700 °C in 10 mbar CO_2 for about 1 hour and subsequently the temperature dropped at 400 °C, the CO_2 gas was evacuated from the NAP-XPS cell and the sample was measured in UHV (about 1×10^{-7} mbar) at 400 °C. The Ni $2p_{3/2}$ spectra shown in Figure 4.3b indicates a slight reduction of NiO to Ni (manifested by the increase of the low BE peak components pointed out by an arrow) after 50 min at 400 °C in UHV. Overall, the results shown in Figure 4.3 demonstrate that the surface state of

Ni/GDC electrode remains stable at 235 °C in UHV, while upon CO_2 evacuation there is a limited NiO reduction. On that account the *quasi in situ* results presented in figure 4.1d are representative of the electrode state in equilibrium with CO_2.
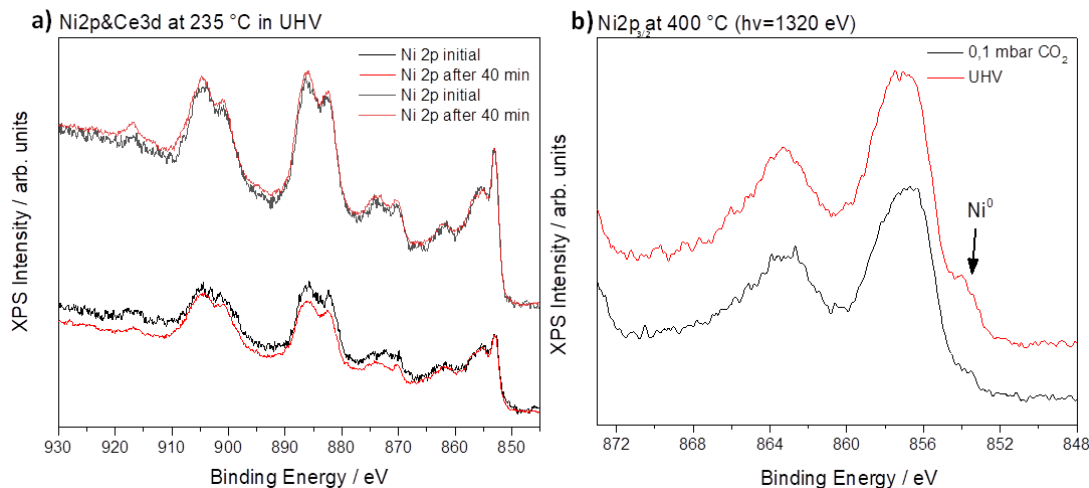
Figure 4.3. a) Ni 2p and Ce 3d spectra recorded at the beginning (black) and at the end (red) of the measurement sequel. The time between the two spectra was about 40 min and the sample was maintained at 235 °C. The difference in the signal to noise ratio between the initial and final spectra is related to the different number of scans in each case b) Comparison of two Ni $2p_{3/2}$ spectra of (partially) oxidized Ni-YSZ electrodes recorded in situ in a synchrotron-based NAP-XPS, in 0.1 mbar CO_2 (black line) and consequently in UHV conditions (red line). The temperature of the sample in both measurements was maintained at 400 °C.

4.3.2. Pertinence of NAP-XPS and electrical measurements correlation

The high surface sensitivity is a major advantage of XPS, allowing retrieving specific information from the electrode area where electrochemistry takes place, i.e. the two or three phase boundaries [177]. On the downside, the collected information originates from the outer 2-4 nm of a $40x10^3$ nm thick electrode (see paragraph 4.2.1 and Figure 4.4 for a schematic representation), thus roughly from 0.01% of the overall electrode volume. Therefore, prior to any attempt to correlate the chemical state as revealed by NAP-XPS, with the electrochemical performance given by electrical and *on line* gas phase measurements, it is important to address possible differences in the chemical state between the inner (close to the interface with the YSZ electrolyte) and outer (at the surface analysed by NAP-XPS) parts of the electrode.
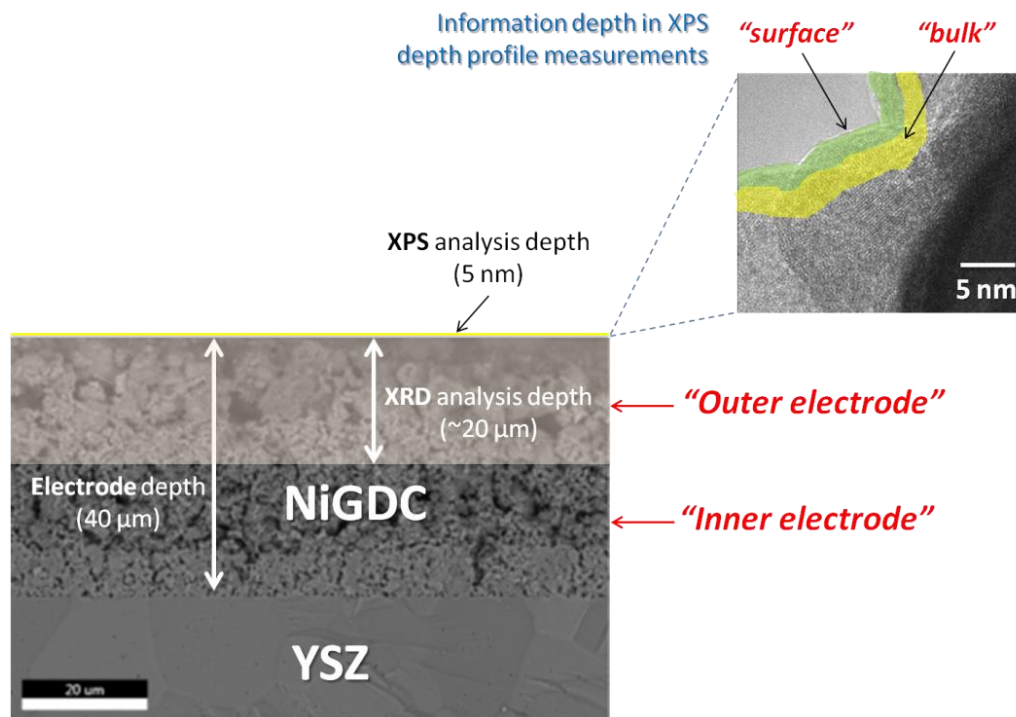
Figure 4.4. Cross sectional SEM and HR-TEM images of the Ni/GDC electrode indicating the XPS and XRD analysis areas. Please note that the purpose of the microscopy images is to illustrate the various terms used in the manuscript and do not necessarily correspond to the samples discussed in the paper.

A key point is to understand whether the electrochemical reaction takes place in a uniform manner within the structure of the porous Ni/GDC or there is a significant hysteresis between the inner and outer parts of the electrode (Fig. 4.4). Evidently, only in the former case the NAP-XPS results are representative of the Ni/GDC electrode in operation. Calculations performed by the collaborating group of Dr. S. Neophytides in FORTH, Patras, Greece, (can be found in [190]) suggested that due to the very low cell operation currents, like those used in the NAP-XPS measurements described below, the current varies linearly along the thickness of the electrode i.e. from the electrolyte to the current collector [191]. Therefore, the electrochemical reaction rate is gradientless within the Ni/GDC electrode i.e. is uniformly distributed across its whole thickness. In this respect, there is essentially no hysteresis in the reaction taking place at the interface close to the YSZ electrolyte and that occurring on the surface of the electrode, where NAP-XPS is measured. Accordingly, despite that fact that NAP-XPS characterizes only a tiny fraction of the extreme surface of the electrode, the chemical analysis under the employed conditions is

considered as representative of the Ni-GDC volume and can be associated with its electrochemical response of the cell.

4.3.3. CO₂ electrolysis over pre-reduced Ni-GDC electrodes
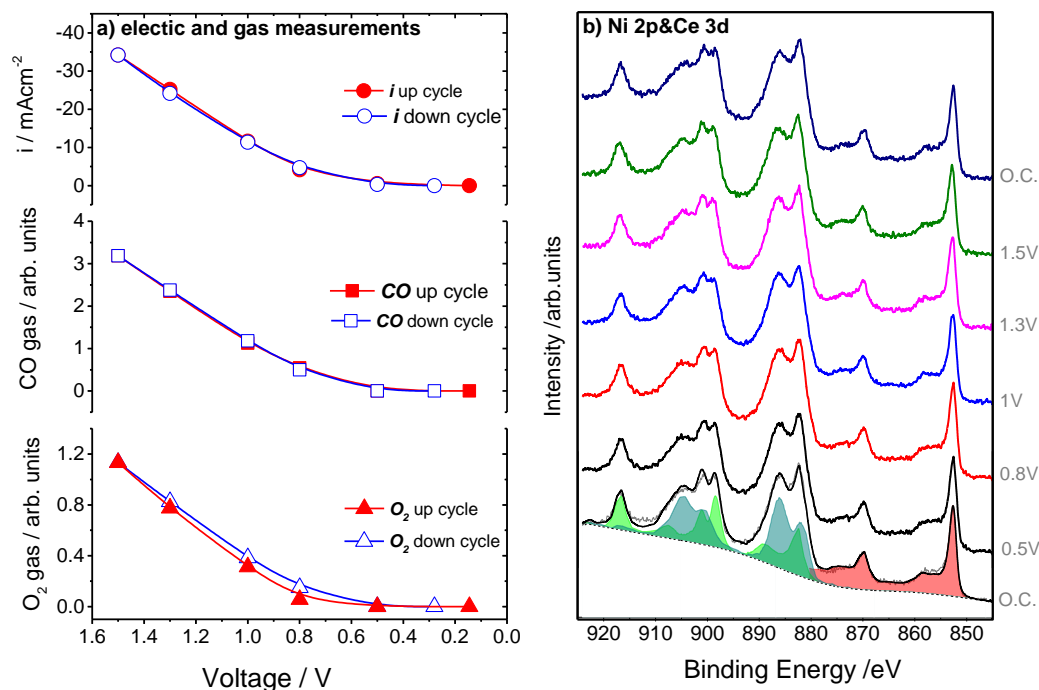
Figure 4.5. *Pre-reduced NiGDC cathode*. (a) The evolution of the cell current density (top), the CO gas QMS signal (middle) and O_2 gas QMS signal (bottom) as a function of the applied voltage for the up (red) and down (blue) potential curves. (b) Operando NAP-XPS Ce 3d and Ni 2p core-level spectra (hν =1065 eV) recorded under various applied potentials in 0.1 mbar CO_2 at 700 °C. Before electrochemical testing the cell was pre-treated in the spectrometer under 0.1 mbar H_2 at 700 °C for 30 min.

Figure 4.5a (*top*) presents the i-V curves of a cell with *pre-red.*NiGDC cathode for the upward (*red*) and downward (*blue*) polarization. The i-V curves of the up and down polarization are almost identical, while a clear change in the slope after 0.5 V characterizes the onset of the electrolysis reaction. The absence of any notable hysteresis in the downward polarization indicates that the cell works reversibly without significant deactivation and rules out carbon deposition. A direct confirmation of this is given by the C 1s spectra shown in Figure 4.2. The shift of the Fermi edge upon polarization was measured from valence band spectra recorded with 1065 eV excitation energy. At the maximum applied voltage (1.5 V) the shift of the Fermi edge, in respect to its

position just before the onset of the CO_2 to CO electrocatalytic reduction (0.5 V), was around 240±50 mV. This value represents the cathode overpotential [89] and it is free from ohmic loses owed to the ionic resistance of the electrolyte. The onset of carbon deposition is reported between –250 mV and –300 mV over Ni-SDC (samarium doped ceria) electrodes [89], therefore limiting the overpotential to 240±50 mV justifies the absence of deposited carbon in our work.
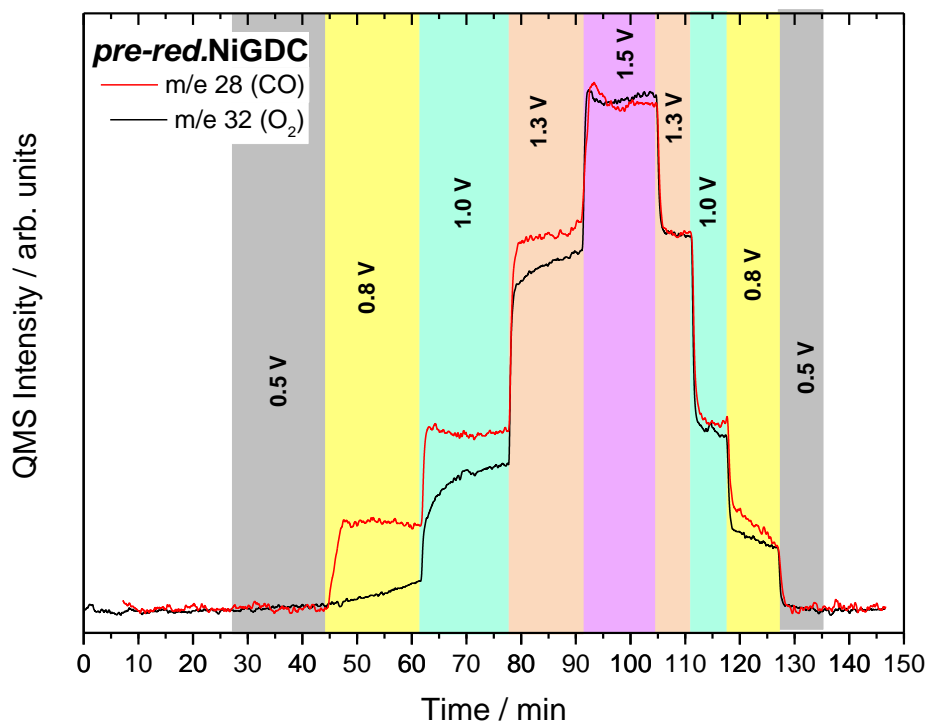
Figure 4.6. **Pre-reduced NiGDC cathode** The evolution of the CO (m/e 28) and O_2 (m/e 32) gas phase signals as a function of time recorded in the NAP-XPS chamber by *on line* mass spectrometry. The measurements performed at 700°C in 0.1 mbar CO_2 atmosphere under various applied biases (highlighted with different colors in the figure) on a cell pre-reduced in the spectrometer under 0.1 mbar H_2 at 700 °C for 30 min (*pre-red.*NiGDC).

We turn now our attention to the analysis of the gas phase in the NAP-XPS cell. Since this cell is a single chamber reactor (both anode and cathode sides are exposed to the same gas environment), the O_2 produced at the anode (Pt electrode) is detected together with CO produced at the cathode side. Figures 4.5 *middle* and *bottom* show the CO and O_2 production as a function of the applied bias (the evolution of the QMS signal with time is shown in figure 4.6). At each applied potential the production of CO is almost identical in the two cycles, while O_2 signal at the up polarization curve is systematically lower than in the down. The Ni 2p and Ce 3d spectra recorded during CO_2

electrolysis are shown in Figure 4.5b (for the down curve only the O.C. spectrum is included for clarity). The Ni 2p peak at 852.6 eV is due to Ni^0 and remains stable throughout the experiment [95]. The Ce 3d spectra correspond to a mixed Ce^{4+}/Ce^{3+} state [95] and are slightly influenced by polarization as will be explained in section 4.3.5.

4.3.4. CO_2 electrolysis over pre-oxidized Ni-GDC electrodes

Next, we investigate the performance of Ni/GDC cathodes pre-oxidized *in situ* under mild oxidative conditions (0.1 mbar O_2 and subsequently H_2O at 700 °C). As mentioned in section 4.3.1 pre-oxidation in the NAP-XPS cell is used to simulate the state of Ni/GDC electrode after few minutes' exposure in CO_2 under realistic 1 bar operation conditions. According to XRD results (Figure 4.7), under these conditions nickel in the bulk of the electrode remains partially reduced. The i-V curves shown in Figure 4.8a (*top*) look very similar to those recorded on the *pre-red.*NiGDC cells. On the contrary, the evolution of the gas products and especially that of CO shown in Figure 4.8a (*middle and bottom*), seems different in the two polarization curves (the evolution of the QMS signal with time is given in Figure 4.9). In particular, CO production at the upward polarization starts at 1.3 V, while in the return curve CO is produced down to 0.8 V, similar to the findings of the *pre-red.*NiGDC electrode. The production of O_2 is increasing with the applied voltage, although some differences between the up and down curves can be observed. Notably at 1 V, relatively higher O_2 production is observed at the upward bias. Interestingly, this correlates well with the higher current density measured at 1 V (see i-V curve at the top).

The corresponding Ni $2p_{3/2}$ spectra shown in Figure 4.8b undergo significant changes upon polarization. Specifically, the initially present Ni 2p spectrum of NiO [93] is preserved up to 1 V, but at higher potentials a characteristic Ni $2p_{3/2}$ component appears at lower energies, indicating partial reduction of NiO to Ni^0. Reduction continues also in the downward polarization and nickel oxidation state is stabilized at about $NiO_{0.4}$. A remarkable observation based on the comparison between spectroscopic and gas phase results in Figure 4.8, is that the onset of the electrocatalytic activity (CO production at 1.3 V) and the appearance of reduced nickel peak in XPS coincide. It is worth noticing that although NiO is not completely reduced as in the pre-reduced sample of Fig. 4.5, the electrocatalytic performance of the pre-oxidized sample is slightly better than that of the pre-reduced one.
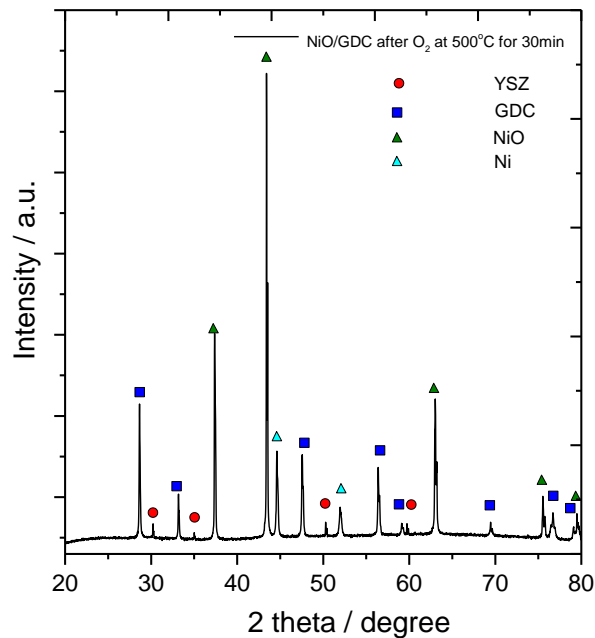
Figure 4.7. ex situ XRD pattern of a Ni/GDC electrode recorded after reduction (1 mbar H_2 at 700 °C, 30 min) and oxidation (1 mbar O_2 at 500 °C, 30 min) treatments applied consequently.
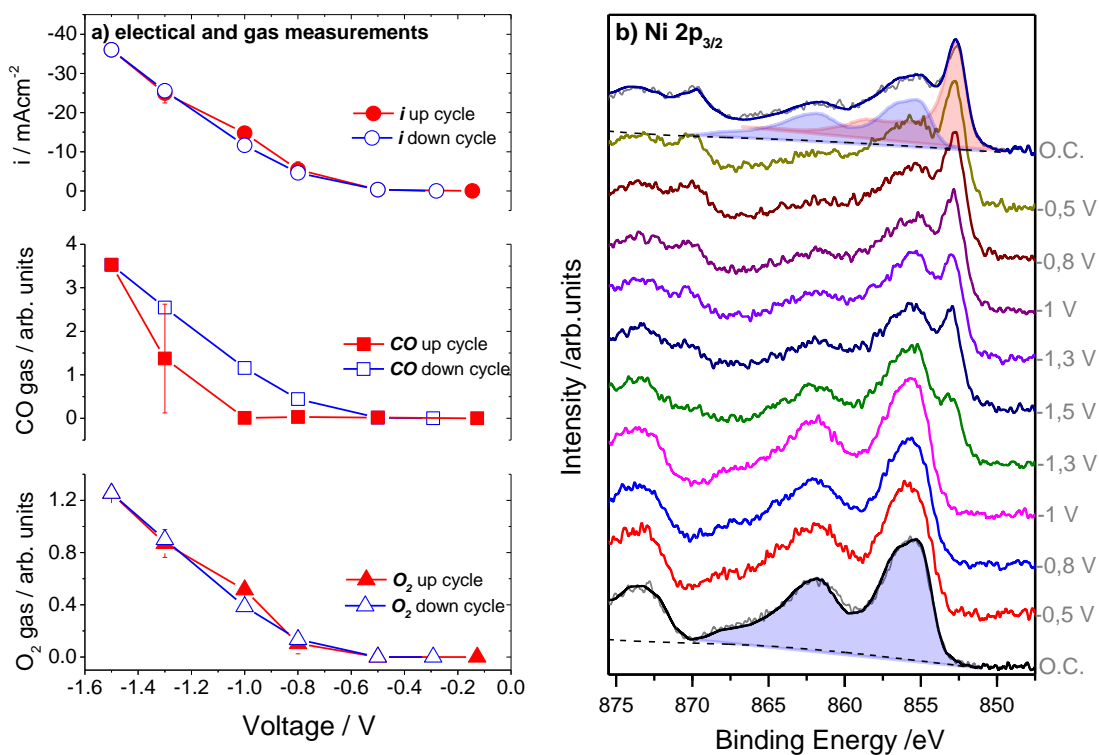
Figure 4.8. **Pre-oxidized NiGDC cathodes** (a) The evolution of the cell current density (top), the CO gas QMS signal (middle) and O_2 gas QMS signal (bottom) as a function of the applied voltage

for the up (red) and down (blue) potential curves. (b) Operando NAP-XPS Ni $2p_{3/2}$ core-level spectra (hν =1065 eV) recorded under various applied potentials in 0.1 mbar CO_2 at 700 °C. Before electrochemical testing the cell was pre-treated in the spectrometer under 0.1 mbar O_2 at 500 °C and consequently in 0.1 mbar H_2O at 700 °C for a total duration of 1 hour.
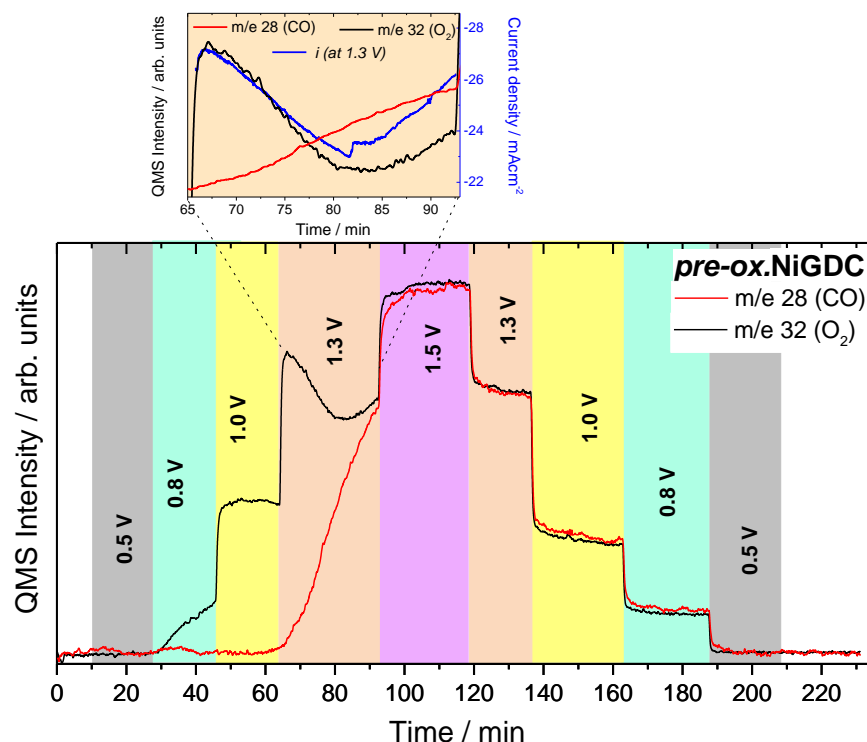
Figure 4.9. Pre-oxidized NiGDC cathode The evolution of the CO (m/e 28) and O_2 (m/e 32) gas phase signals as a function of time recorded in the NAP-XPS chamber by *on line* mass spectrometry. The measurements performed at 700°C in 0.1 mbar CO_2 atmosphere under various applied biases (highlighted with different colors in the figure) on a cell pre-oxidized in the spectrometer under 0.1 mbar O_2 at 500 °C and consequently in 0.1 mbar H_2O at 700 °C for 1 hour (*pre-ox.*NiGDC).

Comparison of the Ce 3d and Ni 2p spectra recorded using 2 photon energies, i.e. two information depths [192] (Figure 4.10) is used to describe the arrangement of the various oxidation states. The enhancement of the Ni^0 as compared to Ni^{2+} component at the more surface sensitive mode (1065 eV) suggests that the two oxidation states are arranged in a core-shell like structure with Ni^0 at the *shell*. Similar analysis of the Ce 3d peak indicates that GDC areas terminate with Ce^{3+} ceria species typically accompanied by a high population of oxygen vacancies [187]. A comparable surface

arrangement of Ni/GDC was found previously for steam electrolysis reaction, indicating that Ni^0/Ce^{3+} is a surface configuration favoured in electrolysis reactions [6,93].
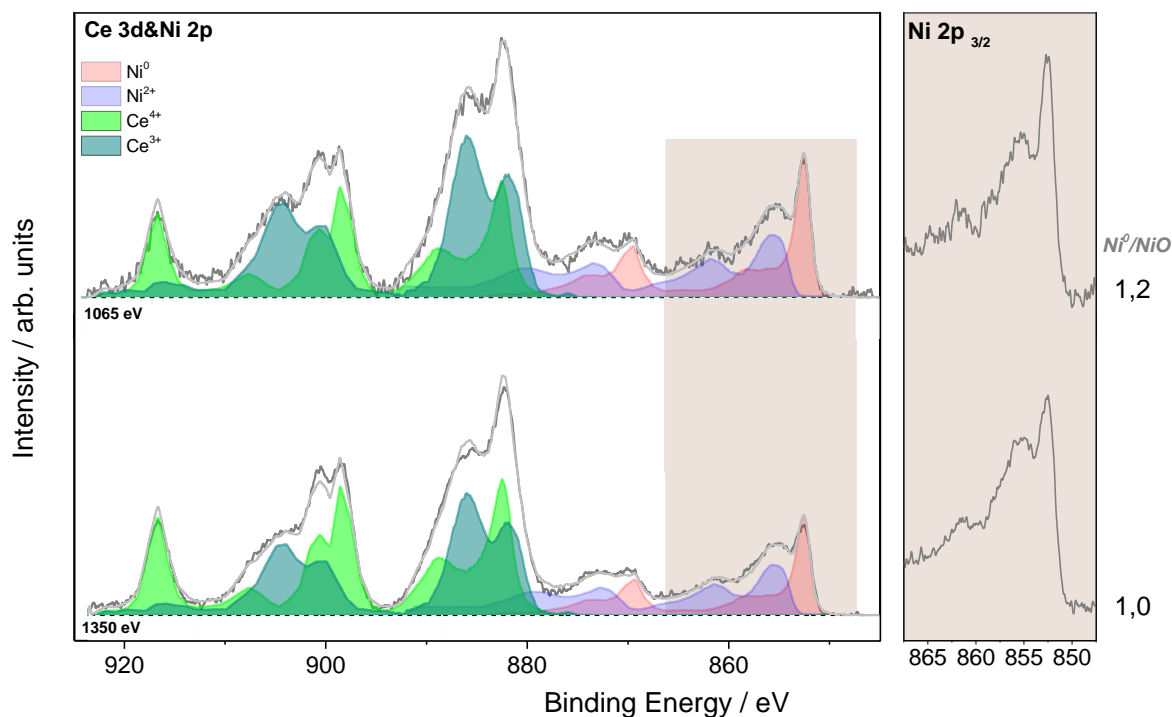
Figure 4.10. Synchrotron-radiation NAP-XPS measurements for Ce 3d and Ni 2p core-level spectra recorded on *pre-ox.*NIGDC at applied potential of 0.8 V (downward curve) in 0.1 mbar CO_2 at 700 °C. The spectra were recorded using two different photon energies (1065 and 1350 eV) corresponding to two different information depths. The deconvolution of the overall peak to metallic Ni^0 (pink), Ni^{2+} (purple), Ce^{3+} (dark green) and Ce^{4+} (light green) is indicated. The Ni $2p_{3/2}$ peak area is magnified at the right part so as to better visualize the differences in the NiO and Ni features.

4.3.5. Correlation of spectroscopic, electrochemical and gas phase results in pre-oxidized and pre-reduced Ni/GDC.

The O_2 and CO as a function of the cell current for the pre-oxidized and pre-reduced cells are compared in Figure 4.11a and 4.11b, respectively. In all cases the production of O_2 (Fig. 4.11a) with current follows the expected linear relationship, even though in the upward curve of the *pre-red.*NiGDC (*red dash line*) O_2 is systematically lower (see also Figure 4.6). The evolution of nickel (*x* of NiO_x) and ceria (*y* of CeO_y) oxidation states with the current density, estimated from the corresponding photoelectron peaks, is shown in Figures 4.11c and 4.11d respectively. As is

evident, in *pre-red.*NiGDC ceria undergoes an initial reduction step (red points in Fig. 4.11c), while the trend is inversed at higher current densities with ceria gradually oxidizing towards an equilibrium oxidation state of $CeO_{1.72}$. Besides, as shown in Figure 4.11d, the nickel oxidation state of *pre-red.*NiGDC is not influenced throughout the polarization experiment. The stability of metallic nickel, combined to the limited ceria oxidation found by NAP-XPS of *pre-red.*NiGDC electrode, do not allow to attribute the systematically lower O_2 production on this sample (fig. 4.11a) to consumption via electrode surface oxidation. If such an oxidation takes place, it should mainly concern the interior parts of the electrode (i.e. bulk) which are not accessible by NAP-XPS, as will be discussed below.

Differences in the gas production between the up and downward polarization were found in the *pre-ox.*NiGDC as well. However, in this case it was not O_2 but CO production which was affected (Figure 4.9). In particular, as shown in Figure 4.11b, in the upward polarization CO is either not detected at all or it is lower than the one expected based on the measured current density. The catalytic CO oxidation to CO_2 by gas O_2 (produced on the anode) is not supported by the evolution of O_2 mass signal. More specifically, as shown in figure 4.11a, O_2 production at the *pre-ox.*NiGDC is proportional to the current density, without any notable differences between the up and down polarization curves. Evidently, in the hypothetical case that O_2 reacts with (two) CO molecules, a decrease in the O_2 production in the upward curve should be observed, which is not the case. Since catalytic CO oxidation is discounted, two different scenarios are put forward to explain the lower CO production observed at the up polarization cycles of *pre-ox.*NiGDC. Carbon monoxide is known to be an efficient reductant for both NiO [193] and ceria [194], so in the first scenario CO is consumed (totally or partially) by reacting with NiO and CeO_2 according to the reactions: $CO+NiO \rightarrow Ni+CO_2$ and $CO+2CeO_2 \rightarrow Ce_2O_3+CO_2$. In the second scenario, current and O_2 on *pre-ox.*NiGDC do not evolve from CO_2 reduction reaction but from another electrochemical reaction that does not involve CO production.

We first examine the compatibility of the first scenario with the NAP-XPS results. Figures 4.11c and 4.11d indicate that ceria and nickel oxides are partially reduced during the upward polarization. However, a closer look in the results reveals that reduction starts at current densities > 15 mA·cm^{-2} (corresponding to 1 V in Fig. 4.8a), but before that nickel and ceria oxidation states remain practically stable. Depth profile (Figure 4.10) suggested that reduced nickel and ceria segregate on the surface of the electrode, therefore an eventual reduction of the electrode at low currents should

be easily detected in photoemission results. Accordingly, CO consumption due to electrode reduction cannot explain the observations in Figure 4.11b, at least not for 5 and 15 mA·cm^{-2} (i.e. 0.8 and 1 V).
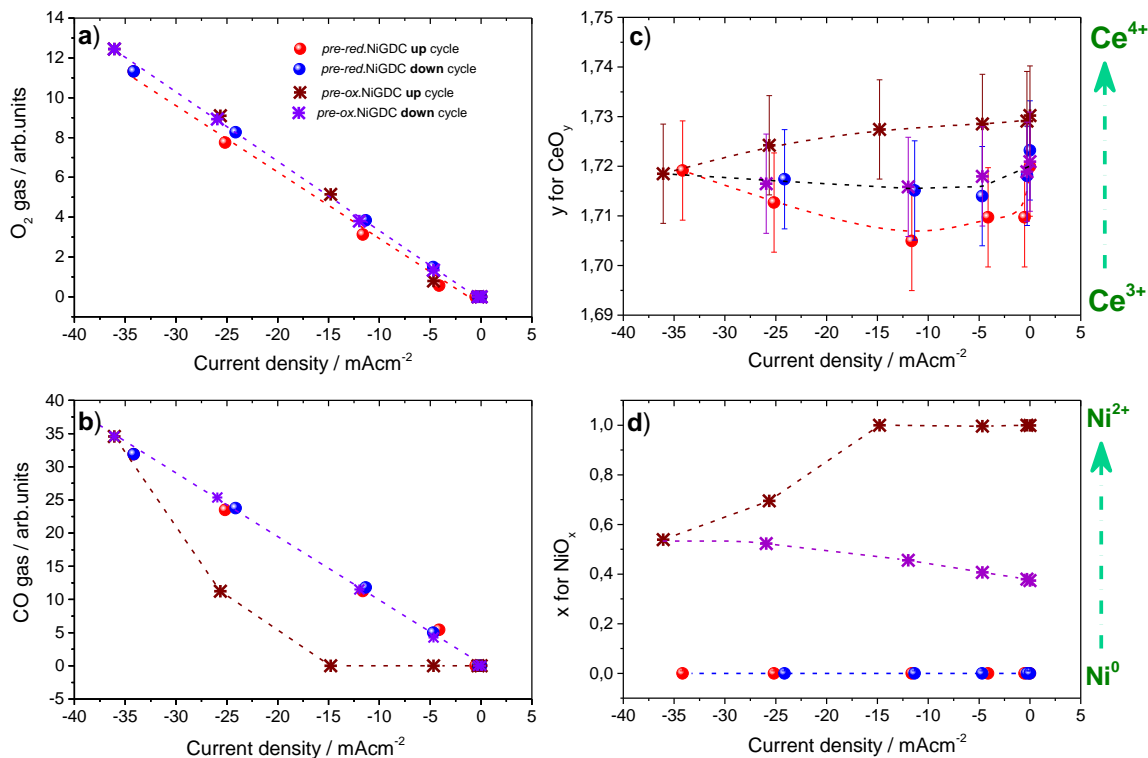
Figure 4.11. The O_2 gas QMS signal (a), the CO gas QMS signal (b) the mean ceria valence *y*, calculated by the Ce 3d photoelectron peak (c) and the mean nickel valence *x*, calculated by the Ni 2p photoelectron peak (d) as a function of the cell current density. The data were recorded upon cathodic potential in 0.1 mbar CO_2 at 700 °C. The pretreatment and sequence of the recording are provided in figure. The lines serve as a guide to the eye.

Now let us consider the possibility that CO is not consumed, but it is not formed at all at low applied potentials over the *pre-ox.*NiGDC (second scenario). This means that the observed current and O_2 should be produced by an alternative electrochemical reaction. Since the gas feed contains only CO_2, the only possible reactions are the electro-reduction of Ni^{2+} and Ce^{4+} to Ni^0 and Ce^{3+}, respectively. In fact, recent CO_2 electrolysis studies over Ni/YSZ cathodes have shown that electro-reduction of NiO to Ni is possible and thermodynamically more favoured, compared to the CO_2 electrochemical reduction [26].

In order to confirm this argument at the specific conditions of NAP-XPS experiment, the standard decomposition (R1) and electrolysis (R2) potentials of NiO (E^0_{NiO}) and CO_2 (E^0_{CO2}), we calculated using the Nernst's equation by the collaborating group of Dr. S. Neophytides (see [190]).

$$NiO \rightarrow Ni + \frac{1}{2}O_2 \qquad \text{(R1)}$$

$$CO_2 \rightarrow CO + \frac{1}{2}O_2 \qquad \text{(R2)}$$
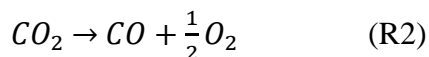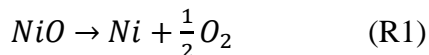
According to the calculations, NiO decomposition (R1) will proceed at 370 mV lower applied potential than CO_2 electrolysis (R2). In this respect, the CO_2 electrolysis on oxidized Ni/GDC electrode surfaces is thermodynamically and kinetically less feasible than the direct electro-reduction of NiO. Thus, it is reasonable to expect that the initiation of the NiO electro-reduction before CO_2 electrolysis and consequently the appearance of measurable reduction current and O_2 signal in Figure 4.8a at 0.8 V is due to NiO decomposition. This argument is supported by supplementary polarization tests performed in inert gas without CO_2 in the feed (see Figure 4.12). In details, reference experiments in Ar atmosphere were performed in the laboratory based VPR (see paragraph 4.2.3 in the experimental part) using similar gas phase and flow conditions with the NAP-XPS results (Figure 4.8a), but lower temperature. The purposed was to investigate the Ni/GDC cell at conditions where only NiO decomposition reaction is possible. The i-V curves in direct CO_2 electrolysis were tested first in order to confirm that the performance of the cell in the VPR reactor resembles that of NAP-XPS chamber shown in figures 4.5 and 4.8. Indeed the i-V profile in direct CO_2 electrolysis conditions shown in figure 4.12 is qualitatively similar to those recorded in the NAP-XPS cell (Figures 4.5 and 4.8). The lower current density in case of VPR experiment is justified by the lower operation temperature. After CO_2 electrolysis tests the Ni/GDC electrode was oxidize in 10 mbar CO_2 for 30 min at 600 °C and subsequently CO_2 exchanged to Ar. The current densities measured in Ar for the up and down polarization, are significantly lower than in CO_2, but not zero. Since electroreduction of Ar is not possible, the measured current should be mainly attributed to NiO reduction. This is also in agreement with the i-V curve in the down polarization cycle where the current at potentials around 1 V becomes practically zero. This is because after the upward polarization the majority of NiO has been reduced, therefore there isn't current production due to NiO decomposition.
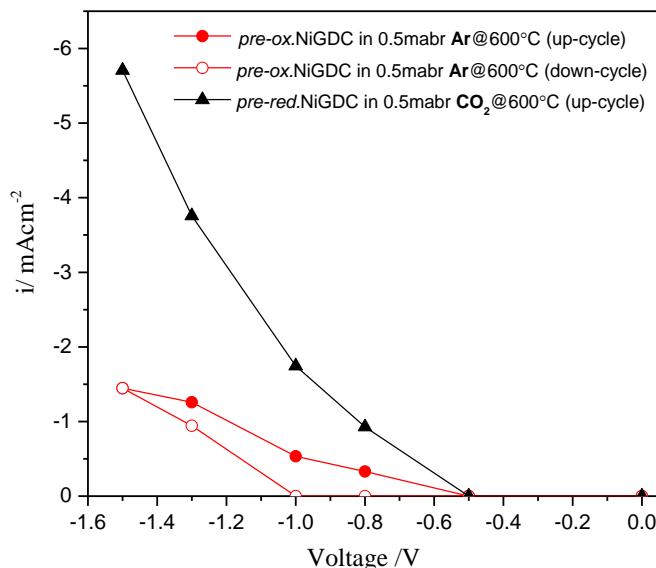
Figure 4.12. The evolution of the cell current density as a function of the applied voltage recored at 600 °C in the VPR using electrochemical cells with NiGDC cathods. (▲) pre-reduced Ni/GDC electrode measured in 0.5 mbar CO_2, (●)pre-oxidized Ni/GDC electrode measured in 0.5 mbar Ar (upwards polarization cycle) and (○) downwards polarization cycle.

Note that although both current and O_2 evolution rates increase progressively with time, the metallic Ni component in the XP spectra is not observed before 1.3 V (Fig. 4.8b). This can be attributed to the fact that oxygen from NiO surface is quickly replaced by the subsurface (bulk) oxygen, which diffuses to the surface with comparable rates to the electrochemical removal of oxygen. In this respect, the electro-reduction process is not detectable by NAP-XPS unless a certain reaction rate is attained (here between 1 and 1.3 V).

At the upward 1.3 V applied voltage, the rate of the evolved O_2 approaches fast to a maximum, which thereafter gradually decreases back again after about 15 min (Figure 4.9). The evolution of current follows closely that of O_2, confirming its electrochemical origin. The profile of CO evolution at 1.3 V follows a monotonic increase, which seems not to correlate with O_2 and i evolution. One can rationalize this observation assuming kinetic effects due to the coupling of the R1 (NiO decomposition) and R2 (CO_2 electrolysis) electrochemical processes. In particular, initially R1 dominates producing mainly O_2 and progressively inducing reduction of NiO. The appearance of metallic Ni on the surface promotes R2 therefore CO production rises. When NiO is adequately reduced, the surface is depleted from oxygen, therefore R1 is suppressed and it is R2 that dominates. The rate of the two reactions at each time of the experiment defines the current

profile as a function of time. Please note that progressive NiO reduction does not only provide more electroactive sides for CO_2 electrolysis, but is also expected to enhance the electronic conductivity of the electrode. Thereafter, during the application of the higher potential values and by following the downward direction, the current density and the formation rates of CO and O_2 coincide, as expected for the CO_2 electrolysis reaction.

Interestingly, although in the case of the *pre-ox.*NiGDC sample nickel remains partially oxidized, the i-V characteristics of the cell do not deteriorate, but are slightly better than those of the fully reduced *pre-red.*NiGDC (figure 4.13). The depth profile measurements (figure 4.10) highlighted that under the aforementioned conditions, a new steady state has been established, having higher degree of oxidation in subsurface layers than on the Ni/NiO surface. This runs counter to the expected trend in which oxide species in vacuum diffuse and accumulate on the surface of the metal due to their lower surface free energy [130,195]. This result can be rationalized by considering that the stronger interaction of CO_2 with Ni^0 species establish a new equilibrium that inhibits the diffusion of oxygen from the inner layers to the outer shell. This can be attributed to the fact that the surface Ni^0 sites react faster with CO_2 than the diffusion-reaction of O from the interior to the surface.
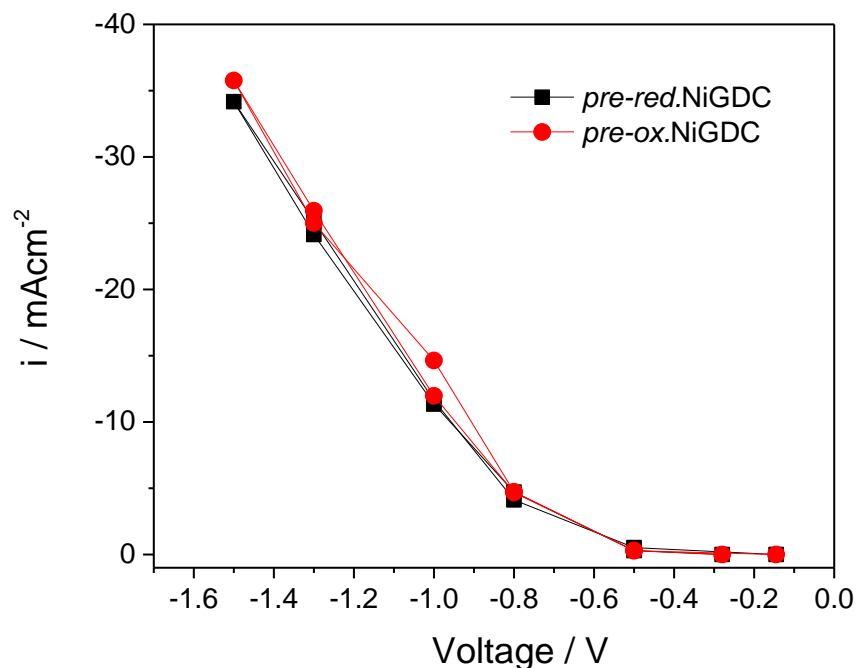
Figure 4.13. I-V curves of cells with *pre-re.*NIGDC (black) and *pre-ox.*NIGDC (red) cathodes during electrocatalytic CO_2 reduction in 0.1 mbar CO_2 at 700 °C.

Eventually we comment on the effect of the pre-treatment (reductive or oxidative) on the oxidation state of ceria observed during polarization. It is clear from Figures 4.1 and 4.11c that although ceria's oxidation state is adapted fast to the CO_2 atmosphere, just before polarization, the *pre-ox.*NiGDC electrode remains more oxidized than *pre-red.*NiGDC. However, during the upward polarization, ceria oxidation state is readjusted to an equilibrium sate of $CeO_{1.72}$ and practically remains unchanged in the backward curve independent of the pre-treatment. This is an intriguing finding, which shows that the GDC acts as a source or sink of mobile oxygen ions, by adapting its oxidation state, similar to the well know property of ceria in catalytic reactions [156,196].

4.3.6. The role of the surface sites on CO_2 electrolysis

Having established the presence of Ni^0 and Ce^{4+}/Ce^{3+} core/shell areas on the Ni/GDC electrode surface during CO_2 electrolysis, we try now to elucidate the mechanism of the electrochemical reaction on these electrodes. To the best of our knowledge, the CO_2 electrolysis mechanism on Ni/GDC electrodes has not been described in detail, however studies exist reporting on the reaction mechanism over Ni/YSZ [165,174] and pure ceria [89,90,197] cathodes. Evidently, different reaction sites are involved in the two electrode types, with TPBs and 2PBs credited as the active areas for Ni/YSZ and pure ceria cathodes respectively. Since Ni/GDC contains both TPBs and 2PBs sites due to the MIEC nature of GDC, one should start with the hypothesis that both type of sites are involved in the reaction, of course depending on their availability. Previous reports have demonstrated that CO_2 reduction reaction on ceria surfaces proceeds through the formation of stable CO_3^{2-} intermediates [89]. The absence of such intermediates shown in Figure 4.2 suggests that ceria sites, or in other words 2PBs, are not directly involved in the CO_2 reduction reaction under the employed conditions. Therefore, the reactivity of Ni/GDC electrode should be attributed to the specific Ni/GDC interface, or in other worlds to the TPBs sites (Figure 4.14).
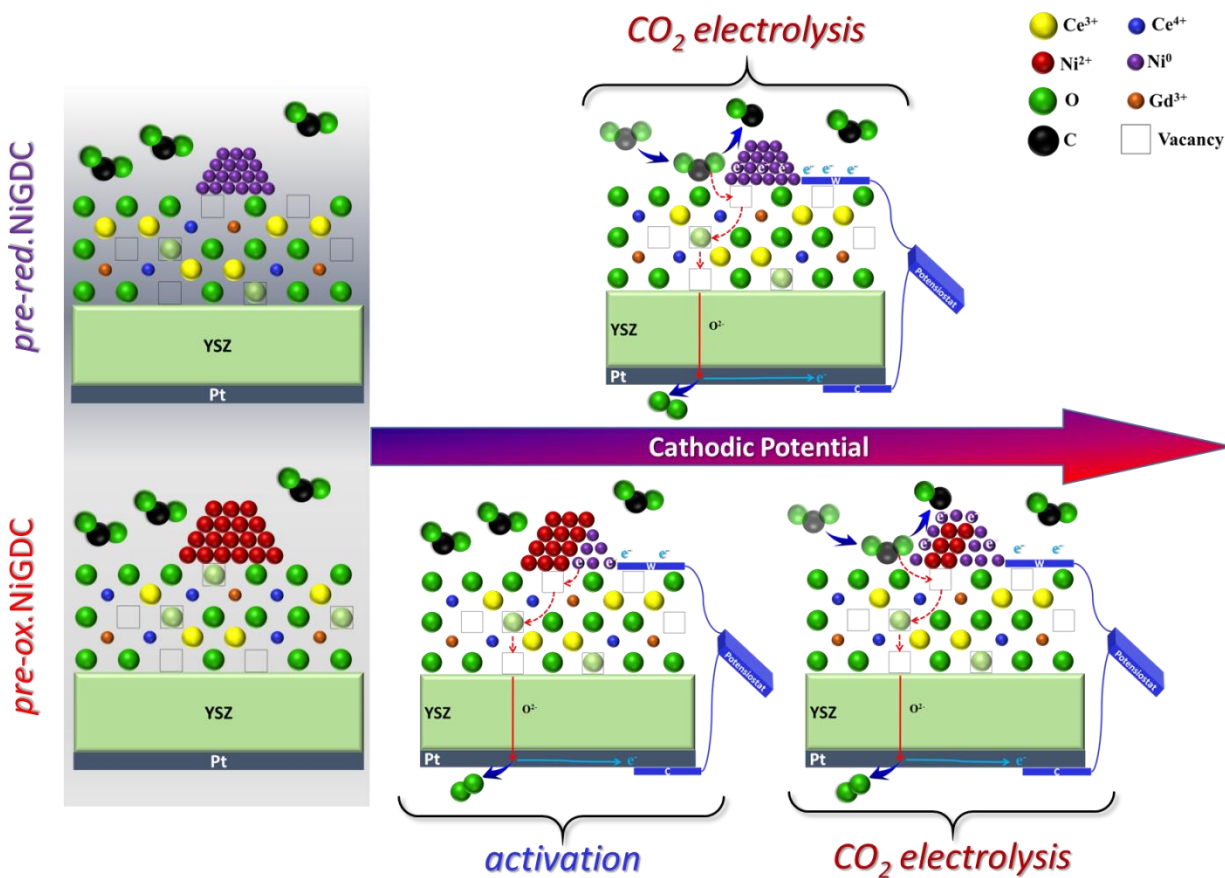
Figure 4.14. Schematic of the proposed activation and reaction mechanism for reduced and oxidized Ni/GDC cathodes. In the activation steps electrons flow in the external circuit and gas O_2 is produced but without CO_2 electroreduction.

There are several findings to support this argument. First, on the *pre-ox.*NiGDC, CO is detected parallel to NiO reduction, since electrical conductivity of nickel particles is indispensable for electron transfer at the TPB. On the same electrode, at 0.8 V and 1 V, CO production was observed only at the downward polarization curve after NiO partial reduction. Since in the up and down polarization curves the temperature, gas mixture and applied bias are identical, one can argue that CO_2 electrolysis does not take place, unless metallic Ni is formed, at least at low potentials. Besides, the similarities of the downward polarization between the two pre-treated electrodes (Figure 4.13) suggest that partial surface reduction of NiO can be equally beneficial for CO_2 electrocatalysis to the complete Ni^0 reduction. Similar results were previously found also in the case of steam electrolysis on Ni/GDC electrodes [93].

4.4. Conclusions

Summarizing, *operando* NAP-XPS was applied to examine Ni/GDC cermet cathodes during CO_2 electrolysis at potentials below the threshold of carbon deposition. It was shown that the functional Ni/GDC surface consists of metallic nickel and partially reduced ceria. Activation of the CO_2 electrolysis reaction is correlated to electro-reduction of NiO to Ni, which is feasible at relatively low CO_2 electrolysis potentials. Partially reduced nickel particles are organized in a core-shell structure, with metallic nickel in the shell and NiO underneath. Interestingly, formation of a nanometer-thick surface Ni layer is adequate to activate and maintain CO_2 electrolysis, while reduction in deeper NiO layers does not further boost the performance. Our findings provide useful insights for the design of efficient electrochemical devices, particularly for direct CO_2 conversion without reductive gas in the feed.

Chapter 5. A simple and efficient method to infiltrate ceria nanoparticles into prefabricated Ni-YSZ cermet electrodes

V. Chapter 5. A simple and efficient method to infiltrate ceria nanoparticles into prefabricated Ni-YSZ cermet electrodes

5.1. Introduction

Our focusing two principal SoA cermet cathode electrodes, nickel combined with yttria stabilized zirconia (Ni/YSZ) and gadolinium doped ceria (Ni/GDC), are most widespread electrode materials in CO_2 electrolysis[8,34-39]. For practical CO_2 electrolysis applications, under the same reaction conditions Ni/GDC usually possess higher CO_2 electrochemical performance, and potentially more stable than Ni-YSZ for CO_2 electrolysis [40], since it can tolerate better oxidizing conditions occurred in the event of leakage or during shutdown periods [9]. However, Ni/GDC cermets have some disadvantages as compared to Ni/YSZ, related to their lower mechanical stability and the higher cost [10]. Intrigued by this observation, we attempt to combine the robust mechanical properties of Ni-YSZ with the enhanced CO_2 oxidation resistance of cerium-based material. Ceria will be functioning as a source of mobile oxygen ions during the polarization as proposed by the two chapters above.

Surface modification of the cathode electrode, by deposition of metals or oxides, appears as an attractive and simple strategy to improve, both performance and stability, of the SOC devices[166,167] and re-activate them after carbon formation [168]. Infiltration of catalytic promoters directly into the pores of ceramic electrodes is probably the simplest preparation method for this aim [99,198]. The heterogeneous microstructure created after infiltration can extend the three/two-phase boundaries (TPBs/DPBs) length and enhance the ionic and electronic conductivities as well as the catalytic activity of the electrode [199–202]. Besides, infiltration over pre-fabricated electrodes allows to combine materials that otherwise could not form a stable bulk composite due to the mismatch of their thermal expansion coefficients. Among others, infiltration of electrodes with cerium based materials has several benefits [203], such as creation of a large amount of TPBs and abundant oxygen vacancies, while can also moderate deactivation at high operating temperatures [166,168,201,202,204–206].

In order to improve the TPBs/DPBs length in SOC electrodes, the infiltrated particles should be located at the electrochemical active area [207,208], deep within the porous electrode, close to the interface with the electrolyte [112]. If the promoting particles are situated near the outermost or intermediate areas of the electrode, the cell performance may not present obvious enhancement or even degrade due to limitation of gas diffusion caused by nanoparticles accumulation into the

electrode pores. On the other hand, since SOCs are high-temperature systems, infiltrated nanoparticles during operation easily tend to coarse/sinter, adversely affecting the long-term stability [113,114]. In order to limit agglomeration issues, the infiltrated nanoparticles should be decorated uniformly and discretely as much as possible into the electrode backbone. Generally speaking, for an efficient electrode infiltration process the number of infiltration/co-firing step(s) should be minimized and the concentration of the promoting nanoparticles within the active electrode area should be optimized.

At present, there are mainly two ways to infiltrate catalysts into SOC electrodes. The most common strategy is to use metal precursor solutions comprised of dissolved metal salts (chlorides, sulfides or nitrides) [100,104,109,201]. After infiltration of the precursor into the electrode, the solution is dried and the dissolved metal salt precipitates. Subsequently, the infiltrated-electrode is fired at high temperature to form nanosized particles. Considering that the catalyst precursor is infused into the porous backbone structure by capillary forces, this process requires many infiltration repetitions using low-concentration metal salts until the desired catalyst loading level is achieved [99,201]. This might be problematic since the precursor dries primarily at the surface of the electrode and blocks the porous structure, eliminating the ability to further incorporate more salt solution deeper into the microstructure.

Alternatively, a straightforward method is to fill the electrode pores with pre-synthesized nanoparticles dispersed into a solvent and finally remove the solvent residuals by calcination. This method allows preselecting the characteristics of the nanoparticles, because synthesis is done beforehand. On the downside, nanoparticles agglomeration may be difficult to control, which challenges efficient infiltration deep inside the porous electrode and produce pore-clogging and gas starvation issues [102,209,210]. In addition, the grain growth after each firing (calcinations) step further reduces the efficacy of the infiltration, increasing potential clogging risks [100,211,212]. Although detailed information about the number of steps is not always provided in the relevant literature, 5-15 infiltration steps are required in general to achieve catalyst loading of around 150 mg per 1 cm^3 electrode backbone [99,201,202,213]. Overall, the necessity of repetitive infiltration steps and multiple firing cycles, is not only a labor-intensive process, but might also cause undesired modifications of the electrode microstructure, such as pore-clogging.

It is common knowledge that the wet chemistry of the precursor solution plays an important role in its penetration ability and consequently to the yield of the deposited material. In addition to

some external engineering solutions, such as pressure or vacuum assistance, the surface tension of the precursor system is vital for the wettability inside the electrode backbone. Since alcohol-based solvents have lower surface tension than water, hence possessing a better wettability on solid surfaces, ethanol is usually added into the aqueous solution to modify the liquid surface tension [108–111]. However, 100% ethanol solvent may limit the solubility of the nanoparticles and unfavorably affect the solution/suspension stability and the drying kinetics after infiltration [212]. Another option to control the dispersion of metal salt solutions into porous structures, is to introduce in the solution dispersant and surfactant additives, such as glycol, citric acid, urea or Triton X-1[105,106]. The surfactant complexes with metal cations assisting the formation of crystal phases and may control the particle size through forming a proper micelle [107]. However, the additives utilized in these studies are specifically associated with the composition of the substrates and/or the nano-catalysts. Therefore, the surfactant system always needs to be re-engineered to respond the change of SOC electrodes or nano-catalyst compositions.

In this chapter, we present a novel and simple infiltration strategy of pre-fabricated Ni/YSZ cermet electrodes via impregnation with hexane solution containing ceria nanoparticles. In this way the challenges of infiltration with aqueous solutions (low wettability, precipitation of precursors, etc.) and the complexities of using surfactants, could be overcome. Therewith, organic solutions containing two types of cerium oxide NPs (CeO_x NPs and $Ni_{0.1}Ce_{0.9}O_{2-y}$ NPs) were infiltrated into pre-reduced Ni/YSZ cermet electrodes acting as a porous backbone. The morphology and microstructure of the modified Ni/YSZ electrodes were examined using several analytical methods. The results demonstrate the higher efficiency of $Ni_{0.1}Ce_{0.9}O_{2-y}$ NPs to infiltrate deep into the pores of the electrode close to the interface with the YSZ electrolyte. More importantly, significant catalysts loading on the Ni/YSZ backbone can be achieved only after a single infiltration/co-firing step, which is a considerable practical improvement as compared to current state of the art methods that require up 20 times more steps.

This chapter is based on the article in preparation: Dingkai Chen, Mathias Barreau, Sylwia Turczyniak-Surdacka, Kamil Sobczak, Marcin Strawski, Anna Efimenko, Detre Teschner, Corinne Petit, and Spyridon Zafeiratos. Ceria nanoparticles as promoters of CO_2 electroreduction on Ni/YSZ: an efficient preparation strategy and insights into the catalytic promotion mechanism. Nano Energy, 2022.

5.2. Experimental

5.2.1. Synthesis of MCeO$_x$ NPs organic solution

Un-doped and 10% Ni-doped (Ni$_{0.1}$Ce$_{0.9}$O$_{2-x}$) CeO$_2$ nanoparticles, abbreviated as CeO$_x$ and NiCeO$_y$, respectively, were prepared from Schiff base metal complexes based on a previously developed procedure[11] that was recently modified to give higher production yield with lower number of synthesis steps [12]. In brief, the first two steps consisted in preparing each of the two monometallic Schiff base complexes (Ce-L and Ni-L) by mixing o-vanillin, 1,3-diaminopropane and the metallic salts (cerium nitrate hexahydrate or nickel acetate tetrahydrate) in methanol under reflux. Then, the nanoparticles were synthesized via mixing of the Schiff bases and their pyrolysis in oleylamine media at 180 °C under inert atmosphere (Ar). After extraction using methanol solvent to precipitate them and subsequent centrifugation, a part of the NPs was dispersed in hexane solution while the rest were calcined under air (at 400 °C for 1h) for classical powder characterization (XPS, XRD *etc.*).

5.2.2. Description of the prefabricated electrochemical cells with Ni/YSZ cermet cathodes

The CeO$_x$ and NiCeO$_y$ NPs were infiltrated directly from hexane solution on commercially available (Kerafol GmbH), electrolyte supported half-cells. The Ni/YSZ electrode of the cell has an overall thickness of 40-45 µm and it consists of 3 layers: the first layer (starting from the electrolyte) is a dense 5 µm thick YSZ barrier layer directly deposited over the 150 µm thick 8 YSZ (8 mol-% Y$_2$O$_3$ stabilized ZrO$_2$) electrolyte support. Above this dense YSZ layer, a composite of 60wt-%Ni/ 40wt-%YSZ is deposited with 25 µm thickness and 30% porosity (before reduction). The electrode terminates with a 10 µm thick of 90wt-%Ni/ 10wt-%YSZ layer at the top (porosity about 50 %). The NPs solution was infiltrated directly on the top of the Ni/YSZ electrode using a 10 µL micropipette. In this work, 50, 100 or 200 µL loading of Ni$_{0.1}$Ce$_{0.9}$O$_{2-y}$ or CeO$_x$ particles in hexane solution were impregnated on electrodes with of about 64 mm^2 area, hereafter referred as 50, 100 or 200CeO$_x$ (NiCeO$_y$)@Ni/YSZ.

5.2.3. Material characterization

Ex-situ characterized methods, including FTIR spectra, TGA, XRD, DLS, TEM-EDX, SEM-EDX, and TOF-SIMS characterizations, have been described in 2.7 section of chapter 2. Quasi *in situ* X-ray photoelectron spectroscopy (XPS) measurements were conducted in an in-house device, especially developed to facilitate pre and post mortem surface characterization of electrodes [148].

The ultra-high vacuum analysis chamber (base pressure $<5\times10^{-9}$ mbar) is equipped with a VSW Class WA hemispherical electron analyzer (150 mm radius) and a monochromatic Al Ka X-ray source (1486.6 eV). Cerium modified Ni/YSZ and pristine Ni/YSZ of about 64 mm^2 area were mounted via two stainless steel clamps on the sample holder and heated by a ceramic heater. The temperature was controlled by a K-type thermocouple mounted on the side of the heater. The holder was first introduced into a load-lock chamber and then transferred to a reaction/electrochemical chamber. In the reaction chamber, the sample was calcinated or reduced in 1.0 mbar O$_2$ at 400 °C or 1.0 mbar H$_2$ at 550 °C for 30 min, respectively. The gas flow into the reaction cell was controlled via calibrated mass flow controllers and the products were monitored by an online quadrupole mass spectrometer (QMS). After treatment, the sample was first cooled to room temperature in gas, then the reactor was evacuated down to 10^{-7} mbar and the sample was transferred under vacuum into the analysis chamber for XPS characterization. XPS measurement of SOC cell electrodes was performed at around 230 °C, where it was found that the conductivity was sufficient to avoid electrostatic charging problems.

5.3. Results and discussion

5.3.1. Physicochemical properties of cerium-based nanoparticles

5.3.1.1 Characterization of the nanoparticles in the hexane solution

The composition of the organic layer around the as-synthesized cerium-based nanoparticles, surfactants, and their corresponding Schiff bases complexes, was investigated via FTIR. The comparison of the NiCeO$_y$ and CeO$_x$ NPs FTIR spectra shown in Figure 5.1a indicates similar peak profiles, suggesting that the composition of the organic layer around the two NP types is identical. The FTIR spectra resemble very much the one of oleylamine (OLA) reference sample included in the figure for comparison. The IR absorption features at 3006-2853 and 1466 cm^{-1} are ascribed to symmetric and asymmetric C–H stretching and to the CH$_2$ deformation modes respectively, originate from OLA around the ceria NPs [214,215]. The peaks located at 1639 and 1582 cm^{-1} are assigned to asymmetric deformation of N–H$^+$ [216], indicating that when the OLA layer interacts with ceria nanoparticles it loses electrons from its amino group (–NH$_2$). Please note in the IR spectrum the absence of peaks in the 1700–400 cm^{-1} wavenumbers for both NiCeO$_y$ and CeO$_x$ NPs. This range is dominated by several features originated from Ce (III)-L or Ni (II)-L

Schiff base complexes (see figure 5.2) used in the synthesis process. Their absence verifies the elimination of these species upon pyrolysis in OLA media.
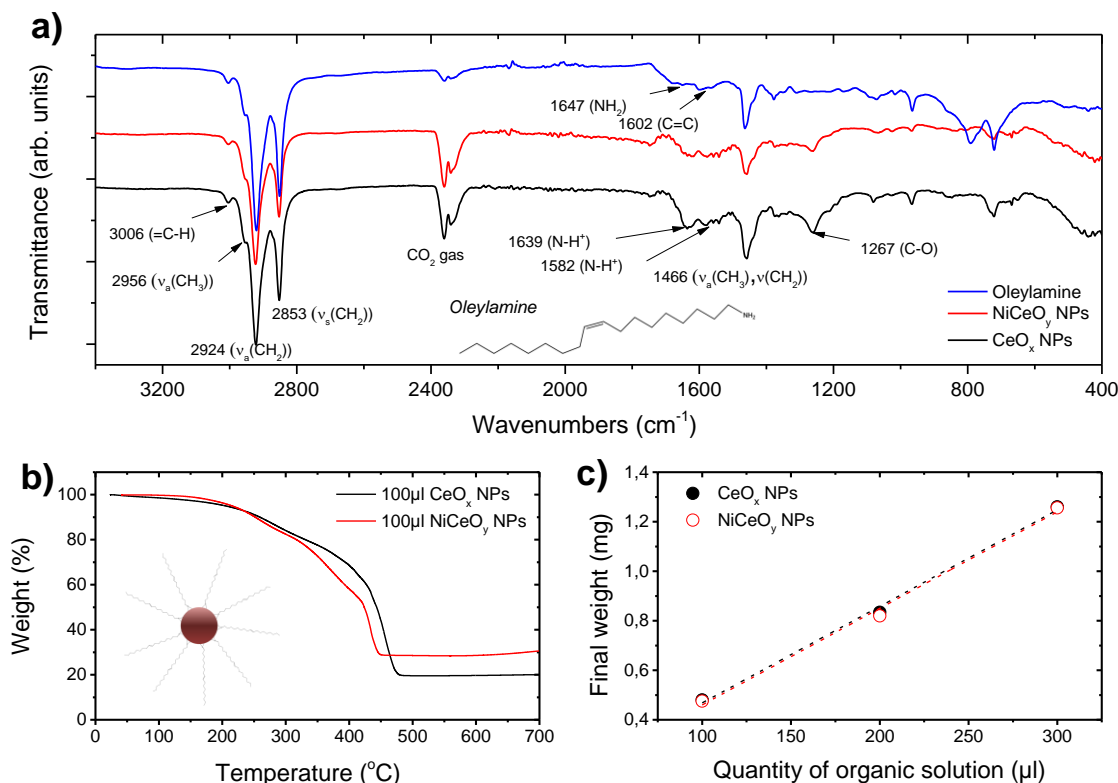
Figure 5.1. (a) FTIR spectrum of as-synthesized CeO_x and $NiCeO_y$ NPs as well as of OLA reference sample. (b) The TGA thermogram of 100µL CeO_x and $NiCeO_y$ NPs in their organic solutions. (c) The final weight of CeO_x and $NiCeO_y$ NPs at 500 °C as a function of different quantities of organic solutions in TGA measurement.

The concentration of $NiCeO_y$ and CeO_x NPs in their organic solutions was evaluated based on Thermogravimetric analysis (TGA). The TGA measurements were conducted in air for 3 different CeO_x and $NiCeO_y$ NPs solution amounts (100 µL, 200 µL, 300 µL). Characteristic TGA thermograms of 100 µL CeO_x and $NiCeO_y$ organic solutions are shown in Figure 5.1b, while the results of the 3 different amounts are summarized in Table 5.1. For both CeO_x and $NiCeO_y$ solutions the initial weight loss shown in Figure 5.1b is due to the evaporation of hexane solvent (around 70 °C) and above 200 °C follows the decomposition of the OLA coating around the NPs [217]. The weight curve stabilizes at 450 and 480 °C for $NiCeO_y$ and CeO_x respectively, meaning that the organic coating was decomposed. Based on above result the mass concentration of the two NPs in their organic solution was calculated for each solution amount. The results in Table 5.1 and

the graphic correlation in Figure 5.1c evidence a linear relationship between the weight of NPs and the amount of the loaded solution which corresponds to a mass concentration in solution of 4.4 ± 0.3 mg/ml similar for both NPs. The TGA results in Table 5.1 show that the final % weight of CeO_x is lower than that of $NiCeO_y$ NPs (average 18.5 ± 0.9 %, and 28.2 ± 0.6 %, respectively). Since the mass concentrations of the two NPs in their organic solution are similar, this difference indicates that the average weight of the protective OLA layer surrounding CeO_x is higher than that in $NiCeO_y$ NPs.
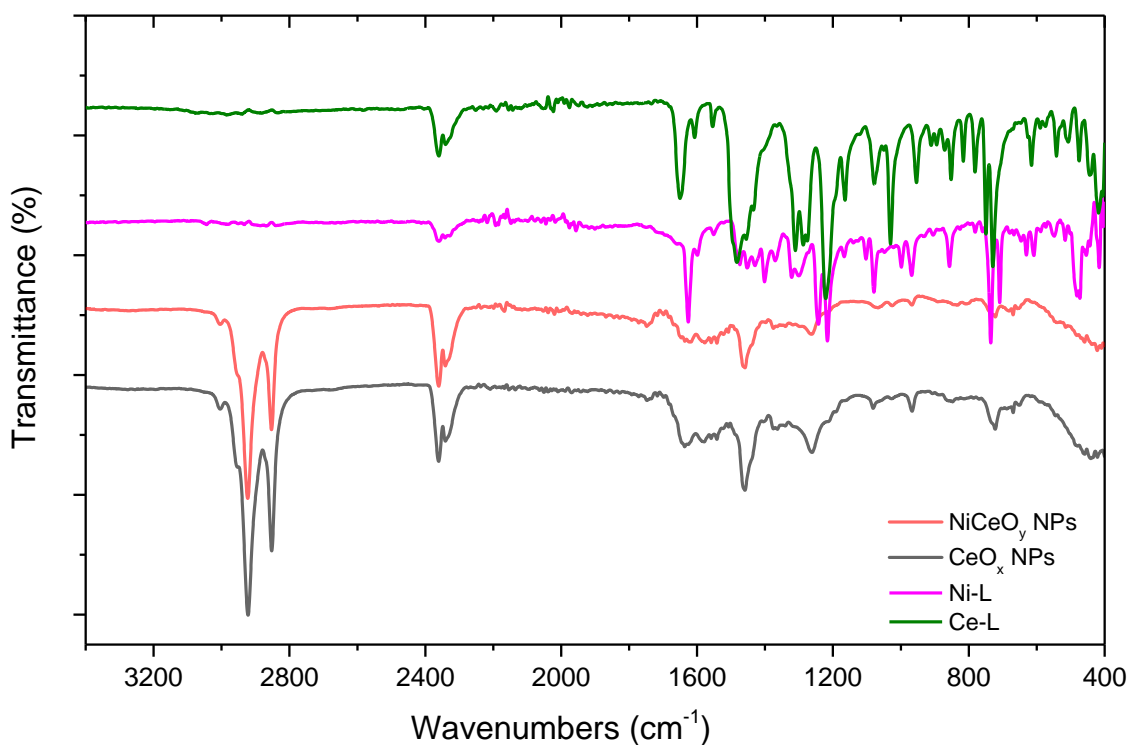
Figure 5.2. FTIR spectrum of Ce (III)-L complex, Ni (II)-L complex, and as-synthesized $NiCeO_y$ and CeO_x NPs.

Table 5.1. TGA quantitative analysis of CeO_x and $NiCeO_y$ NPs in organic solutions.

Loading (µl)	Initial weight (mg 25 °C)	Final weight (mg at 500 °C)	Calculated final mass concentration (mg/ml)	Final weight (% at 500 °C)
CeO_x				
100	2.45	0.48	4.8	19.6
200	4.72	0.83	4.2	17.7
300	6.87	1.26	4.2	18.3
$NiCeO_y$				
100	1.66	0.47	4.8	28.6
200	2.88	0.82	4.1	28.5
300	4.57	1.26	4.2	27.5

5.3.1.2 Structural characterization of the nanoparticles

The crystallinity of the pristine and calcined CeO_x and $NiCeO_y$ NPs were examined by XRD, while the corresponding crystalline sizes were calculated by the Debye-Scherrer equation. The diffraction patterns (Figure 5.3) display the characteristic peaks of CeO_2 fluorite structure. The lack of additional peaks related to Ni-containing phase in case of $NiCeO_y$ NPs suggests the absence of separated nickel aggregates, demonstrating the successful incorporation of the entire quantity of Ni ions into CeO_2 lattice [11]. The crystallite size of the pristine CeO_x and $NiCeO_y$ NPs is calculated around 4.8±0.2 nm and 3.8±0.2 nm, respectively. These results demonstrate that both cerium-based nanoparticles diluted in hexane solution are relatively small (3~5 nm) confirming that the applied synthesis method is able to produce nanosized ceria particles [11,144].

The morphology of the nanoparticles after calcination was investigated by TEM, HAADF and TEM-EDS. Please note that pristine ceria nanoparticles could not be measured by this method due to the decomposition of the OLA layer under the microscope beam. Representative bright field (BF) TEM images displayed in Figure 5.4 show that in both cases the nanoparticles form big aggregates due the removal of the organic protective layer following calcination. Although not easy to distinguish clearly due to the low contrast, areas with individual ceria nanoparticles can be seen in both samples. Those particles have a (pseudo)spherical shape and seem relatively homogeneous in size and morphology. The elemental distribution of the $NiCeO_y$ given in the TEM-EDS images (Figure 5.4a) shows that Ni and Ce elements are well-mixed and uniformly

distributed in the nanoscale. This is also confirmed in the lower magnification images shown in Figure 5.5, which verify the uniform Ni distribution over ceria, with very few spots rich in Ni. In the case of CeO_x sample (Figure 5.4b) the TEM-EDS just confirms the expected composition.
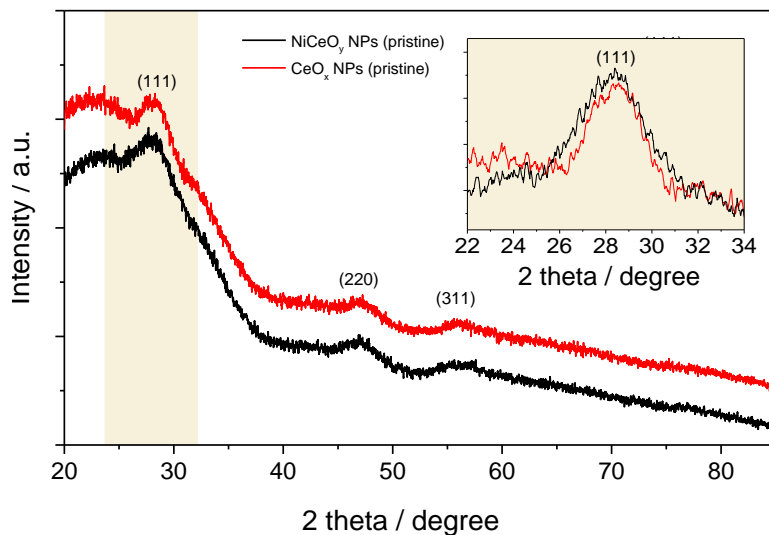
Figure 5.3. XRD patterns of pristine CeO_x and $NiCeO_y$ NPs.
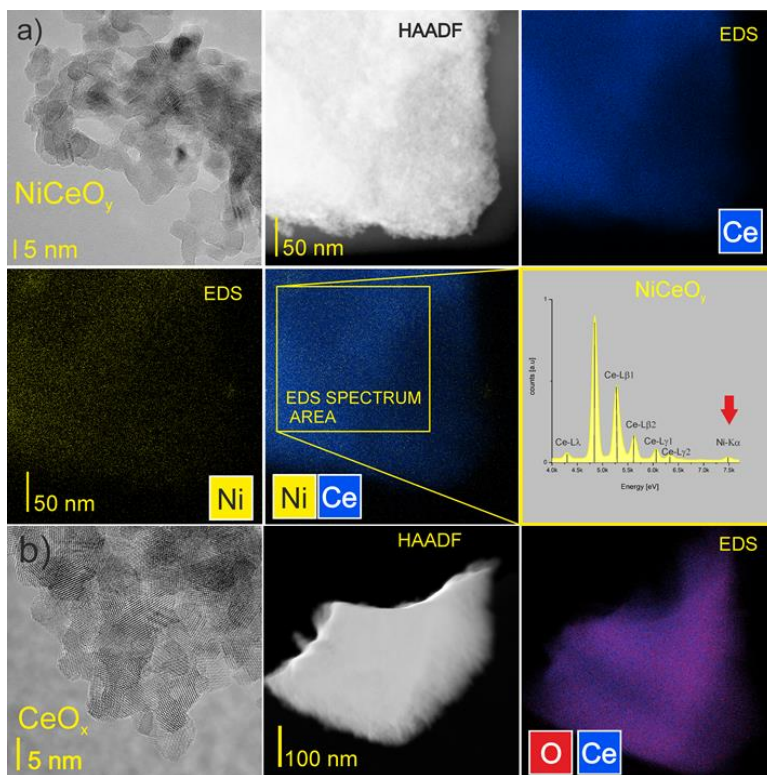
Figure 5.4. TEM and TEM-EDS elemental mapping of (a) $NiCeO_y$ and (b) CeO_x NPs samples after calcination in O_2 at 400^oC.
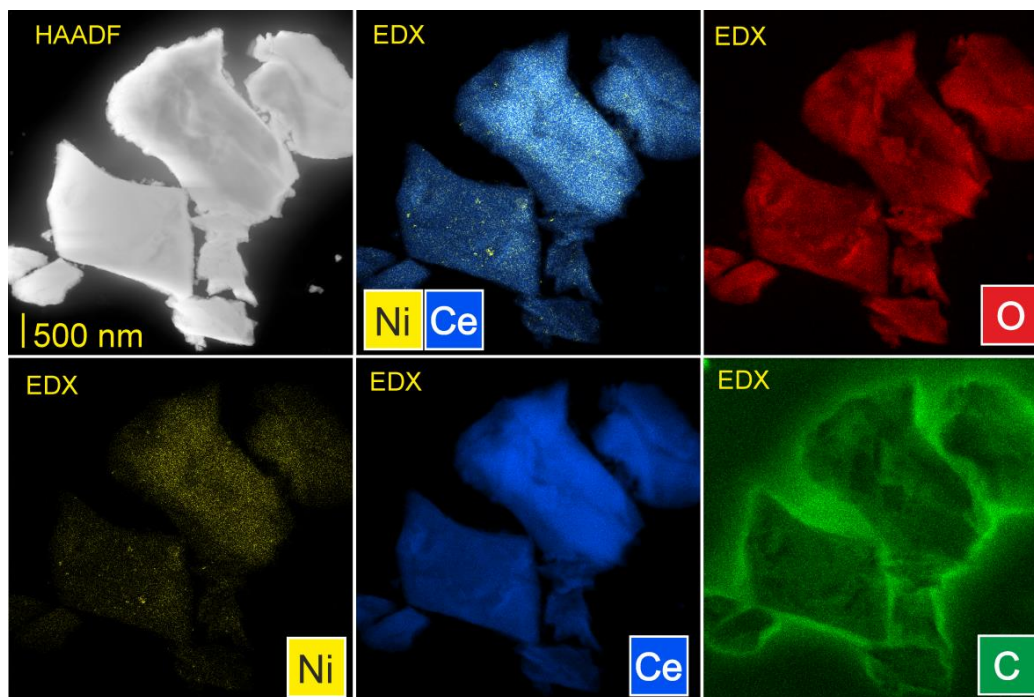
Figure 5.5. HAADF-TEM and TEM-EDS elemental mapping of $NiCeO_y$ NPs samples after calcination in O_2 at 400^oC.

5.3.1.3 Size of the nanoparticles in solution

Dynamic light scattering (DLS) was used to determine the size distribution profile of the CeO_x and $NiCeO_y$ particles in their solution [13]. Note that DLS measurements provide the so-called hydrodynamic radius, which is the overall size of the particles inducing also the organic protecting layer. According the DLS results presented in Figure 5.6 and Table 5.2, the majority (73%) of CeO_x NPs in hexane solution forms aggregates with size around 2.29 µm, which is almost 3 times bigger than $NiCeO_y$ NPs (0.82 µm, 87% of particles). Although bigger CeO_x NPs are expected according to the XRD results (4.8 *vs.* 3.8 nm), the particles size measured by DLS is in the micron scale, which of course cannot be simply be due to the surrounding coating (in general the OLA molecule has a chain length around 2.0 nm). Therefore, the DLS results reflect that CeO_x nanoparticles form bigger agglomerates in hexane solution as compared to $NiCeO_y$.
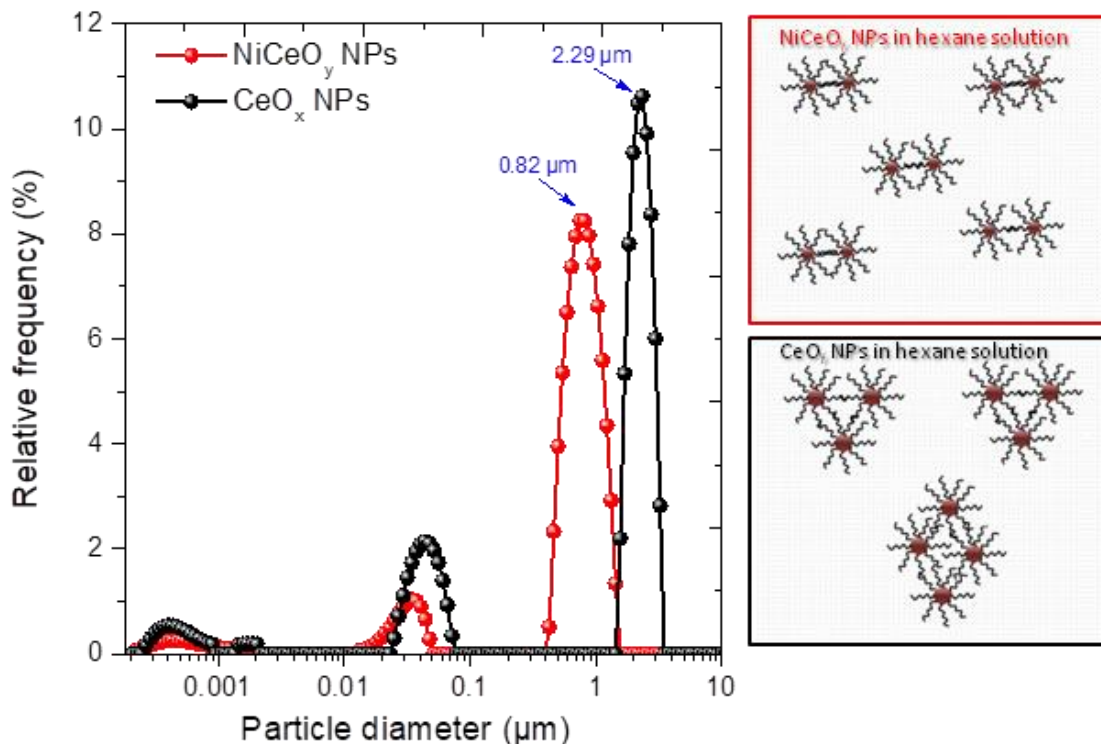
Figure 5.6. (a) The particle size distributions of $NiCeO_y$ and CeO_x NPs in their organic solutions in DLS measurement. (b) Schematic representation of $NiCeO_y$ and CeO_x NPs arrangement in their organic solutions.

Table 5.2. The DLS results of CeO_x and $NiCeO_y$ NPs in their organic solutions.

Sample	Peak 1		Peak 2		Peak 3	
	Particle diameter (μm)	Area (%)	Particle diameter (μm)	Area (%)	Particle diameter (μm)	Area (%)
CeO_x NPs	2.29	73.12	0.044	19.98	0.00049	5.97
$NiCeO_y$ NPs	0.82	86.72	0.031	8.98	0.00067	4.30

The difference in the dispersion of the two types of ceria NPs in the hexane solution can be rationalized based on the DLVO theory typically used to describe the dispersion of colloidal solutions [135–137]. In particular the dispersion of ceria NPs coated by the organic layer depends on the balance between van der Waals attraction forces applied in the core of the particles (ceria NPs) and the steric repulsive forces acting by the ligand (here, OLA). According to the calculated

potential curves (Figure 5.7) explained in detail in 2.5 section of chapter 2, it is the core size of the ceria-based NPs that mainly affects the dispersion in hexane solution. In particular bigger in size NPs apply stronger van der Waals' attractive forces as compared to smaller NPs. Taking into account that the OLA coating is identical for both types of NPs (Figure 5.1a), the bigger crystallite size in case of CeO_x NPs shown by XRD can be held accountable for the poor dispersibility of CeO_x NPs in solution.

Overall, the analysis of nanoparticles in solution revealed that CeO_x and $NiCeO_y$ NPs have nanometer-scale sizes and are protected by an OLA layer. In both cases the particles form aggregates in the hexane solution, however agglomeration is more severe in case of CeO_x which forms 3 times bigger aggregates than $NiCeO_y$. A schematic representation of $NiCeO_y$ NPs and CeO_x NPs in organic solutions is given in Figure 5.6. The effect of above differences for the infiltration into the pores of Ni/YSZ cermet electrode will be discussed in the next section.
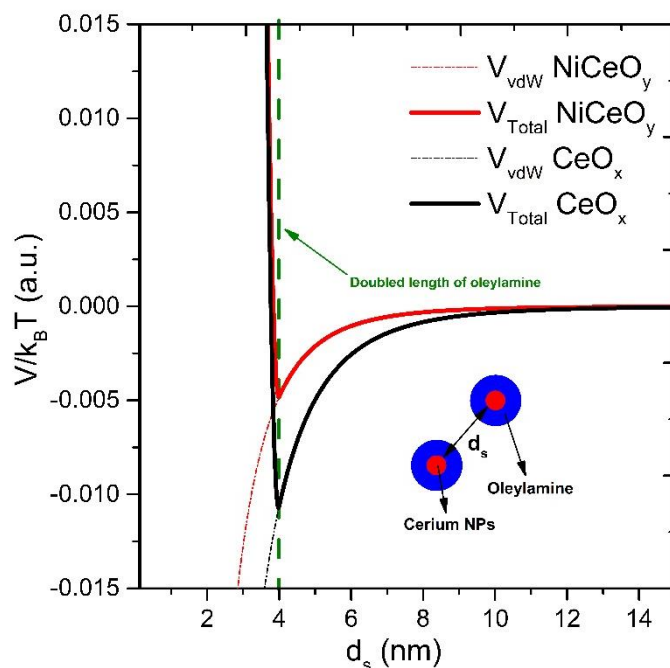
Figure 5.7. The calculated total potential curves between $NiCeO_y$ and CeO_x NPs. The inter-particle distance d_s ($d_s = d - 2r$) was defined as surface-to-surface separation distance between two nanoparticles. As shown in the figure, the repulsive forces arise at the distance, where oleylamine surrounded ceria-based nanoparticles contacts each other.

5.3.2. Infiltration of ceria nanoparticles into the pores of prefabricated Ni/YSZ electrodes

The CeO_x and $NiCeO_y$ NPs solution was infiltrated directly on the surface of Ni/YSZ electrodes with area of about 64 mm^2 using a 10 µL micropipette, as shown schematically in Figure 5.8. Before impregnation, the cell was reduced in H_2, which is usually followed by a significant volume contraction of nickel forming nanopores [201,218]. Unless otherwise stated, the NPs solution was dropped into Ni/YSZ backbone through subsequent 50 µL infiltration/co-firing steps. This solution amount corresponds to about 85 mg ceria NPs loading per cm^3 of Ni/YSZ electrode (calculated by the results of Figure 5.1c and he dimensions of the Ni/YSZ electrode). After each infiltration step the hexane solvent was left to dry at 80 °C in air for about 90 min. Then was applied a calcination (firing) step at 400 °C in air in order to remove the organic residuals related to the coating of the NPs. For the electrochemical tests the calcined cells were subjected to a second reduction in H_2.
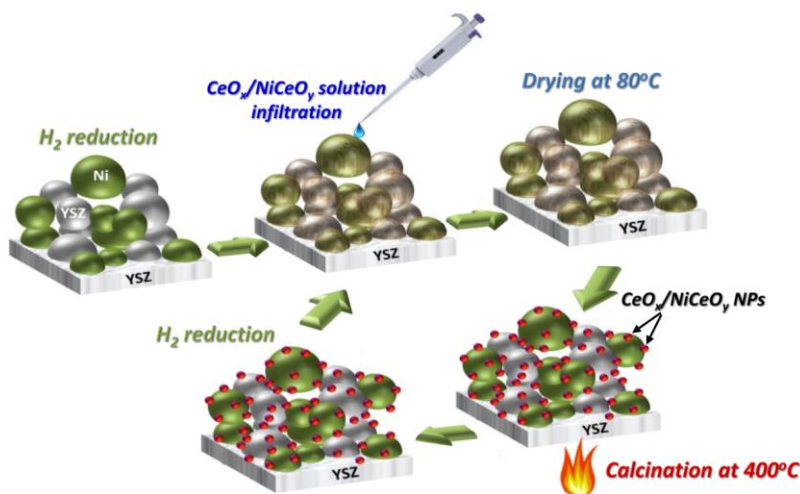
Figure 5.8. Schematic representation of the CeO_x and $NiCeO_y$ NPs infiltration process over pre-fabricated Ni/YSZ electrodes.

5.3.2.1. Comparison of the efficiency of $NiCeO_y$ or CeO_x NPs in hexane solution to infiltrate into the pores of the Ni/YSZ electrodes

a. Macroscopic evidences

In a process with multiple infiltration steps the drying treatment of the precursor plays a key role in the penetration of the organic solution inside the pores of the Ni/YSZ electrode scaffold, affecting in this way the efficiency of the process [212,219]. Initially, the effectiveness of the two solutions to penetrate the pores of the electrode was macroscopically evidenced by following the

Drying Time (min)	50NiCeO$_y$@Ni/YSZ	50CeO$_x$@Ni/YSZ
0		
30		
60		
90		
After calcination and reduction		
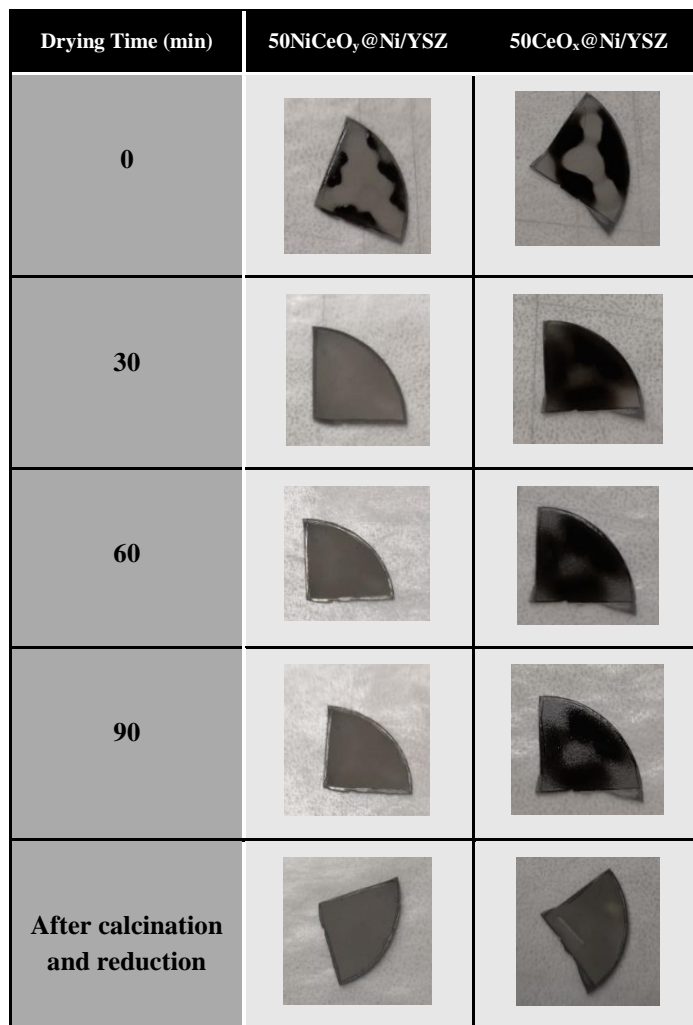
Figure 5.9. Photographs of 50NiCeO$_y$@Ni/YSZ and 50CeO$_x$@Ni/YSZ samples during the drying treatment at 80 ^{o}C, and after calcination and reduction for 30 min in O$_2$ and H$_2$.

changes in the color of the electrode upon drying in air. Figure 5.9 shows photographs of two Ni/YSZ electrodes impregnated with 50 µL of NiCeO$_y$ or CeO$_x$ solution, taken at different drying stages. In the images the organic solution appears darker than the Ni/YSZ support which has a light grey color. Just after drop-casting, the support infiltrated by the NiCeO$_y$ shows less dark areas as compared to CeO$_x$, indicating better spreading and pore-filling in the former case. After drying for 30 min at 80 ^{o}C, the surface of 50NiCeO$_y$@Ni/YSZ seems homogenous in color, while in case of 50CeO$_x$@Ni/YSZ spots with dark and light contrast remains even after 90 min at 80°C. Since hexane evaporates fast at 80 °C (boiling point 68 °C) the homogenous surface color of NiCeO$_y$ infiltrated electrode indicates that the solution was successfully entered the pores of the Ni/YSZ electrode. On the contrary for 50CeO$_x$@Ni/YSZ the appearance of dark spots on the surface

suggests that part of the solution remains on top of the electrode, allowing CeO_x NPs to form a layer on the surface of Ni/YSZ rather than penetrating into its pores.

b. XPS surface analysis

Due to its high surface sensitivity (around 3 nm in case of Ni 2p peak) and the large lateral analysis area (around 0.1 cm^2), X-ray photoelectron spectroscopy is an ideal analytical tool to verify the effectiveness of the infiltration method. In particular, in cases where ceria NPs are left on the surface of Ni/YSZ, this should be marked by an intense XPS signal of cerium followed by an attenuated signal of nickel and YSZ from the support. In case that ceria NPs are effectively penetrating into the Ni/YSZ pores the opposite trend should be observed. In addition to that, the chemical specificity of the technique can be used to analyze the chemical state of the surface after infiltration.

The Ni 2p and Ce 3d XPS spectra of the Ni/YSZ electrode after infiltration with $NiCeO_y$ or CeO_x solutions and subsequent drying and calcinations/reduction treatments are shown in Figure 5.10 (the spectra correspond to the samples at the bottom of figure 5.9). The spectrum of the reduced Ni/YSZ electrode before infiltration is also included for comparison. As expected, prior to the infiltration with ceria NPs the Ni $2p_{3/2}$ peak at 852.6 eV is characteristic of metallic nickel [92]. The Ce 3d peak appears at the high binding energy side of the spectrum, following infiltration with $NiCeO_y$ and CeO_x NPs and drying of the hexane solvent. However, comparison of the two samples clearly shows that the Ni 2p signal disappears after infiltration with CeO_x NPs, while in the case of $NiCeO_y$ the Ni 2p peak remains dominant. This is a clear indication that part of the CeO_x NPs stay on the surface of Ni/YSZ forming a dense layer (> 3nm thickness) that attenuates the Ni 2p signal of the support. On the contrary, since the $NiCeO_y$ NPs are penetrating into the pores of Ni/YSZ the Ni 2p signal is still present in this case. Please note that the Ni 2p signal originates almost exclusively from Ni/YSZ support, as shown by the Ni2p&Ce3d spectra of $NiCeO_y$ NPs in Figure 5.11 (In details, the spectra in Figure 5.11 shows the Ni 2p and Ce 3d XPS peak of $NiCeO_y$ NPs measured by drop casting the hexane solution onto an Au foil. Evidently on the pristine sample the signal is highly attenuated due to the 2 nm oleylamine layer covering the NPs surface. After calcination the Ni 2p and Ce 3d peaks can be clearly distinguished however the intensity of Ni 2p is around 5 % of the overall. This indicates that when $NiCeO_y$ NPs precipitate on the surface of Ni/YSZ the contribution of the Ni 2p signal deriving from $NiCeO_y$ should be minor). Besides, the

C1s peak around 285.5 eV, and the N 1s peak at 400 eV (see Figure 5.12) are attributed to the carbon of the alkyl chains and the amino-groups respectively of OLA [220]. This is a confirmation that the dark color areas shown in figure 5.9 are due to OLA that it is preserved after drying.

After drying, the two electrodes were calcined in 1 mbar O_2 at 400 °C for 30 min to decompose the OLA coating and subsequently reduced in 1 mbar H_2 at 550 °C for 30 min. The treatment was performed in a reaction chamber attached to the XPS device and the gas products during calcination were monitored by a quadrupole mass spectrometer (QMS) installed in the reactor. As shown in Figure 5.13 the oxidation of the organic film (indicated by CO and CO_2 production in the gas phase) takes place around 330 °C for $50NiCeO_y@Ni/YSZ$, while needs higher temperatures (about 400 °C) for $50CeO_2@Ni/YSZ$ in agreement with the TGA results of Figure 5.1. These results confirm that calcination at 400 ºC for around 30 min is sufficient to oxidize the OLA layer in both cases.
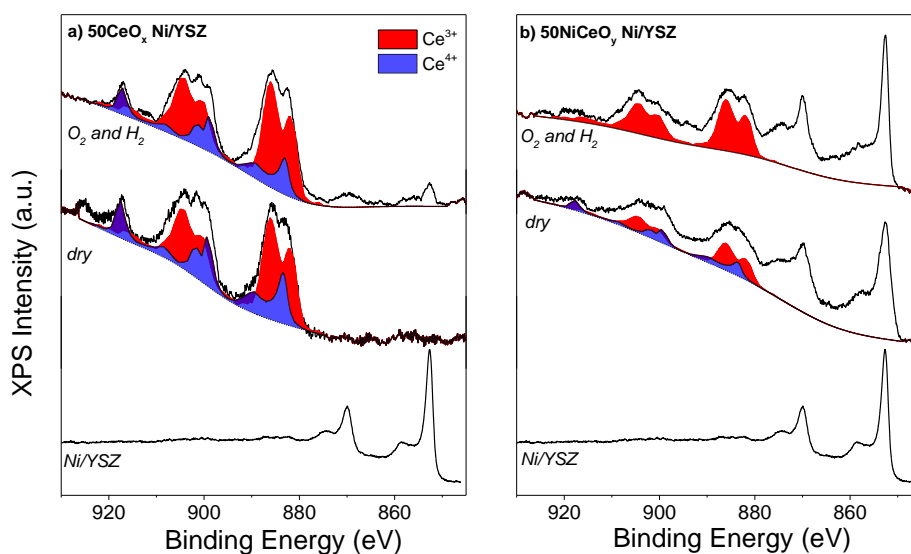
Figure 5.10. The Ni 2p and Ce 3d core level XPS spectra of $50NiCeO_y@Ni/YSZ$, $50CeO_x@Ni/YSZ$ as well as pristine Ni/YSZ electrode a) after drying treatment and b) after calcination and reduction treatment in O_2 at 400 °C and H_2 at 550 °C.

The XPS spectra of $50NiCeO_y@Ni/YSZ$ and $50CeO_x@Ni/YSZ$ after calcination and reduction treatment are included in Figure 5.10. After calcination the Ni 2p signal increases for both electrodes, but in case of $50NiCeO_y@Ni/YSZ$ it is notably higher. This observation is quantified in the bargraphs shown in figure 5.14, where the Ni2p/Ce3d peak area ratio is almost 15 higher in case of $50NiCeO_y@Ni/YSZ$. Similar trend is found also for the Ce 3d/Zr 3d ratio included in figure

5.14. Since nickel signal derives principally from Ni/YSZ while Ce 3d from ceria NPs, this difference implies that less cerium remains on the surface of $50NiCeO_y@Ni/YSZ$ as compared to $50CeO_2@Ni/YSZ$. Taking into account that the two impregnation solutions contain the same amount of NPs, this is indirect evidence that $NiCeO_y$ NPs are efficiently infiltrated inside the pores of Ni/YSZ.
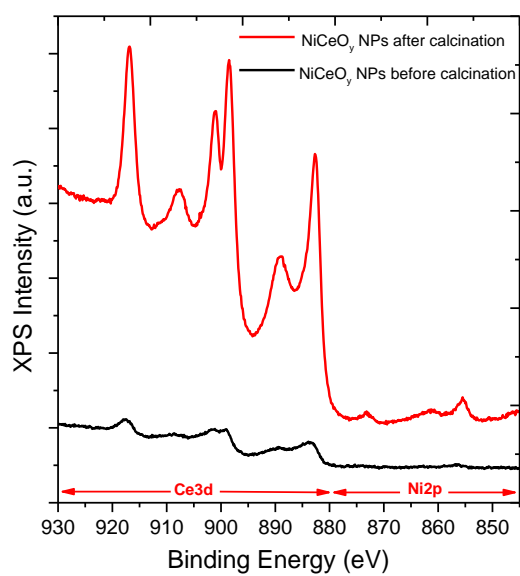
Figure 5.11. Ni2p Ce3d core level XPS spectra of $NiCeO_y$ NPs before and after calcination.
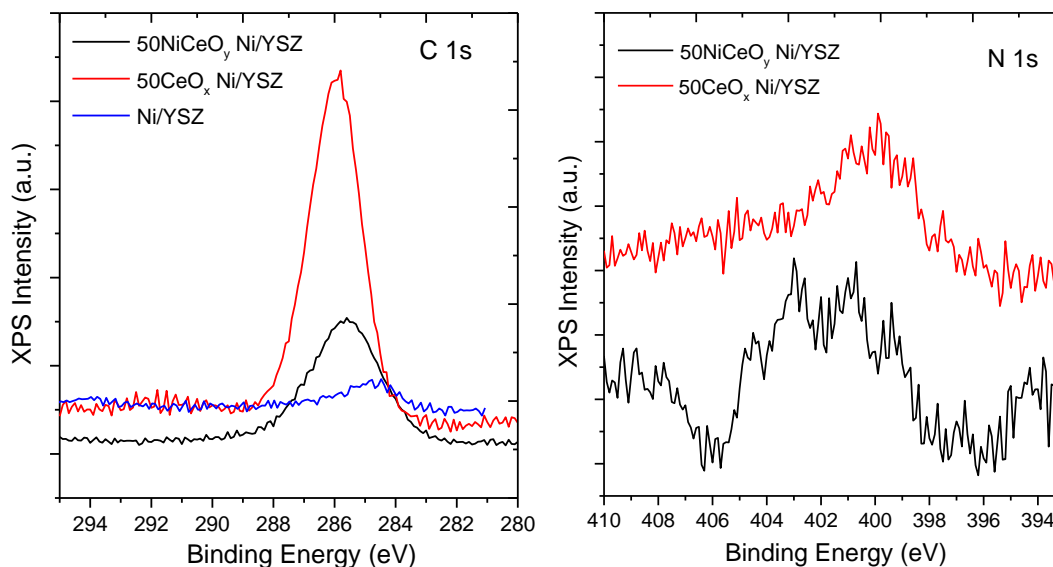
Figure 5.12. C 1s and N 1s core level XPS spectra of $50NiCeO_y@Ni/YSZ$, $50CeO_x@Ni/YSZ$ and Ni/YSZ after drying treatment.
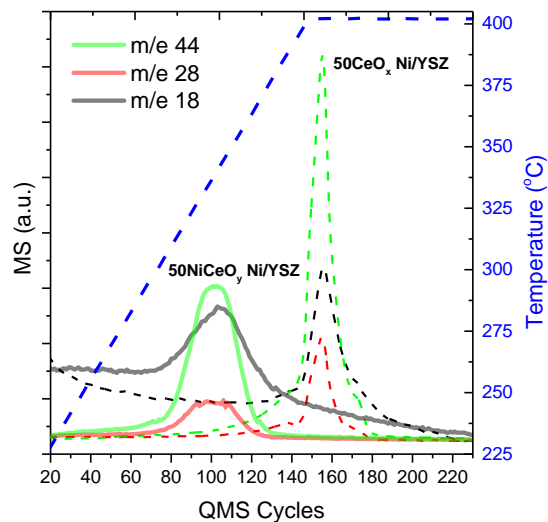
Figure 5.13. Mass spectrum signal of 50NiCeO$_y$ Ni/YSZ and 50CeO$_x$ Ni/YSZ during calcination treatment in O$_2$.
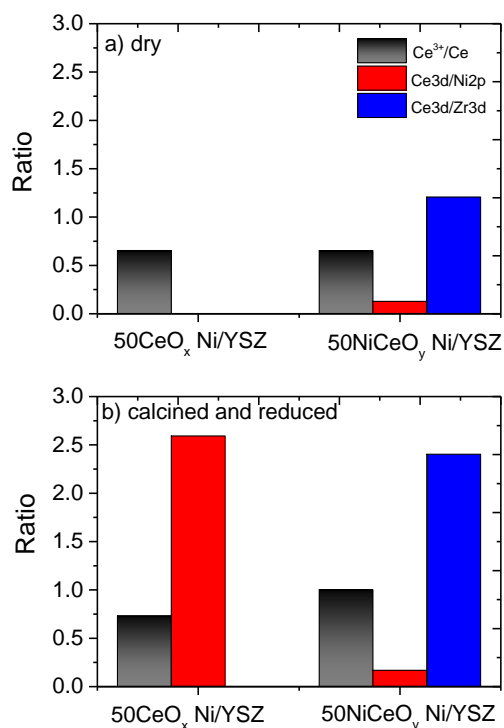
Figure 5.14. The % concentration of Ce^{3+} species, Ce3d/Ni2p and Ce3d/Zr3d ratios of 50NiCeO$_y$ Ni/YSZ and 50CeO$_x$ Ni/YSZ electrodes as derived by the analysis of the XPS spectra shown in figure 5.10. (a) electrode after impregnation and drying at 80 °C in air and (b) electrode after impregnation, drying, calcination at 400 °C and reduction at 550 °C in H$_2$.

The oxidation state of cerium can be estimated by fitting the Ce 3d peak with Ce^{3+} and Ce^{4+} peak profiles of reference oxides [91,95]. As shown in figure 5.10 and quantified in Figure 5.14, after drying, cerium has the same oxidation state in the two samples with around 65% Ce^{3+} and 35% Ce^{4+}. However, after calcinations and reduction ceria in $50NiCeO_y$@Ni/YSZ appear more reduced than $50CeO_x$@Ni/YSZ. Enchantment of ceria reducibility is expected to promote the electrocatalytic performance as shown previously [6,95,131].

c. Vertical distribution of ceria inside Ni/YSZ electrode examined by FIB-SEM/EDS mapping and TOF-SIMS

XPS results and visual inspection gave strong, but indirect, evidences about the higher efficiency of $NiCeO_y$ NPs to infiltrate the pores of Ni/YSZ cermet. To verify that, infiltrated electrodes were analyzed by cross-sectional focused ion beam-scanning electron microscopy (FIB-SEM) combined with energy dispersive X-ray spectroscopy (EDS) elemental mapping. The images shown in Figure 5.15 correspond to two identical Ni/YSZ//YSZ half cells infiltrated with 100 µL $NiCeO_y$ (Figure 5.15a) or CeO_x (Figure 5.15b) NPs (i.e. ceria loading 170 mg/cm^3). In both cases the solution was dropped into pre-reduced Ni/YSZ electrodes, through two times infiltration/co-firing steps (50 µL each time). The porous Ni/YSZ cermet layer, the dense YSZ barrier and the electrolyte can be distinguished in the SEM micrographs. The EDS elemental mapping highlights nickel (*in blue*) and YSZ (*in green*) areas, as well as empty voids (pores) in the cermet. What is of course more interesting here is the distribution of the cerium signal (in red) within the volume of Ni/YSZ. It is clear that in case of $100NiCeO_y$@Ni/YSZ, cerium nanoparticles are evenly dispersed into Ni/YSZ electrode volume. It is remarkable that there is no clear difference in the ceria areas between the inner and outer parts of the electrode. On the contrary, for $100CeO_x$@Ni/YSZ the preferential deposition of ceria on the top of the electrode is evident, although a tiny fraction of ceria particles can be detected in deeper layers (evidently those are related to the smaller NPs aggregates).
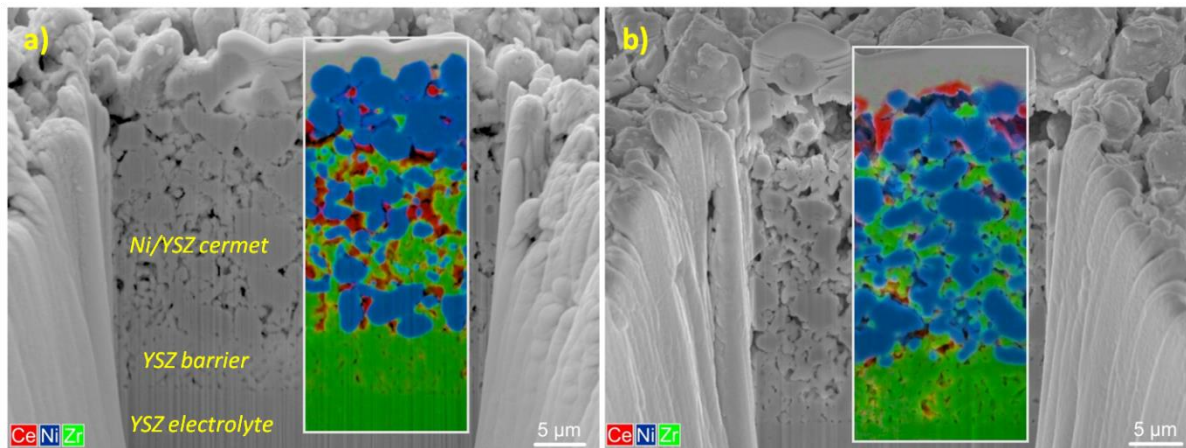
Figure 5.15. Cross-sectional FIB-SEM images and the corresponding EDS elemental mapping of a) 100 NiCeO$_y$@Ni/YSZ and b) 100CeO$_x$@Ni/YSZ after calcination.

TOF-SIMS analysis of 50NiCeO$_y$@Ni/YSZ sample provides useful information about the depth distribution of ceria in Ni/YSZ scaffold. Figure 5.16 shows the evolution of the main electrode elements (nickel, zirconium and cerium) as a function of the sputtering (etching) time. The calibration of the etching depth is estimated from the thickness of each electrode layer (conduction, catalytic and barrier) determined by the SEM cross-section profiles of the Ni/YSZ electrode. The distribution of nickel and zirconium found by TOF-SIMS is consistent with the composition of Ni/YSZ electrode described in the experimental section. In particular, nickel concentration is the highest close to the surface (contact-layer, 90 wt%Ni), becomes less as the analysis proceeds deeper (catalytic-layer, 60 wt% Ni) and drops rapidly when reaching the YSZ barrier (0 wt% Ni). Zirconium concentration follows the reverse depth profile pattern, as anticipated by the electrode composition. Please note that in case of SIMS the exact boundary of each layer is not sharp due to the atomic mixing effect.

The profile of cerium ions related to NiCeO$_y$ NPs inside the electrode volume is of particular interest here. In the near-surface region of the impregnated electrode there is Ce accumulation and Ni and Zr depletion as was indicated also in the XPS spectra of figure 5.10b. However, fast the cerium concentration drops sharply, followed by an equally sharp increase in Ni and Zr ions signal. After that, cerium profile increases gradually in the expense of nickel, and attains a stable concentration when reaching the inner catalytic layer. The cerium signal drops again when the YSZ barrier is reached (but less steep than nickel). This indicates that NiCeO$_y$ NPs penetrate the highly porous 90% Ni conduction layer at the surface and is deposited preferentially into the active
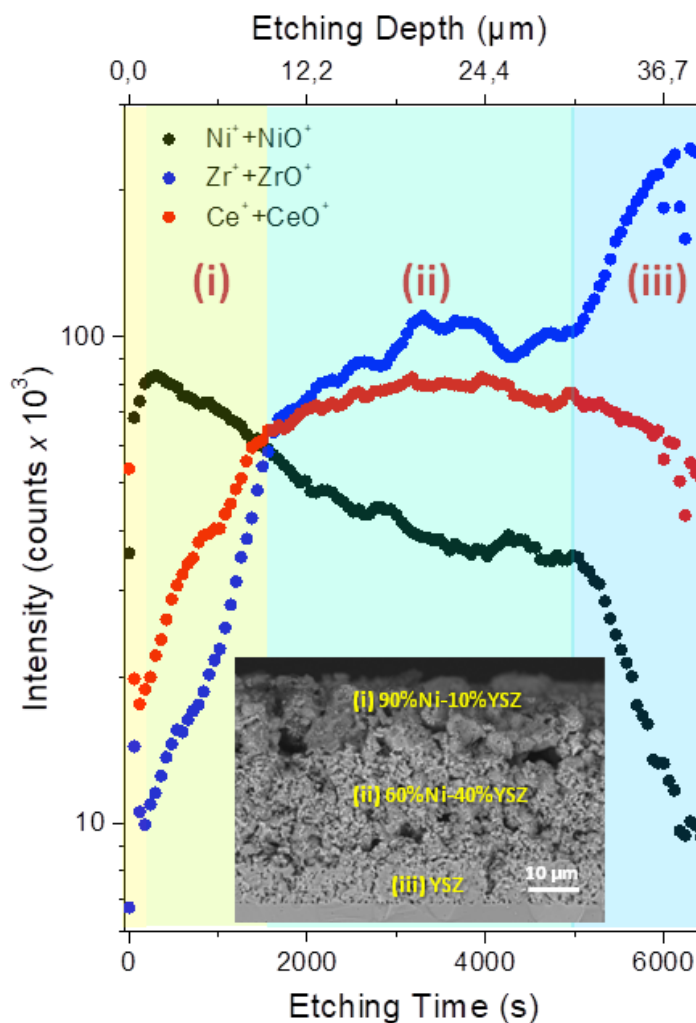
Figure 5.16. TOF-SIMS profiles of 50NiCeO$_y$@Ni/YSZ sample after reduction in H$_2$. The spikes appearing in the Zr signal at high etching times, when the probe has reached the YSZ barrier layer, are probably related to the low conductivity of this layer as compared to Ni/YSZ cermet. A cross sectional SEM image of the electrode is included to visualize the various electrode layers.

catalytic layer just below. The relatively high lateral analysis of TOF-SIMS (40x40 µm^2) not only confirms the FIB-SEM/EDS results but provides a very interesting detail regarding the profile of ceria concentration inside the Ni/YSZ electrode. Namely, it suggests preferential deposition of ceria into the lower catalytic layer, rather than the upper highly-porous conduction electrode layer. The FIB-SEM/EDS and TOF-SIMS results are complementary with XPS and visual inspection observations presented above. All methods converge to a relatively uniform and homogenous distribution of NiCeO$_y$ NPs into the Ni/YSZ pores. It is remarkable that, as shown by TOF-SIMS

profile, just after one infiltration/co-firing step $NiCeO_y$ reach down to the interface of Ni/YSZ electrode with the YSZ electrolyte.

d. The XRD crystallite size of the NPs after deposition

The XRD diffractograms of $100NiCeO_y$@Ni/YSZ and $100CeO_x$@Ni/YSZ electrodes after two infiltration/co-firing steps and subsequent reduction (Figure 5.17) contain the diffraction peaks of Ni, NiO and YSZ of the porous electrode, while lines of ceria NPs are also visible in the pattern (see magnified area inserted in Figure 5.17). The ceria NPs crystallite sizes, calculated based on the XRD patterns (Table 5.3), manifests that CeO_x NPs are bigger than $NiCeO_y$ (9.60 nm instead of 6.81 nm).
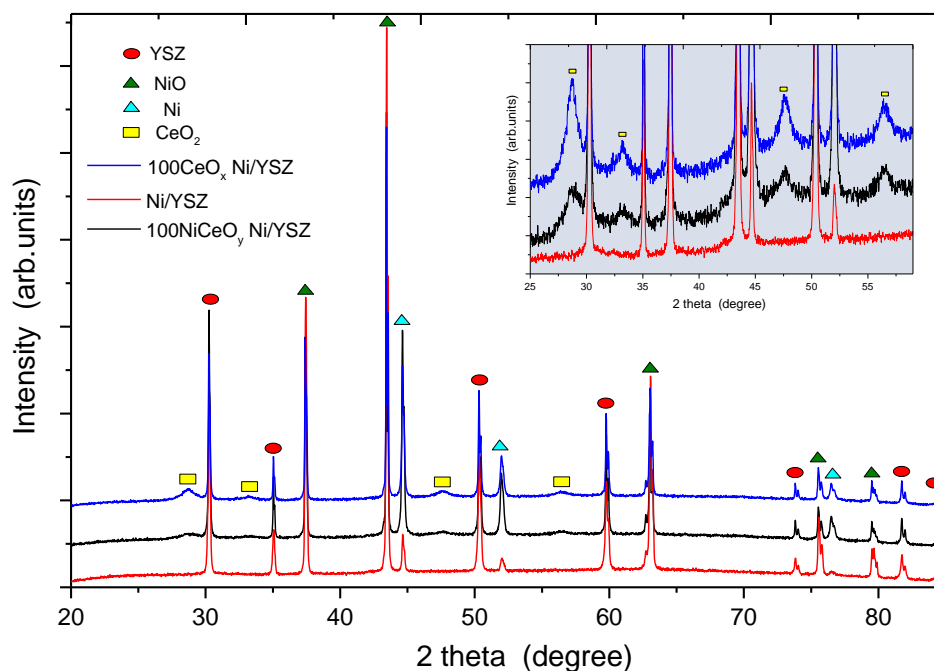
Figure 5.17. XRD patterns of 100 $NiCeO_y$ Ni/YSZ, $100CeO_x$ Ni/YSZ as well as Ni/YSZ after two infiltration/co-firing steps (100 µl $NiCeO_y$ or CeO_x solution was dropped into Ni-YSZ through two times infiltration/co-firing steps, each time for 50µl; Prior to the each infiltration step the electrode was reduced in H_2).

Overall, the above presented results suggest that the better dispersion of the NPs in the solution (i.e. $NiCeO_y$) influences the permeability into the electrode during the infiltration process and promotes the distribution inside the pores of the Ni/YSZ electrode scaffold. On the contrary, solutions containing agglomerated NPs (i.e. CeO_x) will lead eventually to precipitation of the NPs

predominantly on the surface of the electrode which in principle should be avoided. The arrangement of the $NiCeO_y$ and CeO_x NPs in the Ni/YSZ electrode after the infiltration and the subsequent firing step is schematically shown in Figure 5.18.

Table 5.3. Crystallite size results of $NiCeO_y$ and CeO_x NPs measured directly on the 100 $NiCeO_y$ Ni/YSZ and 100 CeO_x Ni/YSZ samples respectively, after two infiltration/co-firing steps.

Sample	Crystallite size (nm)
100CeO_x Ni/YSZ	9.60
100$NiCeO_y$ Ni/YSZ	6.81
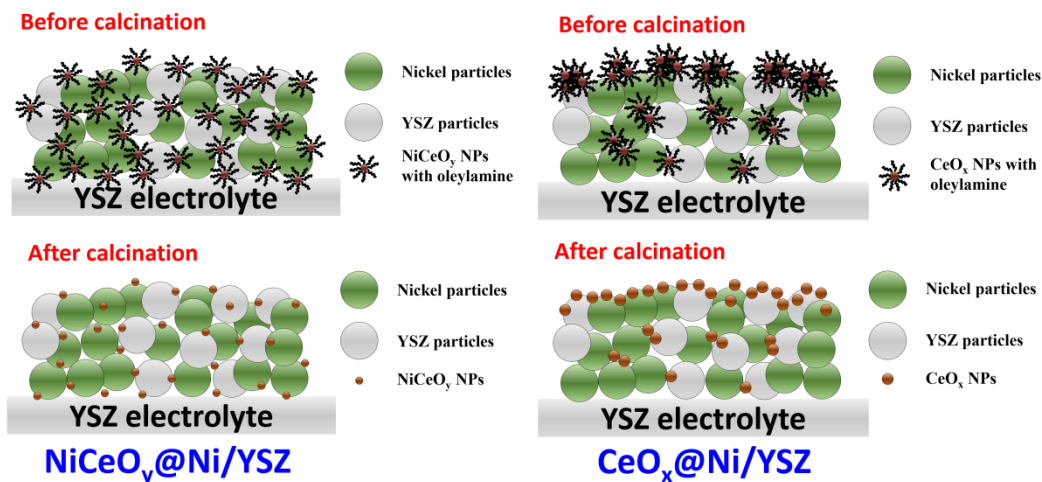
Figure 5.18. Schematic representation of the arrangement of the $NiCeO_y$ and CeO_x NPs over the Ni/YSZ cermet before and after firing step.

5.3.2.2. Optimization of the infiltration process

a. Effect of the number of infiltration/co-firing steps

The above results demonstrated that by the current approach a relatively high loading of the $NiCeO_y$ NPs (around 170 mg/cm^3) can effectively penetrate the pores of a standard Ni/YSZ cermet electrode and reach up to the interface with the electrolyte only after 2 infiltration/co-firing steps. For comparison, literature reports refer to several infiltration steps (>9) to decorate Ni/YSZ with similar loading of gadolinium-doped ceria (CGO) [201,213]. In an eventual scale up of the impregnation process, it is important to reduce the number infiltration/co-firing steps into the
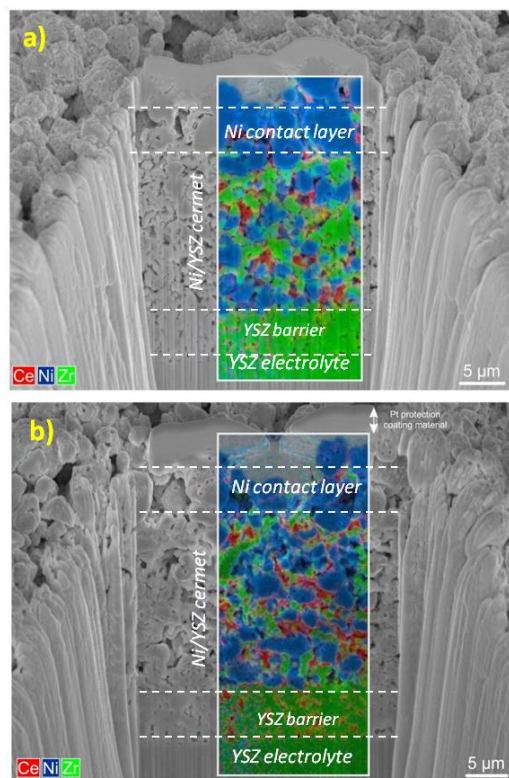
Figure 5.19. Cross-sectional FIB-SEM images and the corresponding EDS elemental mapping of a) 50NiCeO$_y$@Ni/YSZ prepared in 1 infiltration/co-firing step and b) 200NiCeO$_y$@Ni/YSZ prepared in 4 infiltration/co-firing steps (4x50 µl each). After infiltration/co-firing step(s) the samples were reduced in 1 mbar H$_2$ at 550 °C for 30 min. The at.% of Ce as calculated from the EDS was 7.4±0.6 for 50NiCeO$_y$@Ni/YSZ and 12.4±0.6 for 200NiCeO$_y$@Ni/YSZ.

minimum possible. Keeping this in mind we first examine how the distribution of the NiCeO$_y$ NPs into Ni/YSZ is affected by the number of infiltration/co-firing steps. Two Ni/YSZ electrodes were infiltrated with 50 µL and 200 µL NiCeO$_y$ NPs solutions (i.e. 85 and 340 mg/cm^3 loading) following the preparation protocol shown in figure 5.8. This means that 50 µL were impregnated in one step while 200 µL in four steps (4x50 µL each). Figure 5.19 shows the FIB-SEM/EDS images obtained in each case. It is clear that the capacity of the solution to penetrate deep inside the electrode volume is not affected by the solution amount, since in both cases ceria is evenly distributed within the analyzed area. As expected, more cerium is detected in the electrode infiltrated by 200 µL solution as compared to 50 µL. In addition in the former case NiCeO$_y$ NPs can be also distinguished into the YSZ adhesive layer deposited just above the YSZ electrolyte, which is not the case for 50 µL. It is remarkable that despite the four times increase in the amount

of infiltrated solution, there is no evident ceria deposition on the outer surface layers of the electrode. One has to note here that high ceria loadings are not necessarily beneficial for the electrochemical performance, since eventual blocking of the electrode pores will lead to mass transfer problems. However, the results show that the proposed method can be equally efficient for low as well as higher infiltration amounts.

b. Effect of the solution amount in each infiltration step
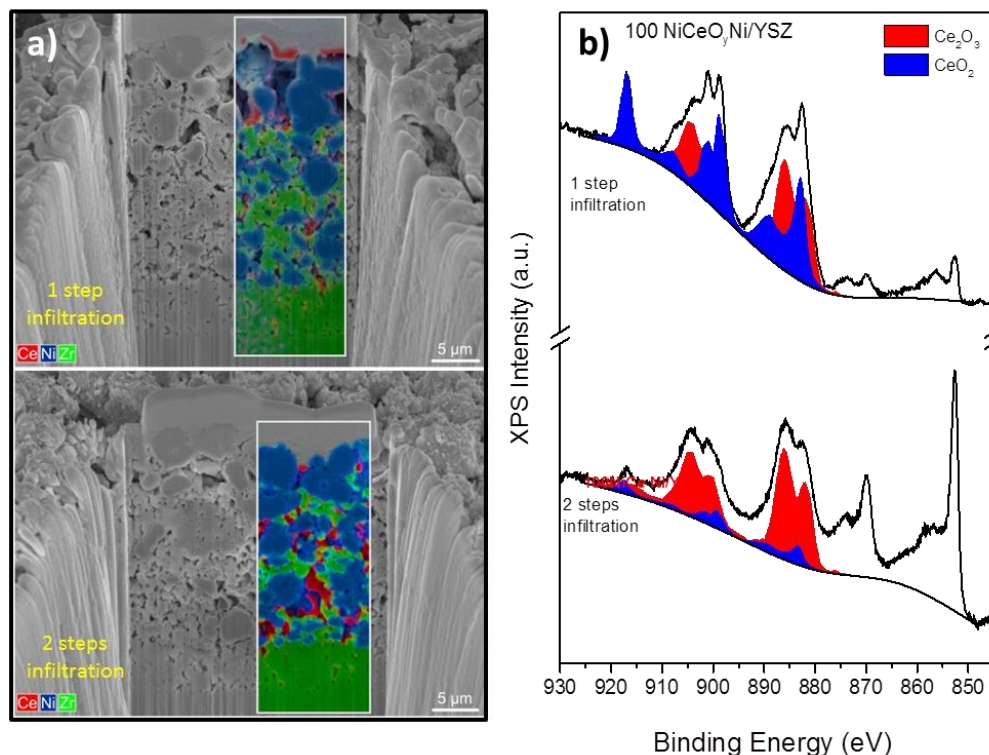
Figure 5.20. a) Cross-sectional FIB-SEM images and the corresponding EDS elemental mapping of 100NiCeO$_y$ Ni/YSZ prepared in 1 (top) and 2 (bottom) infiltration/co-firing step(s) b) Ni 2p and Ce 3d XPS core level spectra of the two electrodes recorded after reduction treatment in 1 mbar H$_2$ for 30 min at 550 ^{o}C via quasi in situ XPS.

We now examine the influence of the solution amount, by infiltrating two Ni/YSZ electrodes with 100 µL NiCeO$_y$ NPs solution following one or two (2x50 µL) steps. In this case apart of FIB-SEM/EDS, we also used *quasi in situ* XPS to investigate potential differences in the chemical state of the electrode in the two cases. As shown in Figure 5.20a in the 1 step process there is significantly more cerium at the top of the electrode, as compared to the 2 steps. This is in line with the XPS results presented in Figure 5.20b, showing that the relative intensity of the Ni 2p

peak decreases in the one step process. This is clear evidence that part of ceria remains on the surface of the Ni/YSZ electrode covering nickel and consequently suppressing the Ni 2p signal.

The precipitation of ceria on the electrode surface in the 1 step process is probably caused due to excess NPs solution which forms a layer on the surface and dries at this spot, rather than penetrating into the pores. The above results indicate that the amount of solution used in the infiltration process is a critical parameter subjected to optimization.

Interestingly, the number of infiltration steps does not only affect the in-depth distribution of $NiCeO_y$ NPs, but also their reducibility after H_2 treatment. According to the deconvolution of the Ce 3d peak shown in Figure 5.20b, relatively more Ce^{3+} is detected in case of 2-steps infiltrated sample, as compared to 1-step. The differences in the reducibility of $NiCeO_y$ NPs in the two processes might be correlated with their dispersion on the support. It is known that under the same reduction condition small ceria nanoparticles are more facile to reduce by H_2 that bulk ceria [11]. Therefore, larger aggregates of $NiCeO_y$ NPs in case of the 1-step infiltrated electrode, might have similar redox behavior with bulk ceria.

5.4. Conclusions

A novel infiltration strategy to surface engineer pre-fabricated Ni/YSZ cermet electrodes is proposed for solid oxide cells (SOC) electrolysis and fuel cell applications. Pure and Ni-doped ceria nanoparticles were prepared in hexane solutions infiltrated into SOC with standard Ni/YSZ cermet electrodes. With the employed infiltration strategy Ni doped-ceria nanoparticles can decorate uniformly the pores of 40 µm thick Ni/YSZ cermet, up to the interface with the YSZ electrolyte, with loading around 85 mg of NPs per cm^3 of Ni/YSZ in a single infiltration/co-firing step. On the contrary, under the same infiltration conditions the distribution of pure ceria NPs inside the electrode is less homogenous. This difference is connected to the dispersion of the NPs in the hexane solution. Ni-doped ceria show also improved surface reducibility, which can be beneficial for the electrocatalytic performance.

This page intentionally left blank

Chapter 6. Investigation of the CO_2 electrolysis reaction over Ni/YSZ cathodes modified by ceria nanoparticles

VI. Chapter 6. Investigation of the CO_2 electrolysis reaction over Ni/YSZ cathodes modified by ceria nanoparticles

6.1. Introduction

Up to date, the most commonly used material for SOCs cathode or anode electrodes, is the nickel yttria-stabilized zirconia composite (Ni/YSZ cermet) due to its low cost, high electron conductivity and thermal compatibility with the other cell components [140,221]. However, Ni/YSZ also exhibits some serious flaws, such as high overpotential losses and relatively poor durability both in single cell and stacks [98]. The degradation of the Ni/YSZ electrode strongly depends on the cell's overpotential, in other words the cathodic polarization [222]. Under strong cathodic polarization (high current densities) the Ni/YSZ interface undergoes various microstructural modifications such as Ni coarsening and migration, destruction of the Ni/YSZ interface, and even formation of ZrO_2 nanoparticles on the Ni surface due to the reduction/re-oxidation of YSZ [213,223,224]. In particular, Ni depletion is considered as the most detrimental factor, which not only causes a reduction in the active triple-phase boundary (TPB) density, decreasing the number of electrochemical active sites, but also leads to the loss of the Ni percolation network, which decreases the electrode conductivity. Therefore, it is necessary to optimize the electrochemical characteristics of traditional Ni/YSZ electrodes.

Currently, the infiltration of electro-catalyst precursor solutions into a conventional Ni/YSZ electrode has shown to be very efficient in improving the electrode performance and durability of SOEC [166,213,225–227]. Several different materials infiltrated to Ni/YSZ electrode include metals, Ce-based oxides, and perovskite-type oxides [166]. Among them, CeO_2-based compounds are recognized as promising additives because they do not react with Ni or YSZ at normal operating conditions of SOEC. Besides, they can create a large amount of TPBs and abundant oxygen vacancies, while they can also moderate deactivation at high operating temperatures.[166,168,201,202,204–206] Several studies have suggested that the addition of ceria over conventional electrode structures enhances the activity of the cell, for example for hydrogen evolution or electrocatalytic CO_2 reduction reaction [109,166,168,201,202,213,226,228,229]. An overview of the previous studies and the method used for the preparation of the cells is given in Table 6.1.

Table 6.1. The list of publications dealing with modification of Ni/YSZ electrodes using CeO_2-based compounds

Infiltration material	Infiltration method	Infiltration steps	Mass loading
$Ce_{0.8}Gd_{0.2}O_{2-x}$[109]	Cerium nitrate $(Ce(NO_3)_3 \cdot 6H_2O)$, gadolinium nitrate $(Gd(NO_3)_3 \cdot 6H_2O)$ dissolved in ethanol; Vacuum process;	Several	9.9 mg of CGO20 per cm^2
Gadolinium-doped ceria (CGO)[201]	Nitrate solution $Ce(NO_3)_3$ and $Gd(NO_3)_3$; Surfactant PEL62; Two-atmosphere reduction (H_2/H_2O);	9 times	~145 mg CGO per 1 cm^3 Ni–YSZ backbone (Ni/YSZ electrode + Ni/YSZ support)
$Ce_{0.8}Gd_{0.2}O_{2-x}$ [166]	$Gd(NO_3)_3 \cdot 6H_2O$ and $Ce(NO_3)_3 \cdot 6H_2O$ in distilled water; Triton X-100 and citric acid as surfactant and chelating agent;	Single-step	0.1 M, 0.5 M, 1 M, 2 M
$Ce_{0.8}Gd_{0.2}O_2$ [202]	CGO nitrate Solution; $Ce(NO_3)_3$, $Gd(NO_3)_3$ and Trix-100 surfactant in a vacuum atmosphere;	5 times	No description
$Ce_{0.8}Gd_{0.2}O_{2-x}$ [213]	CGO $(Ge_{0.8}Gd_{0.2}O_{1.9})$ precursor solution; Ce-nitrate and Gd-nitrate; Surfactant PE-L62;	Several	125 mg CGO per 1 cm^3 Ni/YSZ backbone (Ni/YSZ electrode + Ni/YSZ support)
Gd-doped Ceria (GDC)[226]	GDC nitrate Solution; $Gd(NO_3)_3 \cdot 6H_2O$ and $Ce(NO_3)_3 \cdot 6H_2O$ in distilled water; Triton X-100 and citric acid as surfactant and chelating agent;	Single-step	0.1 M, 0.5 M, 1 M, 2 M
Gd-doped CeO_2 (CGO)[228]	CGO nitrate solution; $Ce(NO_3)_3$ and $Gd(NO_3)_3$; PE-L62 surfactant;	7 times	120 mg CGO per 1 cm^3 Ni/YSZ structure (Ni/YSZ H_2-electrode + Ni/YSZ support)
$Mo_{0.1}Ce_{0.9}O_{2+\delta}$ **(MDC)**[229]	Aqueous solution of $Ce(NO_3)_3 \cdot 6H_2O$ and $(NH_4)_6Mo_7O_{24}$ with citric acid under vacuum;	5, 7 and 9 times	294 mg cm^{-3} after 7 cycles
Gadolinium doped ceria (CGO)[168]	Ce- and Gd-nitrate salts were mixed with water and a surfactant (Triton X-100);	1 time	2 vol-%

To the best of our knowledge the infiltration method proposed in chapter 5 is the sole method that ceria nanoparticles are impregnated via using an organic solvent (hexane) but not aqueous solution. It was shown in the same chapter (chapter 5) that with the proposed infiltration strategy, NiCe NPs can efficiently deposit into the pores of pre-fabricated Ni/YSZ cermet electrodes using maximum 2 infiltration steps. It is therefore reasonable to assume that better distribution of ceria into the pores of the electrode should boost the performance of the cell. To validate this hypothesis, in this chapter the performance of pristine and modified Ni/YSZ electrodes is compared under direct CO_2 and CO_2/H_2 electrolysis conditions. The electrocatalytic results demonstrate that NiCe-modified Ni/YSZ electrodes display superior performance, as compared to pristine and CeO_2 NPs. Furthermore, cells with aged, partially deactivated Ni/YSZ electrodes, can be reactivated after infiltration with NiCe NPs.

6.2. Experimental

6.2.1. Cell fabrication

The same miniature cells (1/4 fragment of a 2 cm diameter button cell), used to study the infiltration process in chapter 5, have been also prepared and used for the electrochemical tests in this chapter. The detailed description of the cells can be found in 5.2.2 section of chapter 5. For the electrochemical tests a Pt counter electrode (anode) was painted symmetrically opposite of the Ni/YSZ cathode electrode using platinum paste (Pt ink 5542-DG, ESL). After painting the Pt electrode, the cells were dried for about 30 min at 100 °C and subsequently fired in air at 980 °C for 10 min (abbreviated as NiO/YSZ//YSZ//Pt). The NiCe Ni/YSZ//YSZ//Pt or CeO_2 Ni/YSZ//YSZ//Pt was prepared by drop-casting of the nanoparticles in hexane solution on the Ni/YSZ cathode side using a 10 µL micropipette. The fabrication process of the NiCe NPs modified Ni/YSZ electrode has been graphically summarized in Figure 5.8 in chapter 5. In this work, 50, 100, 200 µL loading of $Ni_{0.1}Ce_{0.9}O_{2-x}$ containing hexane solution or 100 µL loading of CeO_2 solution was impregnated into the cathode of Ni/YSZ//YSZ//Pt of about 64 mm² area. Please note that before every impregnation step, the cell was pre-reduced in H_2 so that Ni species of NiO/YSZ can be reduced into metallic Ni [218] to facilitate the entry of nanoparticles into the pores of the electrode. NiCe NPs solution was dropped into Ni/YSZ through one to four times infiltration/co-firing step(s), each time for 50µL, hereafter referred as 50, 100, 200 NiCe Ni/YSZ//YSZ//Pt.

6.2.2. Electrocatalytic CO₂ reduction measurements

The electrochemical comparison tests of pristine Ni/YSZ//YSZ//Pt, 100NiCe Ni/YSZ//YSZ//Pt and 100CeO$_2$ Ni/YSZ//YSZ//Pt in direct CO$_2$ and CO$_2$/H$_2$ electrolysis, as well as the electrocatalytic reactivation test of NiCe NPs modified aged Ni/YSZ, were performed in the **flow-through reaction chamber** of the in-house device described in 2.2.2 section of chapter 2. SOEC samples of about 64 mm^2 area were pressed directly on the ceramic heater using stainless steel clamps, while as current collectors in both cathode and anode sides were used gold grids, as shown in Figure 2.5 in chapter 2. The temperature was controlled by a K-type thermocouple mounted on the side of the heater. CO$_2$ electrolysis was tested in the following conditions: i) at 100% CO$_2$ atmosphere (without diluting or reducing gas) in 0.5 mbar, ii) at CO$_2$/H$_2$ atmosphere (96% CO$_2$/4% H$_2$) in 20 mbar at low temperature (550±5°C) (temperature restrictions of the testing setup) and iii) at CO$_2$/H$_2$ (75% CO$_2$/25% H$_2$) in 0.5 mbar at 850°C (in another single reaction chamber able to heat the sample from the rear using an IR-laser [93]). The gas flow into the reaction cell was controlled by mass flow controllers and the products were monitored by a quadrupole mass spectrometer (QMS) connected *online*. Prior to the electrochemical tests, the electrode was calcined for 30 min in 1.0 mbar O$_2$ at 400 °C to remove residual carbon and organic residuals and subsequently underwent reduction in 1.0 mbar H$_2$ at 550 °C for 30 min.

Direct CO$_2$ electrolysis measurements to determine the optimal NiCe NPs loading on Ni/YSZ electrodes as well as the "placebo" experiment with Ni/YSZ impregnated with different hexane loadings (section 6.3.3) were conducted in a **batch laboratory setup**, shown in Figure 2.2 in chapter 2. Please note that the introduction of gases in the batch laboratory set-up was performed in static gas atmosphere with no gases flow (batch mode). The electrochemical cell of about 64 mm^2 area was fixed on the quartz sample holder via two stainless steel clamps and heated from the infra-red lamp, and two gold grids were fixed together as current collectors at both cathode and anode side of the cell, which are connected through the corresponding Au wires to the potentiostat, as shown in Figure 2.2d. The temperature was controlled by a thermocouple mounted on the quartz sample holder. Prior to the electrochemical tests, the electrode was oxidized for 30 min in 5.0 mbar O$_2$ at 400 °C and reduced in 1.0 mbar H$_2$ at 650 °C for 30 min. Therewith, 1 mbar CO$_2$ was introduced into the chamber from a micro gas cylinder containing 100% CO$_2$ through the leak valve for direct CO$_2$ electrolysis at relatively high operation temperature (700±5°C).

Voltages between the working and the counter electrodes and electrochemical impedance spectra (EIS) were applied by using a computer controlled potensiostat/galvanostat (VersaSTAT 3, AMETEK Scientific Instruments). The EIS spectra were recorded in the frequency range of 500 KHz to 0.05 Hz in both galvanostatic and potensiostatic mode. For all electrolysis measurements, the working electrode was grounded and the bias voltage or current was applied between working and counter electrodes. Electrochemical experiments, before and after modification with the ceria-based NPs, were performed at the same button cell. In this way we focus on the influence of surface modification and exclude possible uncertainties due to differences in the bulk cell characteristics.

6.2.3. Benefits and limitations of electrochemical tests on miniature cells

As mentioned above, for the electrochemical tests ¼ fragments of a 1 inch button cell were used (miniature cells). The small size of the cells facilitates both the study of the infiltration procedure as well as the characterization of the cells after infiltrations. Therefore, electrochemical tests over the same miniature cells studied during the preparation, exclude eventual uncertainties caused due to the scale up of the modified cell preparation into 1 inch button cells. Thus, in this thesis one can be reassured that the morphological and chemical characteristic of the cells measured electrochemically, correspond to those obtained by the detailed characterization provided in chapter 5.

Unfortunately due to their small size, miniature-cells could not be evaluated using conventional SOC testing equipment. Therefore, tests were performed in a single chamber reactor attached to the UHV setup, as described in the experimental section. Due to the particularities of the experimental setup and the conditions used for CO_2 electrolysis (low temperature and pressure, low fuel flow, etc.) the obtained current densities measured in this work are lower than those typically reported in conventional button cell tests under different bias voltages. Therefore, the results are always evaluated in comparative basis mainly from the current-voltage (I-V) curves of the cells with pristine and modified Ni/YSZ cathode electrodes under identical reaction conditions. The use of the particular set up for electrochemical tests has also a particular advantage. It allowed surface characterization of electrodes before and after the electrochemical tests. This can help to identify possible surface impurities or carbon deposition which could affect the electrochemical performance and mask the effect of surface modification.

6.3. Results and discussion

6.3.1. Electrocatalytic activity of Ni/YSZ in CO₂ electroreduction before and after infiltration with ceria nanoparticles

    a. Comparison of pristine and NiCe NPs infiltrated cells in direct CO_2 electrolysis

Ni/YSZ//YSZ//Pt and 100NiCe Ni/YSZ//YSZ//Pt miniature cells, prepared with the method described in chapter 5, were evaluated in CO_2 electroreduction conditions. The tests were performed in the mbar pressure range (one of the restrictions of the particular reactor) either in pure CO_2, or in CO_2/H_2 mixtures at two temperatures. Due to the low pressure, the use of balance gas was not necessary. The reactants and the products during electrolysis reaction were monitored *via* online QMS.

The chronoamperometry and EIS measurements of cells with Ni/YSZ and 100NiCe Ni/YSZ electrodes in 0.5 mbar of pure CO_2 at 550ºC are shown in Figure 6.1. Please note that in this particular experiment, the CO_2 electrolysis was initially tested over a Ni/YSZ//YSZ//Pt cell and subsequently the cell was removed from the reactor and impregnated with NiCe NPs solution, before introduced to the reactor and tested again. In this way the comparison of pristine and infiltrated Ni/YSZ cells is straightforward. The current density at each applied potential, shown in figure 6.1a, is significantly improved after infiltration. In particular, the current density over the 100NiCe Ni/YSZ cell increases significantly as compared to the unmodified cell, and this increase becomes more important with the applied voltage. In order to take into account differences in the current evolution as a function of time, in figure 6.1b the results of the current integration over time, or in other words the total electric charge that passes the cell during the electrochemical experiment, are presented. From this graph it is clear that modified cells are up to 5 times more active (total charge or CO_2 electroreduced) as compared to the pristine Ni/YSZ cell.

The gas phase analysis results shown in figure 6.1c, demonstrate considerably higher CO and O_2 production in the modified electrodes, in accordance with the electrical measurements, confirming that the improvement of the performance is due to the higher electrocatalytic activity of the electrode after modification.
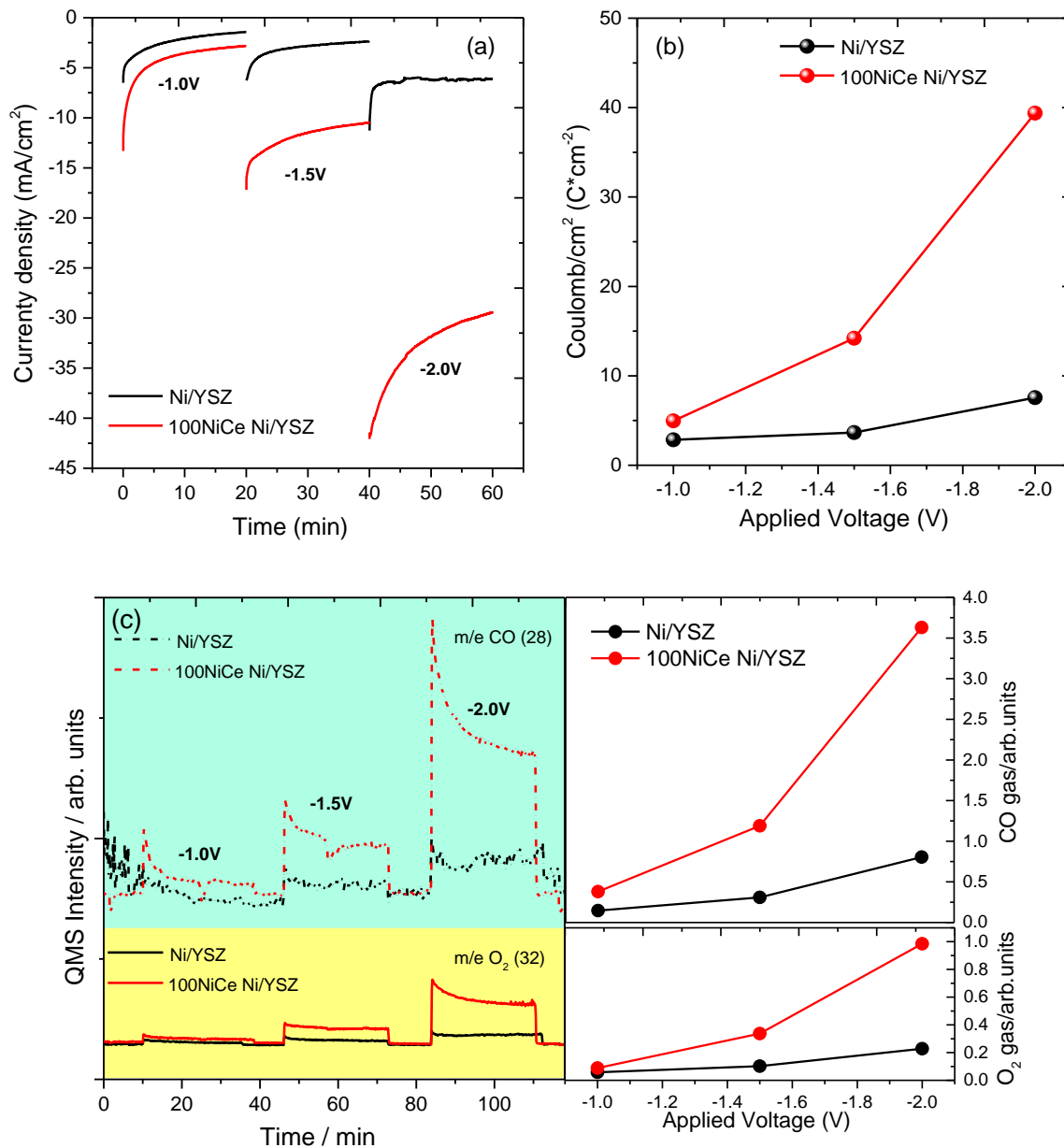
Figure 6.1. (a) Three potential step chronoamperometric measurements as well as corresponding total charge in coulomb **(b)** over Ni/YSZ (black lines) 100NiCe Ni/YSZ (red lines) **c)** The evolution of the CO (m/e 28) and O_2 (m/e 32) gas phase signals recorded by on line QMS in parallel with the chronoamperometric measurements, as well as corresponding integrated O_2 and CO gas QMS signal at each potential. Ni/YSZ (black lines) 100NiCe Ni/YSZ (red lines), Reaction conditions: 0.5 mbar CO_2 at 550 °C.

The Nyquist plots recorded at each applied potential are shown in Figure 6.2a and b. The ohmic resistance R_Ω (real axis value at the high frequency intercept) is related to the conductivity of the

electrolyte and the polarization resistance R_p (diameter of the half circle) is connected with reaction kinetics and external diffusion of CO_2 at the electrode. As seen in Figure 6.2c, where the R_Ω and R_p values are represented, the R_p of the cell decreases significantly after modification with NiCe, indicating an improvement of the reaction kinetics. Similar improvement is also observed in the conductivity of the Ni/YSZ electrode based on the decreased R_Ω values, but the improvement is less important as compared to reaction kinetics.
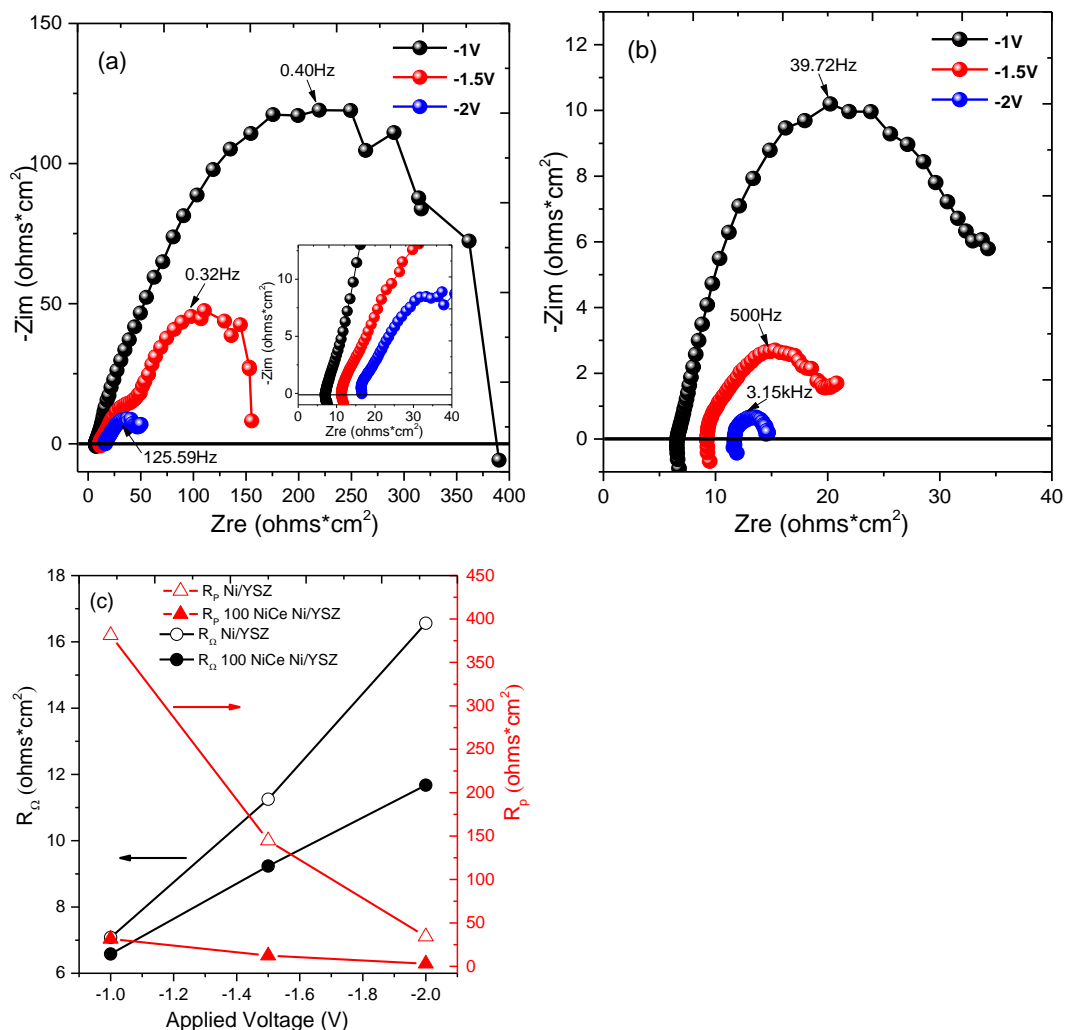
Figure 6.2. EIS of Ni/YSZ (a) and 100NiCe Ni/YSZ (b) under three potential steps in 0.5mbar CO_2 at 550 °C; (c) Ohmic resistance (R_Ω) and polarization resistance (R_p) were calculated based on the impedance spectra of figure 6.2a,b.

b. Comparison of NiCe and CeO₂ NPs infiltrated cells in direct CO₂ electrolysis

We compare now the performance of Ni/YSZ cells modified by CeO_2 nanoparticles (without Ni doping). Since the performance of each pristine Ni/YSZ cell was not always completely identical, and in order to facilitate this comparison, the results are presented as the % increase of the current density in respect to the measurement over pristine Ni/YSZ at the same potential. As shown in Figure 6.3, the NiCe NPs is a far better promoter of Ni/YSZ as compared to CeO_2. The improvement is significant at 1 V and 1.5 V but fades at 2 V where the performance of the two promoters becomes similar.
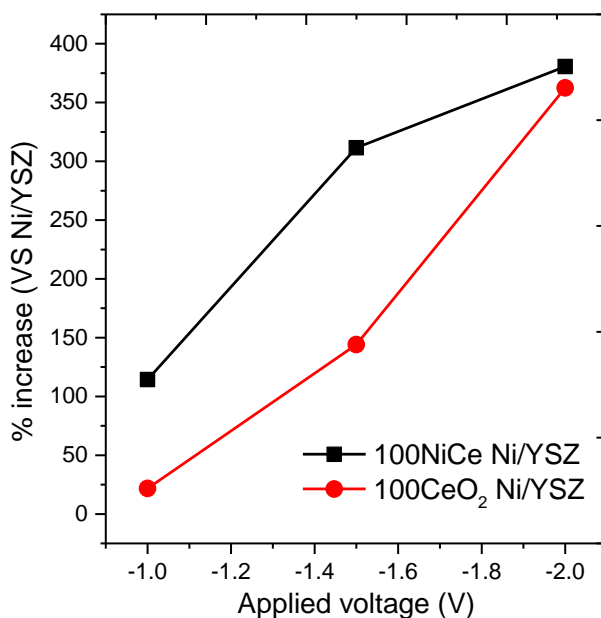
Figure 6.3. % increase of the performance as compared to the parent Ni/YSZ between 100NiCe NPs and 100CeO₂ NPs modified Ni/YSZ//YSZ//Pt based on potentiostatic measurements in 0.5 mbar CO₂ under various applied biases at 550°C.

According to the results discussed in chapter 5, NiCe NPs can uniformly decorate the pores of Ni/YSZ backbone, deep up to the interface with the YSZ electrolyte. On the contrary, CeO_2 nanoparticles remain primarily on the Ni/YSZ surface with limited insertion into its volume. Apart of the infiltration depth, there is another significant difference between undoped and Ni-doped CeO_2 promoter. In particular, the Ni-doping enhances the cerium surface reducibility, as revealed by the Ce 3d spectra shown in Figure 6.4.
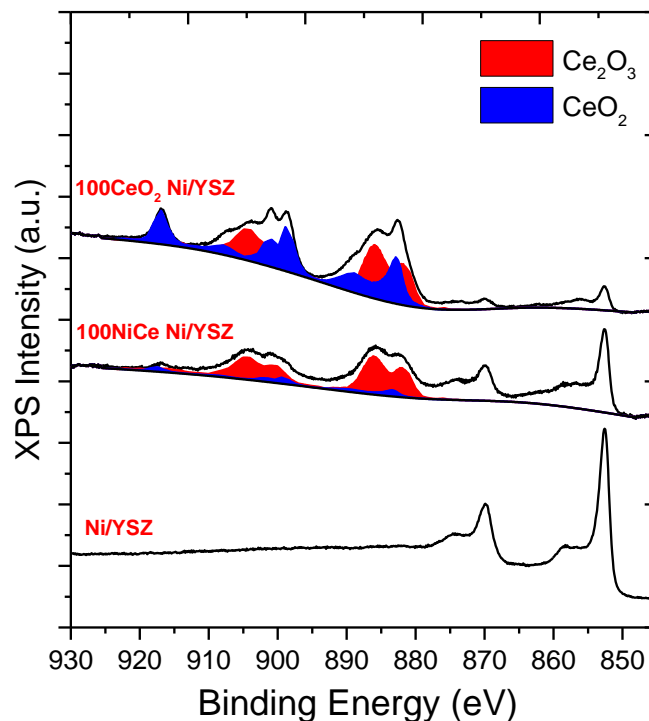
Figure 6.4. Ni 2p Ce 3d XPS core level spectra of Ni/YSZ, 100 NiCe Ni/YSZ, and 100CeO$_2$ Ni/YSZ after reduction treatment in 1 mbar H$_2$ for 30 min at 550°C, prior to the electrochemical tests via quasi in situ XPS equipment (100 NiCe or CeO$_2$, namely 100 µL NiCe or CeO$_2$ solution was dropped into Ni/YSZ through two times infiltration/co-firing step(s), each time for 50µL).

Better distribution into the electrode pores and higher ceria reducibility are sound arguments to justify the improved performance of the NiCe modified cathode. Of course, these two characteristics are related to the creation of additional three-phase boundaries (TPBs) on Ni/YSZ, and also to the abundance of oxygen vacancies.

c. Comparison of NiCe and CeO$_2$ NPs infiltrated cells in CO$_2$/H$_2$ electrolysis

The I-V curves and the electrochemical impedance spectroscopy (EIS) measurements of the parent Ni/YSZ cell as well as of the modified cells impregnated with 100 µL of NiCe and CeO$_2$ are shown in Figure 6.5a. The experiments were performed in 20 mbar 96%CO$_2$-4%H$_2$ mixture at 550 °C. Both ceria modified cells show improved I-V curves as compared to the parent Ni/YSZ, which at the specific conditions can be up to 400 mV lower (or about 30%). Using the EIS results inserted in Figure 6.5a the polarization resistance R$_p$ (diameter of the half circle) decreases in modified electrodes, especially for the NiCe NPs. Lower R$_p$ represents improvement in the reaction kinetics of the electrocatalytic CO$_2$ reduction (e.g. diffusion and conversion of CO$_2$) induced by NiCe and

CeO$_2$ infiltration. The performance of the NiCe modified cell, as demonstrated in the I-V and EIS results, is superior as compared to CeO$_2$ (about 50 mV or 6% lower). However, at the higher current used in the experiment, their performance converges and becomes almost similar, corresponding to the result of Figure 6.3.
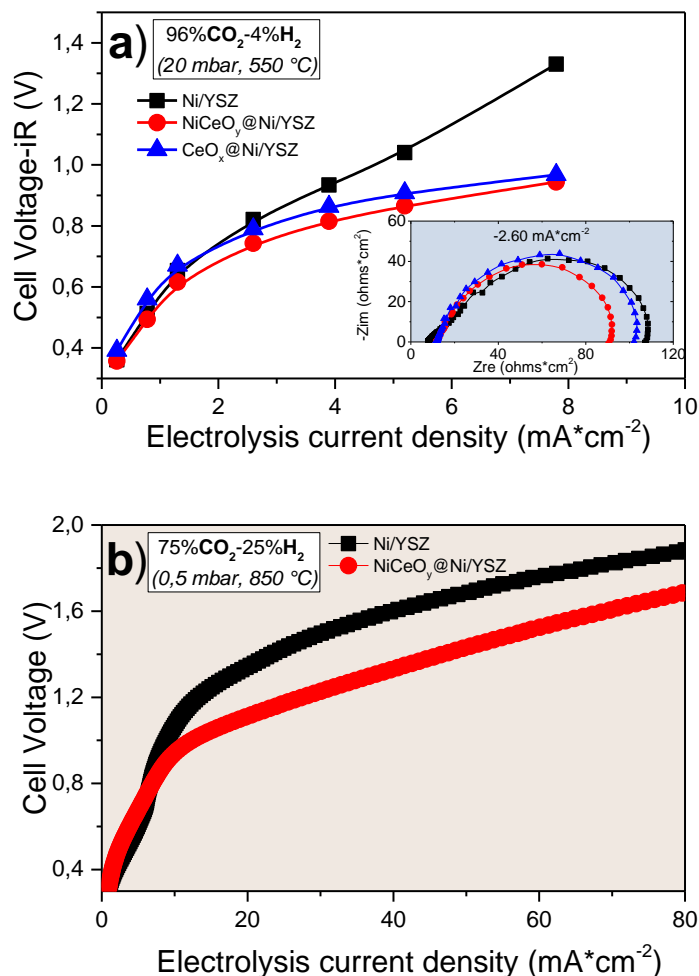
Figure 6.5. (a) Current-Voltage (i-V) curves recorded in single chamber configuration at 550°C in 20 mbar CO$_2$/H$_2$ (96/4) over cells with identical characteristics of Pt counter electrode and YSZ electrolyte but with (■) Ni/YSZ, (▲) 100CeO$_2$ Ni/YSZ and (●) 100NiCe Ni/YSZ cathode electrodes. Inset (a) EIS measurements (Nyquist plots) recorded in galvanostatic mode at -2.6 mA cm^{-2}. The reaction conditions are those in the main part of the figure (b) i-V curves recorded in single chamber configuration at 850°C in 0.5 mbar CO$_2$/H$_2$ (75/25).

The boost of the electrochemical performance of Ni/YSZ after NiCe decoration was also confirmed at higher reaction temperature under slightly different gas mixture and pressure

conditions (see I-V in Figure 6.5b). Two new cells with Ni/YSZ and 100NiCe Ni/YSZ cathodes were examined, using however the same preparation protocol with the I-V measured at 550 °C. As expected, higher operation temperature leads to significantly higher cell currents. For the same current density the NiCe modified electrode can work up to 250 mV lower voltages, or about 15 % improvement.

The quasi in situ XPS analysis of the two electrodes after reaction show only peaks from elements expected on the sample. As shown in the survey spectra of Figure 6.6, no foreign element or impurities are detected after reaction. In addition, the carbon signal is relatively low and similar to all samples, which demonstrates that carbon deposition was not significant in any of the electrodes.
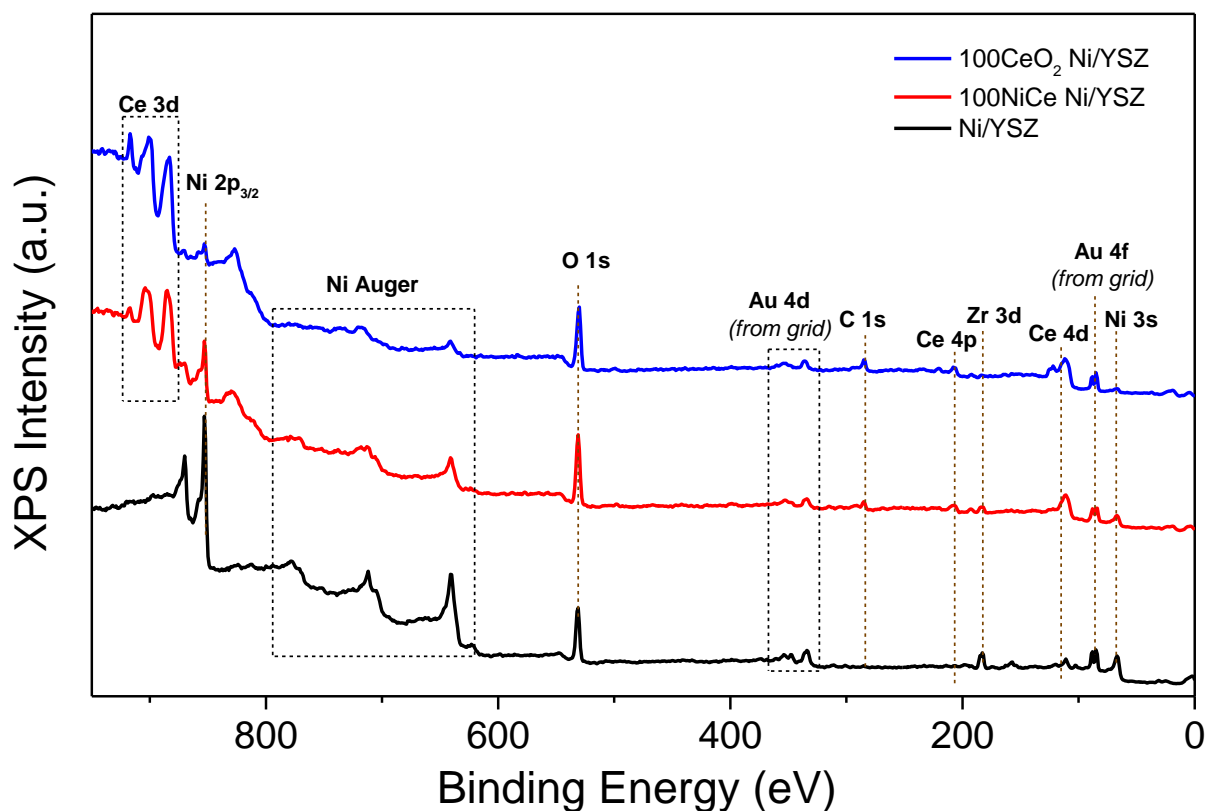
Figure 6.6. XPS survey spectra of 100NiCe Ni/YSZ, 100CeO₂ Ni/YSZ and Ni/YSZ after CO₂/H₂ (96/4) electrochemical tests shown in Figure 6.5a.

6.3.2. Reactivation of aged Ni/YSZ cathodes by infiltration with NiCe NPs

Modifications of the Ni/YSZ electrode microstructure can be induced upon reduction and oxidation (redox) cycles, for example after shut down. The redox cycles can accelerate the degradation of the cell, typically due to the loss of TPBs [16,168]. In particular, in oxidative conditions, the volume expansion of nickel oxide particles, and the consequent shrinkage induced in the following reduction step, will lead to mechanical stress and eventually to microstructural changes such as crack formation or detach between Ni and YSZ particles. These effects are irreversible and result in a permanent cell failure.

In this section we examine the possibility to reactivate degraded Ni/YSZ electrodes, by post-mortem infiltration with NiCe NPs solution. In our tests, in order to accelerate the degradation, the parent Ni/YSZ electrodes were subjected in a set of redox cycles in H_2 and O_2 (1.0 mbar H_2 at 650 °C for 30min each time, 5.0 mbar O_2 at 400 °C for 30min each time, totally five times). Each redox treatment was followed by direct CO_2 electrolysis tests in 0.5 mbar CO_2 at 550°C for 60 min under a constant applied voltage of -2.0 V. Figure 6.7 shows the quasi in situ Ni 2p and Ce 3d XPS spectra obtained from the parent and NiCe modified electrodes after reduction in H_2 and oxidation in O_2. These spectra verify that Ni and ceria are completely reduced in H_2 and oxidized in O_2 for both electrode types.
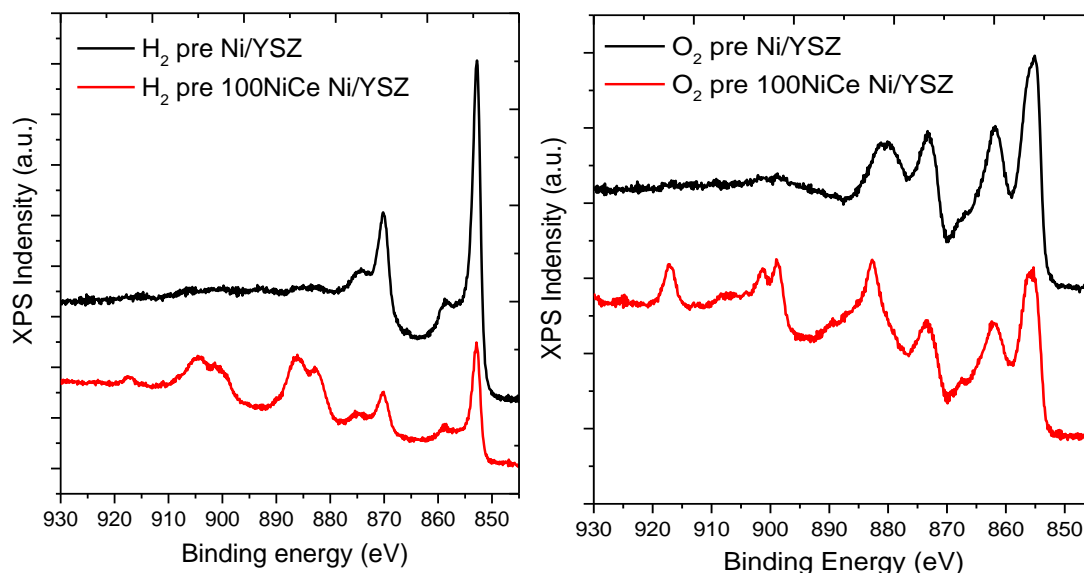
Figure 6.7. Ce 3d and Ni 2p XPS spectra of Ni/YSZ and 100 NiCe Ni/YSZ cathode after H_2 pretreatment or O_2 pretreatment before electrolysis test.

After each pretreatment (reductive or oxidative), the cell was tested in direct CO_2 electrolysis under a constant applied voltage (2 V). The evolution of the cell current as a function of time as well as the corresponding total charge in coulomb are gathered in Figure 6.8 a and b. In case of pristine Ni/YSZ, it is clear that the electrocatalytic CO_2 reduction performance declines constantly after each pretreatment, even if a small improvement after the second reduction and oxidation cycle was observed. Overall, at the end of the 5th redox cycle the current or coulomb quantity at the parent Ni/YSZ electrode declines by around 70% (about 66% for coulomb). In particular, the current density at 2 V drops from 10.22 mA/cm^2 (45.8 C/cm^2) after the first H_2 treatment to 3.05 mA/cm^2 (15.6 C/cm^2) at the third one (Figure 6.8a,b). Similar conclusions can be also drawn by the analysis of the gas phase in the cell shown in Figure 6.8c. According to the analysis of CO and O_2 signal, it is clear that the lower cell currents or coulomb are correlated to lower CO_2 electroreduction rates. The performance of the Ni/YSZ electrode after infiltration with NiCe NPs shows a spectacular improvement. The most striking observation is that the performance does not simply go back to the initial one of Ni/YSZ but becomes almost 3-times better than this of the parent electrode. In particular, after the first H_2 pretreatment, the current density of 100NiCe Ni/YSZ cell increases at around 30 mA/cm^2 (corresponding 142.0 C/cm^2), while at equivalent conditions for Ni/YSZ, it was only 10 mA/cm^2 (45.8 C/cm^2) (figure 6.8a,b). This is followed by a comparable increase also in the CO and O_2 gas phase signals. After 3 redox cycles the cell with the modified Ni/YSZ electrode (100NiCe Ni/YSZ) retains around 63% of its initial current density, and corresponds to 56% of initial coulomb (18.82mA/cm^2 (80.0 C/cm^2) after the third H_2 pretreatment), indicating that the durability of the modified electrode has been obviously improved. The EIS result (Figure 6.8d,e) shows that both the electrode polarization (R_p) as well as the ohmic resistance (R_Ω) over 100NiCe Ni/YSZ cathode dramatically decrease.

Based on the investigation of the morphology and microstructure of modified Ni/YSZ in chapter 5, we know that NiCe nanoparticles can decorate uniformly and discretely inside Ni/YSZ, in electrode areas down to the YSZ electrolyte. Therefore, we argue that ceria nanoparticles probably repair the microstructure of the deactivated electrode by filling in the cracks between the particles previously formed during the redox pretreatment [218,230]. This has a direct effect in increasing electron and ion percolation pathways between nickel and YSZ particles. Of course obviously, the introduction of ceria nanoparticles not only "repairs" the microstructure defects induced by the

redox cycles, but also introduces new active TPB which increase the cell current density up to 3 times as shown above.
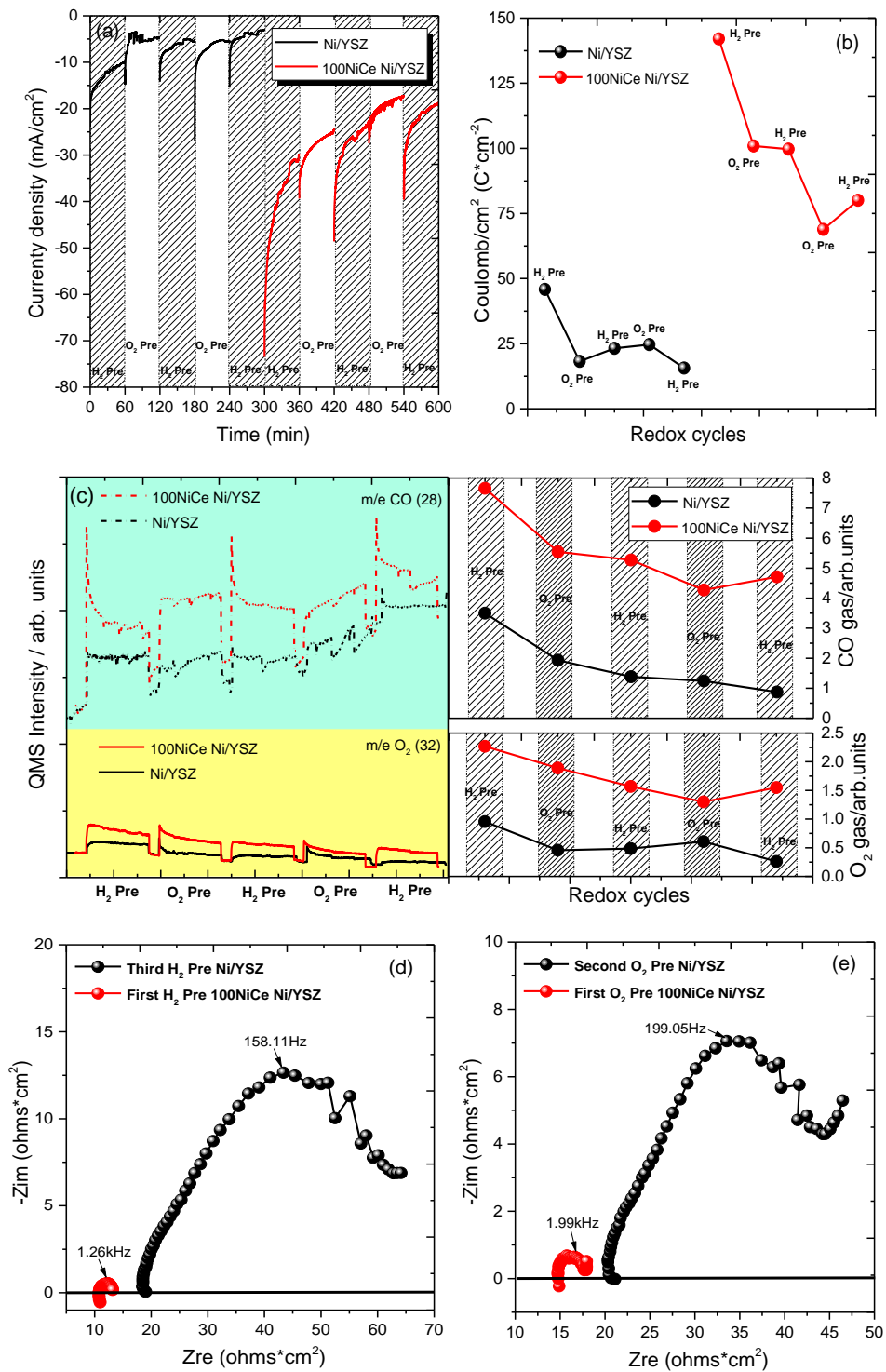
Figure. 6.8. Chronoamperometric measurements (a) as well as corresponding total charge in coulomb (b) over Ni/YSZ (black lines) and 100NiCe Ni/YSZ (red lines) in 0.5mbar CO₂ at several

redox pretreatment cycles and operation temperature of 550°C under a constant applied voltage of -2.0 V; (c) The evolution of the CO (m/e 28) and O_2 (m/e 32) gas phase signals recorded by on line QMS in parallel with the chronoamperometric measurements, and the corresponding integrated O_2 gas QMS signal and integrated CO gas QMS signal at each redox pretreatment cycle; EIS of the Ni/YSZ cell and 100NiCe Ni/YSZ cell after H_2 pretreatment (d) and O_2 pretreatment (e) (each EIS measurement was conducted after potentiostatic measurement for 1h);

Overall, introduction of cerium nanoparticles through the novel impregnation strategy in this study can not only obviously improve the electrocatalytic performance of CO_2 reduction reaction, but also effectively restores and even improves the performance of cells with deactivated Ni/YSZ electrodes.

6.3.3. Optimization of NiCe NPs loading of the modified Ni/YSZ cathodes

The sections discussed above demonstrated that impregnation with Ni-doped ceria nanoparticles significantly promotes the polarization property of the modified Ni/YSZ electrode as compared to both the conventional (parent) unmodified cell and the one infiltrated with undoped ceria NPs. In addition, introduction of cerium nanoparticles into the Ni/YSZ electrodes not only recovers but significantly improves the reactivity of aged Ni/YSZ electrodes. In the next section, we discuss the effect of the NiCe NPs loading on the electrochemical performance of cells with modified Ni/YSZ cathodes.

6.3.3.1 Irreversible passivation experiment of Ni/YSZ electrode

In order to evaluate the effect of the solution and the following calcination procedure and confirm that the improvement of the performance is due to the deposition of the NiCe NPs in the pores of the electrode, we performed the following experiment. The Ni/YSZ electrode was impregnated in pure hexane (which does not contain any NiCe NPs) using increasingly higher loading of hexane. After each impregnation with hexane the electrochemical performance of the cell was compared under identical pure CO_2 electrolysis conditions. Henceforth, we call this experiment "placebo" experiment, since it follows exactly the same procedure with electrochemical tests of infiltrated electrodes, but without the presence of NiCe NPs.

The experimental procedure involves impregnation of the same Ni/YSZ//YSZ//Pt electrode with 50, 100, 150, 200 μL of pure hexane solvent. The effective area of the electrode was about 64 mm², the typical one in this thesis. After each impregnation step, the electrode was subjected to

oxidation-reduction pre-treatments in order to maintain consistent experimental conditions with the electrolysis measurements over NiCe NPs impregnated electrodes. After each hexane loading, I-V and EIS measurements were performed under 1.0 mbar CO$_2$ and 700 °C in the batch laboratory setup shown in Figure 2.2 in chapter 2. Figure 6.9 presents the I-V curves of a Ni/YSZ electrode which was impregnated 4 times with 4 different amounts of pure hexane and subsequently tested in CO$_2$ electrolysis conditions. It is evident that the hexane solution, and the calcination/reduction treatments that follow it, degrade the performance of the cell in a gradual, almost linear manner. For example, at the maximum applied voltage, the current drops almost to the half after the 4th infiltration process.

The placebo experiment clearly showed what was already expected. Namely, calcination and reduction of the electrode accelerates the aging procedures and lead to partial deactivation. However, in this thesis this experiment can be used to exclude the possibility that other factors related to the infiltration process, for example modification of the electrode surface upon the calcinations to remove the residuals of the solution, can favour the electrocatalytic performance. It is therefore NiCe nanoparticles deposited into the pores, that are accountable for the improved electrochemical performance.
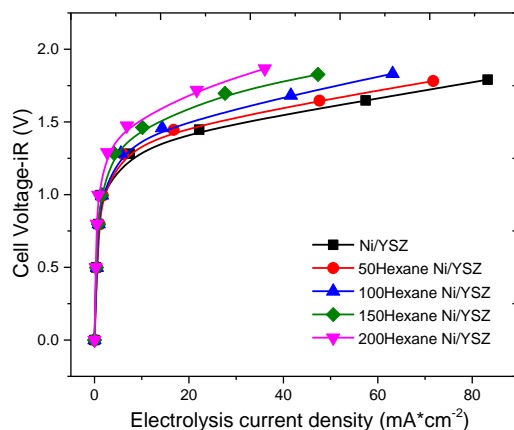
Figure 6.9. I-V curves measured over Ni/YSZ electrode and 50Hexane Ni/YSZ, 100Hexane Ni/YSZ, 150Hexane Ni/YSZ, 200Hexane Ni/YSZ impregnated electrodes under 1.0mbar CO$_2$ electrolysis conditions at 700°C. Please note that different loadings of hexane solution were impregnated on the same Ni/YSZ electrode. In this case the cell voltage was corrected by the iR drop. The R used to calculate the iR was measured by the R$_\Omega$ value found by the Nyquist plots.

The EIS results presented in Figure 6.10 and 6.11 show that both the ohmic and polarization resistances increase due to the hexane infiltration. This just confirms the "aging" of the Ni/YSZ electrode due to the infiltration and the following calcination/reduction treatments that modify the microstructure of the electrode in an unfavorable way for its electrocatalytic performance.
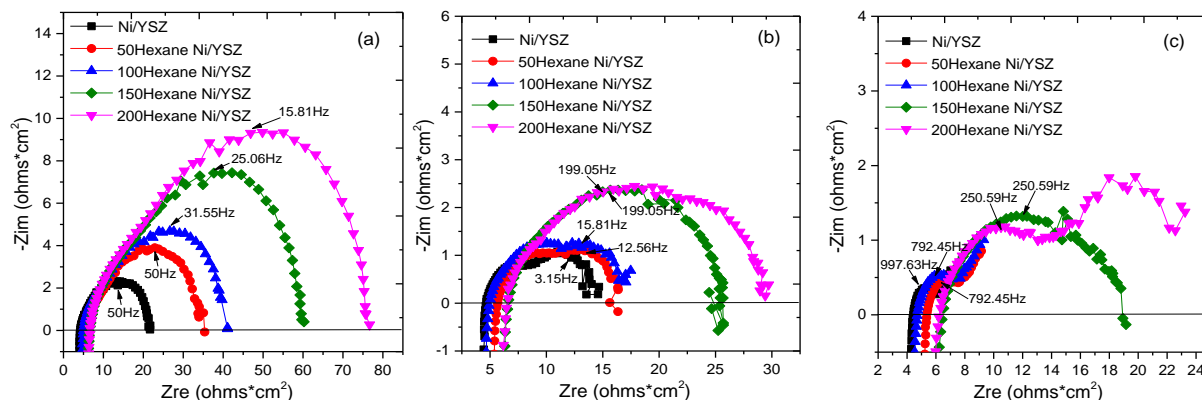
Figure 6.10. Impedance spectra presented in Nyquist form, obtained under constant applied voltage of a) -1.5V, b) -1.8V, and c) -2.0V at 700°C in 1.0 mbar CO_2 over Ni/YSZ cathodes before (black) and after promotion with four different loadings of hexane. Please note that different loadings of hexane solution were impregnated on the same Ni/YSZ electrode.
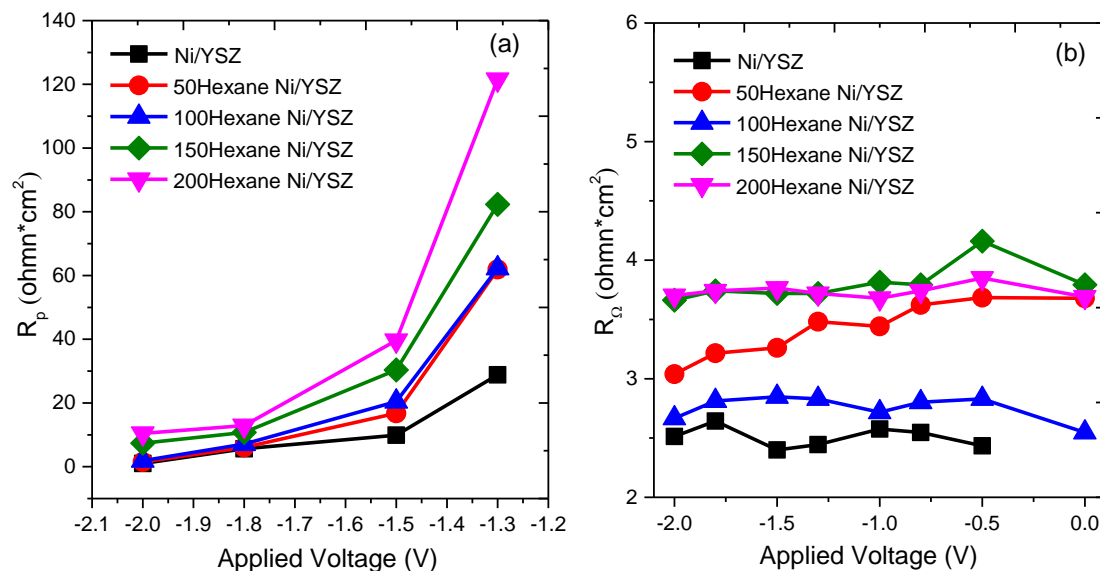
Figure 6.11. a) Polarization resistance (R_p) and b) Ohmic resistance (R_Ω) calculated based on the impedance spectra of figure 6.10. Please note that different loadings of hexane solution were impregnated on the same Ni/YSZ electrode.

6.3.3.2 The effect of NiCe NPs loading in the electrochemical performance of Ni/YSZ electrode

The results of the above "placebo" experiment have shown that the infiltration procedure itself degrades the electrode performance. Therefore, the method proposed in this thesis, which requires a minimum number of infiltration steps to achieve high catalysts loadings, has an additional advantage as compared to multi-step methods typically followed in impregnation with aqueous precursor solutions.

In order to examine the influence of NiCe NPs loading and identify the optimal for CO_2 electrolysis, the Ni/YSZ electrodes were modified using increasingly higher loading of NiCe NPs at the same condition with the sample discussed in paragraph 6.3.3.1. Here, 50, 100, 200 µL of the NiCe NPs in hexane solution were impregnated into an aged Ni/YSZ//YSZ//Pt electrode with effective area of about 64 mm^2. According to the quantification of the NPs concentration in the solution discussed in chapter 5, this corresponds to 85, 170, and 340 mg ceria NPs loading per cm^3 of Ni/YSZ electrode, respectively. The I-V curves presented in Figure 6.12 are in agreement with all the previously presented electrochemical results: promotion with NiCe NPs considerably improves the performance of aged Ni/YSZ electrodes. The interesting point here is that infiltration with 50 µL NiCe NPs (or 85 mg NiCe per cm^3 of Ni/YSZ) significantly improves the cell current density for pure CO_2 electrolysis, while increasing the NiCe NPs loading to the double (100 µL) only produces a slight increase in the current density. At higher NPs loading (200 µL) the cell performance deteriorates, however it remains always better than that of the unmodified electrode. The EIS recorded at 1.5 V, 1.8 V, and 2.0 V reveal that the observed differences between the Ni/YSZ electrode before and after NiCe NPs impregnation is correlated with both R_Ω and R_p contributions, as shown in Figure 6.13. The corrosponding ohmic (R_Ω) and polarization (R_p) resistances, calculated based on impedance spectra, are shown in Figure 6.14. The polarization resistance (figure 6.14a) decreases after addition of NiCe NPs as compared to the parent Ni/YSZ. However, in accordance with the I-V curves, the R_p increases when the loading is higher than 100 µL. Similarly, the R_Ω (see Figure 6.14b) of 50NiCe Ni/YSZ and 100NiCe Ni/YSZ decreases as compared to Ni/YSZ, but for 200NiCe Ni/YSZ the R_Ω deteriorates and becomes higher than Ni/YSZ. This result explains that the electrode conductivity, and not the kinetics of the reaction, is the main limiting factor at high NiCe loadings.
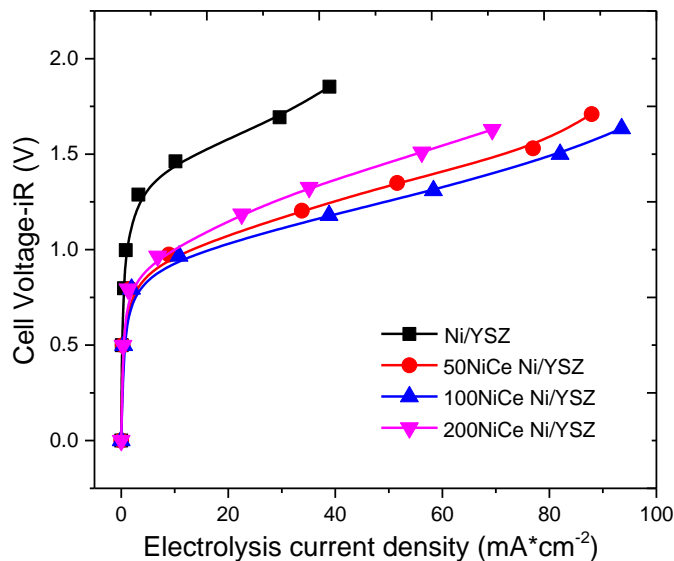
Figure 6.12. I-V curves measured over Ni/YSZ electrode and 50NiCe Ni/YSZ, 100NiCe Ni/YSZ, 200NiCe Ni/YSZ impregnated electrodes under 1.0mbar CO_2 electrolysis conditions at 700°C. Please note that different loadings of NiCe NPs solution were impregnated on the same Ni/YSZ electrode.
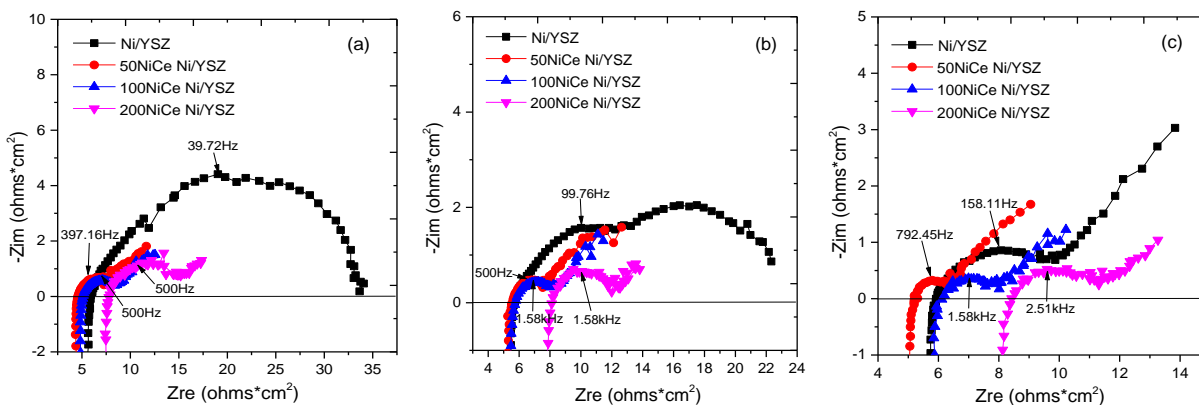
Figure 6.13. Impedance spectra presented in Nyquist form, obtained under constant applied voltage of a) -1.5V, b) -1.8V, and c) -2.0V at 700°C in 1.0 mbar CO_2 over Ni/YSZ cathodes before (black) and after promotion with four different loadings of NiCe NPs. Please note that different loadings of NiCe NPs solution were impregnated on the same Ni/YSZ electrode.
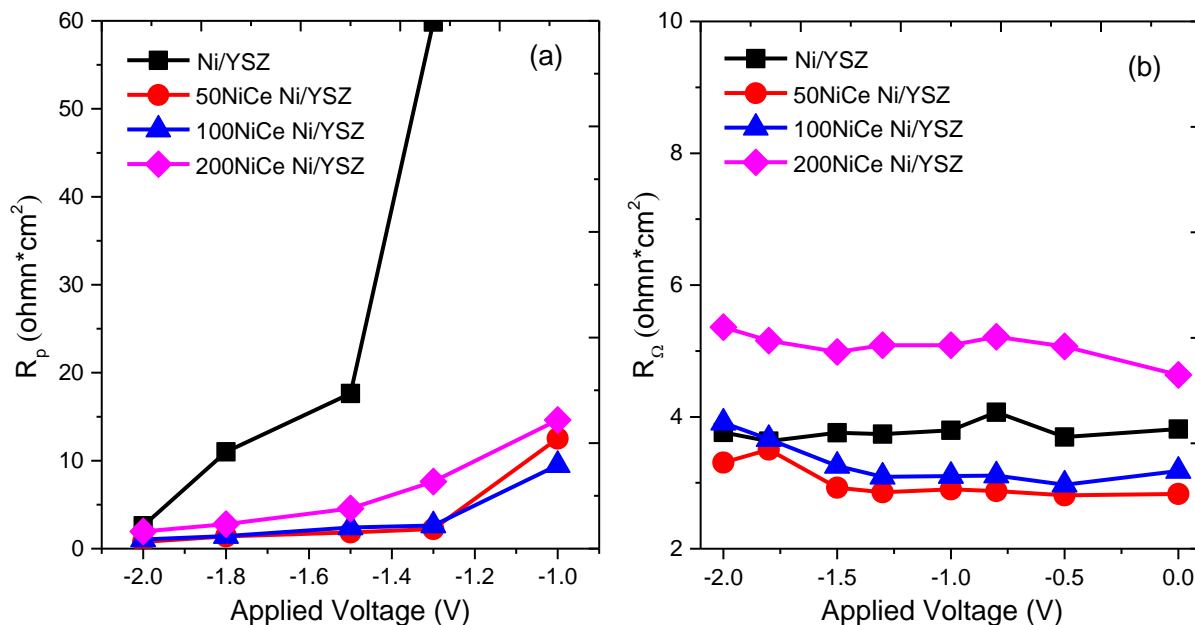
Figure 6.14. a) Polarization resistance (R_p) and b) Ohmic resistance (R_Ω) calculated based on the impedance spectra of figure 6.13. Please note that different loadings of NiCe NPs solution were impregnated on the same Ni/YSZ electrode.

Taking into account that the improvement in case of 100 µL is marginal as compared to 50 µL, it is suggested that the optimal NiCe loading is 85 mg ceria NPs loading per cm^3 of Ni/YSZ electrode. In the concentration of the solution used in all experiments of this thesis, this corresponds to 50 µL NiCe NPs solution which is suggested as the optimal loading at least for pure CO_2 electrolysis. This result is extremely interesting for practical applications, since as it was shown in chapter 5, this loading can be achieved in a single infiltration/co-firing step. In terms of very high loadings, the decrease in the performance can be attributed to two possibilities. One probable reason is that superabundant nanoparticles accumulate into the electrode pores, limiting gases' diffusion, as suggested by the increase of the Rp shown above. Another reason is the higher ohmic resistance of the electrode, which should be mainly due to the contact problems of the electrode with the current collectors. Please note that the electronic conductivity of NiCe NPs is very low, as was found previously by 4 point probe conductivity measurements (data are not included in this thesis).

6.4. Conclusions

In this chapter, we mainly focus on the effect of NiCe NPs in the electrochemical performance of Ni/YSZ for CO$_2$ electroreduction. Although all the experiments were performed using *unconventional* conditions (low pressure, single chamber etc.), as compared to the classical button cell tests, the promoting effect of NiCe NPs in the reaction was verified in comparative basis with the parent/unmodified Ni/YSZ electrode. It was shown that the use of NPs can be equally effective in direct and with reducing gas CO$_2$ electrolysis mixtures, as well as at low and regular electrolysis temperatures. In addition, the results demonstrated that introduction of doped cerium nanoparticles through the novel impregnation strategy not only promotes the electrocatalytic performance for CO$_2$ electrolysis, but can be also used as a method to re-activate aged Ni/YSZ electrodes.

This page intentionally left blank

Chapter 7. General conclusions and perspectives

7.1. Summary and general conclusions of the thesis

The objective of this thesis was to investigate the surface chemistry of Ni/GDC and Ni/YSZ electrodes under SOEC feed gases, and in particular the effect of the electrode surface state in the electrocatalytic performance. To this aim, we studied half cells using state of the art commercial cermet electrodes with standard multilayer configuration (buffer, catalytic and conduction layers), fabricated by classical preparation methods (screen printing). The approach to use functional materials and not to build model samples, is already an innovation in respect to the majority of the studies seeking to understand fundamental physicochemical characteristics of electrochemical devices. On the downside, the complexity of a "real" cell is considerably higher than a model system, which requires characterizing multiple aspects of the materials, starting from its morphological characteristics and going up to the electrochemical performance. Therefore, in this thesis, results of several experimental techniques, some of them performed by collaborating groups, are reported.

If I would like to distinguish one method that contributed the most in the achievements of this thesis, I would choose near-ambient pressure photoelectron spectroscopy (NAP-XPS). The unique characteristics of this method, which allows retrieving chemical and compositional information from the surface of the electrodes in reactive gas atmospheres and under working conditions, was indispensable for the purposes of this thesis. However, this work is not confined just to the description of the surface effects and their role in the electrochemical reactivity of the Ni-based cermet electrodes. It goes one step further, and based on the key role of reduced Ce^{3+} species identified in the Ni-GDC electrodes, proposed and evaluated a rational strategy to develop more robust and active solid oxide electrode for SOC applications. The obtained results of these tests, although I have to admit far for being complete, are very encouraging. They demonstrate that there is a lot of space for improvement of the current SOC technology, without necessarily seeking radically new, and therefore low **TRL** (Technology Readiness Level), electrode materials.

The initial inspiration of this thesis, as explained in chapter 1, was the fact that although Ni/YSZ and Ni/GDC are the state-of-the-art (SoA) cathode electrodes for SOEC applications at present, they are still facing severe degradation and issues related to low activation/conversion efficiencies. The irreversible degradation is mainly related to the mechanical stability of the SOEC devices (cracks, detachment of the electrode layer, adsorbed contaminants, etc.), and it is relatively well understood, since all these effects can be easily demonstrated by post-mortem analysis of the

SOEC devices. However, there is a general consensus that degradation can be also reversible and in some cases the performance can be retrieved back, for example when the operation conditions are modified. The effects that contribute to reversible degradation, especially electrode oxidation, are much more challenging to study because they are dynamic and depend very much on the operational conditions.

In chapter 2, there is a general introduction to the fabrication of standard half cells, including both Ni/YSZ and Ni/GDC. In addition, in the same chapter the description of the laboratory-based setups and the in-situ near-ambient pressure spectroscopy (NAP-XPS) setup are included. Furthermore, details are given about the XPS data processing method, the electrochemical testing techniques, as well as of the standard characterization used in this thesis.

Chapter 3 describes the oxidation of Ni-YSZ and Ni-GDC cermet electrodes by CO_2 and H_2O at conditions relevant to solid oxide electrolysis cells operation [231]. For this study, *in situ* NAP-XPS and other methods (e.g. microscopy) were used. The results (Figure 7.1) show that the degree of nickel oxidation by CO_2 and H_2O is regulated by the presence (*or not*) of ceria in the cermet. In particular, ceria promotes nickel oxidation by H_2O but moderates it in CO_2. This was a rather surprising and unexpected result, since in literature, the two gases are considered as oxidants for the electrode, but it was never reported that the presence of ceria can reverse the extent of nickel oxidation.
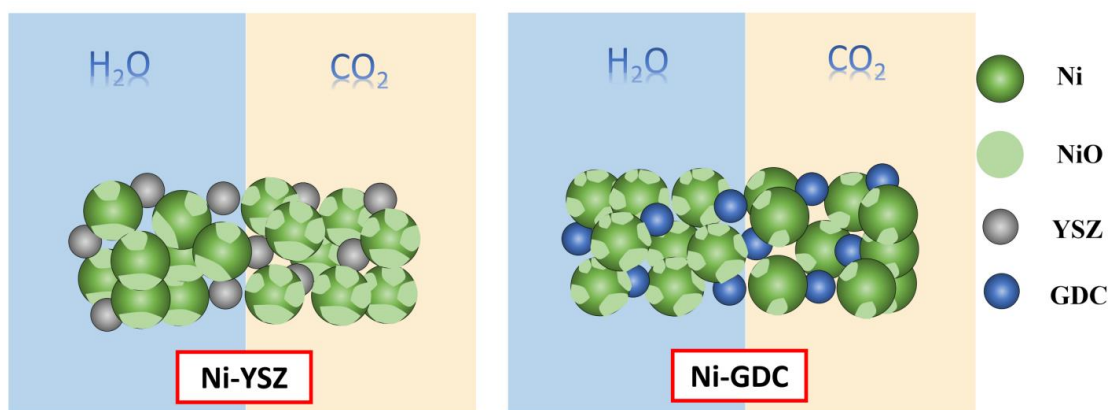
Figure 7.1. A schematic representation of the proposed oxidation scenario in case of the two cermets for each gas environment.

Subsequently, in the next chapter (chapter 4), we combined *operando* NAP-XPS with *online* gas phase analysis as well as electrical measurements over cells with porous Ni/GDC cathodes, to

research how nickel and ceria oxidation states affect to the CO_2 electrolysis performance [190]. Here we employed pure CO_2 (namely, not mixed with a reductant gas), as well as operational conditions bellow the carbon deposition threshold, to focus on the surface oxidation state of the electrode and lift complications related to modifications due to irreversible carbon deposition. The results show that the functional Ni/GDC surface consists of metallic nickel and partially reduced ceria. Activation of the pure CO_2 electrolysis reaction is correlated to electro-reduction of NiO to Ni at relatively low CO_2 electrolysis potentials. Partially reduced nickel particles are organized in a core-shell structure, with metallic nickel in the shell and NiO underneath. The formation of a nanometer-thick surface Ni layer is adequate to activate and maintain CO_2 electrolysis. During pure CO_2 electrolysis, the GDC acts as a source or sink of mobile oxygen ions, while it seems that high population of reduced Ce^{3+} species promotes the CO_2 electrolysis reaction. Besides, the results also confirm that pure CO_2 electrolysis over Ni/GDC cathode is feasible, providing that an optimal electrode surface state can be maintained. As described in chapter 4, this "optimal state" is composed of nickel particles in a core/shell type morphology with NiO in the core and metallic Ni on their surface, in contact with reduced Ce^{3+} species, as shown in Figure 7.2.
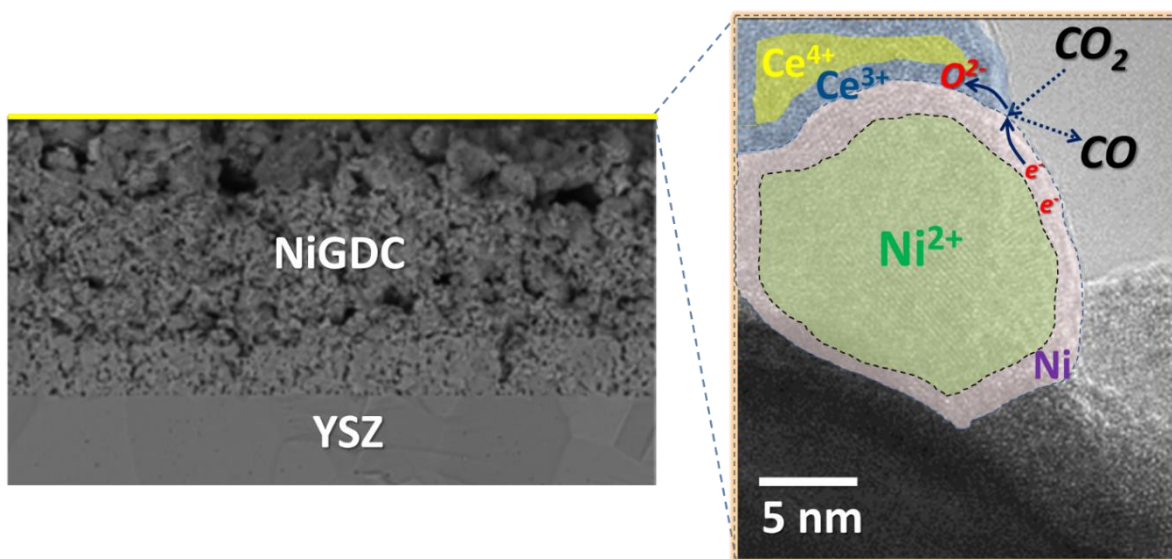
Figure 7.2. Schematic of the proposed optimal surface state of the Ni/GDC cathode for pure CO_2 electrolysis.

Based on the insights obtained in chapters 3 and 4, the concept of how to produce more active cermet electrodes, particularly for direct CO_2 conversion, was conceived. In principle, the

proposed design should work efficiently in the case that the electrochemical devices work in direct CO_2 electrolysis conditions, in other words without reductive gas in the feed. To realize this concept, standard Ni/YSZ electrodes in half cell configuration were used. These cells were modified via infiltration of ceria nanoparticles directly on their surface. The advantage of coating the surface of Ni/YSZ with ceria, instead of using directly Ni/GDC electrodes, is based on previous knowledge regarding the performance of the two cermet electrodes. In particular, Ni/GDC is potentially more stable than Ni-YSZ for CO_2 electrolysis, since it can tolerate better oxidizing conditions that occur in the event of leakage or during shutdown periods. In addition, in practical CO_2 electrolysis applications, Ni/GDC usually possesses higher initial CO_2 electrochemical performance. However, Ni/GDC cermets have some disadvantages as compared to Ni-YSZ, related to their lower mechanical stability which is essential in the fabrication of electrode supported cells. In addition, ceria has relatively higher cost than YSZ, while at strong reducing conditions the electronic conductivity of ceria increases, which can cause short-cut problems in the SOC device.

Intrigued by our observations, we attempt to combine the robust mechanical (bulk) properties of Ni-YSZ with the beneficial surface properties of ceria. As found in chapters 3 and 4, these properties are the enhanced CO_2 oxidation resistance of cerium-based materials and their use as a source of mobile oxygen ions during the polarization. Theoretically, introducing ceria on the surface of Ni/YSZ can provide abundant cerium oxide interface sites on the Ni/YSZ electrode and improve high overpotential losses and poor durability issues, while retaining the advantages of Ni/YSZ, including its excellent thermal and mechanical stability.

However, going from the concept to a practical electrochemical device is not straightforward, and requires facing and solving a lot of technical issues. By reviewing the literature of infiltration methods on cermet electrodes, we came across several key difficulties, such as laborious preparation methods with multiple impregnation/calcination/reduction cycles, pore clogging issues *etc.,* which are actually a brake for scale up and utilization of this method in practice. Therefore in chapter 5, we discuss the impregnation of cerium nanoparticles into the pores of prefabricated Ni/YSZ electrodes, by using a novel and simple strategy, which in our opinion, can be easily scaled up and integrated in the current electrode preparation technologies [232]. According to the proposed method [11,12], un-doped (CeO_x) and Ni-doped ($NiCeO_y$) ceria particles with sizes around 5 nm, are dispersed in hexane solution and applied directly into pre-

fabricated Ni/YSZ cermet electrodes via filling the pores of the electrode with the organic solution (infiltration). Detailed characterization of the particles in solution revealed differences in the ease of agglomeration, with $NiCeO_y$ nanoparticles being better dispersed and forming relatively smaller aggregates. This property was identified as critical for the effectiveness of ceria deposition into the pores of Ni/YSZ cermet. In particular, morphological and microstructural characterization revealed that $NiCeO_y$ nanoparticles, even just after one infiltration/co-firing step, decorate uniformly the pores of Ni/YSZ backbone, deep up to the interface with the electrolyte (Figure 7.3). On the contrary, CeO_x nanoparticles remain primarily on the Ni/YSZ surface with limited insertion into its volume. Notably, the $NiCeO_y$ nanoparticles exhibit enhanced reducibility in H_2 as compared to CeO_x which is expected to influence the dynamic oxygen storage capacity of the modified electrode. The most remarkable property is that, due to the low surface tension of hexane, one infiltration/co-firing step is required to achieve high ceria catalyst loading, while in literature processes with 10 or more steps are described.
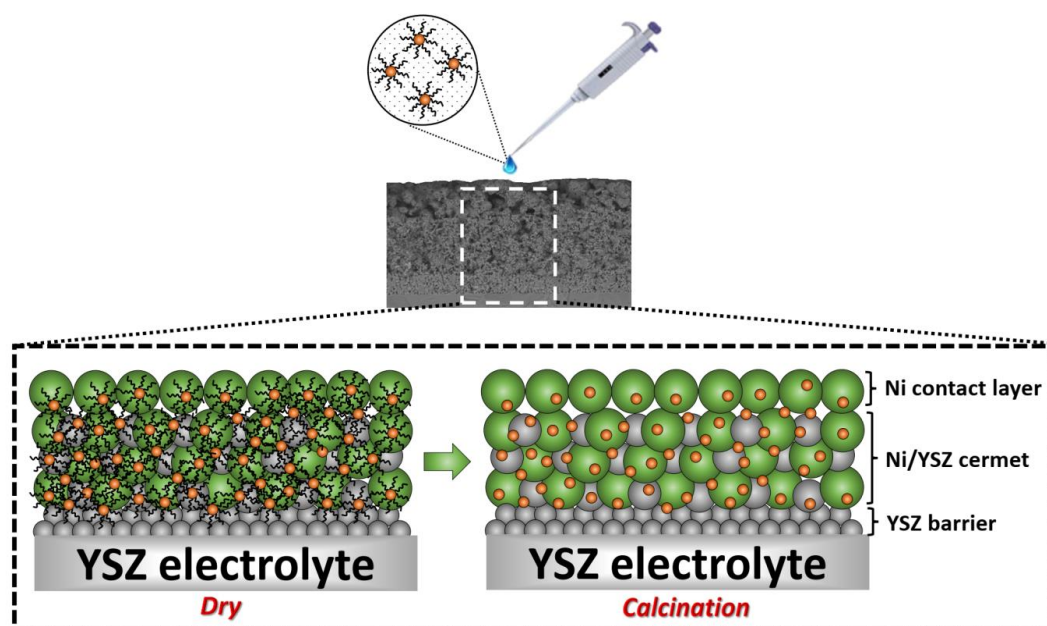
Figure 7.3. Schematic representation of the arrangement of the $NiCeO_y$ NPs over the Ni/YSZ cermet before and after the firing step.

In the last chapter (chapter 6), electrochemical evaluation experiments combined with physicochemical characterization of the cells are discussed. The presented results demonstrate that introduction of doped cerium nanoparticles through the novel impregnation strategy, not only

promotes the electrocatalytic performance for CO_2 electrolysis, but can be also used as an effective and simple method to recover the activity of partially deactivated Ni/YSZ electrodes. Therefore, nanosized Ni-doped CeO_2 oxide is a promising candidate for modification of Ni/YSZ cathode through infiltration method of organic solution in SOC applications.

7.2. Perspectives and proposed future work

In this thesis, the electrolysis performance tests of unmodified and modified Ni/YSZ electrodes through the novel impregnation strategy, were performed on the same miniature cells (1/4 fragment of a 2 cm diameter button cell) used to study the infiltration process. In this way eventual uncertainties caused by the preparation of larger area cells could be avoided. In addition, both miniature cells (pristine and modified) were derived from the same parent button cell, excluding possible uncertainties due to differences in the bulk cell characteristics.

An additional key point of this work was the possibility to perform surface characterization of the modified electrodes before and after the electrochemical tests, so as to identify possible surface impurities or carbon deposition which could affect the electrochemical performance and mask the effect of surface modification. Therefore, the electrochemical tests were conducted in a single chamber reactor attached to the UHV setup. The electrochemical performance during CO_2 electrolysis was evaluated by comparing the current-voltage (I-V) curves of cells with pristine and $NiCeO_y$-modified Ni/YSZ cathodes. The tests were performed at two temperatures in CO_2/H_2 mixtures without balance gas in the mbar pressure range (one of the restrictions using the particular testing setup). Tests involving accelerated aging of cathodes using repeated redox treatments were examined, but unfortunately it was not possible to perform long-term stability tests using this setup. The candidate is aware, that long-term stability is a key question for the practical applications of SOC technology.

Therefore, it is proposed that in the future these electrodes should be tested under conventional operation conditions in order to explore the commercial interest of the proposed method. This means, first in a single cell mode, for example using button cells with modified Ni/YSZ cathodes, and eventually in stack-level. It would be also extremely interesting to test if the proposed infiltration method can be used to re-activate aged electrodes, as indicated in chapter 6. For this purpose one can use button cells after operating for several hundred hours in CO_2-steam electrolysis, infiltrate them with $NiCeO_y$ NPs and test them again to see if, and in which degree, the electrochemical performance is restored.

Another point deserving further study is the observation that pure CO_2 electrolysis over Ni/GDC cathodes is feasible, when an optimal electrode surface state (metallic nickel and partially reduced ceria) is maintained. It is important to be able to remove H_2 from the fuel feed because this will considerably simplify the engineering of electrolysis stacks. Therefore, electro reduction of NiO under polarization demonstrated in our study, is probably an issue to explore in detail. To do so, the optimal operation conditions (gas feed, temperature and polarization) should be determined so as the electrode to be maintained to a mixed oxidation state and to not undergo full reduction by the current or complete oxidation by the CO_2 gas phase. Possibly, theoretical simulations can be also useful in this respect.

In addition, it was shown in this thesis that introduction of ceria nanoparticles on the surface of nickel-based cermet electrodes enhances the oxidation resistance of nickel under CO_2 atmosphere. However, it was also shown that there is a clear pressure gap effect in the oxidation of nickel by CO_2: above 5 mbar nickel oxidation takes place in few minutes, while at lower pressures, oxidation was not observed in the time scale of the experiment. The "anti-oxidant" effect of ceria nanoparticles on the electrode surface should be therefore studied in more detail. For example, cermet electrodes should be exposed in mixtures of CO_2 with inert gas with different CO_2 concentrations and their efficiency for nickel oxidation should be examined. In a later step, the effect of CO_2 concentration can be also studied in electrolysis conditions.

Another critical parameter, which was not studied in detail in this thesis, is the effect of temperature. SOEC devices operate typically in a certain temperature window (650-950 °C), usually defined by the ionic conductivity of YSZ. Therefore it would be interesting to investigate the effect of temperature in the oxidation resistance of Ni/YSZ in CO_2 atmospheres, with and without addition of ceria nanoparticles.

Finally, application of NiCe NPs could be extended to different kinds of SOEC electrode materials and other electrolysis applications such as steam electrolysis and co-electrolysis of CO_2/H_2O. For example, perovskite-based cathode electrodes have attracted more and more attention as the new candidates for cathode materials in SOECs, due to their adequate ionic and electrical conductivity as well as their high stability at high temperature. However, the comparatively poor catalytic activity is the main challenge for most perovskite-related oxides. As shown in this thesis, the infiltrated ceria nanoparticles can easily access the whole volume of the electrode without considerable influence on its macroscopic characteristics (e.g. porosity). Therefore, impregnation

of other type of electrodes with the NiCe NPs used in this study might be an effective approach to increase their electrocatalytic performance, developing more robust and active solid oxide electrodes for fuel cell and electrolysis applications.

Last but not least, the infiltration method proposed here was demonstrated mainly for Ni-doped ceria nanoparticles, but allows implementation of a wide range of different electro-catalysts. Synthesis of other type of nanoparticles with the same method is feasible. For example, ceria could be doped with other cations (e.g. Co, Ru or Pt), or nanoparticles of other catalytic active elements not containing ceria at all (e.g. vanadium oxide, manganese oxide). As shown here, the property which is critical for the efficiency of the infiltration method is the dispersion and the size of the nanoparticles in the hexane solution. If this can be optimized beforehand, then impregnation and testing can be done for several candidate materials, hoping to identify materials which can improve both performance and durability of Ni/YSZ electrodes.

This page intentionally left blank

References

[1]   X. Duan, J. Xu, Z. Wei, J. Ma, S. Guo, S. Wang, H. Liu, S. Dou, Metal-Free Carbon Materials for CO_2 Electrochemical Reduction, Adv. Mater. 29 (2017) 1701784. https://doi.org/10.1002/adma.201701784.

[2]   X. Zhang, Y. Song, G. Wang, X. Bao, Co-electrolysis of CO_2 and H_2O in high-temperature solid oxide electrolysis cells: Recent advance in cathodes, J. Energy Chem. 26 (2017) 839–853. https://doi.org/10.1016/j.jechem.2017.07.003.

[3]   Nasa device extracts breathable oxygen from thin Martian air, The Irish Times. (n.d.). https://doi.org/https://www.irishtimes.com/news/science/nasa-device-extracts-breathable-oxygen-from-thin-martian-air-1.4544767.

[4]   M. Rao, X. Sun, A. Hagen, Durability of solid oxide electrolysis stack under dynamic load cycling for syngas production, J. Power Sources. 451 (2020) 227781. https://doi.org/10.1016/j.jpowsour.2020.227781.

[5]   M. Hubert, J. Laurencin, P. Cloetens, B. Morel, D. Montinaro, F. Lefebvre-Joud, Impact of Nickel agglomeration on Solid Oxide Cell operated in fuel cell and electrolysis modes, J. Power Sources. 397 (2018) 240–251. https://doi.org/10.1016/j.jpowsour.2018.06.097.

[6]   V. Papaefthimiou, M. Shishkin, D.K. Niakolas, M. Athanasiou, Y.T. Law, R. Arrigo, D. Teschner, M. Hävecker, A. Knop-Gericke, R. Schlögl, T. Ziegler, S.G. Neophytides, S. Zafeiratos, On the active surface state of nickel-ceria solid oxide fuel cell anodes during methane electrooxidation, Adv. Energy Mater. 3 (2013) 762–769. https://doi.org/10.1002/aenm.201200727.

[7]   F. Paloukis, K.M. Papazisi, T. Dintzer, V. Papaefthimiou, V.A. Saveleva, S.P. Balomenou, D. Tsiplakides, F. Bournel, J.J. Gallet, S. Zafeiratos, Insights into the Surface Reactivity of Cermet and Perovskite Electrodes in Oxidizing, Reducing, and Humid Environments, ACS Appl. Mater. Interfaces. 9 (2017) 25265–25277. https://doi.org/10.1021/acsami.7b05721.

[8]   V. Singh, H. Muroyama, T. Matsui, S. Hashigami, T. Inagaki, K. Eguchi, Feasibility of alternative electrode materials for high temperature CO_2 reduction on solid oxide electrolysis cell, J. Power Sources. 293 (2015) 642–648. https://doi.org/10.1016/j.jpowsour.2015.05.088.

[9] L. Ye, K. Xie, High-temperature electrocatalysis and key materials in solid oxide electrolysis cells, J. Energy Chem. 54 (2021) 736–745. https://doi.org/https://doi.org/10.1016/j.jechem.2020.06.050.

[10] A. SCIAZKO, T. SHIMURA, Y. KOMATSU, N. SHIKAZONO, Ni-GDC and Ni-YSZ electrodes operated in solid oxide electrolysis and fuel cell modes, J. Therm. Sci. Technol. 16 (2021) JTST0013–JTST0013. https://doi.org/10.1299/jtst.2021jtst0013.

[11] W. Derafa, F. Paloukis, B. Mewafy, W. Baaziz, O. Ersen, C. Petit, G. Corbel, S. Zafeiratos, Synthesis and characterization of nickel-doped ceria nanoparticles with improved surface reducibility, RSC Adv. 8 (2018) 40712–40719. https://doi.org/10.1039/C8RA07995A.

[12] M. Barreau, C. Petit, S. Labidi, K. Sobczak, Surdacka, S. Turczyniak-Surdacka, S. Zafeiratos, Ni doping as a strategy to improve CeO_2 reducibility under CO_2 and H_2O atmospheres, (2022) in preparation.

[13] A.P. Ramos, Dynamic Light Scattering Applied to Nanoparticle Characterization, in: Nanocharacterization Tech., Elsevier Inc., 2017: pp. 99–110. https://doi.org/10.1016/B978-0-323-49778-7.00004-7.

[14] M. Bui, C.S. Adjiman, A. Bardow, E.J. Anthony, A. Boston, S. Brown, P.S. Fennell, S. Fuss, A. Galindo, L.A. Hackett, J.P. Hallett, H.J. Herzog, G. Jackson, J. Kemper, S. Krevor, G.C. Maitland, M. Matuszewski, I.S. Metcalfe, C. Petit, G. Puxty, J. Reimer, D.M. Reiner, E.S. Rubin, S.A. Scott, N. Shah, B. Smit, J.P.M. Trusler, P. Webley, J. Wilcox, N. Mac Dowell, Carbon capture and storage (CCS): The way forward, Energy Environ. Sci. 11 (2018) 1062–1176. https://doi.org/10.1039/c7ee02342a.

[15] F.A. Rahman, M.M.A. Aziz, R. Saidur, W.A.W.A. Bakar, M.R. Hainin, R. Putrajaya, N.A. Hassan, Pollution to solution: Capture and sequestration of carbon dioxide (CO_2) and its utilization as a renewable energy source for a sustainable future, Renew. Sustain. Energy Rev. 71 (2017) 112–126. https://doi.org/10.1016/j.rser.2017.01.011.

[16] Y. Zheng, J. Wang, B. Yu, W. Zhang, J. Chen, J. Qiao, J. Zhang, A review of high temperature co-electrolysis of H_2O and CO_2 to produce sustainable fuels using solid oxide electrolysis cells (SOECs): Advanced materials and technology, Chem. Soc. Rev. 46 (2017) 1427–1463. https://doi.org/10.1039/c6cs00403b.

[17] D.T. Whipple, P.J.A. Kenis, Prospects of CO_2 utilization via direct heterogeneous

electrochemical reduction, J. Phys. Chem. Lett. 1 (2010) 3451–3458. https://doi.org/10.1021/jz1012627.

[18] Z. Yin, D. Gao, S. Yao, B. Zhao, F. Cai, L. Lin, P. Tang, P. Zhai, G. Wang, D. Ma, X. Bao, Highly selective palladium-copper bimetallic electrocatalysts for the electrochemical reduction of CO_2 to CO, Nano Energy. 27 (2016) 35–43. https://doi.org/10.1016/j.nanoen.2016.06.035.

[19] T. Zheng, K. Jiang, H. Wang, Recent Advances in Electrochemical CO_2-to-CO Conversion on Heterogeneous Catalysts, Adv. Mater. 30 (2018) 1802066. https://doi.org/10.1002/adma.201802066.

[20] I. Merino-Garcia, E. Alvarez-Guerra, J. Albo, A. Irabien, Electrochemical membrane reactors for the utilisation of carbon dioxide, Chem. Eng. J. 305 (2016) 104–120. https://doi.org/10.1016/j.cej.2016.05.032.

[21] C.T. Dinh, T. Burdyny, G. Kibria, A. Seifitokaldani, C.M. Gabardo, F. Pelayo García De Arquer, A. Kiani, J.P. Edwards, P. De Luna, O.S. Bushuyev, C. Zou, R. Quintero-Bermudez, Y. Pang, D. Sinton, E.H. Sargent, CO_2 electroreduction to ethylene via hydroxide-mediated copper catalysis at an abrupt interface, Science (80-.). 360 (2018) 783–787. https://doi.org/10.1126/science.aas9100.

[22] S. Ma, R. Luo, S. Moniri, Y. Lan, P.J.A. Kenis, Efficient Electrochemical Flow System with Improved Anode for the Conversion of CO_2 to CO, J. Electrochem. Soc. 161 (2014) F1124–F1131. https://doi.org/10.1149/2.1201410jes.

[23] W. Weng, L. Tang, W. Xiao, Capture and electro-splitting of CO_2 in molten salts, J. Energy Chem. 28 (2019) 128–143. https://doi.org/10.1016/j.jechem.2018.06.012.

[24] B. Deng, X. Mao, W. Xiao, D. Wang, Microbubble effect-assisted electrolytic synthesis of hollow carbon spheres from CO_2, J. Mater. Chem. A. 5 (2017) 12822–12827. https://doi.org/10.1039/c7ta03606j.

[25] Z. Li, D. Yuan, H. Wu, W. Li, D. Gu, A novel route to synthesize carbon spheres and carbon nanotubes from carbon dioxide in a molten carbonate electrolyzer, Inorg. Chem. Front. 5 (2018) 208–216. https://doi.org/10.1039/c7qi00479f.

[26] Y. Song, Z. Zhou, X. Zhang, Y. Zhou, H. Gong, H. Lv, Q. Liu, G. Wang, X. Bao, Pure CO_2 electrolysis over an Ni/YSZ cathode in a solid oxide electrolysis cell, J. Mater. Chem. A. 6

(2018) 13661–13667. https://doi.org/10.1039/c8ta02858c.

[27] R.Z. L Elikan, DH Archer, Oxygen Regeneration in Solid Electrolyte Batteries: Fundamental Considerations, Chem. Eng. Prog. Symp. Ser. 62 (1966) 29.

[28] M. Hecht, J. Hoffman, D. Rapp, J. McClean, J. SooHoo, R. Schaefer, A. Aboobaker, J. Mellstrom, J. Hartvigsen, F. Meyen, E. Hinterman, G. Voecks, A. Liu, M. Nasr, J. Lewis, J. Johnson, C. Guernsey, J. Swoboda, C. Eckert, C. Alcalde, M. Poirier, P. Khopkar, S. Elangovan, M. Madsen, P. Smith, C. Graves, G. Sanders, K. Araghi, M. de la Torre Juarez, D. Larsen, J. Agui, A. Burns, K. Lackner, R. Nielsen, T. Pike, B. Tata, K. Wilson, T. Brown, T. Disarro, R. Morris, R. Schaefer, R. Steinkraus, R. Surampudi, T. Werne, A. Ponce, Mars Oxygen ISRU Experiment (MOXIE), Space Sci. Rev. 217 (2021) 1–76. https://doi.org/10.1007/s11214-020-00782-8.

[29] Y. Song, X. Zhang, K. Xie, G. Wang, X. Bao, High-Temperature CO_2 Electrolysis in Solid Oxide Electrolysis Cells: Developments, Challenges, and Prospects, Adv. Mater. 31 (2019) 1902033. https://doi.org/10.1002/adma.201902033.

[30] J.P. Stempien, Q. Sun, S.H. Chan, Performance of power generation extension system based on solid-oxide electrolyzer cells under various design conditions, Energy. 55 (2013) 647–657. https://doi.org/10.1016/j.energy.2013.03.031.

[31] A. VahidMohammadi, Z. Cheng, Fundamentals of Synthesis, Sintering Issues, and Chemical Stability of $BaZr_{0.1}Ce_{0.7}Y_{0.1}Yb_{0.1}O_{3-\delta}$ Proton Conducting Electrolyte for SOFCs , J. Electrochem. Soc. 162 (2015) F803–F811. https://doi.org/10.1149/2.0021508jes.

[32] T. Ishiyama, H. Kishimoto, K. Develos-Bagarinao, K. Yamaji, T. Yamaguchi, Y. Fujishiro, Decomposition reaction of $BaZr_{0.1}Ce_{0.7}Y_{0.1}Yb_{0.1}O_{3-\delta}$ in carbon dioxide atmosphere with nickel sintering aid, J. Ceram. Soc. Japan. 125 (2017) 247–251. https://doi.org/10.2109/jcersj2.16281.

[33] Mars Oxygen ISRU Experiment - Wikipedia, (n.d.). https://en.wikipedia.org/wiki/Mars_Oxygen_ISRU_Experiment (accessed May 12, 2021).

[34] J. Hartvigsen, S. Elangovan, J. Elwell, D. Larsen, Oxygen Production from Mars Atmosphere Carbon Dioxide Using Solid Oxide Electrolysis, ECS Trans. 78 (2017) 2953–2963. https://doi.org/10.1149/07801.2953ecst.

[35] Y. Shi, Y. Luo, N. Cai, J. Qian, S. Wang, W. Li, H. Wang, Experimental characterization

and modeling of the electrochemical reduction of CO_2 in solid oxide electrolysis cells, Electrochim. Acta. 88 (2013) 644–653. https://doi.org/10.1016/j.electacta.2012.10.107.

[36] Z. Zhan, L. Zhao, Electrochemical reduction of CO_2 in solid oxide electrolysis cells, J. Power Sources. 195 (2010) 7250–7254. https://doi.org/10.1016/j.jpowsour.2010.05.037.

[37] S. Balomenou, K.M. Papazisi, D. Tsiplakides, Ceramic Fuel Electrodes for Reversible Solid Oxide Cells Operating on Carbon Dioxide, ECS Trans. 78 (2017) 3237–3245. https://doi.org/10.1149/07801.3237ecst.

[38] V. Singh, S. Hashigami, H. Muroyama, T. Matsui, T. Inagaki, K. Eguchi, Influence of Fabrication Routes on Microstructure and Electrochemical Performance of Ni–GDC Cathode for High Temperature CO_2 Reduction in Solid Oxide Electrolysis Cells, J. Electrochem. Soc. 163 (2016) F3084–F3090. https://doi.org/10.1149/2.0111611jes.

[39] W. Li, Y. Shi, Y. Luo, Y. Wang, N. Cai, Carbon monoxide/carbon dioxide electrochemical conversion on patterned nickel electrodes operating in fuel cell and electrolysis cell modes, Int. J. Hydrogen Energy. 41 (2016) 3762–3773. https://doi.org/10.1016/j.ijhydene.2016.01.019.

[40] V. Singh, H. Muroyama, T. Matsui, S. Hashigami, T. Inagaki, K. Eguchi, Feasibility of alternative electrode materials for high temperature CO_2 reduction on solid oxide electrolysis cell, J. Power Sources. 293 (2015) 642–648. https://doi.org/https://doi.org/10.1016/j.jpowsour.2015.05.088.

[41] K. Eguchi, T. Hatagishi, H. Arai, Power generation and steam electrolysis characteristics of an electrochemical cell with a zirconia- or ceria-based electrolyte, Solid State Ionics. 86–88 (1996) 1245–1249. https://doi.org/10.1016/0167-2738(96)00295-0.

[42] A. Momma, T. Kato, Y. Kaga, S. Nagata, Polarization behavior of high temperature solid oxide electrolysis cells (SOEC), J. Ceram. Soc. Japan. 105 (1997) 369–373. https://doi.org/10.2109/jcersj.105.369.

[43] J. Yan, H. Chen, E. Dogdibegovic, J.W. Stevenson, M. Cheng, X. D. Zhou, High-efficiency intermediate temperature solid oxide electrolyzer cells for the conversion of carbon dioxide to fuels, J. Power Sources. 252 (2014) 79–84. https://doi.org/https://doi.org/10.1016/j.jpowsour.2013.11.047.

[44] A.L. Dipu, Y. Ujisawa, J. Ryu, Y. Kato, Electrolysis of carbon dioxide for carbon monoxide

production in a tubular solid oxide electrolysis cell, Ann. Nucl. Energy. 81 (2015) 257–262. https://doi.org/10.1016/j.anucene.2015.02.046.

[45] A. Mahmood, S. Bano, J.H. Yu, K.H. Lee, Effect of operating conditions on the performance of solid electrolyte membrane reactor for steam and CO_2 electrolysis, J. Memb. Sci. 473 (2015) 8–15. https://doi.org/10.1016/j.memsci.2014.09.002.

[46] W. Li, Y. Shi, Y. Luo, Y. Wang, N. Cai, Carbon deposition on patterned nickel/yttria stabilized zirconia electrodes for solid oxide fuel cell/solid oxide electrolysis cell modes, J. Power Sources. 276 (2015) 26–31. https://doi.org/10.1016/j.jpowsour.2014.11.106.

[47] F. Bidrawn, G. Kim, G. Corre, J.T.S. Irvine, J.M. Vohs, R.J. Gorte, Efficient reduction of CO_2 in a solid oxide electrolyzer, Electrochem. Solid-State Lett. 11 (2008) B167. https://doi.org/10.1149/1.2943664.

[48] X. Yue, J.T.S. Irvine, Alternative Cathode Material for CO_2 Reduction by High Temperature Solid Oxide Electrolysis Cells , J. Electrochem. Soc. 159 (2012) F442–F448. https://doi.org/10.1149/2.040208jes.

[49] D. Dong, S. Xu, X. Shao, L. Hucker, J. Marin, T. Pham, K. Xie, Z. Ye, P. Yang, L. Yu, G. Parkinson, C.Z. Li, Hierarchically ordered porous Ni-based cathode-supported solid oxide electrolysis cells for stable CO_2 electrolysis without safe gas, J. Mater. Chem. A. 5 (2017) 24098–24102. https://doi.org/10.1039/c7ta06839e.

[50] Y. Tao, S.D. Ebbesen, M.B. Mogensen, Degradation of solid oxide cells during co-electrolysis of steam and carbon dioxide at high current densities, J. Power Sources. 328 (2016) 452–462. https://doi.org/10.1016/j.jpowsour.2016.08.055.

[51] Z. Cao, B. Wei, J. Miao, Z. Wang, Z. Lü, W. Li, Y. Zhang, X. Huang, X. Zhu, Q. Feng, Y. Sui, Efficient electrolysis of CO_2 in symmetrical solid oxide electrolysis cell with highly active $La_{0.3}Sr_{0.7}Fe_{0.7}Ti_{0.3}O_3$ electrode material, Electrochem. Commun. 69 (2016) 80–83. https://doi.org/10.1016/j.elecom.2016.06.008.

[52] Y.Q. Zhang, J.H. Li, Y.F. Sun, B. Hua, J.L. Luo, Highly Active and Redox-Stable Ce-Doped LaSrCrFeO-Based Cathode Catalyst for CO_2 SOECs, ACS Appl. Mater. Interfaces. 8 (2016) 6457–6463. https://doi.org/10.1021/acsami.5b11979.

[53] S. Liu, Q. Liu, J.L. Luo, The excellence of $La(Sr)Fe(Ni)O_3$ as an active and efficient cathode for direct CO_2 electrochemical reduction at elevated temperatures, J. Mater. Chem. A. 5

(2017) 2673–2680. https://doi.org/10.1039/c6ta09151b.

[54]   A.P. Kulkarni, S. Giddey, S.P.S. Badwal, Efficient conversion of CO_2 in solid oxide electrolytic cells with Pd doped perovskite cathode on ceria nanofilm interlayer, J. CO_2 Util. 17 (2017) 180–187. https://doi.org/10.1016/j.jcou.2016.11.014.

[55]   L. Ye, C. Pan, M. Zhang, C. Li, F. Chen, L. Gan, K. Xie, Highly Efficient CO_2 Electrolysis on Cathodes with Exsolved Alkaline Earth Oxide Nanostructures, ACS Appl. Mater. Interfaces. 9 (2017) 25350–25357. https://doi.org/10.1021/acsami.7b07039.

[56]   S. Liu, Q. Liu, J.L. Luo, CO_2-to-CO conversion on layered perovskite with in situ exsolved Co-Fe alloy nanoparticles: An active and stable cathode for solid oxide electrolysis cells, J. Mater. Chem. A. 4 (2016) 17521–17528. https://doi.org/10.1039/c6ta06365a.

[57]   L. Gan, L. Ye, S. Tao, K. Xie, Titanate cathodes with enhanced electrical properties achieved via growing surface Ni particles toward efficient carbon dioxide electrolysis, Phys. Chem. Chem. Phys. 18 (2016) 3137–3143. https://doi.org/10.1039/c5cp06742a.

[58]   Y. Li, B. Hu, C. Xia, W.Q. Xu, J.P. Lemmon, F. Chen, A novel fuel electrode enabling direct CO_2 electrolysis with excellent and stable cell performance, J. Mater. Chem. A. 5 (2017) 20833–20842. https://doi.org/10.1039/c7ta05750d.

[59]   S. Liu, Q. Liu, J.L. Luo, Highly Stable and Efficient Catalyst with in Situ Exsolved Fe-Ni Alloy Nanospheres Socketed on an Oxygen Deficient Perovskite for Direct CO_2 Electrolysis, ACS Catal. 6 (2016) 6219–6228. https://doi.org/10.1021/acscatal.6b01555.

[60]   S. Liu, Q. Liu, J.-L. Luo, In-Situ Exsolved Alloy Nanoparticles on Perovskite for Direct CO_2 Reduction , ECS Trans. 75 (2017) 1–6. https://doi.org/10.1149/07543.0001ecst.

[61]   P. Kim-Lohsoontorn, N. Laosiripojana, J. Bae, Performance of solid oxide electrolysis cell having bi-layered electrolyte during steam electrolysis and carbon dioxide electrolysis, in: Curr. Appl. Phys., North-Holland, 2011: pp. S223–S228. https://doi.org/10.1016/j.cap.2010.11.114.

[62]   S.P. Jiang, A comparison of O_2 reduction reactions on porous (La,Sr)MnO_3 and (La,Sr)(Co,Fe)O_3 electrodes, Solid State Ionics. 146 (2002) 1–22. https://doi.org/10.1016/S0167-2738(01)00997-3.

[63]   B. Zhu, I. Albinsson, C. Andersson, K. Borsand, M. Nilsson, B.E. Mellander, Electrolysis studies based on ceria-based composites, Electrochem. Commun. 8 (2006) 495–498.

https://doi.org/10.1016/j.elecom.2006.01.011.

[64]   J.B. Goodenough, Oxide-ion electrolytes, Annu. Rev. Mater. Res. 33 (2003) 91–128. https://doi.org/10.1146/annurev.matsci.33.022802.091651.

[65]   T. Ishihara, J. Tabuchi, S. Ishikawa, J. Yan, M. Enoki, H. Matsumoto, Recent progress in LaGaO$_3$ based solid electrolyte for intermediate temperature SOFCs, Solid State Ionics. 177 (2006) 1949–1953. https://doi.org/10.1016/j.ssi.2006.01.044.

[66]   N.M. Sammes, G.A. Tompsett, H. Näfe, F. Aldinger, Bismuth based oxide electrolytes - Structure and ionic conductivity, J. Eur. Ceram. Soc. 19 (1999) 1801–1826. https://doi.org/10.1016/S0955-2219(99)00009-6.

[67]   M.A. Laguna-Bercero, Recent advances in high temperature electrolysis using solid oxide fuel cells: A review, J. Power Sources. 203 (2012) 4–16. https://doi.org/10.1016/j.jpowsour.2011.12.019.

[68]   C. Jin, Y. Mao, N. Zhang, K. Sun, Fabrication and characterization of Ni-SSZ gradient anodes/SSZ electrolyte for anode-supported SOFCs by tape casting and co-sintering technique, Int. J. Hydrogen Energy. 40 (2015) 8433–8441. https://doi.org/10.1016/j.ijhydene.2015.04.088.

[69]   H. Miao, G. Liu, Y. Zhang, C. He, Y. Zheng, W.G. Wang, Improving the electrochemical properties of SSZ electrolyte-supported solid oxide fuel cells, Ceram. Int. 40 (2014) 14621–14626. https://doi.org/10.1016/j.ceramint.2014.06.048.

[70]   D.J.L. Brett, A. Atkinson, N.P. Brandon, S.J. Skinner, Intermediate temperature solid oxide fuel cells, Chem. Soc. Rev. 37 (2008) 1568–1578. https://doi.org/10.1039/b612060c.

[71]   P. Hjalmarsson, X. Sun, Y.L. Liu, M. Chen, Durability of high performance Ni-yttria stabilized zirconia supported solid oxide electrolysis cells at high current density, J. Power Sources. 262 (2014) 316–322. https://doi.org/10.1016/j.jpowsour.2014.03.133.

[72]   D. The, S. Grieshammer, M. Schroeder, M. Martin, M. Al Daroukh, F. Tietz, J. Schefold, A. Brisse, Microstructural comparison of solid oxide electrolyser cells operated for 6100 h and 9000 h, J. Power Sources. 275 (2015) 901–911. https://doi.org/10.1016/j.jpowsour.2014.10.188.

[73]   M. Keane, H. Fan, M. Han, P. Singh, Role of initial microstructure on nickel-YSZ cathode degradation in solid oxide electrolysis cells, Int. J. Hydrogen Energy. 39 (2014) 18718–

18726. https://doi.org/10.1016/j.ijhydene.2014.09.057.

[74]   A. Hauch, S.D. Ebbesen, S.H. Jensen, M. Mogensen, Solid Oxide Electrolysis Cells: Microstructure and Degradation of the Ni/Yttria-Stabilized Zirconia Electrode, J. Electrochem. Soc. 155 (2008) B1184. https://doi.org/10.1149/1.2967331.

[75]   J.T.S. Irvine, D. Neagu, M.C. Verbraeken, C. Chatzichristodoulou, C. Graves, M.B. Mogensen, Evolution of the electrochemical interface in high-temperature fuel cells and electrolysers, Nat. Energy. 1 (2016) 1–13. https://doi.org/10.1038/nenergy.2015.14.

[76]   Y. Tao, S.D. Ebbesen, M.B. Mogensen, Carbon Deposition in Solid Oxide Cells during Co-Electrolysis of H_2O and CO_2, J. Electrochem. Soc. 161 (2014) F337–F343. https://doi.org/10.1149/2.079403jes.

[77]   Y. Tao, S.D. Ebbesen, W. Zhang, M.B. Mogensen, Carbon nanotube growth on nanozirconia under strong cathodic polarization in steam and carbon dioxide, ChemCatChem. 6 (2014) 1220–1224. https://doi.org/10.1002/cctc.201300941.

[78]   T. Kushi, Effects of sulfur poisoning on degradation phenomena in oxygen electrodes of solid oxide electrolysis cells and solid oxide fuel cells, Int. J. Hydrogen Energy. 42 (2017) 9396–9405. https://doi.org/10.1016/j.ijhydene.2017.01.151.

[79]   J. Kim, H. Il Ji, H.P. Dasari, D. Shin, H. Song, J.H. Lee, B.K. Kim, H.J. Je, H.W. Lee, K.J. Yoon, Degradation mechanism of electrolyte and air electrode in solid oxide electrolysis cells operating at high polarization, Int. J. Hydrogen Energy. 38 (2013) 1225–1235. https://doi.org/10.1016/j.ijhydene.2012.10.113.

[80]   F. Tietz, D. Sebold, A. Brisse, J. Schefold, Degradation phenomena in a solid oxide electrolysis cell after 9000 h of operation, J. Power Sources. 223 (2013) 129–135. https://doi.org/10.1016/j.jpowsour.2012.09.061.

[81]   M.A. Laguna-Bercero, R. Campana, A. Larrea, J.A. Kilner, V.M. Orera, Electrolyte degradation in anode supported microtubular yttria stabilized zirconia-based solid oxide steam electrolysis cells at high voltages of operation, J. Power Sources. 196 (2011) 8942–8947. https://doi.org/10.1016/j.jpowsour.2011.01.015.

[82]   R. Knibbe, M.L. Traulsen, A. Hauch, S.D. Ebbesen, M. Mogensen, Solid Oxide Electrolysis Cells: Degradation at High Current Densities, J. Electrochem. Soc. 157 (2010) B1209. https://doi.org/10.1149/1.3447752.

[83] K. Chen, S.P. Jiang, Failure mechanism of (La,Sr)MnO$_3$ oxygen electrodes of solid oxide electrolysis cells, Int. J. Hydrogen Energy. 36 (2011) 10541–10549. https://doi.org/10.1016/j.ijhydene.2011.05.103.

[84] M. Keane, M.K. Mahapatra, A. Verma, P. Singh, LSM-YSZ interactions and anode delamination in solid oxide electrolysis cells, Int. J. Hydrogen Energy. 37 (2012) 16776–16785. https://doi.org/10.1016/j.ijhydene.2012.08.104.

[85] V. Duboviks, R.C. Maher, M. Kishimoto, L.F. Cohen, N.P. Brandon, G.J. Offer, A Raman spectroscopic study of the carbon deposition mechanism on Ni/CGO electrodes during CO/CO$_2$ electrolysis, Phys. Chem. Chem. Phys. 16 (2014) 13063–13068. https://doi.org/10.1039/c4cp01503g.

[86] T.L. Skafte, P. Blennow, J. Hjelm, C. Graves, Carbon deposition and sulfur poisoning during CO$_2$ electrolysis in nickel-based solid oxide cell electrodes, J. Power Sources. 373 (2018) 54–60. https://doi.org/10.1016/j.jpowsour.2017.10.097.

[87] Y. Choi, E.C. Brown, S.M. Haile, W.C. Jung, Electrochemically modified, robust solid oxide fuel cell anode for direct-hydrocarbon utilization, Nano Energy. 23 (2016) 161–171. https://doi.org/10.1016/j.nanoen.2016.03.015.

[88] T.L. Skafte, B.R. Sudireddy, P. Blennow, C. Graves, Carbon and Redox Tolerant Infiltrated Oxide Fuel-Electrodes for Solid Oxide Cells, ECS Trans. 72 (2016) 201–214. https://doi.org/10.1149/07207.0201ecst.

[89] T.L. Skafte, Z. Guan, M.L. Machala, C.B. Gopal, M. Monti, L. Martinez, E. Stamate, S. Sanna, J.A. Garrido Torres, E.J. Crumlin, M. García-Melchor, M. Bajdich, W.C. Chueh, C. Graves, Selective high-temperature CO$_2$ electrolysis enabled by oxidized carbon intermediates, Nat. Energy. 4 (2019) 846–855. https://doi.org/10.1038/s41560-019-0457-4.

[90] J. Wang, S.R. Bishop, L. Sun, Q. Lu, G. Vardar, R. Bliem, N. Tsvetkov, E.J. Crumlin, J.J. Gallet, F. Bournel, I. Waluyo, B. Yildiz, Threshold catalytic onset of carbon formation on CeO$_2$ during CO$_2$ electrolysis: Mechanism and inhibition, J. Mater. Chem. A. 7 (2019) 15233–15243. https://doi.org/10.1039/c9ta03265g.

[91] V. Papaefthimiou, D.K. Niakolas, F. Paloukis, T. Dintzer, S. Zafeiratos, Is Steam an Oxidant or a Reductant for Nickel/Doped-Ceria Cermets?, ChemPhysChem. 18 (2017) 164–170. https://doi.org/10.1002/cphc.201600948.

[92] F. Paloukis, K.M. Papazisi, T. Dintzer, V. Papaefthimiou, V.A. Saveleva, S.P. Balomenou, D. Tsiplakides, F. Bournel, J.-J.J. Gallet, S. Zafeiratos, Insights into the Surface Reactivity of Cermet and Perovskite Electrodes in Oxidizing, Reducing, and Humid Environments, ACS Appl. Mater. Interfaces. 9 (2017) 25265–25277. https://doi.org/10.1021/acsami.7b05721.

[93] V. Papaefthimiou, D.K. Niakolas, F. Paloukis, D. Teschner, A. Knop-Gericke, M. Haevecker, S. Zafeiratos, Operando observation of nickel/ceria electrode surfaces during intermediate temperature steam electrolysis, J. Catal. 352 (2017) 305–313. https://doi.org/10.1016/j.jcat.2017.06.005.

[94] D. Sarantaridis, A. Atkinson, Redox cycling of Ni-based solid oxide fuel cell anodes: A review, in: Fuel Cells, John Wiley & Sons, Ltd, 2007: pp. 246–258. https://doi.org/10.1002/fuce.200600028.

[95] B. Mewafy, F. Paloukis, K.M. Papazisi, S.P. Balomenou, W. Luo, D. Teschner, O. Joubert, A. Le Gal La Salle, D.K. Niakolas, S. Zafeiratos, Influence of Surface State on the Electrochemical Performance of Nickel-Based Cermet Electrodes during Steam Electrolysis, ACS Appl. Energy Mater. 2 (2019) 7045–7055. https://doi.org/10.1021/acsaem.9b00779.

[96] Y. Yu, B. Mao, A. Geller, R. Chang, K. Gaskell, Z. Liu, B.W. Eichhorn, CO_2 activation and carbonate intermediates: An operando AP-XPS study of CO_2 electrolysis reactions on solid oxide electrochemical cells, Phys. Chem. Chem. Phys. 16 (2014) 11633–11639. https://doi.org/10.1039/c4cp01054j.

[97] Z.A. Feng, M.L. Machala, W.C. Chueh, Surface electrochemistry of CO_2 reduction and CO oxidation on Sm-doped CeO_{2-x}: Coupling between Ce^{3+} and carbonate adsorbates, Phys. Chem. Chem. Phys. 17 (2015) 12273–12281. https://doi.org/10.1039/c5cp00114e.

[98] E. Lay-Grindler, J. Laurencin, J. Villanova, P. Cloetens, P. Bleuet, A. Mansuy, J. Mougin, G. Delette, Degradation study by 3D reconstruction of a nickel-yttria stabilized zirconia cathode after high temperature steam electrolysis operation, J. Power Sources. 269 (2014) 927–936. https://doi.org/10.1016/j.jpowsour.2014.07.066.

[99] J. Xu, X. Zhou, L. Pan, M. Wu, K. Sun, Oxide composite of $La_{0.3}Sr_{0.7}Ti_{0.3}Fe_{0.7}O_{3-\delta}$ and CeO_2 as an active fuel electrode for reversible solid oxide cells, J. Power Sources. 371 (2017) 1–

9. https://doi.org/10.1016/j.jpowsour.2017.10.016.

[100] T.Z. Sholklapper, C.P. Jacobson, S.J. Visco, L.C. Dejonghe, Synthesis of dispersed and contiguous nanoparticles in solid oxide fuel cell electrodes, Fuel Cells. 8 (2008) 303–312. https://doi.org/10.1002/fuce.200800030.

[101] Y. Huang, J.M. Vohs, R.J. Gorte, SOFC cathodes prepared by infiltration with various LSM precursors, Electrochem. Solid-State Lett. 9 (2006) A237. https://doi.org/10.1149/1.2183867.

[102] T. Fengqiu, H. Xiaoxian, Z. Yufeng, G. Jingkun, Effect of dispersants on surface chemical properties of nano-zirconia suspensions, Ceram. Int. 26 (2000) 93–97. https://doi.org/10.1016/S0272-8842(99)00024-3.

[103] P. Kim-Lohsoontorn, Y.M. Kim, N. Laosiripojana, J. Bae, Gadolinium doped ceria-impregnated nickel-yttria stabilised zirconia cathode for solid oxide electrolysis cell, Int. J. Hydrogen Energy. 36 (2011) 9420–9427. https://doi.org/10.1016/j.ijhydene.2011.04.199.

[104] E. Ruiz-Trejo, A. Atkinson, N.P. Brandon, Metallizing porous scaffolds as an alternative fabrication method for solid oxide fuel cell anodes, J. Power Sources. 280 (2015) 81–89. https://doi.org/10.1016/j.jpowsour.2015.01.091.

[105] Z. Jiang, Z. Lei, B. Ding, C. Xia, F. Zhao, F. Chen, Electrochemical characteristics of solid oxide fuel cell cathodes prepared by infiltrating $(La,Sr)MnO_3$ nanoparticles into yttria-stabilized bismuth oxide backbones, in: Int. J. Hydrogen Energy, Pergamon, 2010: pp. 8322–8330. https://doi.org/10.1016/j.ijhydene.2009.12.008.

[106] J.D. Nicholas, S.A. Barnett, Measurements and Modeling of $Sm_{0.5}Sr_{0.5}CoO_{(3−x)}$–$Ce_{0.9}Gd_{0.1}O_{1.95}$ SOFC Cathodes Produced Using Infiltrate Solution Additives, J. Electrochem. Soc. 157 (2010) B536. https://doi.org/10.1149/1.3284519.

[107] X. Lou, Z. Liu, S. Wang, Y. Xiu, C.P. Wong, M. Liu, Controlling the morphology and uniformity of a catalyst-infiltrated cathode for solid oxide fuel cells by tuning wetting property, J. Power Sources. 195 (2010) 419–424. https://doi.org/10.1016/j.jpowsour.2009.07.048.

[108] A. Buyukaksoy, V. Petrovsky, F. Dogan, Optimization of Redox Stable Ni-YSZ Anodes for SOFCs by Two-Step Infiltration, J. Electrochem. Soc. 159 (2012) F841–F848. https://doi.org/10.1149/2.075212jes.

[109] R. Fernández-González, J.C. Ruiz-Morales, J. Canales-Vázquez, J.R. Jurado, A. Makradi, P. Núñez, Decreasing the polarisation resistance of a Ni-YSZ solid oxide fuel cell anode by infiltration of a ceria-based solution, Int. J. Hydrogen Energy. 41 (2016) 19731–19736. https://doi.org/10.1016/j.ijhydene.2016.03.092.

[110] J. Karczewski, B. Bochentyn, S. Molin, M. Gazda, P. Jasinski, B. Kusz, Solid oxide fuel cells with Ni-infiltrated perovskite anode, Solid State Ionics. 221 (2012) 11–14. https://doi.org/10.1016/j.ssi.2012.06.002.

[111] J. Shen, Y. Chen, G. Yang, W. Zhou, M.O. Tadé, Z. Shao, Impregnated $LaCo_{0.3}Fe_{0.67}Pd_{0.03}O_{3-\delta}$ as a promising electrocatalyst for "symmetrical" intermediate-temperature solid oxide fuel cells, J. Power Sources. 306 (2016) 92–99. https://doi.org/10.1016/j.jpowsour.2015.12.021.

[112] O. Ozmen, S. Lee, G. Hackett, H. Abernathy, J.W. Zondlo, E.M. Sabolsky, Efficient and controlled nano-catalyst solid-oxide fuel cell electrode infiltration with poly-norepinephrine surface modification, J. Power Sources. 485 (2021) 229232. https://doi.org/10.1016/j.jpowsour.2020.229232.

[113] E.C. Miller, Q. Sherman, Z. Gao, P.W. Voorhees, S.A. Barnett, Stability of Nickel-Infiltrated Anodes in Intermediate Temperature SOFCs, ECS Trans. 68 (2015) 1245–1254. https://doi.org/10.1149/06801.1245ecst.

[114] J. Mason, I. Celik, S. Lee, H. Abernathy, G. Hackett, Performance Degradation Predictions Based on Microstructural Evolution Due to Grain Coarsening Effects in Solid Oxide Fuel Cell Electrodes, J. Electrochem. Soc. 165 (2018) F64–F74. https://doi.org/10.1149/2.0721802jes.

[115] D.K. Niakolas, J.P. Ouweltjes, G. Rietveld, V. Dracopoulos, S.G. Neophytides, Au-doped Ni/GDC as a new anode for SOFCs operating under rich CH_4 internal steam reforming, Int. J. Hydrogen Energy. 35 (2010) 7898–7904. https://doi.org/10.1016/J.IJHYDENE.2010.05.038.

[116] V. Saveleva, Investigation of the anodes of PEM water electrolyzers by operando synchrotron-based photoemission spectroscopy, (2018).

[117] W. Luo, S. Zafeiratos, Tuning Morphology and Redox Properties of Cobalt Particles Supported on Oxides by an in between Graphene Layer, J. Phys. Chem. C. 120 (2016)

14130–14139. https://doi.org/10.1021/acs.jpcc.6b03595.

[118] D.E. Starr, Z. Liu, M. Hävecker, A. Knop-Gericke, H. Bluhm, Investigation of solid/vapor interfaces using ambient pressure X-ray photoelectron spectroscopy, Chem. Soc. Rev. 42 (2013) 5833–5857. https://doi.org/10.1039/c3cs60057b.

[119] X. Liu, W. Yang, Z. Liu, Recent progress on synchrotron-based in-situ soft X-ray spectroscopy for energy materials, Adv. Mater. 26 (2014) 7710–7729. https://doi.org/10.1002/adma.201304676.

[120] J.W. John F. Watts, An Introduction to Surface Analysis by XPS and AES, Wiley,2003, n.d.

[121] A. Knop-Gericke, E. Kleimenov, M. Hävecker, R. Blume, D. Teschner, S. Zafeiratos, R. Schlögl, V.I. Bukhtiyarov, V. V. Kaichev, I.P. Prosvirin, A.I. Nizovskii, H. Bluhm, A. Barinov, P. Dudin, M. Kiskinova, Chapter 4 X-Ray Photoelectron Spectroscopy for Investigation of Heterogeneous Catalytic Processes, Adv. Catal. 52 (2009) 213–272. https://doi.org/10.1016/S0360-0564(08)00004-7.

[122] L. Zhong, D. Chen, S. Zafeiratos, A mini review of in situ near-ambient pressure XPS studies on non-noble, late transition metal catalysts, Catal. Sci. Technol. 9 (2019) 3851–3867. https://doi.org/10.1039/c9cy00632j.

[123] M.C. Biesinger, B.P. Payne, A.P. Grosvenor, L.W.M. Lau, A.R. Gerson, R.S.C. Smart, Resolving surface chemical states in XPS analysis of first row transition metals, oxides and hydroxides: Cr, Mn, Fe, Co and Ni, Appl. Surf. Sci. 257 (2011) 2717–2730. https://doi.org/10.1016/j.apsusc.2010.10.051.

[124] E. Bêche, P. Charvin, D. Perarnau, S. Abanades, G. Flamant, Ce 3d XPS investigation of cerium oxides and mixed cerium oxide ($Ce_xTi_yO_z$), Surf. Interface Anal. 40 (2008) 264–267. https://doi.org/https://doi.org/10.1002/sia.2686.

[125] S. Kato, M. Ammann, T. Huthwelker, C. Paun, M. Lampimäki, M.-T. Lee, M. Rothensteiner, J.A. van Bokhoven, Quantitative depth profiling of Ce^{3+} in Pt/CeO_2 by in situ high-energy XPS in a hydrogen atmosphere, Phys. Chem. Chem. Phys. 17 (2015) 5078–5083. https://doi.org/10.1039/C4CP05643D.

[126] R.C. Maher, G. Kerherve, D.J. Payne, X. Yue, P.A. Connor, J. Irvine, L.F. Cohen, The Reduction Properties of M–Doped (M=Zr, Gd) CeO_2/YSZ Scaffolds Co–Infiltrated with

Nickel, Energy Technol. 6 (2018) 2045–2052. https://doi.org/10.1002/ente.201800146.

[127] A.P. Grosvenor, M.C. Biesinger, R.S.C. Smart, N.S. McIntyre, New interpretations of XPS spectra of nickel metal and oxides, Surf. Sci. 600 (2006) 1771–1779. https://doi.org/10.1016/j.susc.2006.01.041.

[128] D. Channei, B. Inceesungvorn, N. Wetchakun, S. Ukritnukun, A. Nattestad, J. Chen, S. Phanichphant, Photocatalytic Degradation of Methyl Orange by CeO_2 and Fe–doped CeO_2 Films under Visible Light Irradiation, Sci. Rep. 4 (2014) 5757. https://doi.org/10.1038/srep05757.

[129] B.P. Payne, M.C. Biesinger, N.S. McIntyre, The study of polycrystalline nickel metal oxidation by water vapour, J. Electron Spectros. Relat. Phenomena. 175 (2009) 55–65. https://doi.org/10.1016/j.elspec.2009.07.006.

[130] S. Zafeiratos, S. Kennou, The interaction of oxygen with ultrathin Ni deposits on yttria-stabilized ZrO_2(1 0 0), Surf. Sci. 482–485 (2001) 266–271. https://doi.org/10.1016/S0039-6028(01)00929-3.

[131] W.C. Chueh, A.H. McDaniel, M.E. Grass, Y. Hao, N. Jabeen, Z. Liu, S.M. Haile, K.F. McCarty, H. Bluhm, F. El Gabaly, Highly Enhanced Concentration and Stability of Reactive Ce^{3+} on Doped CeO_2 Surface Revealed In Operando, Chem. Mater. 24 (2012) 1876–1882. https://doi.org/10.1021/cm300574v.

[132] T. Tabakova, Effect of additives on the WGS activity of combustion synthesized CuO/ CeO_2 catalysts, 8 (2007) 101–106. https://doi.org/10.1016/j.catcom.2006.05.032.

[133] WebCrossSections,(n.d.). https://vuo.elettra.eu/services/elements/WebElements.html (accessed June 2, 2021).

[134] M. Grossi, B. Riccò, M. Grossi, B. Riccò, M. Grossi, B. Riccò, Electrical impedance spectroscopy (EIS) for biological analysis and food characterization : a review To cite this version : HAL Id : hal-01579247 Electrical impedance spectroscopy (EIS) for biological analysis and food characterization : a review, (2017) 303–325.

[135] P.S. Shah, J.D. Holmes, K.P. Johnston, B.A. Korgel, Size-selective dispersion of dodecanethiol-coated nanocrystals in liquid and supereritical ethane by density tuning, J. Phys. Chem. B. 106 (2002) 2545–2551. https://doi.org/10.1021/jp0139311.

[136] T. Arita, J. Yoo, Y. Ueda, T. Adschiri, Size and size distribution balance the dispersion of

colloidal CeO₂ nanoparticles in organic solvents, Nanoscale. 2 (2010) 689–693. https://doi.org/10.1039/b9nr00395a.

[137] S. Usune, M. Ando, M. Kubo, T. Tsukada, K.I. Sugioka, O. Koike, R. Tatsumi, M. Fujita, S. Takami, T. Adschiri, Numerical simulation of dispersion and aggregation behavior of surface-modified nanoparticles in organic solvents, J. Chem. Eng. Japan. 51 (2018) 492–500. https://doi.org/10.1252/jcej.17we197.

[138] B. Faure, G. Salazar-Alvarez, A. Ahniyaz, I. Villaluenga, G. Berriozabal, Y.R. De Miguel, L. Bergström, Dispersion and surface functionalization of oxide nanoparticles for transparent photocatalytic and UV-protecting coatings and sunscreens, Sci. Technol. Adv. Mater. 14 (2013). https://doi.org/10.1088/1468-6996/14/2/023001.

[139] B. Vincent, J. Edwards, S. Emmett, A. Jones, Depletion flocculation in dispersions of sterically-stabilised particles ("soft spheres"), Colloids and Surfaces. 18 (1986) 261–281. https://doi.org/10.1016/0166-6622(86)80317-1.

[140] A. Hauch, R. Küngas, P. Blennow, A.B. Hansen, J.B. Hansen, B. V Mathiesen, M.B. Mogensen, Recent advances in solid oxide cell technology for electrolysis, Science (80-.). 370 (2020). https://doi.org/10.1126/science.aba6118.

[141] S.D. Ebbesen, R. Knibbe, M. Mogensen, Co-Electrolysis of Steam and Carbon Dioxide in Solid Oxide Cells, J. Electrochem. Soc. 159 (2012) F482--F489. https://doi.org/10.1149/2.076208jes.

[142] A. Jun, J. Kim, J. Shin, G. Kim, Achieving High Efficiency and Eliminating Degradation in Solid Oxide Electrochemical Cells Using High Oxygen-Capacity Perovskite, Angew. Chemie Int. Ed. 55 (2016) 12512–12515. https://doi.org/https://doi.org/10.1002/anie.201606972.

[143] S.D. Ebbesen, M. Mogensen, Electrolysis of carbon dioxide in Solid Oxide Electrolysis Cells, J. Power Sources. 193 (2009) 349–358. https://doi.org/10.1016/j.jpowsour.2009.02.093.

[144] J.S. Elias, M. Risch, L. Giordano, A.N. Mansour, Y. Shao-Horn, Structure, bonding, and catalytic activity of monodisperse, transition-metal-substituted CeO₂ nanoparticles, J. Am. Chem. Soc. 136 (2014) 17193–17200. https://doi.org/10.1021/ja509214d.

[145] A. Kaliyaraj Selva Kumar, Y. Zhang, D. Li, R.G. Compton, A mini-review: How reliable

is the drop casting technique?, Electrochem. Commun. 121 (2020) 106867. https://doi.org/https://doi.org/10.1016/j.elecom.2020.106867.

[146] F. Paloukis, K.M. Papazisi, S.P. Balomenou, D. Tsiplakides, F. Bournel, J.J. Gallet, S. Zafeiratos, In situ X-ray photoelectron spectroscopy study of complex oxides under gas and vacuum environments, Appl. Surf. Sci. 423 (2017) 1176–1181. https://doi.org/10.1016/j.apsusc.2017.06.219.

[147] L. Zhong, T. Kropp, W. Baaziz, O. Ersen, D. Teschner, R. Schlögl, M. Mavrikakis, S. Zafeiratos, Correlation between Reactivity and Oxidation State of Cobalt Oxide Catalysts for CO Preferential Oxidation, ACS Catal. 9 (2019) 8325–8336. https://doi.org/10.1021/acscatal.9b02582.

[148] S. Turczyniak, D. Teschner, A. Machocki, S. Zafeiratos, Effect of the surface state on the catalytic performance of a Co/CeO_2 ethanol steam-reforming catalyst, J. Catal. 340 (2016) 321–330. https://doi.org/10.1016/j.jcat.2016.05.017.

[149] A.G. Marrani, V. Novelli, S. Sheehan, D.P. Dowling, D. Dini, Probing the Redox States at the Surface of Electroactive Nanoporous NiO Thin Films, ACS Appl. Mater. Interfaces. 6 (2014) 143–152. https://doi.org/10.1021/am403671h.

[150] F. El Gabaly, K.F. McCarty, H. Bluhm, A.H. McDaniel, Oxidation stages of Ni electrodes in solid oxide fuel cell environments , Phys. Chem. Chem. Phys. 15 (2013) 8334–8341. https://doi.org/10.1039/c3cp50366f.

[151] S. Zafeiratos, S. Kennou, Gold/nickel ultrathin bimetallic overlayers on yttria-stabilized ZrO_2 (100), J. Phys. Chem. B. 106 (2002). https://doi.org/10.1021/jp0124591.

[152] S. Rhatigan, M. Nolan, CO_2 and water activation on ceria nanocluster modified TiO_2 rutile (110), J. Mater. Chem. A. 6 (2018) 9139–9152. https://doi.org/10.1039/C8TA01270A.

[153] S.E. Rawadieh, M. Altarawneh, I.S. Altarawneh, M.A. Batiha, L.A. Al-Makhadmeh, A kinetic model for evolution of H_2 and CO over Zr-doped ceria, Mol. Catal. 498 (2020) 111256. https://doi.org/10.1016/j.mcat.2020.111256.

[154] J. Carrasco, D. Lõpez-Durán, Z. Liu, T. Duchoň, J. Evans, S.D. Senanayake, E.J. Crumlin, V. Matolín, J.A. Rodríguez, M.V. Ganduglia-Pirovano, In situ and theoretical studies for the dissociation of water on an active Ni/CeO_2 Catalyst: Importance of strong metal-support interactions for the cleavage of O-H bonds, Angew. Chemie - Int. Ed. 54 (2015) 3917–3921.

https://doi.org/10.1002/anie.201410697.

[155] P. Li, X. Chen, Y. Li, J.W. Schwank, A review on oxygen storage capacity of CeO_2-based materials: Influence factors, measurement techniques, and applications in reactions related to catalytic automotive emissions control, Catal. Today. 327 (2019) 90–115. https://doi.org/https://doi.org/10.1016/j.cattod.2018.05.059.

[156] T. Staudt, Y. Lykhach, N. Tsud, T. Skála, K.C. Prince, V. Matolín, J. Libuda, Ceria reoxidation by CO_2: A model study, J. Catal. 275 (2010) 181–185. https://doi.org/10.1016/j.jcat.2010.07.032.

[157] Z.A. Feng, F. El Gabaly, X. Ye, Z.X. Shen, W.C. Chueh, Fast vacancy-mediated oxygen ion incorporation across the ceria-gas electrochemical interface, Nat. Commun. 5 (2014) 1–9. https://doi.org/10.1038/ncomms5374.

[158] C. Balaji Gopal, M. García-Melchor, S.C. Lee, Y. Shi, A. Shavorskiy, M. Monti, Z. Guan, R. Sinclair, H. Bluhm, A. Vojvodic, W.C. Chueh, Equilibrium oxygen storage capacity of ultrathin $CeO_{2-\delta}$ depends non-monotonically on large biaxial strain, Nat. Commun. 8 (2017). https://doi.org/10.1038/ncomms15360.

[159] H. Wang, S. Luo, M. Zhang, W. Liu, X. Wu, S. Liu, Roles of oxygen vacancy and O_x^- in oxidation reactions over CeO_2 and Ag/CeO_2 nanorod model catalysts, J. Catal. 368 (2018) 365–378. https://doi.org/https://doi.org/10.1016/j.jcat.2018.10.018.

[160] A. Cadi-Essadek, A. Roldan, X. Aparicio-Anglès, N.H. De Leeuw, CO_2 and H_2 Adsorption and Reaction at Nin/YSZ(111) Interfaces: A Density Functional Theory Study, J. Phys. Chem. C. 122 (2018) 19463–19472. https://doi.org/10.1021/acs.jpcc.8b03488.

[161] Y. Jing, H. Matsumoto, N.R. Aluru, Mechanistic Insights into Hydration of Solid Oxides, Chem. Mater. 30 (2018) 138–144. https://doi.org/10.1021/acs.chemmater.7b03476.

[162] S. Zafeiratos, F.E. Paloukis, M.M. Jaksic, S.G. Neophytides, Thermal stability of electrodeposited nickel on vanadium: Evidence for oxygen diffusion and intermetallic phase formation, Surf. Sci. 552 (2004). https://doi.org/10.1016/j.susc.2004.01.021.

[163] B. Ren, J. Li, G. Wen, L. Ricardez-Sandoval, E. Croiset, First-Principles Based Microkinetic Modeling of CO_2 Reduction at the Ni/SDC Cathode of a Solid Oxide Electrolysis Cell, J. Phys. Chem. C. 122 (2018) 21151–21161. https://doi.org/10.1021/acs.jpcc.8b05312.

[164] F. Wang, H. Kishimoto, T. Ishiyama, K. Develos-Bagarinao, K. Yamaji, T. Horita, H. Yokokawa, Electrochemically Induced Nickel/Ceria Interaction in Solid Oxide Electrochemical Cells with Oxide Ion Conducting Electrolyte, J. Electrochem. Soc. 166 (2019) F587--F593. https://doi.org/10.1149/2.0451910jes.

[165] S. Gunduz, D.J. Deka, U.S. Ozkan, Advances in High-Temperature Electrocatalytic Reduction of CO_2 and H_2O, 1st ed., Elsevier Inc., 2018. https://doi.org/10.1016/bs.acat.2018.08.003.

[166] B.-K. Park, R. Scipioni, D. Cox, S.A. Barnett, Enhancement of Ni–$(Y_2O_3)_{0.08}(ZrO_2)_{0.92}$ fuel electrode performance by infiltration of $Ce_{0.8}Gd_{0.2}O_{2−\delta}$ nanoparticles, J. Mater. Chem. A. 8 (2020) 4099–4106. https://doi.org/10.1039/C9TA12316D.

[167] B.-K. Park, S.A. Barnett, Boosting solid oxide fuel cell performance via electrolyte thickness reduction and cathode infiltration, J. Mater. Chem. A. 8 (2020) 11626–11631. https://doi.org/10.1039/D0TA04280C.

[168] T.L. Skafte, J. Hjelm, P. Blennow, C. Graves, Reactivating the Ni-YSZ electrode in solid oxide cells and stacks by infiltration, J. Power Sources. 378 (2018) 685–690. https://doi.org/10.1016/j.jpowsour.2018.01.021.

[169] Z. Huang, Z. Zhao, H. Qi, X. Wang, B. Tu, M. Cheng, Enhancing cathode performance for CO_2 electrolysis with $Ce_{0.9}M_{0.1}O_{2−\delta}$ (M=Fe, Co, Ni) catalysts in solid oxide electrolysis cell, J. Energy Chem. 40 (2020) 46–51. https://doi.org/https://doi.org/10.1016/j.jechem.2019.02.007.

[170] W. Yue, Y. Li, Y. Zheng, T. Wu, C. Zhao, J. Zhao, G. Geng, W. Zhang, J. Chen, J. Zhu, B. Yu, Enhancing coking resistance of Ni/YSZ electrodes: In situ characterization, mechanism research, and surface engineering, Nano Energy. 62 (2019) 64–78. https://doi.org/10.1016/j.nanoen.2019.05.006.

[171] S. Wang, H. Jiang, Y. Gu, B. Yin, S. Chen, M. Shen, Y. Zheng, L. Ge, H. Chen, L. Guo, Mo-doped $La_{0.6}Sr_{0.4}FeO_{3-\delta}$ as an efficient fuel electrode for direct electrolysis of CO_2 in solid oxide electrolysis cells, Electrochim. Acta. 337 (2020) 135794. https://doi.org/10.1016/j.electacta.2020.135794.

[172] Y. Li, P. Li, B. Hu, C. Xia, A nanostructured ceramic fuel electrode for efficient CO_2/H_2O electrolysis without safe gas, J. Mater. Chem. A. 4 (2016) 9236–9243.

https://doi.org/10.1039/C6TA02830F.

[173] Y. Luo, W. Li, Y. Shi, N. Cai, Mechanism for reversible CO/CO_2 electrochemical conversion on a patterned nickel electrode, J. Power Sources. 366 (2017) 93–104. https://doi.org/10.1016/j.jpowsour.2017.09.019.

[174] Y. Luo, Y. Shi, W. Li, N. Cai, Elementary reaction modeling of reversible CO/CO_2 electrochemical conversion on patterned nickel electrodes, J. Power Sources. 379 (2018) 298–308. https://doi.org/10.1016/j.jpowsour.2018.01.016.

[175] W. Wang, L. Gan, J.P. Lemmon, F. Chen, J.T.S. Irvine, K. Xie, Enhanced carbon dioxide electrolysis at redox manipulated interfaces, Nat. Commun. 10 (2019). https://doi.org/10.1038/s41467-019-09568-1.

[176] J. Wang, S.R. Bishop, L. Sun, Q. Lu, G. Vardar, R. Bliem, N. Tsvetkov, E.J. Crumlin, J.-J. Gallet, F. Bournel, I. Waluyo, B. Yildiz, Threshold catalytic onset of carbon formation on CeO_2 during CO_2 electrolysis: mechanism and inhibition, J. Mater. Chem. A. 7 (2019) 15233–15243. https://doi.org/10.1039/C9TA03265G.

[177] Y. Han, H. Zhang, Y. Yu, Z. Liu, In Situ Characterization of Catalysis and Electrocatalysis Using APXPS, ACS Catal. 11 (2021) 1464–1484. https://doi.org/10.1021/acscatal.0c04251.

[178] Y. Jiang, F. Chen, C. Xia, A review on cathode processes and materials for electro-reduction of carbon dioxide in solid oxide electrolysis cells, J. Power Sources. 493 (2021) 229713. https://doi.org/https://doi.org/10.1016/j.jpowsour.2021.229713.

[179] W.C. Chueh, Y. Hao, W. Jung, S.M. Haile, High electrochemical activity of the oxide phase in model ceria-Pt and ceria-Ni composite anodes, Nat. Mater. 11 (2012) 155–161. https://doi.org/10.1038/nmat3184.

[180] B. Bozzini, M. Amati, C. Mele, A. Knop-Gericke, E. Vesselli, An in situ near-ambient pressure X-ray photoelectron spectroscopy study of CO_2 reduction at Cu in a SOE cell, J. Electroanal. Chem. 799 (2017) 17–25. https://doi.org/10.1016/j.jelechem.2017.05.011.

[181] B. Bozzini, M. Amati, P. Bocchetta, S. Dal Zilio, A. Knop-Gericke, E. Vesselli, M. Kiskinova, An in situ near-ambient pressure X-ray Photoelectron Spectroscopy study of Mn polarised anodically in a cell with solid oxide electrolyte, Electrochim. Acta. 174 (2015) 532–541. https://doi.org/10.1016/j.electacta.2015.05.173.

[182] A.K. Opitz, A. Nenning, C. Rameshan, M. Kubicek, T. Götsch, R. Blume, M. Hävecker, A. Knop-Gericke, G. Rupprechter, B. Klötzer, J. Fleig, Surface Chemistry of Perovskite-Type Electrodes During High Temperature CO_2 Electrolysis Investigated by *Operando* Photoelectron Spectroscopy, ACS Appl. Mater. Interfaces. 9 (2017) 35847–35860. https://doi.org/10.1021/acsami.7b10673.

[183] S. Hu, L. Zhang, Z. Cao, W. Yu, P. Zhang, X. Zhu, W. Yang, Cathode activation process and CO_2 electroreduction mechanism on $LnFeO_{3-\delta}$ (Ln=La, Pr and Gd) perovskite cathodes, J. Power Sources. 485 (2021) 229343. https://doi.org/10.1016/j.jpowsour.2020.229343.

[184] S. Turczyniak, D. Teschner, A. Machocki, S. Zafeiratos, Effect of the surface state on the catalytic performance of a Co/CeO_2 ethanol steam-reforming catalyst, J. Catal. 340 (2016) 321–330. https://doi.org/10.1016/j.jcat.2016.05.017.

[185] J.J. Yeh, I. Lindau, Atomic subshell photoionization cross sections and asymmetry parameters: 1<Z<103, At. Data Nucl. Data Tables. 32 (1985) 1–155. https://doi.org/10.1016/0092-640X(85)90016-6.

[186] M.A. Henderson, C.L. Perkins, M.H. Engelhard, S. Thevuthasan, C.H.F. Peden, Redox properties of water on the oxidized and reduced surfaces of CeO_2(1 1 1), Surf. Sci. 526 (2003) 1–18. https://doi.org/10.1016/S0039-6028(02)02657-2.

[187] A. Schaefer, B. Hagman, J. Höcker, U. Hejral, J.I. Flege, J. Gustafson, Thermal reduction of ceria nanostructures on rhodium(111) and re-oxidation by CO_2, Phys. Chem. Chem. Phys. 20 (2018) 19447–19457. https://doi.org/10.1039/c8cp01505h.

[188] W.L. Jang, Y.M. Lu, W.S. Hwang, C.L. Dong, P.H. Hsieh, C.L. Chen, T.S. Chan, J.F. Lee, A study of thermal decomposition of sputtered {NiO} films, {EPL} (Europhysics Lett. 96 (2011) 37009. https://doi.org/10.1209/0295-5075/96/37009.

[189] W. Brückner, R. Kaltofen, J. Thomas, M. Hecker, M. Uhlemann, S. Oswald, D. Elefant, C.M. Schneider, Stress development in sputtered NiO thin films during heat treatment, J. Appl. Phys. 94 (2003) 4853–4858. https://doi.org/10.1063/1.1609052.

[190] D. Chen, D.K. Niakolas, V. Papaefthimiou, E. Ioannidou, S.G. Neophytides, S. Zafeiratos, How the surface state of nickel/gadolinium-doped ceria cathodes influences the electrochemical performance in direct CO_2 electrolysis, J. Catal. 404 (2021) 518–528.

[191] P.I. Giotakos, S.G. Neophytides, Physical modeling of the electrochemical impedance

spectra for the O_2 reduction reaction in HTPEM fuel cells' cathodic electrochemical interface, Electrochim. Acta. 292 (2018) 285–291. https://doi.org/https://doi.org/10.1016/j.electacta.2018.08.141.

[192] W.H. Doh, V. Papaefthimiou, T. Dintzer, V.V. Dupuis, S. Zafeiratos, Synchrotron radiation X-ray photoelectron spectroscopy as a tool to resolve the dimensions of spherical core/shell nanoparticles, J. Phys. Chem. C. 118 (2014) 26621–26628. https://doi.org/10.1021/jp508895u.

[193] C. Dueso, M. Ortiz, A. Abad, F. García-Labiano, L.F. De Diego, P. Gayán, J. Adánez, Reduction and oxidation kinetics of nickel-based oxygen-carriers for chemical-looping combustion and chemical-looping reforming, Chem. Eng. J. 188 (2012) 142–154. https://doi.org/10.1016/j.cej.2012.01.124.

[194] D. Knapp, T. Ziegler, Methane dissociation on the ceria (111) surface, J. Phys. Chem. C. 112 (2008) 17311–17318. https://doi.org/10.1021/jp8039862.

[195] I.-K. Oh, L. Zeng, J.-E. Kim, J.-S. Park, K. Kim, H. Lee, S. Seo, M.R. Khan, S. Kim, C.W. Park, J. Lee, B. Shong, Z. Lee, S.F. Bent, H. Kim, J.Y. Park, H.-B.-R. Lee, Surface Energy Change of Atomic-Scale Metal Oxide Thin Films by Phase Transformation, ACS Nano. 14 (2020) 676–687. https://doi.org/10.1021/acsnano.9b07430.

[196] T. Montini, M. Melchionna, M. Monai, P. Fornasiero, Fundamentals and Catalytic Applications of CeO_2-Based Materials, Chem. Rev. 116 (2016) 5987–6041. https://doi.org/10.1021/acs.chemrev.5b00603.

[197] Z.A. Feng, C. Balaji Gopal, X. Ye, Z. Guan, B. Jeong, E. Crumlin, W.C. Chueh, Origin of Overpotential-Dependent Surface Dipole at CeO_{2-x}/Gas Interface during Electrochemical Oxygen Insertion Reactions, Chem. Mater. 28 (2016) 6233–6242. https://doi.org/10.1021/acs.chemmater.6b02427.

[198] B. Mo, J. Rix, U. Pal, S. Basu, S. Gopalan, Improving SOFC Anode Electrocatalytic Activity Using Nanoparticle Infiltration into MIEC Compositions, J. Electrochem. Soc. 167 (2020) 134506. https://doi.org/10.1149/1945-7111/ABB70F.

[199] J. Dailly, A. Delrue, M. Ancelin, M. Marrony, Nanoparticles Infiltration into SOFC Cathode Backbones, ECS Trans. 78 (2017) 1979–1991. https://doi.org/10.1149/07801.1979ecst.

[200] H. Lv, Y. Zhou, X. Zhang, Y. Song, Q. Liu, G. Wang, X. Bao, Infiltration of $Ce_{0.8}Gd_{0.2}O_{1.9}$

nanoparticles on $Sr_2Fe_{1.5}Mo_{0.5}O_{6-\delta}$ cathode for CO_2 electroreduction in solid oxide electrolysis cell, J. Energy Chem. 35 (2019) 71–78. https://doi.org/10.1016/j.jechem.2018.11.002.

[201] X. Tong, P.V. Hendriksen, A. Hauch, X. Sun, M. Chen, An Up-scalable, Infiltration-Based Approach for Improving the Durability of Ni/{YSZ} Electrodes for Solid Oxide Cells, J. Electrochem. Soc. 167 (2020) 24519. https://doi.org/10.1149/1945-7111/ab6f5c.

[202] Y. Wang, X. Lin, L. Zhang, G. Xiao, C. Guan, J. Yang, X. Lv, D. Liu, J.-Q. Wang, Three-dimensional microstructural characterization of solid oxide electrolysis cell with $Ce_{0.8}Gd_{0.2}O_2$-infiltrated Ni/YSZ electrode using focused ion beam-scanning electron microscopy, J. Solid State Electrochem. 25 (2021) 1633–1644. https://doi.org/10.1007/s10008-021-04926-w.

[203] X. Zhang, Y. Song, F. Guan, Y. Zhou, H. Lv, G. Wang, X. Bao, Enhancing electrocatalytic CO_2 reduction in solid oxide electrolysis cell with $Ce_{0.9}Mn_{0.1}O_{2-\delta}$ nanoparticles-modified LSCM-GDC cathode, J. Catal. 359 (2018) 8–16. https://doi.org/10.1016/j.jcat.2017.12.027.

[204] J. Xu, B. Xue, Y.M. Liu, Y.X. Li, Y. Cao, K.N. Fan, Mesostructured Ni-doped ceria as an efficient catalyst for styrene synthesis by oxidative dehydrogenation of ethylbenzene, Appl. Catal. A Gen. 405 (2011) 142–148. https://doi.org/10.1016/j.apcata.2011.08.001.

[205] M. Shen, J. Wang, J. Shang, Y. An, J. Wang, W. Wang, Modification ceria-zirconia mixed oxides by doping sr using the reversed microemulsion for improved Pd-only three-way catalytic performance, J. Phys. Chem. C. 113 (2009) 1543–1551. https://doi.org/10.1021/jp808962r.

[206] P.J. Gasper, Y. Lu, A.Y. Nikiforov, S.N. Basu, S. Gopalan, U.B. Pal, Detailed electrochemical performance and microstructural characterization of nickel–Yttria stabilized zirconia cermet anodes infiltrated with nickel, gadolinium doped ceria, and nickel–Gadolinium doped ceria nanoparticles, J. Power Sources. 447 (2020) 227357. https://doi.org/https://doi.org/10.1016/j.jpowsour.2019.227357.

[207] T. Nagasawa, K. Hanamura, Prediction of overpotential and effective thickness of Ni/YSZ anode for solid oxide fuel cell by improved species territory adsorption model, J. Power Sources. 353 (2017) 115–122. https://doi.org/10.1016/j.jpowsour.2017.03.154.

[208] K. Miyawaki, M. Kishimoto, H. Iwai, M. Saito, H. Yoshida, Comprehensive understanding

of the active thickness in solid oxide fuel cell anodes using experimental, numerical and semi-analytical approach, J. Power Sources. 267 (2014) 503–514. https://doi.org/10.1016/j.jpowsour.2014.05.112.

[209]   B. Timurkutluk, C. Timurkutluk, M.D. Mat, Y. Kaplan, Anode-supported solid oxide fuel cells with ion conductor infiltration, Int. J. Energy Res. 35 (2011) 1048–1055. https://doi.org/10.1002/ER.1832.

[210]   J. Qiao, K. Sun, N. Zhang, B. Sun, J. Kong, D. Zhou, Ni/YSZ and Ni-CeO$_2$/YSZ anodes prepared by impregnation for solid oxide fuel cells, J. Power Sources. 169 (2007) 253–258. https://doi.org/10.1016/j.jpowsour.2007.03.006.

[211]   S.P. Jiang, Nanoscale and nano-structured electrodes of solid oxide fuel cells by infiltration: Advances and challenges, Int. J. Hydrogen Energy. 37 (2012) 449–470. https://doi.org/10.1016/j.ijhydene.2011.09.067.

[212]   O. Ozmen, Investigation of Nano-ceria Catalyst Infiltration of Solid Oxide Fuel Cell (SOFC) Electrodes Using Bio-Inspired Catechol Surfactants, Grad. Theses, Diss. Probl. Reports. (2019). https://doi.org/https://doi.org/10.33915/etd.7378.

[213]   S. Ovtar, X. Tong, J.J. Bentzen, K.T.S. Thydén, S.B. Simonsen, M. Chen, Boosting the performance and durability of Ni/YSZ cathode for hydrogen production at high current densities: Via decoration with nano-sized electrocatalysts, Nanoscale. 11 (2019) 4394–4406. https://doi.org/10.1039/c8nr07678b.

[214]   J. Vidal-Vidal, J. Rivas, M.A. López-Quintela, Synthesis of monodisperse maghemite nanoparticles by the microemulsion method, Colloids Surfaces A Physicochem. Eng. Asp. 288 (2006) 44–51. https://doi.org/10.1016/j.colsurfa.2006.04.027.

[215]   L. Hu, C. De Montferrand, Y. Lalatonne, L. Motte, A. Brioude, Effect of cobalt doping concentration on the crystalline structure and magnetic properties of monodisperse Co$_x$Fe$_{3-x}$O$_4$ nanoparticles within nonpolar and aqueous solvents, J. Phys. Chem. C. 116 (2012) 4349–4355. https://doi.org/10.1021/jp205088x.

[216]   M.S. Kuo, S.J. Chang, P.H. Hsieh, Y.C. Huang, C.C. Li, Efficient Dispersants for TiO$_2$ Nanopowder in Organic Suspensions, J. Am. Ceram. Soc. 99 (2016) 445–451. https://doi.org/10.1111/jace.14009.

[217]   F. Lan, J. Bai, H. Wang, The preparation of oleylamine modified micro-size sphere silver

particles and its application in crystalline silicon solar cells, RSC Adv. 8 (2018) 16866–16872. https://doi.org/10.1039/C8RA02620C.

[218] A. Faes, Q. Jeangros, J.B. Wagner, T.W. Hansen, J. Van Herle, A. Brisse, R. Dunin-Borkowski, A. Hessler-Wyser, In situ Reduction and Oxidation of Nickel from Solid Oxide Fuel Cells in a Transmission Electron Microscope, ECS Trans. 25 (2019) 1985–1992. https://doi.org/10.1149/1.3205743.

[219] X. Zhu, C. Guan, Z. Lü, B. Wei, Y. Li, W. Su, A rapid preparation of acicular Ni impregnated anode with enhanced conductivity and operational stability, J. Power Sources. 256 (2014) 424–429. https://doi.org/10.1016/J.JPOWSOUR.2014.01.058.

[220] D. Wilson, M.A. Langell, XPS analysis of oleylamine/oleic acid capped Fe_3O_4 nanoparticles as a function of temperature, Appl. Surf. Sci. 303 (2014) 6–13. https://doi.org/10.1016/j.apsusc.2014.02.006.

[221] O. Posdziech, K. Schwarze, J. Brabandt, Efficient hydrogen production for industry and electricity storage via high-temperature electrolysis, Int. J. Hydrogen Energy. 44 (2019) 19089–19101. https://doi.org/10.1016/j.ijhydene.2018.05.169.

[222] M. Chen, Y.-L. Liu, J.J. Bentzen, W. Zhang, X. Sun, A. Hauch, Y. Tao, J.R. Bowen, P.V. Hendriksen, Microstructural Degradation of Ni/YSZ Electrodes in Solid Oxide Electrolysis Cells under High Current, J. Electrochem. Soc. 160 (2013) F883–F891. https://doi.org/10.1149/2.098308JES.

[223] S.D. Ebbesen, C. Graves, A. Hauch, S.H. Jensen, M. Mogensen, Poisoning of Solid Oxide Electrolysis Cells by Impurities, J. Electrochem. Soc. 157 (2010) B1419. https://doi.org/10.1149/1.3464804.

[224] A. Nechache, B.A. Boukamp, M. Cassir, A. Ringuedé, Premature degradation study of a cathode-supported solid oxide electrolysis cell, J. Solid State Electrochem. 2018 231. 23 (2018) 109–123. https://doi.org/10.1007/S10008-018-4116-7.

[225] X. Tong, S. Ovtar, K. Brodersen, P.V. Hendriksen, M. Chen, Large-area solid oxide cells with $La_{0.6}Sr_{0.4}CoO_{3-\delta}$ infiltrated oxygen electrodes for electricity generation and hydrogen production, J. Power Sources. 451 (2020) 227742. https://doi.org/10.1016/J.JPOWSOUR.2020.227742.

[226] S.A. Barnett, B.-K. Park, R. Scipioni, Effect of Infiltration on Performance of Ni-YSZ Fuel

Electrodes, ECS Trans. 91 (2019) 1791. https://doi.org/10.1149/09101.1791ECST.

[227] E. Hernández, F. Baiutti, A. Morata, M. Torrell, A. Tarancón, Infiltrated mesoporous oxygen electrodes for high temperature co-electrolysis of H_2O and CO_2 in solid oxide electrolysis cells, J. Mater. Chem. A. 6 (2018) 9699–9707. https://doi.org/10.1039/C8TA01045E.

[228] X. Tong, S. Ovtar, K. Brodersen, P.V. Hendriksen, M. Chen, A 4×4 cm^2 Nanoengineered Solid Oxide Electrolysis Cell for Efficient and Durable Hydrogen Production, ACS Appl. Mater. Interfaces. 11 (2019) 25996–26004. https://doi.org/10.1021/ACSAMI.9B07749.

[229] Y. Chen, J. Bunch, C. Jin, C. Yang, F. Chen, Performance enhancement of Ni-YSZ electrode by impregnation of $Mo_{0.1}Ce_{0.9}O_{2+\delta}$, J. Power Sources. 204 (2012) 40–45. https://doi.org/10.1016/J.JPOWSOUR.2012.01.019.

[230] F.S. Torknik, M. Keyanpour-Rad, A. Maghsoudipour, G.M. Choi, Effect of microstructure refinement on performance of $Ni/Ce_{0.8}Gd_{0.2}O_{1.9}$ anodes for low temperature solid oxide fuel cell, Ceram. Int. 40 (2014) 1341–1350. https://doi.org/https://doi.org/10.1016/j.ceramint.2013.07.015.

[231] D. Chen, M. Barreau, T. Dintzer, S. Turczyniak-Surdacka, F. Bournel, J.-J. Gallet, S. Zafeiratos, Surface oxidation of Ni-cermet electrodes by CO_2 and H_2O and how to moderate it, J. Energy Chem. 67 (2022) 300–308. https://doi.org/10.1016/j.jechem.2021.10.002.

[232] D. Chen, M. Barreaua, S. Turczyniak-Surdacka, K. Sobczak, M. Strawski, A. Efimenko, D. Teschner, C. Petit, S. Zafeiratos, Ceria nanoparticles as promoters of CO_2 electroreduction on Ni/YSZ: an efficient preparation strategy and insights into the catalytic promotion mechanism, Nano Energy, In preparation (2022).

Curriculum Vitae

Dingkai Chen

Nationality: Chinese   Gender: Male   Date of birth: 10/01/1991

Address: 2B Route D'Oberhausbergen, 67200, Strasbourg, France

Phone: +33 766158216   Email: dingkai.chen@etu.unistra.fr & cdk684983@163.com

Educational Background

2018.09-present   University of Strasbourg   Strasbourg, FRANCE

PhD student: Major in Physical Chemistry

2014.09-2017.07 Kunming University of Science and Technology   Kunming, CHINA

Master of Engineering: Major in Environmental Engineering

2010.09-2014.07   Guangdong Ocean University   Zhanjiang, CHINA

Bachelor of Agriculture: Major in Agricultural Resources and Environment

Relevant Research Experiences

2018.09-present Institut de chimie et procédés pour l'énergie, l'environnement et la santé (ICPEES) UMR 7515 du CNRS National Center of Scientific Research (CNRS) & University of Strasbourg (UDS)

Supervisor: Dr. Spyridon Zafeiratos (HdR)

2014.09-2017.07 Advanced environmental functional material innovation team, Kunming University of Science and Technology

Supervisor: Professor Yongming Luo

Present Research Activity

- Investigation of the surface chemistry of cermet electrodes during high-temperature CO_2 Electrolysis via evaluation of surface characteristics by means of advanced characterization techniques (Synchrotron XPS, etc.) to establish a structure-performance relationship.

Journal Papers

- **Dingkai Chen**, Mathias Barreau, Thierry Dintzer, Sylwia Turczyniak-Surdacka, Fabrice Bournel, Jean-Jacques Gallet and Spyridon Zafeiratos*. Surface oxidation of Ni-cermet electrodes by CO_2 and H_2O and how to moderate it. *Journal of Energy Chemistry*, **2022**, 67, 300-308.

- **Dingkai Chen**, Dimitrios K. Niakolas, Vasiliki Papaefthimiou, Evangelia Ioannidou, Stylianos G. Neophytides, and Spyridon Zafeiratos*. How the surface state of nickel/gadolinium-doped ceria cathodes influences the electrochemical performance in direct CO_2 electrolysis. *Journal of Catalysis*, **2021**, 404, 518-528.

- **Dingkai Chen,** Mathias Barreau*, Sylwia Turczyniak-Surdacka, Kamil Sobczak, Marcin Strawski, Anna Efimenko, Detre Teschner, Corinne Petit, and Spyridon Zafeiratos*. Ceria nanoparticles as promoters of CO_2 electroreduction on Ni/YSZ: an efficient preparation strategy and insights into the catalytic promotion mechanism. *Nano Energy*, in preparation (2022).

- **Dingkai Chen**, Basma Mewafy, Fotios Paloukis, Liping Zhong, Vasiliki Papaefthimiou, Thierry Dintzer, Kalliopi Papazisi, Stella Balomenou, Dimitrios Tsiplakides, Detre Teschner, Virginia Pérez-Dieste, Carlos Escudero, Spyridon Zafeiratos*. Revising the Role of Chromium on the Surface of Perovskite Electrodes: Poison or Promoter for the Solid Oxide Electrolysis Cell Performance? *Journal of Catalysis*, **2020**, 381, 520–529.

- **Dingkai Chen**, Dehua Zhang, Dedong He, Jichang Lu, Liping Zhong, Caiyun Han, Yongming Luo*. Relationships between oxygen species and activity/stability in heteroatoms (Zr, Y) doped cerium based catalysts for catalytic decomposition of CH_3SH. *Chinese Journal of Catalysis*, **2018**, 39, 1929-1941.

- **Dingkai Chen**, Dedong He, Jichang Lu, Liping Zhong, Feng Liu, Jiangping Liu, Jie Yu, Gengping Wan, Sufang He, Yongming Luo*. Role of Surface Lattice Oxygen and Bulk

Lattice Oxygen Migration in the Oxidation of Hydrocarbons over Ceria-based Oxygen Carriers: XPS and Designed H_2-TPR investigations. *Applied Catalysis B: Environmental*, **2017**, 218, 249-259.

- **Dingkai Chen**, Dedong He, Jichang Lu, Feng Liu, Jiangping Liu, Jie Yu, Han Caiyun, Gao Xiaoya, He Sufang, Luo Yongming*. Preparation, characterization and CH_3SH catalytic decomposition of ceria-zirconia solid solution. *Journal of the Chinese rare earth society*, **2017**, 36(2), 172-182.

- Yutong Zhao, **Dingkai Chen**, Jiangping Liu, Dedong He, Xiaohua Cao, Caiyun Han, Jichang Lu*, YongmingLuo*. Tuning the metal-support interaction on chromium-based catalysts for catalytically eliminate methyl mercaptan: Anchored active chromium species through surface hydroxyl groups. *Chemical Engineering Journal*, **2020**, 389, 124384.

- Liping Zhong, **Dingkai Chen**, Spyridon Zafeiratos*. A mini review of in situ near-ambient pressure XPS studies on non-noble, late transition metal catalysts. *Catalysis Science & Technology*, **2019**, 9, 3851.

- Dedong He, **Dingkai Chen**, Husheng Hao, Jie Yu, Jiangping Liu, Jichang Lu, Gengping Wan, Sufang He, Kongzhai Li, Yongming Luo*. Enhanced activity and stability of Sm-doped HZSM-5 zeolite catalysts for catalytic methyl mercaptan (CH_3SH) decomposition. *Chemical Engineering Journal*, **2017**, 317, 60-69.

- Dedong He, **Dingkai Chen**, Husheng Hao, Jie Yu, Jiangping Liu, Jichang Lu, Feng Liu , Gengping Wan, Sufang He, Yongming Luo*. Structural/surface characterization and catalytic evaluation of rare-earth (Y, Sm and La) doped ceria composite oxides for CH3SH catalytic decomposition. *Applied Surface Science*, **2016**, 390, 959-967.

- Liping Zhong, Mathias Barreau*, **Dingkai Chen**, Valérie Caps, Michael Haevecker, Detre Teschner, David H. Simonne, Elisa Borfecchia, Walid Baaziz, Břetislav Šmíd, Spyridon Zafeiratos*. Effect of manganese promotion on the activity and selectivity of cobalt catalysts for CO preferential oxidation. *Applied Catalysis B: Environmental*, **2021**, 297, 120397.